# Narrow-linewidth, continuous-wave, intracavity terahertz lasers based on stimulated polariton scattering

By

**Yameng Zheng**

A thesis submitted to Macquarie University
for the degree of Doctor of Philosophy
Department of Physics and Astronomy
February 2019

MACQUARIE
University
SYDNEY · AUSTRALIA

Except where acknowledged in the customary manner, the material presented in this thesis is, to the best of my knowledge, original and has not been submitted in whole or part for a degree in any university.

Yameng Zheng

# Acknowledgements

I would like to express my profound gratitude to so many people who supported me during my PhD candidature. Without any of you, this thesis would not have been possible to complete.

First and foremost, I would like to gratefully acknowledge my supervisor Prof. Helen Pask, who gives me the opportunity to be part of her group and work on this excellent project. She has always been supportive and provided encouragement to overcome the difficulties I encountered in studies and my personal life. Her enthusiasm for academic research and the optimistic attitude to life have influenced me a lot. I have really appreciated her great effort in assisting me to complete this thesis.

I am deeply grateful to my supervisor Dr. Andrew Lee who has offered me such professional supervision and support. He has always being ready to help in the lab, discuss all the more difficult issues I encountered through my PhD study. I have learned immensely from him as a researcher and consider myself lucky to have benefited greatly from the skills of research under his guidance. I deeply appreciate the benefit of those research skills he has imparted to me.

My PhD journey has encountered difficulties due to family health issues. At one point I considered giving up my study to look after my family in the last year of study. Andrew provided the necessary encouragement and support that persuaded me to continue my study. The support he gave me provided a beacon of hope through his trust to build my confidence to continue the research work. Andrew's support has been invaluable in completing my work and I am extremely fortunate to have had the opportunity to work with him over the past few years.

I am also thankful to many other professors who have supported me over these years. Amongst them, David Spence in sharing his valuable inputs on the most complicated aspects of laser theory including his informed expertise during the trip to the ASSL conference with him. Deb Kane provided me with many opportunities to demonstrate the fundamental science for children. Rich Mildren's knowledgeable expertise that I gained much value, and his generosity in inviting me to join his group activities.

I would also like to express my gratitude to my colleagues, Tiago, Ran, Quan, Robert, Chris, Josh, Ondrej, Aaron, Andrea, Ben, Devika, Lisa, Danny, Ash, James, Adam, Liz, Vivienne, Mega, Victoria. And our 2018 KOALA committees: Dan, Thomas, Michelle, Atiyeh, Yang. It was my great pleasure to work with you. I was also lucky to have technical support from the METS which is an invaluable support service. Thanks for my special office mates: Soumya, Tushar, Saurabh, Mojtaba, Xuezong, Zhenxu, Muye, organising birthday celebration, farewell party, culture exchanging, sightseeing, weekend hikes, eating out. Together your interest in me have provided such wonderful support.

I am thankful to the excellent staff from the Department of Physics and Astronomy, High Degree Research Office, Campus Well Being, for their kind help in solving many problems. Special thanks to Carmen, Margaret, Jane, for their kindly help, understanding, and support through this challenging and rewarding period. I would also like to acknowledge the International Macquarie Research Excellence Scholarship (iMQRES), Postgraduate Research Fund (PGRF), in providing the financial support for me to conduct this research and attend the national and international conferences during my PhD candidature.

It is a pleasure to thank Peter and Teresa for being friends and family members and accompanying me to through my experience especially during the last period at the end of my PhD candidature. They have treated me like their daughter and looked after me all the time. It has been a great honour to stay with them in Australia. The place they provide is not only a room but a warm home full of love. Thanks for filling my memory with the moments: watching the sunrise at Byron Bay, dining together at Yum Cha, decorating the Christmas tree, etc. I still can remember your happiness when you first tasted the fish we had in Mrs Stone. Thanks, and love you, both.

I am also thankful to my wonderful and special friends, Cun, Liuen, Qing, Jingyi, Xiaoxia, Xiaoxue, Jipeng, Xiantao, Sicong, Zishan, Bingyan, Lixin for offering me their advice, accompanying me through my low moods. The help they have brought to my life makes me feel very warm and touched. Because of you, I understand the meaning of "A friend in need is a friend indeed". And also thank you for friends I have met here in Australia: Richal, Linghui, Hui, Haimei, Wenjie, Casey, Yuanyuan, Zibing, Mingzi, Yixuan, Elina, Jingxiang, Yurong, Ming, Shengshen, Katie, Lucy, Wendy, Wenwen, Zichun, Yue, Kaixin, Yan, Qiang, Xin, Yulong, Xianlin, Haili, Zizhen, Hangrui, Shilun, Yalei. It would have not been so much fun without you.

A very special gratitude goes out to my special friend Bingyu, who is the most amazing person in my life. I adore and value him so much and thank you for making me feel comfortable not only when I need it most, but every day. I have enjoyed every moment we have spent together. Thank you for spending time with me. Your care and attentiveness mean the world to me!

My deepest gratitude also goes to my family, my parents, sister and relatives, whose endless love and support have made me strong enough to overcome the tough periods I encountered. A special thanks to my mum, because of her strong personality enabling her to undertake major surgery and begin a long journey of recovery. My family's support has provided the foundation of my success in my PhD study.

Finally, I would like to say I am very fortunate to share the success of my studies with my supervisors, colleagues, friends and family members, and because of your commitment and love, I feel I am a much better person. Thank you for sharing and contributing to my life's achievement as I truly am very appreciative of your support and love.

# Abstract

Terahertz radiation has attracted strong interest in non-destructive testing, spectroscopy, and imaging due to its absorption by many organic and inorganic materials, and its transmission through many substances such as textiles. Terahertz laser sources based on the stimulated polariton scattering process have been proven to be an effective method to generate terahertz radiation, and this is a rapidly developing field of research. Intracavity configurations based on this technology offer an opportunity to achieve continuous wave terahertz generation, an approach which has not been extensively investigated. Continuous wave terahertz sources are highly desirable for a wide range of applications due to the characteristics of being simply interfaced with detectors such as Golay cells and pyroelectric detectors, and portable spectrometers. What is of particular significance is that the linewidth of the emission of these sources can be made very narrow, as required for high-resolution terahertz spectroscopy.

This thesis focuses on developing an intracavity continuous wave terahertz laser source based on the stimulated polariton scattering process. The thesis starts by describing the design and optimisation of a continuous wave, intracavity terahertz laser source. Studies have been made with regards to the analysis of the state-of-art in this laser source, identifying its shortcomings and enhancing its power scaling capacity and stability. The main factors influencing the SPS-driven continuous wave terahertz characteristics have been addressed, leading to a maximum terahertz power of 23.1 $\mu$W being generated, a ten times increase over the previously reported work. Beam distortion due to photorefractive and thermal effects has been overcome by optimising the pump scheme.

Development of this intracavity THz source with regards to linewidth narrowing is also studied. The core technology to achieve linewidth narrowing is the implementation of an etalon in the fundamental laser resonator. The thesis offers insight into using an etalon in two different ways in these THz sources. The first examined case is where an etalon is used as an intracavity band-pass filter, and its tuning characteristic as a function of tilt angle is investigated. A key finding here is that losses induced by etalon tilt (and hence walk-off) play a critical role. The second examined case is where an etalon is used at normal incidence, to deliberately form a coupled cavity with unique pass-band structure. In both cases, highly effective linewidth narrowing is observed.

A surprising and important finding is that narrowing of the linewidth in the SPS laser leads to an improvement in the THz output power, and this is supported through investigation of phase matching efficiency. Single longitudinal mode operation is successfully achieved in the system, taking advantage of coupled cavity effects formed by an etalon aligned at normal incidence in the cavity. This method brings the terahertz linewidth down to 70 MHz (compared to the linewidth of 100 GHz in the "free running" case) and delivers an output THz power of 18.2 $\mu$W.

# Contents

# List of Figures

# List of Tables

# List of Acronyms (In Alphabetic Order)

| | |
|---|---|
| BWO | Backward wave oscillator |
| CW | Continuous wave |
| DFG | Difference frequency generation |
| FEL | Free electron laser |
| FP | Fabry-Perot |
| FS | Fused silica |
| FSR | Free spectral range |
| FWHM | Full width at half maximum |
| FTIR | Fourier transform infrared reflectance spectroscopy |
| HR | High reflectivity |
| Is-TPG | Injection seeded terahertz parametric generator |
| KTA | Potassium titanyl arsenate (KTiOAsO4) |
| KTP | Potassium titanyl phosphate (KTiOPO4) |
| LD | laser diode |
| $LiNbO_3$ | Lithium niobate |
| $MgO:LiNbO_3$ | Magnesium oxide-doped lithium niobate |

| | |
|---|---|
| Nd:GdVO$_4$ | Neodymium-doped Gadolinium Vanadate |
| Nd:YAG | Neodimium-doped yttrium aluminium garnet |
| Nd:YVO$_4$ | Neodymium-doped Yttrium Orthovanadate |
| NIR | Near-infrared |
| OC | Output coupler |
| OPO | Optical parametric oscillator |
| OR | Optical rectification |
| PA | Photoconductive antenna |
| QCL | Quantum cascade laser |
| ROC | Radius of curvature |
| RTP | Rubidium titanyl phosphate (RbTiOPO4) |
| spi-TPG | Stokes-pulse-injected terahertz-wave parametric generator |
| SPS | Stimulated polariton Scattering |
| SRS | Stimulated Raman Scattering |
| TDS-THz | Terahertz time-domain spectroscopy |
| THz | Terahertz |
| TIR | Total internal reflection |
| TO | transverse optical |
| TPG | Terahertz parametric generator |
| TPO | Terahertz parametric oscillator |
| YAG | Yttrium aluminium garnet |

# 1

# Introduction

## 1.1 The "Terahertz Gap"

The far-infrared region of the electromagnetic spectrum, between 0.3 and 10 THz, is known as the THz frequency band [1] (See Figure 1.1). It lies in the frequency gap between microwave and millimetre waves. The THz frequency band has long been considered the last remaining gap in the electromagnetic spectrum, because of the difficulty in generating this radiation, and because it has rich scientific opportunities [2]. The terahertz frequency range of the electromagnetic spectrum has remained relatively unexplored as compared to the neighbouring millimetre-wave and infrared spectral range, primarily due to the lack of convenient and efficient radiation sources.

Today, terahertz technology is finding use in an increasingly wide variety of imaging and spectroscopy applications in the fields of astronomy [3, 4], remote sensing and monitoring of the earth's atmosphere [5], bio-medical imaging [6, 7], detection of concealed weapons and drugs [8, 9], information and communication technology [10, 11], non-destructive evaluation [12, 13], quality control of food and agricultural products [14, 15], and so forth [16–18]. It attracts strong interest in spectroscopy [19, 20] from the fact that many molecules, for example, carbon dioxide, water, nitrogen, oxygen, have strong characteristic rotational and vibrational absorption features in the terahertz range, and THz radiation can penetrate particularly well through non-polar and non-metallic materials. Additionally, proteins and DNA can be probed in the terahertz region, due to various conformational and binding states in heavier molecules. Terahertz radiation is also useful for imaging [21–25] because many materials, for example paper, plastics and ceramics, are transmissive in the terahertz and microwave region. Due to the different absorption of materials in the terahertz frequency range, the fingerprint property for each material can be determined simultaneously with imaging and can provide better contrast identification of different materials.

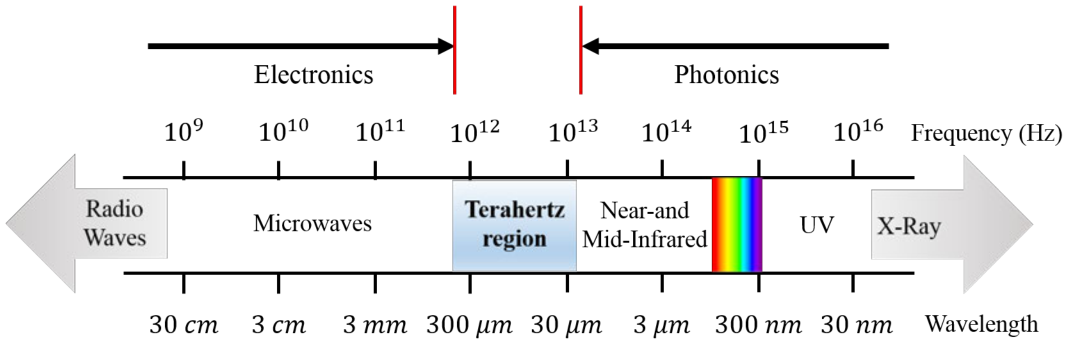


Figure 1.1: The "terahertz gap" in the electromagnetic spectrum.

With respect to spectral fingerprinting, the application of narrow-linewidth THz radiation is particularly interesting as it enables differentiation of overlapping spectral features, with high resolution. This is particularly useful in the identification of pharmaceuticals, and biological molecules wherein components are often combined.

## 1.2 Terahertz source technology

Terahertz (THz) radiation is highly desirable for a wide range of applications across various fields, and there have been numerous breakthroughs in THz source technologies [26], including the development of THz time-domain spectroscopy, THz imaging, and high power THz generation by means of nonlinear effects.

The development of terahertz sources can be classified into two approaches: electronic and photonic. Electronic methods extend the frequency from the microwave to THz, through high frequency electron oscillations. Backward wave oscillators (BWO) [27–29] and free electron lasers (FEL) [30] use electronic approaches to generate terahertz signal and are already well established at low frequencies (generally < 1 THz). Photonics has led the way to the realisation of many important THz devices. Optical methods of generating THz radiation generally use lasers, either pulsed or continuous wave, and methods include optical rectification (OR) [31, 32], photoconductive antennas (PA) [33, 34], quantum cascade lasers (QCL) [35–38], difference frequency generation (DFG) [39–48], and stimulated polariton scattering (SPS) [49–57].

Among these terahertz sources, the terahertz radiation obtained through PA and OR based on ultra-short pulses has the characteristics of broad spectral bandwidth, short pulse duration and high peak power, and can be used with terahertz time-domain spectroscopy (THz-TDS). A particular downside of this technology is the low spectral brightness and the need for coherent detection methods. A QCL is an electrically pumped unipolar photonic device in which light emission takes place due to intersubband optical transitions in the two dimensional quantum well of a semiconductor heterostructure. The advantages of THz QCLs are that they are small in size and are easy to integrate. However, high energy consumption and the need for low temperature cryogenic operation limit their applications. Also, they are not broadly frequency-tunable. Nonlinear optical frequency conversion is generally more flexible; and approaches such as DFG and SPS offer high spectral brightness, at room temperature. Although the conversion efficiency may be considered low, the method of nonlinear optical frequency conversion is an effective way to generate THz radiation. SPS is one of the most practical and efficient approaches because it can generate a frequency-tunable output, and operate in either pulsed or continuous wave modalities. The next sections describe the development and design of THz sources based on SPS.

## 1.3 Terahertz sources based on the SPS process

Efficient and widely tunable THz generation based on the stimulated polariton scattering process were reported in the pioneering works of Pantell, Puthoff, and others in the late 1960s to the early 1970s [58–61]. The first observation of tunable stimulated Raman emission was reported by Gelbwachs *et al.* [59], using a Q-switched ruby laser to excite the $A_1$ symmetry 248 $cm^{-1}$ polariton mode in a lithium niobate crystal. Sussman investigated, both experimentally and theoretically, the stimulated polariton scattering process in lithium niobate [60]. In 1975, a continuously tunable submillimetre wave source using the 248 $cm^{-1}$ polariton mode in $LiNbO_3$ was reported by Pantell [61]. The study of THz laser sources based on the stimulated polariton scattering process was then apparently silent for 20 years until scientists revisited it again in the 1990s. Since then, the THz technology gap for practical sources has steadily been filled using this technology.

### 1.3.1 SPS theory

Polaritons, in the context of this work, are the waves originating from the coupling of photon and phonon fields within a material, and this coupling occurs in materials which have transitions that are both infrared and Raman-active. THz radiation can be generated from the efficient parametric scattering of laser light via polaritons, and stimulated polariton scattering (SPS) is effectively stimulated Raman scattering (SRS) by polaritons. The scattering process involves both second- and third-order nonlinear processes. Ionic vibration modulates the electronic vibrations, and electron-ion interaction occurs leading to polariton generation at THz frequencies. In the context of this work, strong interaction occurs between the fundamental beam, the Stokes beam and the polariton waves, enabling a method of efficient THz generation.

Within SPS-active media, the polariton mode behaves like a pure photon, but in the lower frequency region, but it manifests like a phonon close to resonance ($\omega_0$). The frequency of these modes is dependent on their wavevector. In a crystalline material, the dispersion relation of the polariton must be considered. $LiNbO_3$ is a crystal which has transverse optical (TO) $A_1$ symmetry modes, and the dispersion relation of such a mode with frequency $\omega_0$ is illustrated in Figure 1.2. The polariton mode in $LiNbO_3$ at 248 $cm^{-1}$ is the one of particular interest for THz generation around 1-4 THz due to the high nonlinear gain [62] ($d_{33}$ = 25.2 $pm/V$ at 1063 nm) and very low absorption. The dual "photon/phonon" character of the polariton mode gives rise to complex nonlinearities.

SPS is a process in which stimulated Stokes radiation results from an interaction between photons and polariton modes in an SPS crystal. In a polariton laser, a fundamental laser field is typically utilised to generate the Stokes and THz fields. The frequency of the polariton field must lie on the dispersion curve. Fundamental ($\omega_f$), Stokes ($\omega_S$) and polariton ($\omega_{THz}$) waves satisfy conservation of energy and momentum: $\omega_f = \omega_S + \omega_{THz}$ and $\vec{\kappa_f} = \vec{\kappa_S} + \vec{\kappa_{THz}}$ (Refer to Figure 1.2). Hence the simultaneous solution of the dispersion curve and the phase matching condition yield Stokes and polariton (THz) frequencies. For every interaction angle between the fundamental and Stokes fields, there would be an infinite number of THz and Stokes wavevector pairs satisfying these energy conservation laws and phase matching conditions (represented in Figure 1.2 as different phase matching lines for different angles $\theta$). As a consequence, the frequency of the Stokes and THz fields can be tuned continuously by adjusting the interaction angle ($\theta$) between the fundamental and Stokes fields.

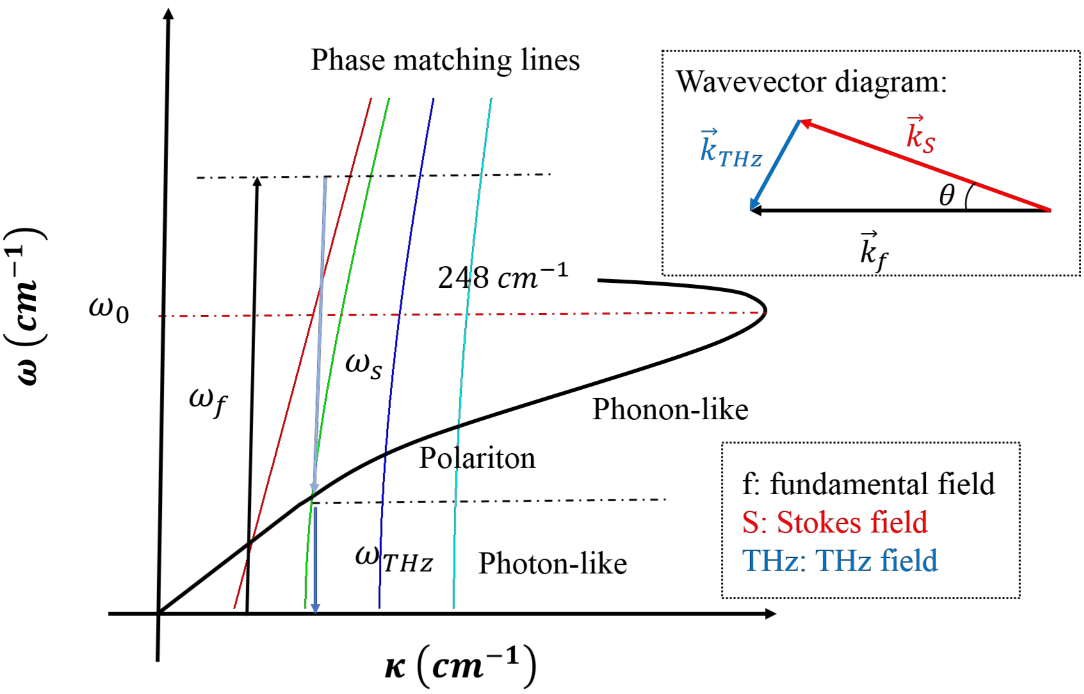


Figure 1.2: Diagram illustrating the dispersion relation close to a polariton mode in $LiNbO_3$, along with phase matching lines for various angles ($\theta$).

Throughout the literature, SPS THz sources have commonly been reported as THz parametric sources, due to the parametric manner in which the Stokes (idler) and polariton (signal) fields are generated from the fundamental (pump) field. The theory of SPS is highly complex, and comprehensive descriptions can be found in [60, 63].

### 1.3.2 External and internal cavity designs for SPS sources

Terahertz parametric sources typically have three main configurations, specifically the terahertz parametric generator (TPG), the external cavity terahertz oscillator (TPO) and the intracavity terahertz laser, as shown in Figure 1.3.

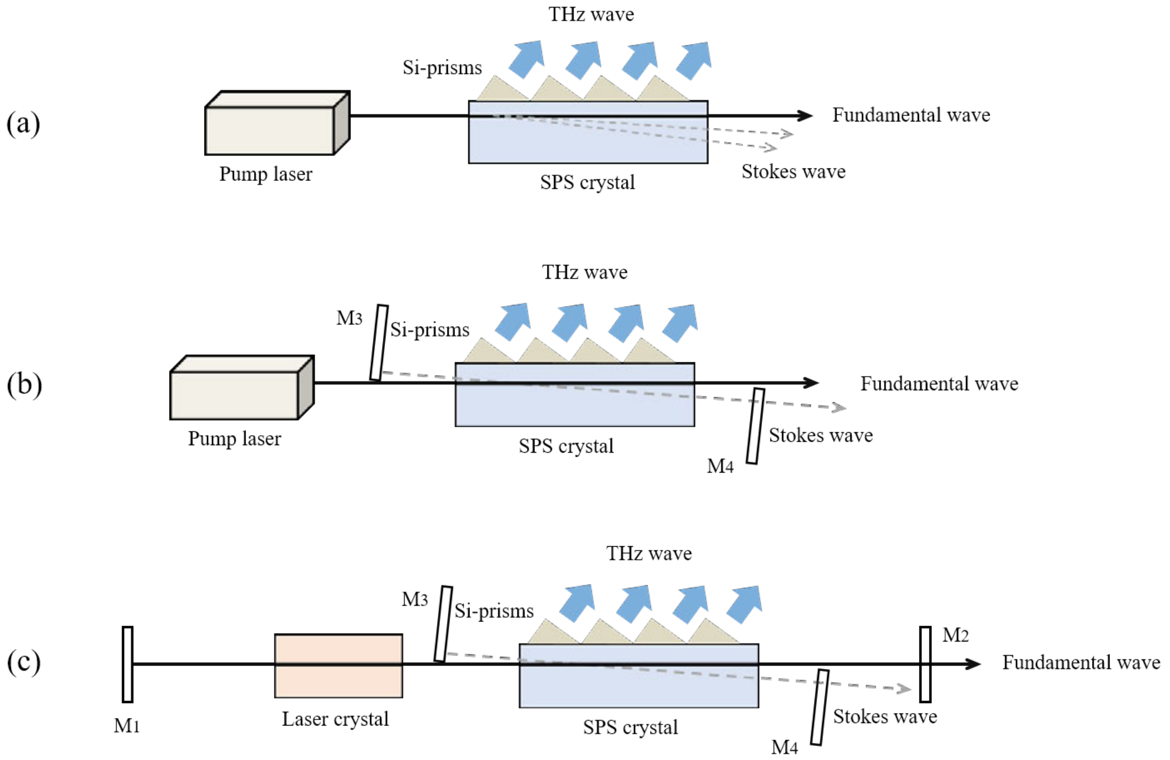


Figure 1.3: Key THz-SPS-based source designs: (a) TPG; (b) TPO; (c) Intracavity terahertz laser.

#### i. Terahertz parametric generator

The terahertz parametric generator has the simplest design of the three configurations, because it does not have a resonator. Typically a pump beam is focused into an SPS crystal to generate the Stokes beam, as shown in Figure 1.3 (a). The fundamental power converted into Stokes power must be used in either a single or double pass, so it requires a very high intensity (the order of 1 GW/cm$^{-2}$) to reach the SPS threshold. A terahertz parametric generator usually uses a pulsed laser for the a fundamental wave, with high peak intensity.

**ii. Terahertz parametric oscillator**

The typical schematic of a terahertz parametric oscillator is shown in Figure 1.3 (b), where an SPS crystal is positioned within a resonator and is externally pumped by a fundamental laser with high intensity. The amplification of the Stokes and THz signals inside the cavity greatly reduces the required fundamental intensity down to 1-100 MW/cm$^2$, much lower than that in the TPG configuration. External terahertz parametric oscillators have been widely used for efficient conversion of fundamental lasers running in the Q-switched nanosecond, mode-locked picosecond regimes.

In the literature [49], researchers use TPG and TPO to describe external cavity THz systems which make use of the SPS process because of the similarity to optical parametric generators and oscillators. TPG and TPOs are both external cavity arrangements, where a high-power pump laser is used to drive the SPS process. There has been great success in adopting extracavity terahertz laser configurations for building tunable, room temperature operation laser systems.

**iii. Intracavity terahertz lasers**

The schematic of an intracavity terahertz laser is shown in Figure 1.3 (c). Unlike external cavity terahertz lasers that require a specialised fundamental laser to provide high intensity, intracavity terahertz lasers have an SPS crystal placed within the resonator of a conventional solid-state laser (e.g. an Nd laser at 1063 nm). Both the fundamental and Stokes laser fields have their own resonators which are bounded by cavity mirrors, having high reflectivity at fundamental and Stokes wavelengths, for their cavity mirror coatings. Intracavity terahertz lasers can be used in both pulsed [51] and CW regimes [53].

Intracavity terahertz lasers have several advantages compared to external cavity terahertz lasers. Firstly, intracavity terahertz lasers typically use a low-cost laser diode (LD) rather than an expensive high-power fundamental laser. Furthermore, intracavity terahertz lasers usually have a high-Q cavity for the fundamental field, generating a sufficient circulating fundamental intracavity intensity to reach SPS threshold at relatively low LD pump powers. Therefore, the intracavity configuration is ideal for CW operation. Even for LD pump powers of only a few watts, resonating powers at the fundamental wavelength of as high as a kilowatt can be achieved, enabling the CW terahertz laser threshold to be reached easily for small mode sizes of around 500 $\mu$m diameter in SPS crystals. Intracavity terahertz laser configurations have been used in the regimes of Q-switched [52, 56, 64–66] and CW operation [53]. All the terahertz lasers developed in this thesis employ this type of configuration.

### 1.3.3 Development of THz sources based on the SPS process

Terahertz laser sources based on the stimulated polariton scattering process are versatile and known for their wide tuning range, which has good potential application in THz spectroscopy and multi-spectral imaging. There were significant developments in this type of THz laser source, with high powers, from the 1960s.

#### i. Extracavity SPS THz sources

$LiNbO_3$ is a most suitable SPS crystals for generating THz waves [67]. The first TPG was achieved in an a-cut, 3.3 cm long, $LiNbO_3$ crystal, by J.M. Yarborough *et al.* [59]. The tuning range of this laser source covered from 50-238 $\mu$m (6-1.26 THz), and the peak power went to 5 W. Researchers from Standford University reported a tunable terahertz laser source spanning into the frequency range of 150-700 $\mu$m (2-0.43 THz) [61] in 1975.

Due to the large absorption (10-100 cm$^{-1}$) and refractive index (around 5.2) of $LiNbO_3$ in the THz range, most of the THz photons generated within an SPS crystal are absorbed or totally reflected at the surface of the crystal. Several methods have been developed to overcome the out-coupling difficulties. A grating structure on the surface of $LiNbO_3$ was proposed to out-couple the THz wave directly to free space with around 250 times higher output power [68] compared to coupling out of an angled surface [69]. In 1997, a single silicon prism was used to extract terahertz from a $LiNbO_3$ crystal [70]. To improve the emitting characteristics, arrayed Si-prism couplers were later adopted, greatly improving the coupling efficiency and terahertz tunability [71]. This Si prism array has become the de-facto method of out-coupling the THz field from SPS crystals in linear configurations.

Another efficient way of out-coupling THz photons is to use a surface-emitted configuration, in which the beam is emitted perpendicularly to the surface of the crystal. Such a design has been implemented by Ikari in 2006 [72]. The advantages of the surface-emitted configuration are that the terahertz wave is extracted without any output coupler (e.g. Si prism), so it has better beam quality, and the attenuation is low due to the short path in the SPS crystal.

Much effort has been made on improving the output energy and tuning range of terahertz laser sources based on the SPS process. Up to now, silicon prisms and the surface-emitted configuration are the two main, effective ways to extract terahertz radiation, as shown in Figure 1.4.

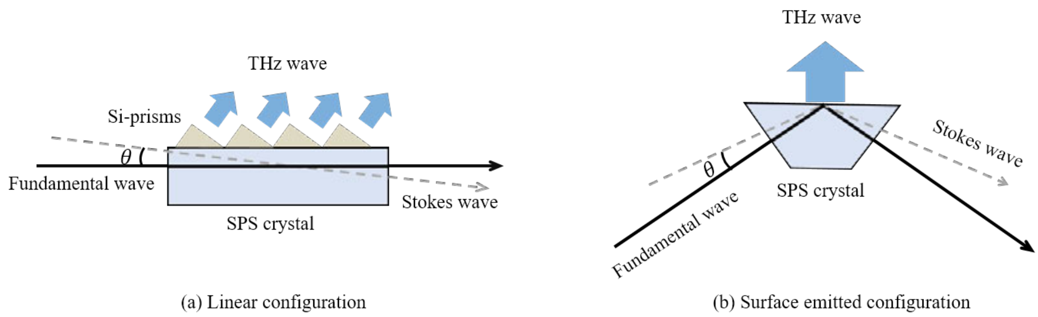


Figure 1.4: The linear (a) and surface-emitted (b) configurations

To reduce the absorption coefficient in the terahertz range, Shikata found that the absorption coefficient within $LiNbO_3$ decreased with crystal temperature. Controlling the temperature of a $LiNbO_3$ crystal to 78 K, the laser threshold dropped 32%, and an enhancement of 125 times in terahertz energy was achieved [73].

Further improvements to THz output power were made with the use of MgO-doped crystals. Here, 5% mol $MgO:LiNbO_3$ crystal has been proven the best doping concentration (in congruent crystals), because it provides 5 times greater gain and a higher optical damage threshold compared to undoped $LiNbO_3$ [67, 74]. Progressive improvements to the performance of these sources have been reported. Ikari [75] demonstrated how the interaction area of fundamental, Stokes and terahertz fields can be increased to improve the terahertz conversion efficiency, using a larger beam diameter of the fundamental wave. Li reported a 0.87-2.73 THz tunable source with 9.12 $\mu$W average power, corresponding to a conversion efficiency of $9.7 \times 10^{-6}$, pumped by a 10 Hz pulsed laser [76]. With a $LiNbO_3$ slab, Wang *et al.* [77] successfully obtained 3.56 times total THz power of a conventional surface-emitted configuration, in which the oscillating Stokes beams were totally reflected at the slab surface and propagated in a zigzag path, emitting up to 5 beams perpendicularly to the crystal surface. Wu and Ikari [78] recycled the pump beam and increased the THz output almost four times in magnitude. A phase matched gain peak near 4 THz from lithium niobate was reported using an off-axis extracavity terahertz SPS laser [79].

Most of the SPS sources in the literature are pumped with nanosecond lasers. Picosecond lasers have also been used to effectively pump TPG systems. For example, a 0.7-3 THz tunable SPS source with an impressive output power of 50 kW peak power was achieved, using a single mode, 420 ps microchip laser and a seed laser for the Stokes/idler field [80]. High repetition rate picosecond lasers have also been used effectively in synchronous pumping setups for high power THz generation [81–83].

#### ii. Intracavity SPS THz sources

Extracavity terahertz lasers based on the SPS process have the advantages of simple structure and being easily frequency-tuned, but the conversion efficiency (pump-to-THz) is typically very low compared to intracavity SPS terahertz lasers. Intracavity techniques have far lower pump power requirements and can be made highly efficient. By utilising an intracavity configuration, the fundamental field undergoes multiple passes through the SPS crystal. Such an approach has been investigated by Edwards *et al.* who have demonstrated promising results from a resonator formed around a 50 mm long Mg:$LiNbO_3$ crystal, placed within the cavity of an end-pumped, Q-switched, Nd:YAG laser [51]. They obtained an excellent tuning range and output power, tunable from 1.2-3.05 THz, with a maximum energy of 5 nJ being detected. Lee and Pask [52] reported a very compact, laser diode end-pumped, THz laser source, which generated frequency tunable radiation in a bulk Mg:$LiNbO_3$ crystal. This THz system operated with a very low threshold (2.4 W diode power), and high conversion efficiency (6.45 $\mu$W average output power at 1.82 THz for 5 W diode pump power), compared to the system of Edwards. They also observed cascaded stimulated polarition scattering and discussed the potential enhancement of the THz output from cascading in the pulsed system [56]. Surface-emitted configurations have also been applied to the intracavity SPS laser, where Ortega [65] demonstrated a power output of 56.8 $\mu$W and wide frequency tunability (1.46-3.84 THz).

The SPS process can be excited by a large rang of laser wavelengths. The Macquarie University group demonstrated the use of a fundamental wavelength of 1342 nm, to completely avoid the negative effect of free-carrier generation within the high-resistivity silicon prisms (used to extract THz emission from $MgO:LiNbO_3$). THz power of up to 23.6 $\mu$W (62.3 $\mu$W when chopped at a 50% duty cycle) was detected at 1.33 THz in the intracavity SPS laser [66]. The motivation for using a fundamental wavelength of 1342 nm was to improve the THz out-coupling efficiency.

**iii. Other SPS-active crystals**

Nonlinear crystals like KTP and its isomorphs (RTP, KTA etc.) exhibit excellent physical and optical characteristics, and have been used to generate terahertz radiation from 4-13.5 THz. A KTP based extracavity THz oscillator was first presented in 2014 [50], achieving three separated frequency tuning bands (3.17-3.44 THz; 4.19-5.19 THz; 5.55-6.13 THz). An experiment with a similar result was performed with KTA crystals using silicon prism mediated out-coupling and a surface-emitted configuration [84]. The terahertz emission gaps in KTP and KTA terahertz parametric oscillators are due to suppression of the SPS process induced by infrared absorbing modes in those crystals.

Terahertz laser sources using the SPS process have been achieved both in intracavity [54, 85] and extracavity [86] configurations. The maximum average THz power has now exceeded 0.1 mW at 4.1 THz, corresponding to a diode-to-THz conversion efficiency of $2.1\times10^{-5}$ [85], this result achieved in an RTP crystal. This was an important milestone for the intracavity SPS laser. To further expand the tunability, the terahertz frequency was extended to over 10 THz, achieved using 532 nm pumping (fundamental wave) in KTP, in an external cavity [57].

## 1.4 CW terahertz sources based on the SPS process

Pulsed and continuous wave (CW) are two different output modalities of coherent light sources, and therefore also of coherent terahertz sources. Due to the high peak intensities of pulsed radiation especially in the ps and fs regimes, numerous, pulsed terahertz sources have been demonstrated (refer to Section 1.3.3). However, CW THz sources are highly desirable for a wide range of applications such as imaging and spectroscopy. For example, a first CW

THz transmission image of a human liver which contains cancerous tissue was presented, and cancerous and regular tissue can be distinguished [87]. Unlike pulsed THz imaging, CW imaging affords a compact, simple, fast, and relatively low-cost system. Since it does not require a pump-probe system for detection, the complexity of the optics involved can be greatly reduced and, since it does not require a time delay scan, image formation can take place more quickly. Additionally, CW THz sources are often regarded as being better suited than pulsed sources because the linewidth is not limited by the pulse duration transform limit, and hence the linewidth can potentially be made narrower for application in high-resolution spectroscopy.

CW THz sources have been demonstrated in the past employing difference-frequency mixing of two lasers [88], parametric generation [89, 90], and quantum cascade lasers [91, 92]. Established techniques to generate CW terahertz radiation are limited, either in output power or frequency tunability. THz sources based on the SPS process have been considered as an effective method for the generation of CW THz radiation. In particular, the intracavity configuration makes it possible to reach the SPS threshold in the CW regime.

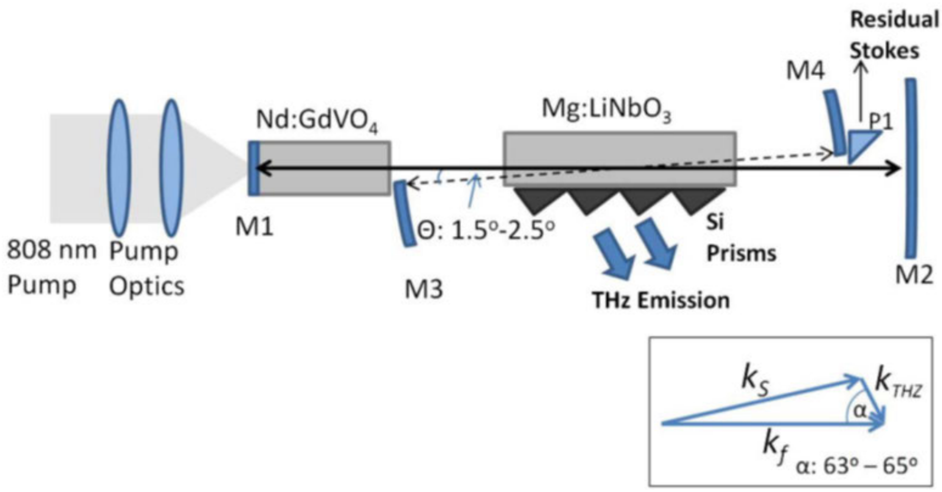


Figure 1.5: The intracavity CW THz SPS laser layout (reproduced from [53]).

The first CW intracavity terahertz oscillator based on the SPS process was demonstrated in 2014, at Macquarie University [53], and used a conventional Nd:GdVO$_4$ fundamental laser with an intracavity Mg:LiNbO$_3$ crystal, in a linear configuration, with silicon prisms for THz out-coupling. The system is capable of producing frequency tunable radiation across the range of 1.5-2.3 THz and requires only 2.3 W of incident diode pump power to reach the SPS threshold. The maximum THz output power was 2.3 $\mu$W for just 5.9 W of incident diode pump power, at the frequency of 1.8 THz. As shown in Figure 1.5 (reproduced from [53]), the nonlinear material is placed inside the fundamental cavity, making use of the high intracavity intensity (>10 MW/cm$^2$) to achieve the SPS threshold. This intracavity configuration provided an opportunity to achieve CW operation and did not require a high power pump source as is the case in external-cavity designs. Terahertz frequency tuning was achieved by rotating the Stokes cavity (Mirrors $M_3$ and $M_4$) so as to vary the angle $\theta$.

The first intracavity CW SPS THz laser demonstration was followed by numerous other developments in solid-state laser technology, particularly in intracavity SRS lasers [93–97] at Macquarie University. The interplay between the SPS and SRS phenomena in intracavity systems requires similar laser design expertise. Macquarie University's first terahertz source was reported in 2013 in the pulsed regime [52]. Shortly after that, the versatility of intracavity SPS lasers was demonstrated in CW operation using a high-Q resonator [53]. Up to now, terahertz sources based on the intracavity SPS process have experienced substantial development with regards to power scaling and frequency extension in pulsed systems. However, little work has been reported on the development of intracavity CW SPS THz laser sources. At the time of commencement of this project, the CW SPS laser only delivered THz power of 2.3 $\mu$W.

## 1.5 Narrow linewidth THz laser sources

Narrow-band, tunable sources in the 1-3 THz frequency range are particularly important for spectral fingerprinting and imaging applications involving many organic and inorganic compounds. In particular, a potential application field is high-resolution spectroscopy, which requires very narrow linewidth output at key frequencies. The linewidth of the THz field generated by nanosecond pulse SPS lasers is around a few hundreds of GHz [98]. This is adequate for many spectroscopic measurements of solids and liquids, as the spectral lines of these are typically broad.

Narrow linewidth THz laser sources for specific applications have stringent requirements such as single frequency operation, narrow linewidth, low-intensity noise and high-frequency stability. Apart from the properties mentioned above, other laser characteristics of high power, wavelength tunability, excellent spatial beam quality can also be critical, depending on the specific needs of the applications. Ultimately, it is still challenging to generate decent, narrow linewidth levels, with frequency tunable which operate at room temperature.

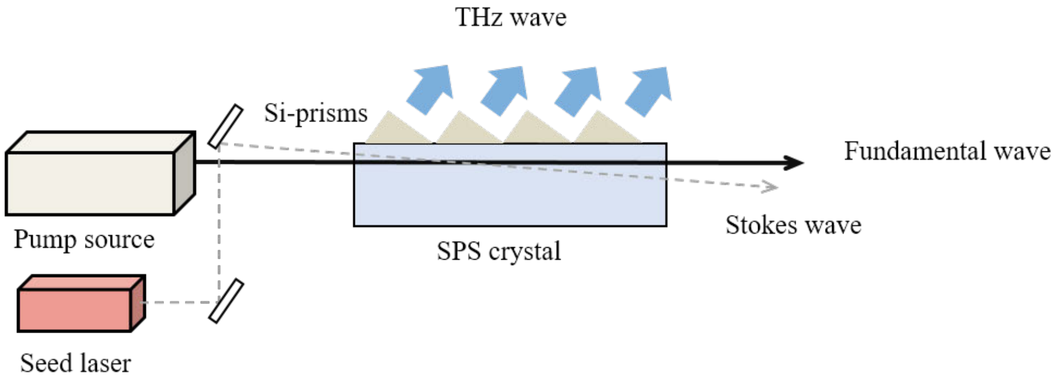


Figure 1.6: Schematic diagram of the injection-seeded terahertz parametric generator (Is-TPG).

Several methods have been carried out to overcome this hurdle. The seeded injection approach has been applied to TPG systems to narrow the linewidth. The principle of injection seeding is to couple a narrow linewidth laser into the SPS crystal, to seed the Stokes/idler field. A typical injection seeded THz parametric generation setup is shown in Figure 1.6.

The vast majority of THz systems demonstrated to date have been based on extracavity, pulsed designs. Here, the linewidth can be reduced by introducing a single longitudinal mode laser either in the pump or idler fields, respectively. A fourier transform limited TPGs ($\delta\nu$<200 MHz), was demonstrated in 2001 [99]. The generation of a linewidth of 100 MHz with a 0.7-3 THz frequency tunable range has been well developed using lithium niobate crystals by Kawase *et al.* [100–102]. Guo *et al.* also reported an all solid state, narrow linewidth and wavelength-agile THz wave parametric generator, which could be rapidly and smoothly tuned over the range from 0.6 to 2.4 THz with a narrow linewidth of 50 MHz [103].

The effectiveness of seeding the Stokes/idler field was demonstrated by Hayashi. The tunability was enhanced to 0.9-3 THz with high intensity pumping from a subnanosecond microchip Nd:YAG laser [104]. Using the combination of a TPO and a Stokes-pulse-injected terahertz-wave parametric generator (spi-TPG) to enhance the high-energy THz output has been proposed [105] and, this scheme achieved 1.8 times as large an output power as that obtained from the TPO for the same pump density. Injection seeding was also used in TPOs both extracavity [106] and intracavity [55], but seeding into a cavity was much more complicated because of the seeding angle. Walsh *et al.* [55] reported a THz source continuously tunable over 20 GHz with a linewidth < 100 MHz (close to the transform limit of 1-10 ns pulses) and settable anywhere in the range of 1-3 THz, employing an injection-seeded intracavity TPOs. The intracavity TPO has the benefits of a lower threshold and enhanced efficiency and power over a similar extracavity device.

Another promising method to achieve linewidth narrowing is using optical Fabry-Perot etalons to narrow the linewidth of the fundamental field, and hence the Stokes and THz fields. The transmission profile of an etalon is determined by the reflectivity and thickness of the etalon. Typically, etalons are chosen so that only a narrow slice of frequencies near the centre of the laser gain bandwidth experiences a net roundtrip gain within the laser cavity, and can oscillate. Therefore, an etalon may act as a mode selector, as shown in Figure 1.7.

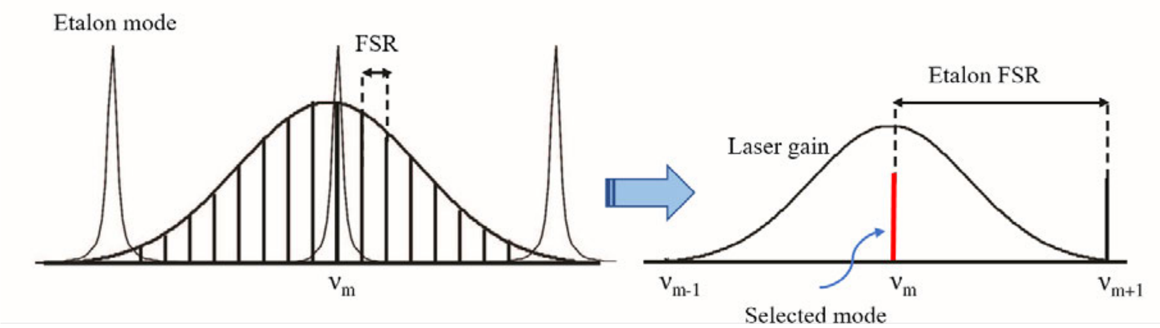


Figure 1.7: Example of laser longitudinal mode selection using a Fabry-Perot etalon.

Inserting two etalons into an intracavity SPS laser, one in the fundamental cavity and the other in the Stokes cavity, was reported by Edwards *et al.* [107], achieving linewidths of < 5 GHz at the frequency of 1-3 THz. However, the established techniques to generate narrow-band THz radiation rely on pulsed systems with either intracavity or extracavity configurations, which are limited as to low power and minimum achievable linewidth because of the pulse duration transform limit. Very few CW THz sources have been demonstrated, both in intracavity [53] [88] and extracavity [108] configurations. Furthermore, less work has been reported on narrowing the linewidth [89] of solid-state SPS THz sources. At the time of commencing this thesis work, there is no research targeting THz linewidth narrowing in intracavity solid-state SPS sources in the CW regime.

## 1.6 Thesis outline

This thesis focuses on investigating the opportunity for greatly enhancing the performance of CW THz sources based on SPS. CW THz systems can be made compact, reliable and cost-effective, with a narrow linewidth output, which can be used for a range of THz applications. In particular, when made narrow linewidth, they have particular application in high-resolution spectroscopy. This thesis begins with an analysis of the state of the art in CW SPS THz sources, identifying their shortcomings and enhancing their power scaling capacity and stability. This thesis then progresses into an investigation of linewidth narrowing of these sources through the application of intracavity etalons. These etalons are utilised in two unique ways, depending on whether the etalon aligns to the cavity. An etalon acts as a bandpass filter when it is misaligned to the cavity, and forms a coupled cavity in the laser system when aligned on-axis. The important outcomes of this work are a considerable reduction in the linewidth, and also an increase in the THz output power, when introducing an etalon in the laser cavity. The last but most important achievement is successfully reaching single longitudinal mode operation both in the fundamental and Stokes fields, so that the THz linewidth is narrowed in the intracavity SPS laser.

Chapter 2 provides an overview of the equipment and techniques used in this thesis work. It includes details of laser cavity design, in particular, focusing on implementing SPS in the continuous wave regime and description of the terahertz output coupling method. Etalons as linewidth narrowing element, applied to the CW THz laser, is introduced, and details of the optical spectrometers with different resolution and the general diagnostic equipment such as laser power meters, beam profiler, Golay Cell used in this research are given.

Chapter 3 demonstrates the improvements of a CW intracavity THz laser, delivering the highest THz power from any CW intracavity THz laser, based on the SPS process. This chapter discusses the system design and characterisation, detailing how to reach the SPS threshold, address thermal loading, and overcome the photorefractive effect in MgO:$LiNbO_3$. What is of particular significance is that the core technology is based on mature 1 $\mu$m solid-state laser designs, which are well established, and the components and coating techniques are well developed.

The effects of etalons working in two different ways are comprehensively investigated in Chapters 4 and 5. Chapter 4 investigates the application of etalons act as a bandpass filter (this may be considered the "traditional" way of using etalons). Several etalons with different thickness and reflectivity are investigated for linewidth narrowing. The linewidths of the fundamental and Stokes fields are considerably decreased compared to the "free-running" case. Also, a surprising finding is that the THz power continues to increase when the linewidth of the fundamental and Stokes fields are narrowed. The effect of etalon tilt angle on the laser characteristics has been studied, and here walk-off losses have been found to play a significant role.

In Chapter 5, an investigation into coupled cavity effects formed by deliberately inserting an etalon at normal incidence is presented. The properties of the coupled cavity are analysed using self-made software code, and the impact of the effect on the THz linewidth is investigated. The potential impact of the coupled cavity effect on the performance of the THz laser is discussed. Here, a narrow linewidth SPS CW laser is achieved, by taking advantage of the coupled cavity configuration. What is more, it is observed again that constraining the linewidth in the fundamental field spectrum leads to an improvement in the performance of the CW THz laser. It also demonstrates that using an etalon deliberately at normal incidence gives rise to more flexibility in levels of linewidth narrowing, because the laser works with both coated and uncoated etalons.

Further linewidth reduction with a high finesse etalon, in the CW THz laser, is presented in Chapter 6. To the best of the authors' knowledge, this chapter describes the narrowest linewidth output ever achieved from a laser-based CW THz source. By using an etalon at normal incidence, single longitudinal mode operation of both fundamental and Stokes fields is successfully achieved in the system. The mystery that narrowing the fundamental linewidth in the SPS laser does lead to the improvement on THz output power is well explained, based on an investigation of phase mismatch.

Chapter 7 summarises the key findings and conclusions of this research work and presents and outlines the prospects of future work.

# 2

# Key design considerations for CW THz laser

This chapter describes the general methods and equipment used in this thesis. Section 2.1 describes the basic considerations of cavity design, the implementation of SPS within the cavity of a CW Nd laser to yield a CW THz laser and the THz output coupling method used in this work. The fundamental theory of optical etalons is present in Section 2.2, and Section 2.3 covers the general diagnostic equipment used in this research.

## 2.1 Experimental methods

### 2.1.1 Laser cavity design

The laser cavity design goal in this thesis is to design a laser to operate stably over a desired range of pumping powers and to improve the laser performance by optimising the mode matching between the pumping beam and $TEM_{00}$ cavity mode in the laser crystal. Some basic theory for laser cavity design was used in this section along with ABCD resonator modelling using the LASCAD software package.

**i. Nd:$GdVO_4$ laser crystal as active media**

High intracavity powers are required in order to reach SPS threshold. This requires a laser material capable of sustaining high pump powers while exhibiting a high gain and limited thermal lensing.

Table 2.1: Physical and optical properties of Nd:$GdVO_4$, Nd:$YVO_4$ and Nd:YAG crystals

| Item | | Nd:$GdVO_4$ | Nd:$YVO_4$ | Nd:YAG | Ref. |
|---|---|---|---|---|---|
| Thermal conductivity $\kappa$ (W/m/K) | $\kappa_c$ | 10.5 | 12.1 | 10.1 | [109] |
| | $\kappa_a$ | 8.5 | 8.9 | - | |
| Specific heat capacity C (kJ/kg/K) | | 1.0 | 0.8 | 0.59 | [110] |
| Density $\rho$ (g/cm$^{-3}$) | | 5.47 | 4.24 | 4.56 | [111] |
| Thermal expansion $\alpha$ ($10^{-6}$) | $\alpha_c$ | 7.3 | 8.4 | 8.2 | [111] |
| | $\alpha_a$ | 1.5 | 2.2 | - | |
| Refractive index @ 1064 nm | $n_c$ | 2.19 | 2.16 | 1.82 | [111] |
| | $n_a$ | 1.97 | 1.95 | - | |
| dn/dT ($10^{-6}$/K) @ 1063 nm | E ‖ c | 13.8 | 3.0 | 7.3 | [111] |
| | E ‖ a | 10.1 | 8.6 | - | |
| Upper-level life time $\tau$ ($\mu$s) | | 95 | 100 | 230 | [111] |
| Stimulated emission cross section $\sigma$ ($10^{-19}$ cm$^2$) | | 7.6 | 15.6 | 6.5 | [111] |
| Absorption coefficient @ 808 nm 1.1% at.(cm$^{-1}$) | E ‖ c | 78 | 40 | 8 | [112] |
| | E ‖ a | 18 | 9 | - | |

Although there are many kinds of laser active media for solid state lasers, the use of Nd-doped YAG, $YVO_4$ and $GdVO_4$ [113] is widespread and their performance is outstanding. Compared to other Nd-doped laser crystals, Nd:$GdVO_4$ crystals have several advantages. The Nd:$GdVO_4$ crystal has the features of strong absorption at both 808 nm and 879 nm, high emission cross section at the fundamental wavelength of 1063 nm [112] and because it generates emission polarised along the c-axis. In Nd:$GdVO_4$, both broad homogeneous absorption lines and homogeneous emission lines feature high peak cross section. In addition, the uniaxial crystal Nd:$GdVO_4$ shows strong polarisation dependent absorption transition due to the anisotropic crystal field.

At the same neodymium concentration the absorption coefficient of Nd:$GdVO_4$ is seven times higher and the emission line is 80% broader in comparison with Nd:YAG [114].

It is desirable to use laser crystals with high thermal conductivities, Nd:$GdVO_4$ is the crystal which can realise highly efficient laser oscillation near the quantum limit and it has a higher thermal conductivity of 12 W $m^{-1}$ $K^{-1}$ [109, 110]. The studies of other thermal properties of Nd:$GdVO_4$ crystal, such as thermal expansion and specific heat, have shown that the Nd:$GdVO_4$ crystal is suitable for high power lasers. For those reasons, Nd:$GdVO_4$ has been used in this thesis, and its properties are listed in Table 2.1.

**ii. Thermal considerations**

It is well known that thermal loading of the laser crystal can affect laser performance. Here, the various thermal effects and ultimately thermal lensing are reviewed and analysed.

The absorption of pumping light in the laser crystal and SPS crystal, the inelastic nature of SPS in the SPS crystal and the absorption by impurity ions are the three main heating sources to result in thermal loading of the crystal. In general, thermal loading gives rise to a number of thermo-optic effects.

Thermal lensing is one of major challenges for SPS lasers, which arises from thermal loading. Thermal lensing can be contributed to in three ways: the variation of refractive index with temperature, the variation of bulk refractive index with stress and the bulging of the end faces due to thermal expansion. The contribution of each of these effects results in an effective thermal lens with focal length (f) [115], which can be expressed as:

$$\frac{1}{f} = \frac{P_{heat}}{\pi \kappa_c \omega_p^2}[\frac{1}{2}\frac{\mathrm{d}n}{\mathrm{d}t} + \alpha C_{\gamma,\phi} n_0^3 + \frac{\alpha \gamma_0 (n_0 - 1)}{L}] \tag{2.1}$$

where $\mathrm{d}n/\mathrm{d}t$ is the thermo-optic coefficient, $\kappa_c$ is thermal conductivity, $P_{heat}$ is the heat load, $\omega_p$ is the average spot radius of the heating area in the crystal,$n_0$ is the refractive index without pumping, $\alpha$ is the thermal expansion coefficient, $C_{\gamma,\phi}$ is the photo-elastic coefficient, L is the length of the crystal and $\gamma_0$ is the length of the end section of the crystal.

In the end-pumping laser, the thermal lens is mostly dominated by the first term, which is proportion to $\mathrm{d}n/\mathrm{d}t$, and the variation of refractive index with temperature can be expressed by $\mathrm{d}n/\mathrm{d}t$. Omatsu *et al.* [116] measured thermal lenses of an Nd: $GdVO_4$ self-Raman crystal both in a low-Q cavity (no SRS) and high-Q cavity and found that with the SRS process the thermal lensing was much stronger. In the low-Q cavity, the slopes of thermal lens power were 1.16 ± 0.1 D/W at 808 nm and 0.85 ±0.1 D/W at 879 nm with the 5 W pump power. In the high-Q cavity, the slopes of thermal lens power were 1.28 ± 0.15 D/W at 808 nm and 0.73 ± 0.087 D/W at 879 nm without SRS (7 W incident pump power). With SRS, the strongest thermal lens powers were 36 ± 4.3 D and 28 ± 3.4 D/W (808 nm vs 879 nm at 17.5 W pump power), corresponding to the slopes of thermal lens power were 2.6 ± 0.3 D/W and 2.0 ±0.1 D/W. The increased thermal lens in the high-Q cavity was attributed to the phonon energy deposited in the crystal and possibly impurity ion absorption. The thermal lensing measured by Omtsu *et al.* [116] can be used as a reference for estimating the thermal lensing in the CW THz laser, because they used the same laser crystal as this thesis.

Several strategies can be considered to alleviate thermal lensing in the CW SPS laser. The first is to use in-band pumping of 879 nm [112]. Another is to optimise the pumping scheme. To reduce thermal lensing, the $\pi$-polarisation together with chopping the pump was used in this thesis. These strategies will be investigated in detail in in Section 3.2.1. The technology of managing effects of thermal lensing through resonator design will be discussed in Section 3.2.2.

### iii. Laser cavity design methods

Considering laser cavity design is beneficial to manage thermal effects. The first step is optimising the mode matching between the pumping beam and $TEM_{00}$ cavity mode in the laser crystal using the laser cavity design software LASCAD [117].

ABCD matrix can express the laser resonator and the $TEM_{00}$ mode can be expressed by a complex wave q [118]:

$$\frac{1}{q} = \frac{1}{R} - i\frac{\lambda}{\pi\omega^2} \tag{2.2}$$

where R is the radius of the wavefront, $\omega$ is the radius of the $TEM_{00}$ mode and $\lambda$ is the wavelength of the laser. In a stable cavity, q should remain the same after a round-trip in the cavity. The round-trip ray-transfer matrix M can be expressed as

$$M = \begin{pmatrix} A & B \\ C & D \end{pmatrix} \tag{2.3}$$

then combining Equation 2.2 and 2.3:

$$q = \frac{Aq + B}{Cq + D} \tag{2.4}$$

Applying the resonator ray-transfer matrix parameters to the wave function:

$$\frac{1}{q} = \frac{D - A}{2B} - i\frac{\sqrt{4 - (A + D)^2}}{2B} \tag{2.5}$$

For a stable laser cavity, the right hand side of Equation 2.5 must be positive.

$$(A + D)^2 \leqslant 4 \tag{2.6}$$

Therefore, the $TEM_{00}$ cavity mode width can be expressed as:

$$\omega^2 = \frac{2B\lambda}{\pi\sqrt{4 - (A + D)^2)}} \tag{2.7}$$

The ABCD matrix is used to calculate the laser resonator stability for designing the fundamental field resonator in this thesis. In order to achieve mode matching between pump and laser, the beam waist can be calculated using Equation 2.7 and this is a guide to estimate the pump and fundamental resonator mode diameters. A plane-concave cavity structure was employed to compensate for the thermal effect and improve stability and efficiency.

**iv. Diode pump scheme**

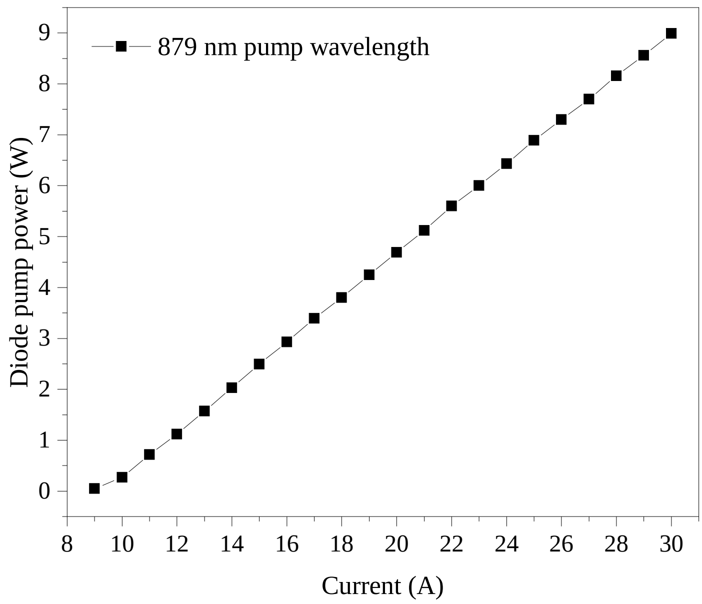


Figure 2.1: Diode pump power measured after the pump lenses and polarising cube. Cooling water temperature was 20°.

The laser diode used for fundamental resonator pumping is provided by LIMO GmbH. The laser diode is continuous wave, emitting a wavelength of 879 nm, and is fibre-coupled with 200 $\mu$m core diameter, 0.22 NA, with 30 W maximum output power. The laser diode output performance is shown in Figure 2.1. The linewidth of the laser diode is about 3 nm, wider than the absorption bandwidth of Nd:$GdVO_4$ crystal at 879 nm reported in [112]. The central wavelength of LD output shows the usual red-shift as the diode module heats up with increased input current around 0.005 nm/A. The wavelength of the LD output must be well-controlled to match the absorption peak of the laser crystal. To achieve this, tuning the temperature of the cooling water was used in the experiments. In order to maintain emission at 879 nm, the water temperature was maintained at 20°C. 20°C was the optimal cooling temperature for the pump power range of 2 to 9 W and was consistently used through the whole thesis.

The laser diode was collimated and refocused the fibre output into the laser crystal (Nd:$GdVO_4$) using a pair of aspheric lenses with a magnification ratio of 1:2 (Thorlabs LA1131-B-EFL 50 mm and Thorlabs LA1131-B-EFL 100 mm). This yielded a focused spot diameter of 400 $\mu$m (beam waist of 200 $\mu$m).

### 2.1.2 Implementing SPS in the continuous regime

#### i. Linear resonator geometry for an intracavity polariton laser

As described in the introduction (Section 1.3.3), the CW THz laser incorporates separate but coupled resonators for the fundamental and Stokes fields.

In this thesis, both resonators had a linear geometry, as shown in Figure 2.2. The fundamental cavity was formed by $M_1$ and $M_2$, with the cavity length of 185 mm. The Stokes cavity was formed by $M_3$, $M_4$, and the cavity length is 110 mm. The axes of those two cavities intersected inside the MgO:$LiNbO_3$ crystal. The Stokes cavity was mounted on a high-precision rotation stage to enable fine tuning and consequently the fine adjustment of the Stokes wavelength and THz frequency. The angle between the fundamental and Stokes cavities at which the SPS fields are generated typically ranges from 0.5-5.0 ° (internal angle), corresponding to the angle between the fundamental and THz fields of 60-65 °.

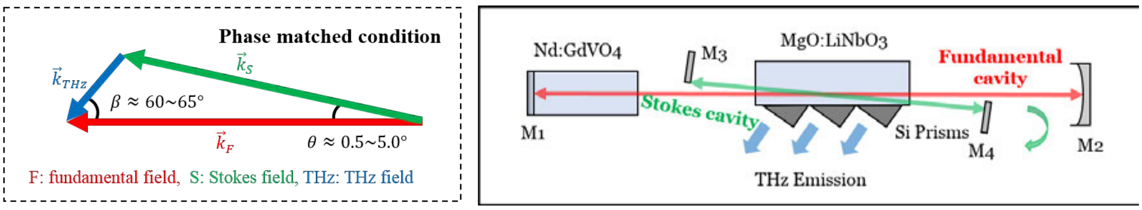


Figure 2.2: The linear resonator setup.

A series of high-resistivity silicon prisms was used to effectively extract the THz output. The silicon prisms were cut at the critical angle of 40° that the propagation THz field exits close to the normal incidence. The THz coupling method will be presented in detail in Section 2.1.3.

#### ii. Cavity mirror coating requirements

Cavity mirrors are especially important optical elements in CW intracavity SPS lasers, because they generally have to maintain very high reflectivity. SPS threshold and slope efficiency are affected by round-trip losses at fundamental and Stokes resonators. Reducing round-trip losses can greatly decrease the SPS threshold and improve the optical conversion efficiency. In order to achieve this, high reflectivity (HR) coatings (R>99.999%) at both fundamental and Stokes cavities are used. This high reflectivity combined with small cavity mode diameter will enable generation of a high intensity intracavity field. The coating requirements is similar to cavity ring-down measurements which also require very high reflectivity coating mirrors [119, 120].

Table 2.2: Coating specification of the laser mirrors used in the fundamental and Stokes resonators

| **Mirror set** | **Resonator** | **Specification** | **Manufacture** |
|---|---|---|---|
| **1.** | Fundamental | $M_1$: HR>99.994% @ 1063 nm | ATF |
| | | HT>99.930% @ 879 nm | ATF |
| | | $OC_1$: T=5% @ 1063 nm | CVI |
| **2.** | Fundamental | $M_1$: HR>99.994% @ 1063 nm | ATF |
| | | HT>99.930% @ 879 nm | ATF |
| | | $OC_2$: HR>99.995% @ 1063 nm | LASER OPTIK |
| **3.** | Stokes | $M_3$: HR>99.999% @ 1060 nm-1080 nm | ATF |
| | | $M_4$: HR>99.999% @ 1060 nm-1080 nm | ATF |

For the work described in this thesis, mirrors from custom coating runs were used extensively. Each coating run included substrates with a range of curvatures. The specifications of mirrors coatings are summarised in Table 2.2. Specific, manufacturer-supplied coating are shown in Appendix A.2.

For the fundamental resonator, the input mirror $M_1$ was directly coated on the front surface of the Nd:$GdVO_4$ crystal, with high transmission for 879 nm and high reflectivity for 1063 nm. Two output couplers were used during this work. Output coupler OC1, having 5% transmission was used to evaluate the fundamental laser performance and OC2, having R>99.995%, was used in the CW THz laser system.

The Stokes resonator consists of a pair of high reflectivity D-shaped mirrors, shown in Figure 2.3. The design of D-shape avoided clipping of the fundamental beam and to enable wide Stokes wavelength and THz frequency tunability. The mirrors were highly reflective at the near infrared (1060 nm to 1080 nm), and also maximise the Stokes field intensity inside the Stokes cavity.

Figure 2.3: D-shaped Stokes mirror attached to mechanical mount.

#### iii. Nonlinear crystal: $MgO{:}LiNbO_3$

Lithium niobate crystals are nowadays looked upon as one of the most popular and important materials for nonlinear frequency conversion and are widely used in THz sources to generate THz in the range of 1-3 THz [121]. Lithium niobate crystal is selected as SPS crystal, due to its high nonlinear optical coefficient and low optical absorption over a wide wavelength range. However, the $LiNbO_3$ crystal exhibits photorefractive damage, which leads to beam distortion and hence limits the pump power that can be sent through a congruent $LiNbO_3$ crystal. To overcome this problem, the most common solution is to use magnesium-doped $LiNbO_3$ that contains 5 mol.% magnesium oxide (MgO), so $MgO{:}LiNbO_3$ was used into in this thesis. The main optical properties reported in the literature for 5 at.% $MgO{:}LiNbO_3$ are summarised in Table 2.3.

Table 2.3: Main optical properties of 5 at.% $MgO:LiNbO_3$ extracted from the literature

| **Property** | **Value** | **Reference** |
|---|---|---|
| Refractive index | 2.23 @ 1063 nm | [122] |
| | 5-5.2 @ 0.4-1.8 THz | [123] |
| Transparency range | 0.4-5 $\mu$m | [122] |
| Nonlinear coefficient | $d_{33}$ =25 pm/V @1063 nm | [62] |
| Laser damage threshold | 2.5 J/cm$^2$ | [124] |
| THz absorption | 10-70 cm$^{-1}$ @ 1-2.4 THz | [67] |

### 2.1.3 Terahertz output coupling

For a linear SPS laser, THz extraction is a critical consideration, due to the high refractive index in MgO: $LiNbO_3$ crystal at THz frequencies. In the frequency range of 1-3 THz, the refractive index is around 5.2 [123]. The total internal reflection (TIR) angle is approximately 11° from the crystal to air. The THz radiation is being generated at the angle of about 25° to the normal of the crystal surface, so the THz radiation cannot be extracted from the crystal.

Several methods have been investigated in the literature to avoid the total internal reflection of the THz field. One technique to extract THz output was proposed by M. A. Piestrup in 1975 [61], cutting the end of the crystal at the angle (25°) to make the THz wave emerge approximately normal to the exit surface. However, the Fresnel reflection is very high (around 42%) and only fields in close proximity to the cut edge can be extracted using this method, also there is significant variability in emission angle when frequency tuning. Another way was using a monolithic grating coupler fabricated on the crystal surface [68]. For a grating coupler, the output direction change is relatively large due to the Bragg condition and the wide tuning range of the THz wave.

The most effective and widely used method to extract THz emission is employing a prism coupler attached to the emitting surface of the lithium crystal [70, 71]. High resistivity silicon is used in THz optics due to its low THz absorption across a broad frequency range. The use of Si prisms, which has a uniform refractive index of 3.42 [49] across the frequency range 1-2 THz, results in the THz field emission angle remaining largely unchanged as the frequency of the THz field is tuned. It can increase the TIR angle to around 41° at the crystal to the silicon surface and reduce the Fresnel reflection to 8.5%. The silicon prism array was convinced to offer the least angular dispersion, so is the best option for output coupling.

The silicon prism implementation is shown in Figure 2.4 and the actual silicon prisms in this work are shown Figure 2.5. $\theta$ and $\beta$ are the interacting angles between fields in SPS process and $\delta$ is the refracting angle into the prisms, depends on the incident angle of the THz field in the crystal's side face ($\alpha$).

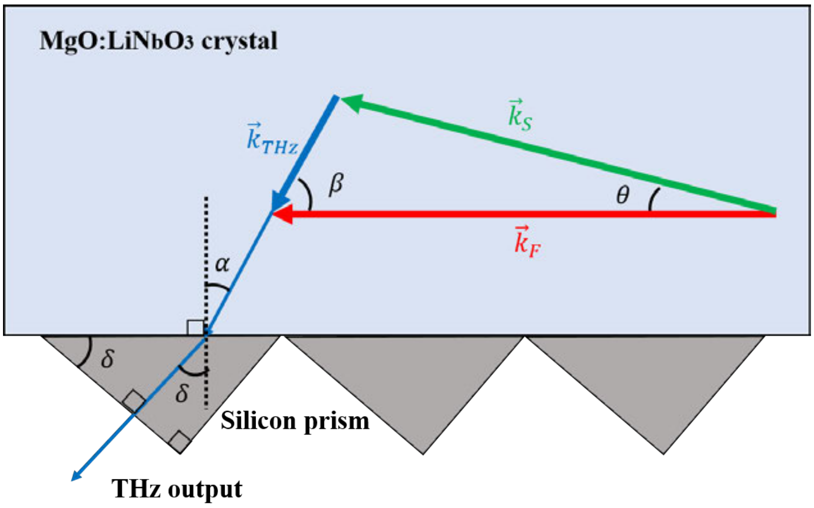


Figure 2.4: The silicon prism design and refraction of THz field from the SPS crystal into air.

The generated THz emission in the SPS THz lasers, simultaneously generate undesirable free carriers that then absorb the THz radiation. Free carriers in Si simply arise from the photoelectric effect. The band-gap energy of Si is 1.12 eV (at 300 K) [66, 125] (corresponding to a photon wavelength of 1120 nm). Free carrier generation is hence unavoidable with excited wavelength of 1 $\mu$m. A strategy to minimise the effect of free carriers, is to deflect residual pump light away from the Si prism-air interface [49]. Therefore, effect was made to block any residual pump and NIR beams. In order to reduce the inherent absorption of THz wave as it propagates through the SPS crystal, the fundamental and Stokes beams were designed to propagate as close to the MgO:LiNbO$_3$ / Si prism surface as possible.

The surface-emitted configuration is another way of extracting THz radiation. Here, the fundamental and Stokes fields are totally intenally reflected inside the SPS crystal such that the THz field is generated at an angle not subjected to total internal reflection [65, 72]. It was not used in this thesis but could be attractive for future work.

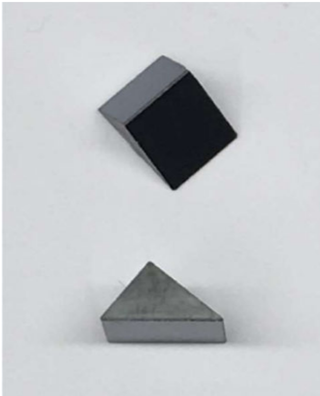

Figure 2.5: Silicon prisms for $MgO:LiNbO_3$.

## 2.2 Etalons as linewidth narrowing elements

A bulk etalon is a plate with two faces polished flat and parallel with these faces either uncoated or coated for selected reflectivity. These Fabry-Perot etalons have transmission passbands at discrete optical frequencies and they are widely used for laser wavelength tuning, and laser linewidth control [126]. In this work, solid etalons were used in two ways to achieve linewidth narrowing.

The spectral output from a laser is determined by the gain bandwidth of the laser active material and the properties of the laser resonator, itself, a Fabry-Perot resonator. Typically, within the laser gain bandwidth of the laser material, many longitudinal modes can be supported. When an etalon is inserted at a small angle to the laser resonator, it acts simply as a bandpass transmission filter.

Interference between the reflections from each surface of a solid etalon leads to a periodic spectral transmission, which can be characterised by the separation of the transmission peaks in frequency or wavelength space, referred to as the free spectral range (FSR: $\Delta\nu$ or $\Delta\lambda$) and the full width at half maximum of the peaks (FWHM:$\delta\nu$). FSR [115] is determined by the optical thickness of the etalon (d), refractive index (n) and the width of the peaks (the finesse of the etalon: F) is determined by the reflectivity of the surfaces. F is related to the mirror reflectivity. The FSR is given by Equation 2.8:

$$\theta_{int} = arcsin(\frac{\theta_{ext}}{n}), \Delta\lambda = \frac{{\lambda_0}^2}{2n_0 d \cos\theta_{int}}, or \Delta\nu = \frac{c}{2n_0 d \cos\theta_{int}}. \quad (2.8)$$

It is defined that the ratio of the spacing between the adjacent passbands and the passband width as finesse: $F = \Delta\nu/\delta\nu$ (Equcation 2.9). The FWHM is the frequency interval between the two points on either side of the transmission curve where the intensity falls to half its maximum value.

$$F = \pi[2arcsin(2 + \frac{4R}{(1-R)^2})^{-1/2}]^{-1} \approx \frac{\pi R^{1/2}}{1-R}. \quad (2.9)$$

The FWHM cavity linewidth is the frequency interval between the two points on either side of the transmission curve where the intensity falls to half its maximum value.

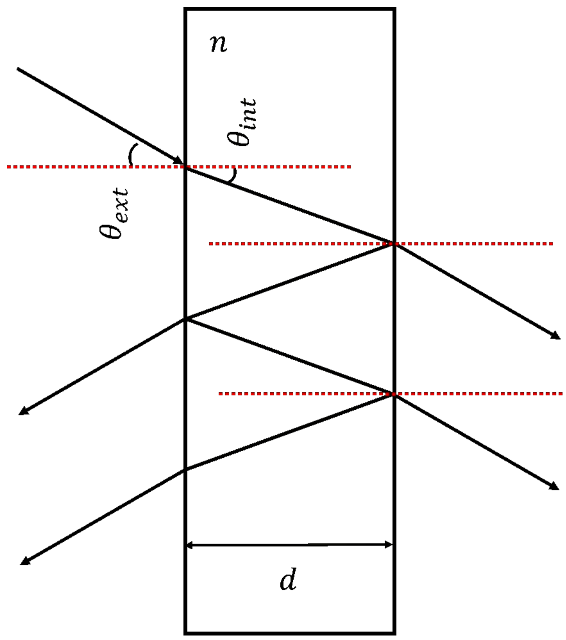


Figure 2.6: Interference of an etalon.

In this thesis, nine different etalons were selected, purchased from Light Machinery Inc. (Canada). Four were uncoated YAG etalons, and five were coated fused silica etalons. A summary of key parameters of these etalons are given in Table 2.4. YAG etalons were used because the refractive index for YAG material is higher than fused silica (1.81 vs 1.44) and were able to provide higher reflectivity for uncoated etalon. Also, they are better optically and more damage-resistant. $\theta_{ext}@T_{max}$ is the etalon tilt external angle at maximum transmission.

Table 2.4: Summary of key parameters of different etalons used in modelling.

| **No.** | **Material** | **d** | **R** | **Coated** | **FSR** | **F** | **FWHM** | **Full width @ T=98%** | $\theta_{ext}$ **@ T$_{max}$** |
|---|---|---|---|---|---|---|---|---|---|
| A1. | YAG | 25 $\mu$m | 8.4% | No | 3267 GHz/ 12.17 nm | 1.0 | 3287 GHz/12.24 nm | 481 GHz/1.812 nm | 9.73° |
| A2. | YAG | 50 $\mu$m | 8.4% | No | 1633 GHz/ 6.12 nm | 1.0. | 1644 GHz/6.16 nm | 239 GHz/0.90535 nm | 9.73° |
| A3 | YAG | 100 $\mu$m | 8.4% | No | 817 GHz/3.07 nm | 1.0 | 822 GHz/3.09 nm | 120 GHz/0.4518 nm | 5.59° |
| A4. | YAG | 500 $\mu$m | 8.4% | No. | 164 GHz/0.62 nm | 1.0 | 164 GHz/0.62 nm | 23.9GHz/0.0903 nm | 2.44° |
| B5. | FS | 50 $\mu$m | 30% | Yes | 2050 GHz/7.67 nm | 2.5 | 835 GHz/3.12 nm | 121 GHz/0.45475 nm | 6.32° |
| B6. | FS | 100 $\mu$m | 30% | Yes | 1025 GHz/3.85 nm | 2.5 | 417 GHz/1.57 nm | 60.4 GHz /0.2275 nm | 6.318° |
| B7. | FS | 250 $\mu$m | 30% | Yes | 410 GHz/1.54 nm | 2.5 | 167 GHz/0.63 nm | 24.2 GHz/ 0.0908 nm | 4.435 ° |
| B8. | FS | 300 $\mu$m | 30% | Yes | 342 GHz/1.29 nm | 2.5 | 139 GHz/0.52 nm | 20.0 GHz/0.07522 nm | 2.485° |
| C9. | FS | 250 $\mu$m | 60% | Yes | 409 GHz/1.54 nm | 6.0 | 68 GHz/0.256 nm | 3.85 nm/1025 GHz | 4.436° |

## 2.3 General diagnostic equipment

This section presents the general diagnostic equipment used throughout the experiments in this thesis.

### 2.3.1 Laser power meter

Two different laser power meters were used to measure the output powers in this thesis. The diode pump power, and the laser output power using T=5% output coupler was measured by a Thorlabs Inc. optical power meter PM100D. A Thorlabs thermal sensors (S310C) and photodiode-based sensors (S130C) power meter features both digital and analogue output and a wide range of optical power measurement from 500 pW to 500 mW. Either of there sensors were used interchangably depending on required sensitivity.

### 2.3.2 Beam profiler

In order to investigate the spatial properties of the near-infrared laser beams, a Spiricon laser beam profiler (Model SP620U) was used to measure the fundamental and Stokes fields beam profiles.

### 2.3.3 Oscilloscope

A digital oscilloscope (Tektronix TDS 3054) was used for the temporal analysis of the laser output. The bandwidth is 500 MHz and the sampling rate is 5 Giga-Samples/second. For example, the oscilloscope was connected to Golay Cell, chopper or scanning confocal Fabry-Perot interferometer to check and record the temporal behaviour of spectra in the different CW THz laser setups.

### 2.3.4 THz detector

The most commonly used THz detectors are thermal effect detectors, such as the Bolometer, Golay Cell and Pyroelectric detector. They are based on the material's thermal absorption of broad-spectrum electromagnetic radiation waves. They can directly measure the energy and average power of radiation waves and are generally in-coherent detectors. The THz detector used to measure the THz radiation in this thesis is a Golay Cell, because it is an efficient detecting devices and it has excellent sensitivity at room temperature and flat optical response over a wide wavelength range. An example of THz signal detected by Golay Cell is demonstrated in Figure 2.8.


Figure 2.7: Working principle of the Golay Cell. Image was from the manufacturer's website [127].

The Golay cell detector is a optoacoustical detector. It was proposed by Marcel J. E. Golay in 1947 [128, 129]. The basic principle is shown in Figure 2.7. The incident wave enters the absorption material of the Golay Cell detector. It heats the gas in the chamber and results in a pressure difference across the membrane, causing the membrane to deform. The reflected light from the membrane is recorded by a photo-electrical probe after passing through a grating, so that the deformation and the intensity of the radiation are measured.

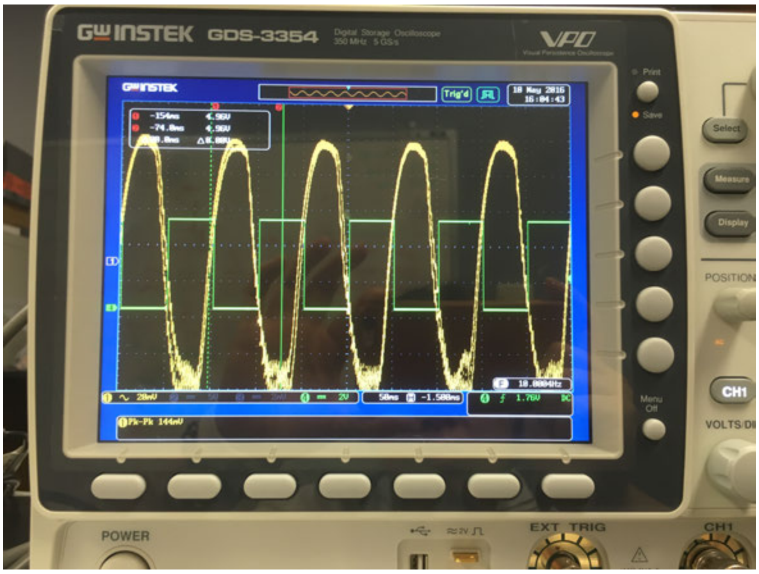


Figure 2.8: An example of THz signal detected by Golay Cell.

The Golay Cell used in this research was purchased from the Tydex company (Model: GC-1T, is shown in Figure 2.9). It has an optical responsibility of 81.85 KV/W @ 10 Hz and a noise equivalent power of $1.4 \times 10^{-10}$ W/Hz$^{1/2}$ @ 15 Hz (provided by the data-sheet from Tydex). The THz output powers ($\mu$W) were calculated based on the conversion of detected THz signal (mV) from Golay Cell. The frequency-dependent transmission of losses was considered, including through a THz long pass filter and TPX lens.

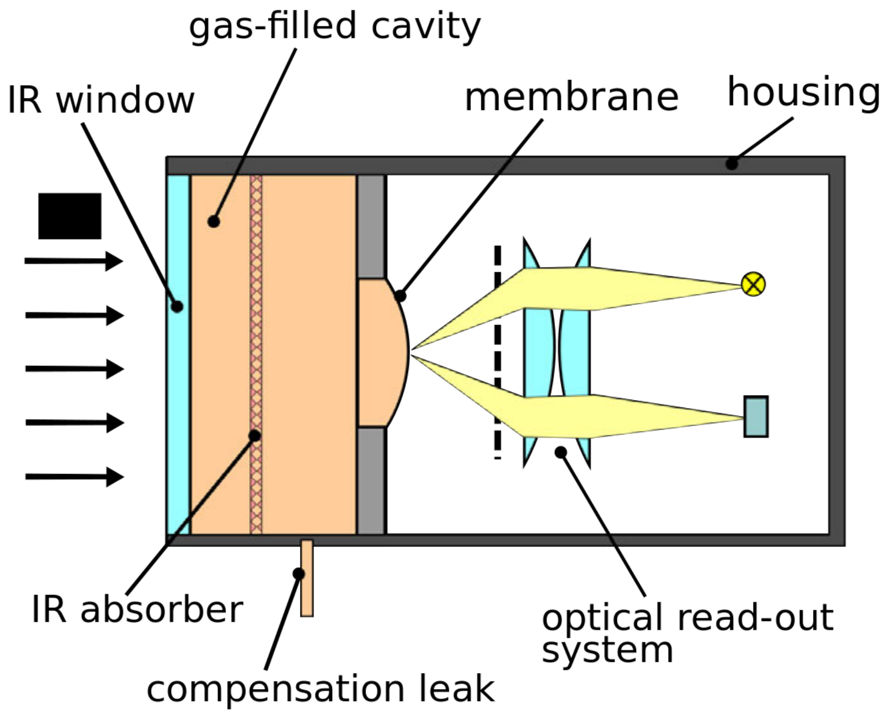


Figure 2.9: Photo of Golay cell Tydex. Image was from the manufacturer's website [130].

### 2.3.5 Optical spectrometers

Output wavelength and linewidth are most important characteristics of laser systems developed in this work. Regularly, we use optical spectrometers to measure the wavelength of the laser output in both fundamental and Stokes spectral regions. To measure the linewidth of a laser, the instruments and their resolution need to be taken into consideration. In this thesis, several optical spectrometers with different resolutions were used to obtain more detailed spectra. The details of each instrument are mentioned below.

**i. Ocean Optics spectrometer HR4000**

The Ocean Optics spectrometer HR4000 is a versatile high-resolution spectrometer. The HR4000 has a 3648-element CCD-array detector from Toshiba that enables optical resolution as precise as 0.2 nm (FWHM). Figure 2.10(a) shows the spectrum measured by HR4000, which is limited due to instrument resolution. The HR4000 is responsive from 788 nm to 1214 nm, and can be used for CW and pulsed regimes. This type of spectrometer is a dispersive spectrometer, which spatially disperses the input radiation. This spectral information is then captured on a CCD. The advantage of this design is that response time and sensitivity is only limited by that of the CCD.

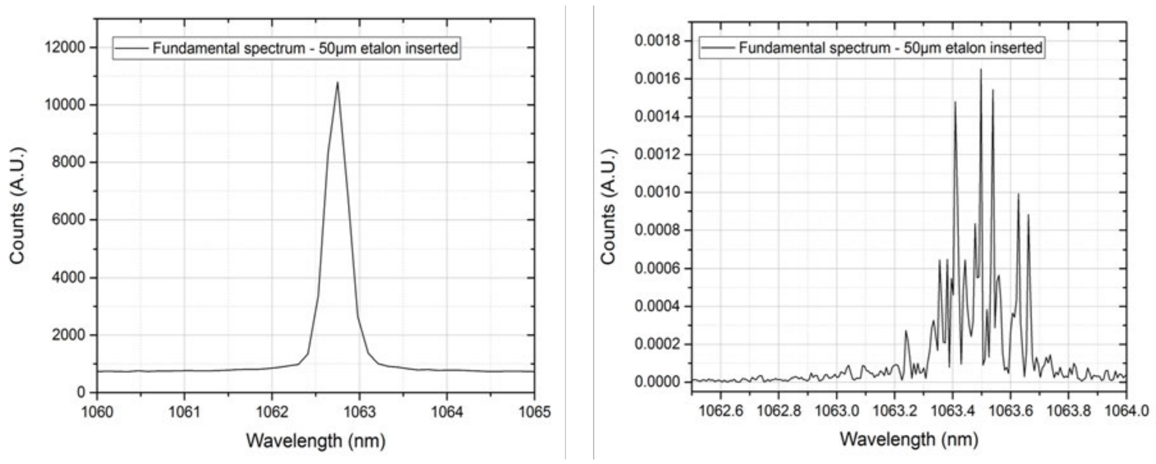


Figure 2.10: An example of spectrum measured by (a) HR4000 and (b) Bristol Wavemeter.


Figure 2.11: Photo of Ocean Optics spectrometer HR4000. Image was from the manufacturer's website [131].

The Ocean Optics spectrometer HR4000 [131] consists of 10 parts, as shown in Figure 2.12. Light from an optical fibre enters through the SMA connector **(1)**. And the SMA 905 bulkhead provides a precise position for the end of the fiber, entrance slit, absorbing filter and aperture. Light passes through the slit **(2)**, which acts as the entrance aperture. A filter **(3)** limits the bandwidth of light entering the spectrometer. Light reflects from a collimating mirror **(4)**, as a collimated beam, towards the grating **(5)**. The mirror is matched to the 0.22 numerical aperture of the optical fiber. The collimating mirror reflects photons to a diffraction grating, which splits photons by wavelength. Grating characteristics including groove density and dispension are important considerations when building a spectrometer. The diffraction grating then spreads light across the focusing mirror **(6)**, which directs light at each wavelength onto the detector **(8)**. Each pixel represents a portion of the spectrum that is translated into an answer with spectroscopy software.

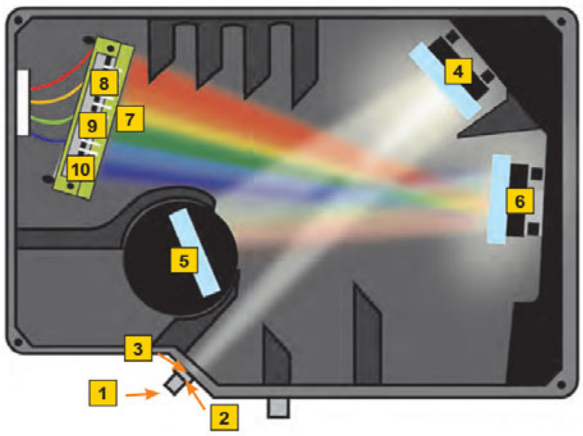


Figure 2.12: Inside the optical bench of the Ocean Optics spectrometer HR4000. Image was from the manufacturer's website [131]. **(1)**: SMA 905 connector, **(2)**: Fixed Entrance Slit, **(3)**: Longpass Absorbing Filter, **(4)**: Collimating Mirror, **(5)**: the Grating and wavelength Range, **(6)**: Focusing Mirror, **(7)**: Detector Collection Lens (optional), **(8)**: a CCD array detector, **(9)**: Variable Longpass Order-sorting Filter (optional), **(10)**: Detector Upgrade (optional).

#### ii. Bristol spectrum analyser

The 771A Laser Spectrum Analyser [132] from Bristol Instruments combines Michelson interferometer technology with fast Fourier transform analysis resulting in a unique instrument that operates as both a high-resolution spectrum analyser and a high-accuracy wavelength meter. With a spectral resolution of up to 2 GHz, and wavelength accuracy as high as ± 0.2 parts per million, this instrument can cover the wavelength range from visible to infrared. However, the optical spectrum analyser only operates at CW, quasi-CW (repetition rate >10 MHz), and pulsed (repetition rate >50 kHz) regimes.


Figure 2.13: Photo of Bristol Spectrum Analyser Wavemeter-771A. Image was from the manufacturer's website [132].

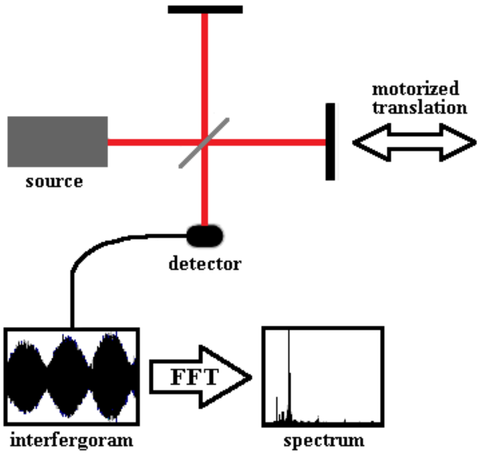


Figure 2.14: Working principle of Bristol Spectrum Analyser Wavemeter-771A.

The Michelson interferometer is employed in many scientific experiments and became well known for its use by Albert Michelson and Edward Morley in the famous Michelson-Morley experiment[133]. The Bristol Wavemeter 771A is used this method combined with fast Fourier-transform spectrograph [134]. Figure 2.14 illustrates the operation of a Fourier transform spectrometer. Light from the source is split into two beams by a half-silvered mirror, one is reflected off a fixed mirror and one off a movable mirror, which introduces a time delay - the Fourier-transform spectrometer is just a Michelson interferometer with a movable mirror. The beams interfere, allowing the temporal coherence of the light to be measured at each different time delay setting, effectively converting the time domain into a spatial coordinate. By making measurements of the signal at many discrete positions of the movable mirror, the spectrum can be reconstructed using a Fourier transform of the temporal coherence of the light. The higher resolution of this device, in comparison to a grating spectrometer, is shown in Figure 2.10 b, where fine spectral information is resolved.

### iii. Scanning Fabry-Perot interferometers

Scanning Fabry-Perot (FP) Interferometers [135] are spectrum analysers that are frequently used to examine the fine structure of the spectral characteristics of CW lasers. Two versions of these interferometers were used to resolve the linewidth of fundamental and Stokes fields in this work. The SA200-8B model provides a Free Spectral Range (FSR) of 1.5 GHz, a minimum finesse of 200, and a resolution of 7.5 MHz, while SA210-8B model offers an FSR of 10 GHz, a minimum finesse of 150, and a resolution of 67 MHz. Both of two interferometers were used for longitudinal mode observation in the laser resonator operating at fundamental and Stokes wavelengths. The limitation of using F-P interferometer is that the input signal must be CW or it must at least be stable over a full wavelength scan.

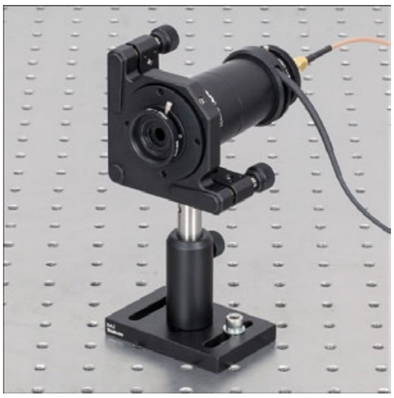

Figure 2.15: Photo of Thorlabs scanning F-P interferometer. Image was from the manufacturer's website [135].

The confocal FP cavity consists of two nearly identical, spherical mirrors, separated by their common radius of curvature and transmits only very specific frequencies. These transmission frequencies are tuned by adjusting the length of the cavity using piezoelectric transducers, as shown in Figure 2.16. The transmitted light intensity is measured using a photodiode, amplified by the transimpedence amplifier, and then displayed by an oscilloscope.

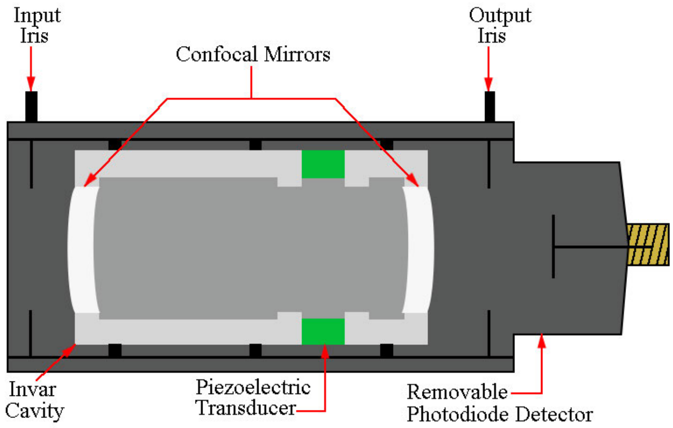


Figure 2.16: Working principle of Thorlabs scanning F-P interferometer. Image was from the manufacturer's website [135].

A summary of the instruments and their operating requirements used in the thesis are summarised in the Table 2.5.

Table 2.5: Lists of spectra and linewidth measurement instruments and specifications

| **Devices** | **Resolution** | **Requirements** | **Acquisition time** |
|---|---|---|---|
| Ocean Optics HR4000 | 0.2 nm / 53 GHz | CW or pulsed | 4 ms-20 s |
| Bristol Wavemeter 771A | 0.01 nm / 2.65 GHz | CW or high repetition pulsed | 1-2s |
| 10 GHz F-P interferometer | 0.00026 nm / 70 MHz | CW | 0.01-0.1 s |
| 1.5 GHz F-P interferometer | 7.5 MHz | CW | 0.01-0.1 s |

# 3

# Optimisation of intracavity CW THz lasers

## 3.1 Introduction

Chapter 2 presented a review of the key requirements of the SPS process and the design principles of intracavity THz lasers based on SPS. In this chapter, work was focused on improving laser performance specifically output power and beam quality of an intracavity CW THz laser source.

CW THz sources have been often regarded as being better suited for some applications than pulsed sources because they have a much higher spectral brightness at the desired frequency [87] and can be simpler to implement. They are also compatible with rapidly developing THz focal plane detection array technologies [136, 137]. The first intracavity CW THz laser based on the SPS process was reported in our group in 2014 [53]. However, the THz output power was only 2.3 $\mu$W, which may be not ideal for some applications. Therefore, it is necessary to build a CW THz source with decent THz output power and other optimised characteristics such as uniform beam profile and narrow linewidth.

In this chapter, the design, construction and characterisation of the CW intracavity THz polariton laser will be described in detail. Here, significant improvements have been made following the previous work published by our group in [53]. Several methods have been implemented into our intracavity CW THz polariton laser by taking advantage of its physical simplicity, implementing strategies to alleviate thermal effects in the fundamental laser crystal such as using polarised 879 nm diode pumping and chopping the pump, and reducing photorefractive effects in the $LiNbO_3$ crystal by electrically shorting around the crystal.

## 3.2 System design and characterisation

The advantage of using an intracavity configuration is because it is more efficient, and it can achieve high power output, only needing a few watts diode pump power compared to the extracavity configuration. As both Stokes and THz fields are driven by the fundamental field, it is essential that the fundamental field is optimised. Within the context of this thesis, fundamental refers to the fundamental field at a wavelength of 1063 nm.

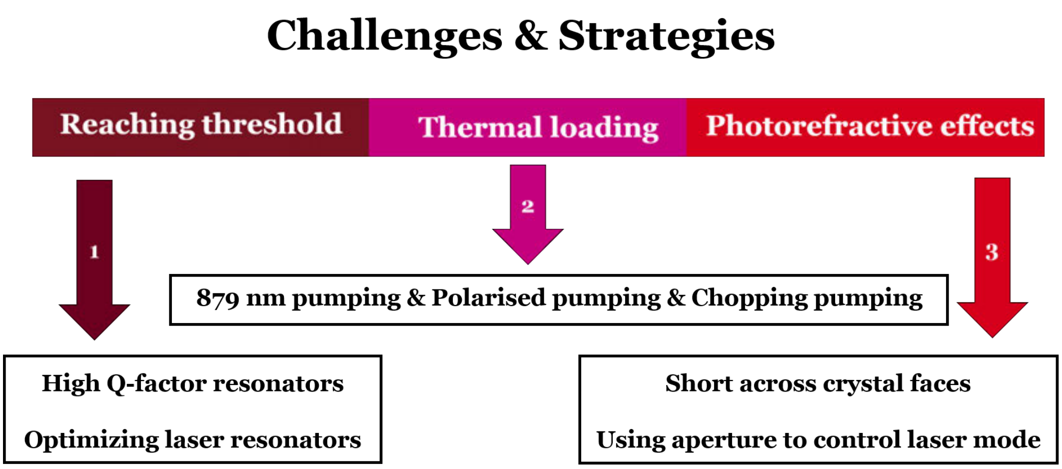


Figure 3.1: Overview of system design and characterisation.

Therefore, in order to build good lasers, system design and characterisation are essential for consideration. Building an effective and efficient intracavity CW THz laser is faced with several challenges. Reaching SPS threshold, thermal loading, photorefractive effects are three main challenges in CW polariton lasers, especially for CW lasers. In order to overcome these challenges, some strategies have been considered and presented in this section, and the flowchart is shown in Figure 3.1. Chopping the pump diode was used in this chapter to reduce thermal loading in the laser and SPS crystal, aiming to obtain high THz power.

### 3.2.1 Reaching SPS threshold

#### i. High Q-factor resonators

SPS threshold is hard to reach, especially for CW regimes. It requires extremely high intensity in the laser resonator (of order 1-100 MW/cm$^2$ as detailed in Section 1.3.2). In order to achieve threshold for the non-linear SPS process, an intracavity configuration and very high resonator Q-factors were used. This is in contrast to previously-reported, pulsed SPS THz sources [52] which incorporate an intracavity Q-switch to generate the high peak powers required to reach SPS threshold. Here, extremely high reflectivity (more than 99.99%) mirrors along with low-loss AR coatings on the crystal interfaces were applied into the fundamental and Stokes resonators. The mirror coating difference between pulsed system and CW system based on the similar intracavity configuration are presented in Table 3.1. Coating requirements are very high for CW regime THz lasers otherwise threshold for SPS process cannot be reached.

Table 3.1: Comparison of mirrors used in intracavity pulsed and CW system

| **Mirror coating** | | **Pulsed regime** | | **CW regime** |
|---|---|---|---|---|
| | Lee2013 [52] | Lee2015 [56] | Ortega2017 [65] | in this thesis |
| $M_1$ | 99.9% | 99.99% | 99.99% | 99.994% |
| $M_2$ | 99.4% | 99% | 99.4% | 99.995% |
| $M_3$ | 99.99% | 99.99% | 99.9% | 99.999% |
| $M_4$ | 99.9% | 99% | 99% | 99.999% |

To meet these high reflectivity requirements, ion beam sputtering is used for the coatings. In addition to high mirror reflectivity, low internal scattering and reflection loss in critical. Here, ion beam sputtered AR coatings are used. Also, mirror $M_1$ is directly applied to the laser crystal.

**ii. Optimising laser resonators**

Laser resonators were optimised based on the design of making use of relatively small resonator modes (500 $\mu$m diameter) and shorter cavity length. Under conditions of CW pumping, the system was sensitive to vibrations and small adjustments to the resonator alignment for both fundamental and Stokes fields, was critical. Also, the system is sensitive to losses, thus the ability to carefully adjust the position of crystals and mirrors is important, as are high quality AR coatings on the crystals.

In summary, the strategy to achieve a low SPS threshold is ensuring high-Q factors in both fundamental and Stokes resonators, which can be achieved by using high reflectivity coatings, reducing losses in the laser resonators and aligning these resonators to achieve good overlap between the fundamental and Stokes fields in the nonlinear SPS crystal.

### 3.2.2 Thermal loading in the laser crystal

Thermal loading arises mainly from pump heating and as we have speculated elsewhere, there may be an additional contribution in such high-Q cavity due to absorption by impurity ions. Heat generation inside solid-state laser media is due to the quantum defect between the pump energy and the radiation, and due to also the imperfect radioactive quantum efficiency. Without effective heat removal from the laser media, thermal problems such as thermal lensing and thermal birefringence present one of major limitation for the power scaling of the solid-state laser. Especially in the CW intracavity THz laser, the intracavity intensity is high which has the potential for severe thermal loading, and consequently strong positive thermal lensing occurs in the laser crystal, and its effects on laser operation must be considered. Therefore, how to reduce thermal loading became another key design consideration for the laser system.

**i. Using vanadate crystal**

Achieving high power output to reach SPS threshold requires a laser material capable of sustaining high pump powers while exhibiting a high gain and limited thermal lensing. It should be associated with an efficient pump. A common combination used in high-beam-quality high-gain lasers is a neodymium-doped laser crystal associated with an end-pumping configuration. Nd:$GdVO_4$ crystal was chosen as the laser crystal due to its excellent crystal properties used in CW laser, discussed in Section 2.1.1.

#### ii. Optimising the pump schemes

The thermal lens effect within the laser crystal, produced by pump radiation is one of the main factors affecting the characteristics of laser diode pumped solid state lasers, especially for end-pumped configurations. The thermal lens effect can not only influence the stability of cavity but change the spot sizes of the $TEM_{00}$ mode, all of which will distinctly limit the power scaling of the $TEM_{00}$ laser. In order to reduce the thermal lens effect and therefore obtain lasers with superior beam quality, a number of methods were used.

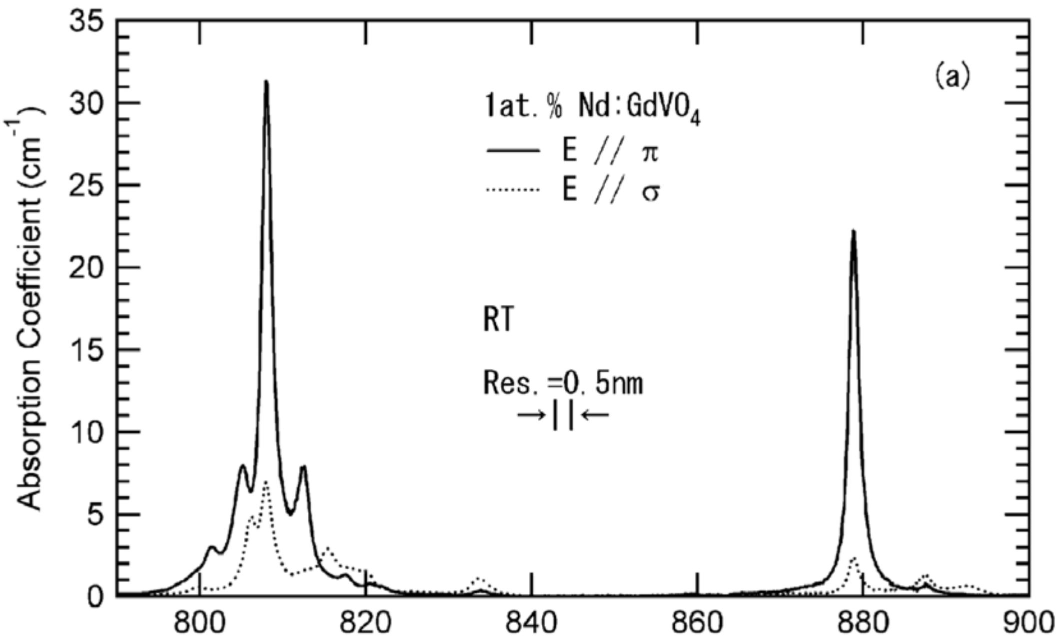


Figure 3.2: Absorption spectrum of 1at% Nd:$GdVO_4$ crystal along $\pi$ and $\sigma$ direction [112].

The laser crystal (Nd:$GdVO_4$) has several strong absorption bands at wavelengths readily accessible by laser diodes. 808 nm, 879 nm, and 888 nm are three wavelengths can be used for diode pump wavelength. The absorption spectrum of Nd:$GdVO_4$ crystal with 1% doping concentration is shown in Figure 3.2.

Quantum defect for a given laser transition is determined by the wavelength of the pump relative to the emission wavelength; a reduction of this defect could improve the laser performance, reduce the heat generation and enable the scaling to high powers. The laser parameters in incident pump power are also influenced by the pump absorption efficiency.

Table 3.2: Comparison of pumping wavelength for 1 a.t.% Nd:$GdVO_4$ crystal [112]

| $\lambda_a$ **(nm)** | **808 nm** | **879 nm** | **888 nm** |
|---|---|---|---|
| $\Delta\lambda_a$ (nm) | 1.6 | 1.5 | 1.6 |
| $\alpha_c$ ($cm^{-1}$) | 31.3 | 22.2 | 1.5 |
| $\alpha_a$ ($cm^{-1}$) | 7.0 | 2.5 | 1.5 |
| Quantum effect (%) | 24.1 | 17.3 | 16.5 |

Nd:$GdVO_4$ lasers are traditionally pumped into the strong absorbing $^4F_{5/2}$ level at 808 nm, and this introduces a parasitic upper quantum defect between the pumping and the emitting laser level. The shortcoming for 808 nm pump in Nd:$GdVO_4$ lasers is the relatively high quantum defect (24%), in combination with the strong absorption coefficients of the pump, causing strong thermal problems to limit the laser performance. The additional heat deposited in the laser crystal from the SPS lasers makes the thermal loading even worse.

The quantum defect in lasers could reduce by elimination of this upper quantum defect by pumping directly into the emitting level $^4F_{3/2}$ (879 nm or 888 nm). In an attempt to alleviate the thermal loading in the Nd:$GdVO_4$ crystal, direct excitation at 879 nm was introduced in 2003 [138] and has become a popular pumping approach. Compared to traditional pumping at 808 nm, the pumping of Nd:$GdVO_4$ crystal at 879 nm leads to the reduction of quantum defect ratio from 24.1% to 17.3% in the case of $^4F_{3/2}$ to $^4F_{11/2}$ emission, which reduces the thermal loading by 28% at 1.06 $\mu$m. Pumping at this wavelength has been successfully used to generate high output power in the infrared at 1063 nm [139], 1341 nm [140], 912 nm [141] and in the visible at 532 nm [142], 456 nm [143], 671 nm [144]. It has also been used as pumping source in Raman lasers [145–149].

Direct excitation at 888 nm is not well suited for pumping Nd:$GdVO_4$ is because of its very weak absorption. Overall, considering all the pros and cons, 879 nm was chosen as the pump wavelength.

The absorption of Nd:$GdVO_4$ crystal is polarisation-dependent. The absorption coefficients for light polarised along both c- and a-axis at three main pump peaks are summarised in Table 3.2. Here, $\lambda_a$ is central wavelength; $\Delta\lambda_a$ is absorption bandwidth and $\alpha_c$, $\alpha_a$ are absorption coefficients at c- and a-axis, respectively. The unpolarised dependence of the absorption features in Nd:$GdVO_4$ crystal present a challenge to the efficient use of pump radiation. The drawback of unpolarised pumping is that the weak absorption along the a-axis can cause substantial amounts of pump power to remain unabsorbed. In contrast, the absorption cross-section for pump light polarised along the c-axis ($\pi$ polarisation) is considerably stronger (up to 8.9 times) than for pump light polarised along the a-axis ($\sigma$ polarisation).

Absorption of pump light injected into a laser crystal has a large influence on the overall conversion efficiency of the whole system. Absorption coefficient and crystal length are the foremost parameters determining the efficiency of pump absorption. It is found that up to 45% of the incident pump power along a-axis was unabsorbed using the Nd:$GdVO_4$ crystal in our setup, which was greatly reducing the laser efficiency. In order to improve absorption efficiency and reduce unabsorbed pump power, $\pi$ polarisation was selected to pump the Nd:$GdVO_4$ crystal in the fundamental cavity. This was done with the use of a polarising beam spliter. Note that half of the diode power was therefore was not utilised in this system. Selecting this polarisation of highest absorption served to minimise heating in the laser crystal, as well as to minimise residual pump radiation impinging on the MgO:$LiNbO_3$ crystal and intracavity etalons, which will be detailed in Chapters 4 and 5.

Table 3.2 shows the absorption coefficient for different pump wavelength and polarisation of 1 a.t. %-doped, Nd:$GdVO_4$ crystal. For those crystals doped with lower Nd concentration, the associated values are deduced given that absorption coefficient is directly proportional to the dopant concentration [150]. In this system, 0.3 a.t.%-doped Nd:$GdVO_4$ was used, so the absorption coefficient with 879 nm, $\pi$-polarisation was $\alpha_c$ @ 879 nm=6.67 cm$^{-1}$. For comparison, in Lee's CW THz laser [53], 808 nm, unpolarised pump was used, so the absorption coefficients with $\sigma$- and $\pi$ are $\alpha_a$ @ 808 nm=2.1 cm$^{-1}$, $\alpha_c$ @ 808 nm=9.39 cm$^{-1}$, respectively. Accordingly, different equations are applied in the unpolarised pumping and polarised cases. For the unpolarised at 808 nm, the residual pump power P(z) along crystal length x can be expressed:

$$P(z) = \frac{1}{2}P_0[exp(-\alpha_c z) + exp(-\alpha_a z)], \tag{3.1}$$

assuming the incident pump power $P_0$ is spread equally over the two polarisations [151]. For polarised pumping, a purely exponetial equation is used for simulation as below

$$P(z) = P_0 exp(-\alpha_c z), \tag{3.2}$$

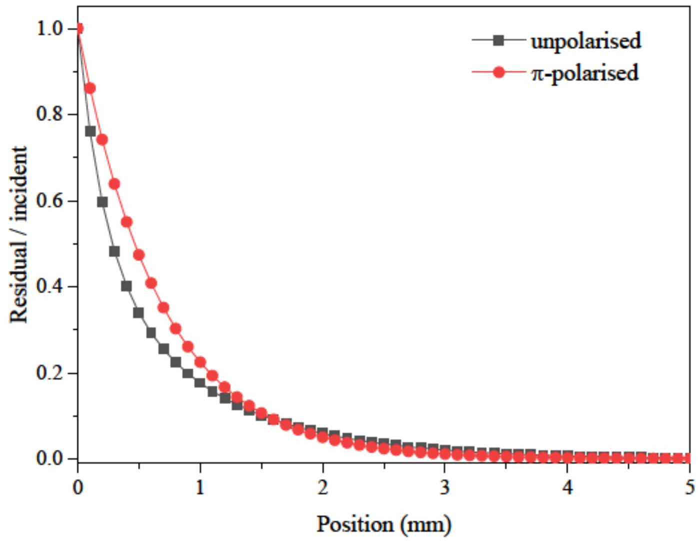


Figure 3.3: Numerical analysis of the residual pump power in 0.3 a.t.% doped Nd:$GdVO_4$ with different pump scheme (a) 808 nm unpolarized pump (used in [53]), (b) 879 nm $\sigma$-polarised pump (used in this thesis work).

The pump absorption with crystal position with pumping scheme in this thesis and Lee's work was calculated, shown in Figure 3.3. It is notable that for a fixed Nd:$GdVO_4$ crystal, the pump light with $\pi$-polarisation along the crystal c-axis is strongly absorbed. The absorption of unpolarised pump light is not absorbed as strong as $\pi$-polarisation. Therefore, the $\pi$-polarisation was used in this thesis to improve the absorption efficiency and reduce the residual pump.

Applying an optical chopper in the intracavity laser system proved to be a simple and effective way to alleviate thermal loading [94, 149]. The resonator was found to be very sensitive to the strong thermal lens in the Nd:$GdVO_4$ laser crystal, and for this reason this technique was introduced into my system. A chopper (400 Hz, 50% duty cycle) was placed after the diode fibre which can achieve quasi-CW operation. In this mode of operation, the THz output power that could be achieved by pumping the crystal harder, without taking the risk of a thermal fracture because of the thermal loading was lower compared to the pure CW case. It is because altering the duty-cycle of the pump enables the pump enables the system to dissipate some of the accumulated heat. The net result of which is lower accumulated heat.

In summary, for these reasons, $\pi$ polarisation pumping with the pump wavelength of 879 nm, and 50% duty cycle pump were chosen for optimisation of the pump source.

### 3.2.3 Photorefractive effects

Photorefractive effects developing in the SPS crystal are another phenomena which may arise in intracavity THz laser sources, which limit the laser performance. Two mechanisms can cause the refractive index changes. One is the photorefractive effect due to charge redistribution (optically induced refractive index changes). And the other is the thermo-optic effect due to a temperature change which is caused by heat accumulation inside the crystal because of photon absorption [152].

The photorefractive effects degrade the quality of integrated optical devices based on lithium niobate, especially for high light intensities. The pyroelectric effect causes charge build up and refractive index change. This can then lead to localised beam distortion and a phase mismacth. The light induced index changes are generated by optical excitation of charge carriers which migrate and are subsequently trapped at new sites [153]. The charge carriers result from impurity ions - especially transition metal ions. Even nominally pure lithium niobate crystals usually contain an accidental iron contamination of a few ppm. The iron ions are known as the main source of the photorefractive effect [154].

The most common solution to suppress photorefractive damage $LiNbO_3$ is to dope it with magnesium oxide [155]. Using $MgO{:}LiNbO_3$ crystal can effectively suppress photorefractive damage compared to use congruent $LiNbO_3$ crystals, because it has remarkably stronger resistance to the optical damage than undoped one [156], and nonlinear coefficients slightly increase with the dopant level [62]. $MgO{:}LiNbO_3$ crystal can suffer from photorefractive damage if a pyroelectric field is created by homogeneous heating of the crystal. A theoretical analysis has been conducted to solve the effects of pyroelectrically induced whole-beam refractive index changes in $MgO:LiNbO_3$ crystal [152], showing that the MgO doping changes some of the crystal properties significantly, e.g., the photoconductivity is 1-2 orders of magnitude larger than in congruent $LiNbO_3$, and the bulk-photovoltaic field is 2 orders of magnitude smaller in $MgO:LiNbO_3$ than in congruent $LiNbO_3$ [157]. The most common solution to manage photorefractive effects is to use magnesium-doped $LiNbO_3$ that contains at least 5 mol.% magnesium oxide (MgO) [155]. Therefore, 5% $MgO:LiNbO_3$ crystal was used in the system.

The method of short-circuiting the c-faces of the crystal through the application of conductive paint on the c-faces and electrically contacting them, have been proposed by Schwesyg [152] and was applied in this work and also in [53]. This method will help prevent the crystal developing surface charges during heating or cooling. This will hold-off any pyroelectric effects homogeneously throughout the crystal. However, this will have somewhat limited benefit to localised temp distribution due to residual absorption of propagating fundamental, Stokes modes, for example.

## 3.3 Overview of experimental setup

The experimental setup of an intracavity terahertz SPS laser is shown in Figure 3.4, and was developed based on the intracavity system reported earlier by our group [53]. The fundamental laser cavity was formed by mirror $M_1$ (HR coating with R ~ 99.994% at 1063 nm - 1173 nm and T> 99.930% at 879 nm) which was coated directly on the $Nd:GdVO_4$ laser crystal and end mirror $M_2$ which had a radius of curvature (ROC) of 500 mm and an HR coating with R> 99.995% at 1063 nm (based on transmission measurements we performed).

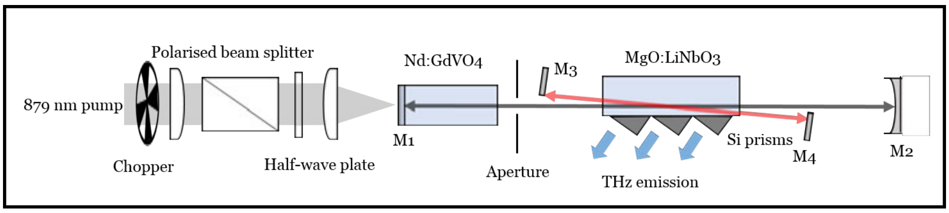


Figure 3.4: Experimental setup of intracavity THz laser - viewed from the top.

The laser gain medium, was a $Nd:GdVO_4$ crystal (0.3% a.t. Nd-doping, cut for propagation along the a axis) with dimensions of 5 mm × 5 mm × 13 mm, on the end of which mirror $M_1$ has been deposited. Pump light at 879 nm was provided by laser diode module (LIMO GmbH) and is delivered via an optical fibre with a core diameter of 200 $\mu$m to a pair of aspheric lenses, which image the end of the fibre into the laser medium with a 1:2 ratio (Thorlabs LA1131-B - EFL 50 mm and Thorlabs LA1131-B - EFL 100 mm). The nonlinear crystal, congruent $MgO:LiNbO_3$ (provided by HC Photonics Corp.) had dimensions of 5 mm × 5 mm × 20 mm, and its crystallographic z-axis in the vertical plane, parallel to the polarisation of the laser. The x-axis of the crystal was parallel to the laser axis and the 20 mm long side of the lithium niobate. The 5% a.t. MgO-doping was used to ensure high damage threshold [158] and high SPS conversion efficiency [67].

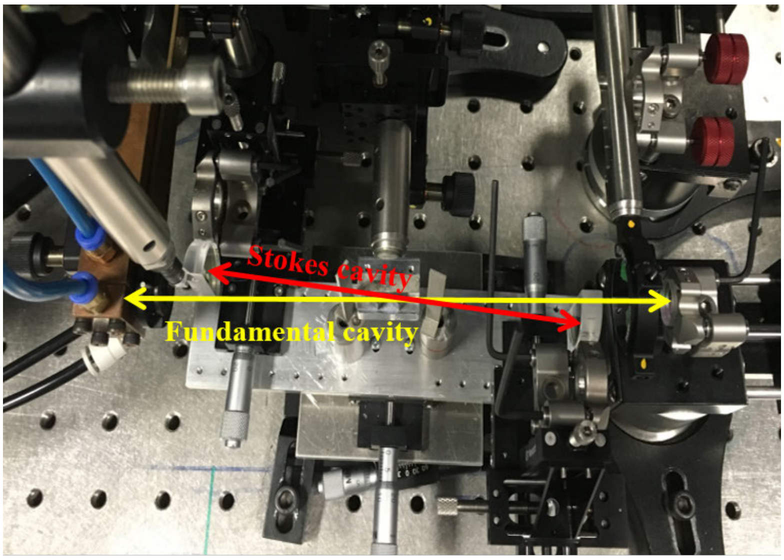


Figure 3.5: Photograph of the experimental setup.

The resonator that formed the Stokes cavity was formed by the 1 m ROC D-shaped mirrors $M_3$ and $M_4$ ( to enable oscillation of the fundamental and Stokes fields without clipping). Stokes mirrors are both HR coated and their R ~ 99.999% from 1060 nm to 1080 nm (as measured by the supplier). The total lengths of the fundamental and Stokes resonators were 180 mm and 115 mm, respectively. To achieve phase matching and angle tuning, the Stokes cavity was mounted on a high precision rotation stage (Thorlab model: PR01), and it enabled its rotation about the z-axis of the $MgO:LiNbO_3$ crystal. The angular rotation range is 0 - 6°.

High resistivity (R>10 k$\Omega$cm$^{-1}$) silicon prisms (supplied by Crystran Ltd) were used to overcome TIR and extract generated THz radiation as described in section 2.1.3. And the method of liquid-mediated adhesion [159] was used to attach the silicon prisms to the polished (y-axis) surface of the MgO:LiNbO$_3$ crystal. The overall view of the intracavity CW THz laser is shown in Figure 3.5.

## 3.4 Experimental results

In this section, the laser performance with optimised arrangement are presented in detail. Significant improvements is achieved by using the new setup compared to Lee's work on the CW intracavity laser reported in [53].

A step-wise approach was taken to improving the performance of the CW THz system reported by Lee [53] following the before mentioned design optimisations. Specific areas of the laser which were focused on using (a) a new pump scheme: 879 nm, polarised diode pumping; (b) adding an aperture after the laser crystal to limit high-order transverse modes.

### 3.4.1 Characterisation of the fundamental laser

It is difficult to build an intracavity CW THz laser. For an intracavity laser, the fundamental laser performance is very important and it determines whether you can reach SPS threshold. Therefore, it is necessary to optimise the fundamental laser.

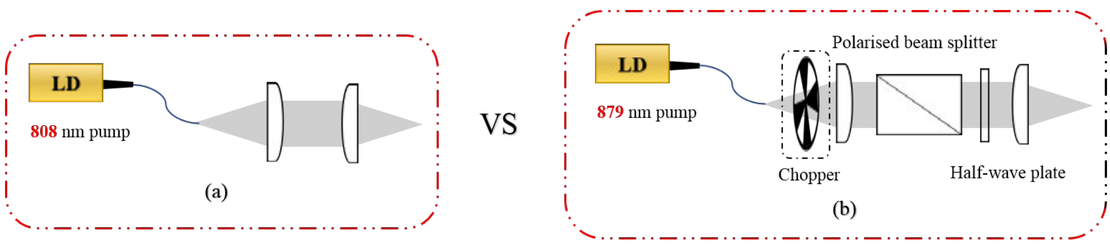


Figure 3.6: Pump schemes in (a) 2014 Lee's CW THz paper [53], (b) this thesis.

#### i. Optimising of the pump scheme

In order to do so, optimising the pump schemes was the first step, shown in Figure 3.6 with the comparison of Lee's pump scheme [53]. As it mentioned in section 3.2, Nd:GdVO$_4$ crystal is polarisation-dependent, and has strong absorption at $\pi$-polarisation, so $\pi$-polarisation was achieved by using a polarising beam splitter and a half-wave plate. In addition, 879 nm pump wavelength is better for alleviating thermal loading in a fundamental laser. Considering these properties, 879 nm, $\pi$-polarisation pump scheme was selected for fundamental laser in this thesis. Figure 3.7 prevents measurements of the unabsorbed pump power to enable a comparison of pumping scheme in this thesis and the 2014 CW THz laser [53].

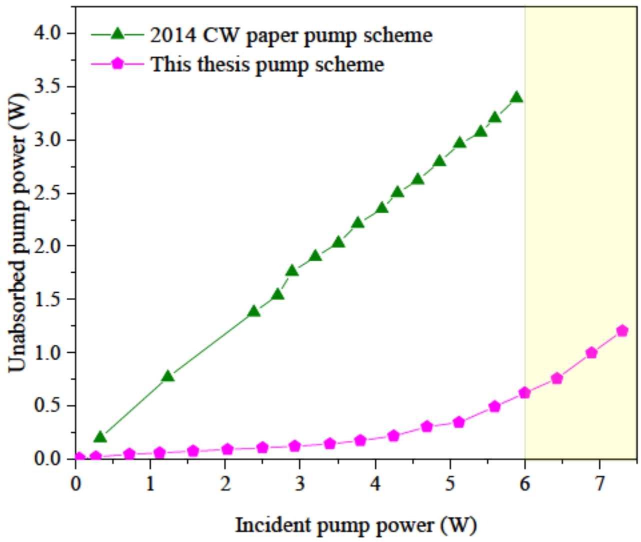


Figure 3.7: Comparison of pump schemes with 2014 CW paper (808 nm, unpolarised pump) and this thesis (879 nm, $\pi$-polarised pump). The data from the 2014 result was obtained via private communication with Lee [160].

It is clear to see from Figure 3.7 that 879 nm, $\sigma$-polarisation pump scheme had less unabsorbed power than 808 nm, unpolarised pump scheme. The average ubabsorbed pump power of the 2014 CW THz laser is more than 50%, and especially at high pump power, this increases to 60%. In contrast, the polarised pump at 879 nm scheme in this thesis is highly absorbed, and 90% of pump power is absorbed. The advantage in this work is that lower unabsorbed pump power will result in far less heating of the laser crystal (Nd:$GdVO_4$) and SPS crystal ($LiNbO_3$) in this THz laser, which will benefit laser performance.

### ii. Optimisation of the 1063 nm fundamental laser

The method to examine the laser performance of the fundamental field is to use a high transmission output coupler. As the fundamental mirrors used in the THz laser is very high reflecting, the leaking power is very tiny, so it is difficult to observe the fundamental power changes by optimising cavity. To make sure the laser behaves in its best performances, a

T=5% output coupler was used, and the output power is shown in Figure 3.8.

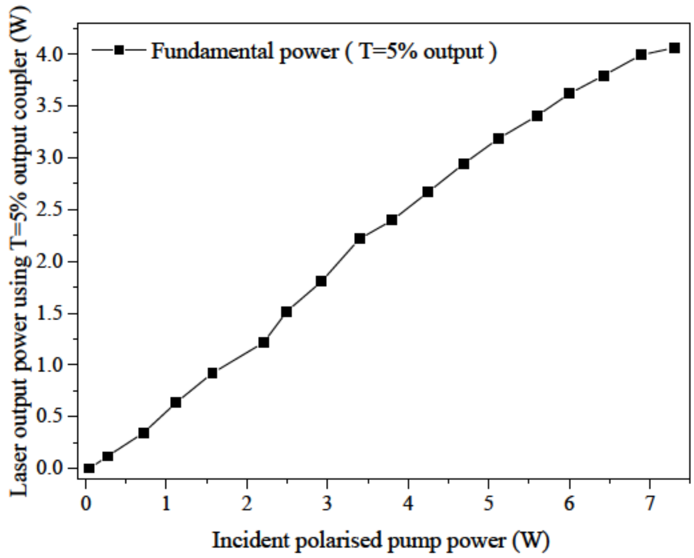


Figure 3.8: Fundamental field laser output power using T=5% output coupler.

The laser output power in the fundamental field linearly increases with incident polarized pump power and the slope efficiency is around 56%. It is noteworthy that the crystal and mirror positions are optimised and the mode matching between the laser mode and pump spot are achieved. This is comparable with other published solid-state Nd-based CW lasers at the similar incident diode pump power [139, 161–163], so this result suggests good mode matching and an optimised system for the fundamental field.

The laser was very sensitive to alignment, to make sure the laser output is continuously increasing and the beam profile is $TEM_{00}$ required frequent adjusting the position of optical components in the fundamental laser resonator.

Next, the T=5% output coupler was replaced by high reflectivity mirror and little to no adjustment on HR mirror was necessary to get it lase.

Figure 3.9 shows the fundamental output power in the cases of with and without MgO:$LiNbO_3$ in the high-Q fundamental cavity. The reduction in fundamental power when the MgO:$LiNbO_3$ crystal was inserted is significant, and these losses may arise from scattering, AR coating and absorption in MgO:$LiNbO_3$ which will also impact the ability to reach SPS threshold.

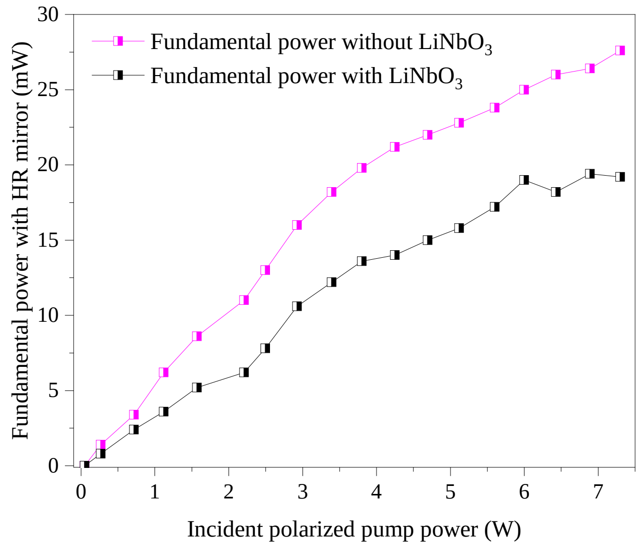


Figure 3.9: Transmitted fundamental power (measured through $M_2$ ), with and without the intracavity MgO:$LiNbO_3$ crystal in a high-Q cavity.

### 3.4.2 Power scaling

To improve the THz laser performance and prepare for the work on linewidth narrowing in the next step, the optimisation of laser system was investigated here with the optimised pump optics and resonator alignment.

The system was power-scaled under the condition of chopped pumping (50% duty-cycle, 400 Hz), producing quasi-CW THz output. Figure 3.10 shows the power transfer curves for the fundamental, Stokes and THz fields as a function of incident polarised pump power. The fundamental and Stokes output power were measured by using a thermal power meter (Thorlabs S310C), through $M_2$ and $M_4$, respectively. In order to detect the Stokes power, a 90° prism was used to reflect the Stokes beam transmitted through $M_4$. The THz signal was chopped with a mechanical chopper (Thorlabs MC2000B) at a frequency of 10 Hz (50% duty cycle) and focused into a Golay Cell (Tydex, GC-1P) with a 50 mm focal length TPX lens.

For this study, the angle between the fundamental and Stokes resonators was fixed and tuning was not considered. The Stokes resonator was angled to generate a wavelength of

1069.43 nm, with corresponding THz radiation being generated at 1.66 THz because it delivered the lowest possible threshold at this angle and highest THz power, as shown in Figure 3.16.

The threshold for the fundamental field is 0.2 W incident pump power, and threshold for the SPS laser occurred for just 2.5 W incident pump power, similar to [53] where the threshold was 2.3 W. Compared to the 2014 CW THz laser [53], the system was less sensitive to vibrations and small adjustments to the resonator alignment (both fundamental and Stokes fields). The overall efficiency and power scaling capacity of the system are 10 times greater, with the maximum instantaneous THz power of 23.1 $\mu$W (under the incident pump power of 5.1 W) being generated. This is in contrast to a maximum of 2.3 $\mu$W (under the incident pump power of 5.9 W) being generated in [53].

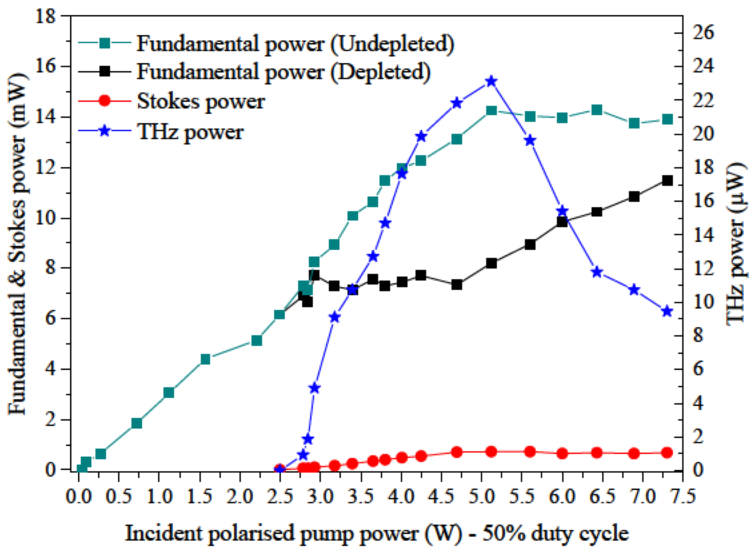


Figure 3.10: Output powers for fundamental, Stokes and THz fields in an intracavity CW THz laser.

Similar behaviours of power scaling in [53] were observed: the THz power rapidly increased to a maximum output; and thereafter, started a rapid drop with the increased incident pump power and accompanied with significant instability of the fundamental field and quite sensitive to cavity alignment. This behaviour is a consequence of both strong thermal lensing and phase mismatch, which will be discussed in the coming chapters. Chopped diode pump with 50% duty cycle was used to effectively reduce thermal loading effects [149].

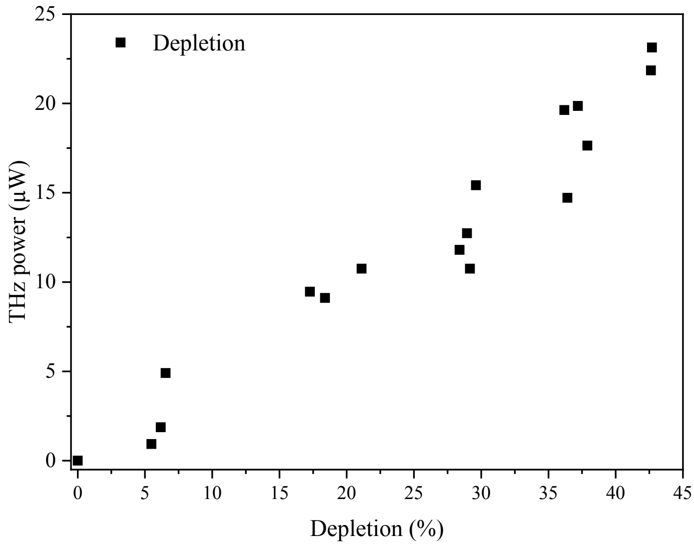


Figure 3.11: THz output power as a function of fundamental depletion.

Depletion of the fundamental field via SPS was determined by measuring the change in fundamental field power when the Stokes field was lasing or not, and this is shown in Figure 3.11. The depletion can indicate the efficiency of the SPS process. In this work, the depletion percentage is proportional to detected THz power. The maximum THz power of 23.1 $\mu$W is detected with maximum depletion of 42.7%. The maximum fundamental field depletion that could be achieved was higher in the case of this setup compared to our earlier work (42.7% c.f. 36% [53]). These observations are consistent with a reduced thermal load when chopping the incident diode pump, and consequently reduced thermal lensing within the laser crystal. This was one of the factors which led to greater resonator stability, and improved power scaling capacity. Other significant factors are the control of beam distortion and generation of free-carriers in silicon prisms (managed with the use of blocking windows and an intracavity aperture) used for out-coupling the THz radiation.

### 3.4.3 Spectral characteristics

The spectra of the residual fundamental and Stokes fields were measured using a fibre-coupled spectrometer (Ocean Optics HR4000) with a resolution of 0.17 nm. Figure 3.12 a shows the fundamental spectrum and Figure 3.12 b shows the corresponding Stokes spectrum.

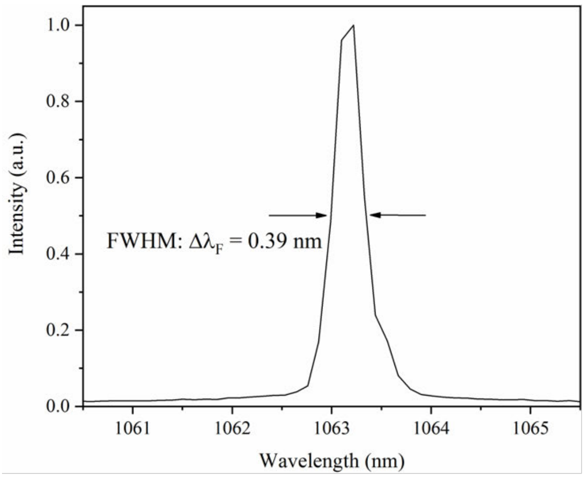


(a)

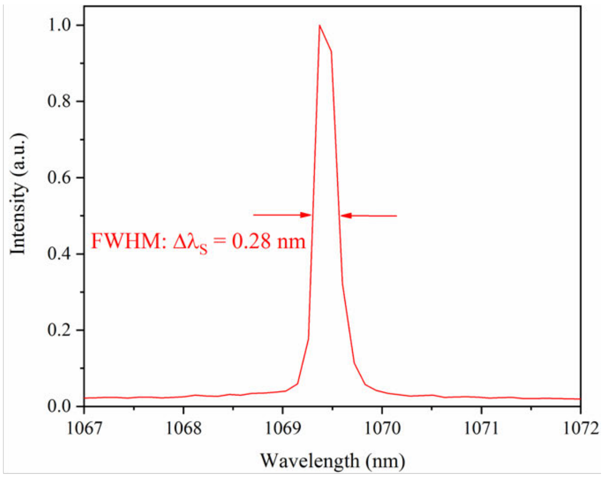


(b)

Figure 3.12: Spectra from the intracavity CW THz laser (measured using HR4000) in (a) fundamental field and (b) Stokes field.

We found that no other spurious lines except the desired wavelength of 1063 nm was present as the pump power increased until 6.5 W. Another fundamental wavelength appeared when the incident pump was over 6.5 W, and at the same time the SPS process became less effective. This is mainly due to competition between two laser polarisations ($\sigma$ and $\pi$ polarisation) in the high Q-factors fundamental field. When the incident pump power increased above 6.5 W, 1063 nm (fundamental wavelength of the desired $\pi$-polarisation) and 1066 nm (fundamental wavelength of the undesired $\sigma$-polarisation) both lase with the 1066 nm line reaching lasing threshold. In this process, the fundamental intensity distributed in these two polarisations and $\sigma$ polarisation is no contribution to generate THz, therefore, this is another reason which may cause THz power decline. The fundamental laser with the 1066 nm present can be suppressed by adjusting the output coupler, but still, suffers from thermal loading and as a result of dropped THz output.

The FWHM linewidth of the fundamental and Stokes fields were measured at the maximum THz output point and the values were 0.39 nm (102 GHz) and 0.28 nm (72 GHz), respectively. The linewidth is broad and this is due to many longitudinal modes oscillating in such high Q-factor cavity. The Stokes linewidth is narrower than fundamental field because of higher SPS threshold limiting mode oscillating in the Stokes field. The linewidth of the THz field can be estimated based on measured fundamental and Stokes values using the method mentioned in [107], is 72 GHz.

### 3.4.4 Beam profiles

The beam profiles both in fundamental and Stokes was measured by a laser beam profiler (Thorlabs BC106-VIS). It is very important to note that no beam distortion was observed and no patterning occurred in fundamental and Stokes fields through the whole pump range. The beam profiles with four different pump powers can be seen in Figure 3.15 a and Figure 3.15 b, respectively. This is in contrast to the 2014 CW laser in [53]. In [53], high-order modes were observed and the mode structure was increasingly distorted in the fundamental field with increased pump power (no distortion presented in the Stokes field), which can be clearly seen in Figure 3.13.

Beam distortion due to photorefraction limits the usability of lithium noibate crystals for SPS process in a polariton THz laser. Unfortunately, congruent $LiNbO_3$ exhibits photorefractive damage, which is light-induced refractive index changes that alter the optical wavefronts and disturb the phase matching in SPS process. Photorefractive damage leads to beam distortion and hence limits the maximum output power.

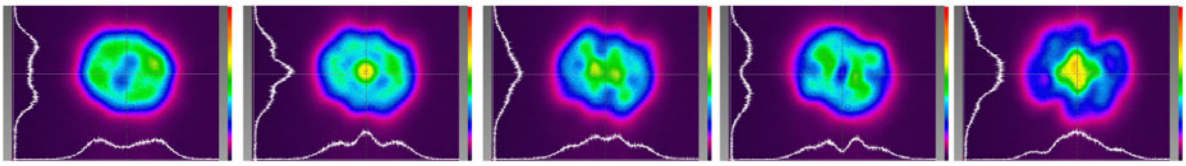

Figure 3.13: Beam distortion of fundamental field in the 2014 CW intracavity THz laser reported in [53].

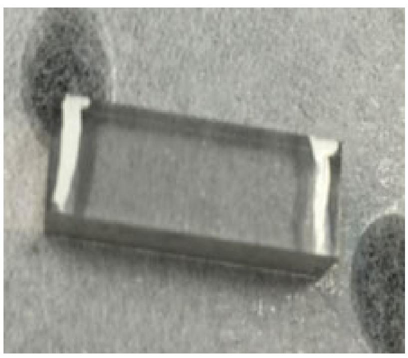

Figure 3.14: Photo of a $MgO:LiNbO_3$ crystal used in this work. The shorting lines are seen at each end of the crystal.

In order to overcome these problems, some methods are taken into consideration. As in [53], short-circuiting the c-surfaces of the $MgO:LiNbO_3$ crystal by painting gold or silver conducting paste and connecting each surface (shown in Figure 3.14), this method can prevent the crystal developing surface charges during heating or cooling and this will hold-off any pyroelectric effects homogeneously throughout the crystal [152]. To make sure the crystal was totally shorted between each surface, the resistance was measured. When the crystal was well shorted, the resistance is around tens of Ohms. However, this may be of limited benefit as the strong near-infrared fields are creating spatially inhomogeneous heating in the crystal when the fundamental and Stokes beam propagates through the crystal. This will cause localised heating and pyroelectric fields which cannot be screened by short-circuiting the crystal. In addition, pyroelectrically-induced refractive index profile which is induced by the thermo-optic effects also have an influence on beam distortion and light scattering. Therefore, shorting the $MgO:LiNbO_3$ crystal will not completely solve pyroelectric refractive index variations due to high intensity propagating modes.

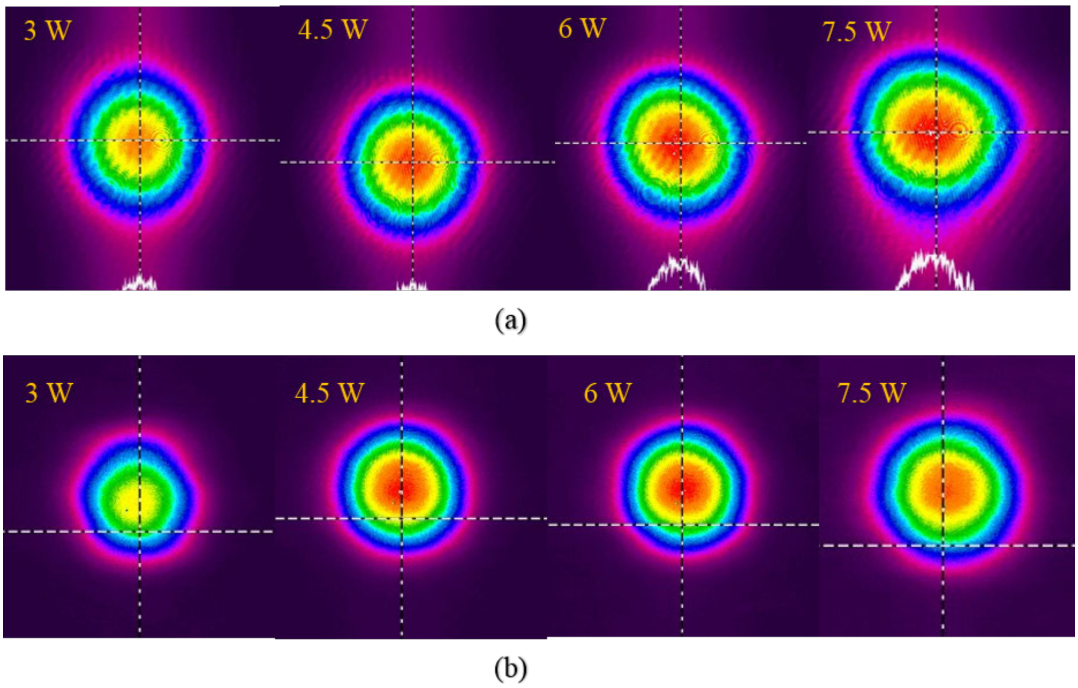


Figure 3.15: Beam profile in an intracavity CW THz laser at different incident pump power with aperture in (a) fundamental field, (b) Stokes field.

An intracavity aperture was used in the fundamental cavity, after the laser crystal. The aperture constrains the number of oscillating transverse modes and reduces the amount of residual pump light propagating through to the MgO:LiNbO$_3$ crystal. A TEM$_{00}$-like fundamental mode is produced using this method.

### 3.4.5 Tunability

The THz frequency was inferred from the difference in frequency between Stokes and fundamental wavelength. Figure 3.16 shows the THz tunability at the incident diode pump power of 6.5 W. The Stokes tuning range can cover from 1068.18 nm to 1077.34 nm, but the detected THz tuning range in this laser is from 1.30 THz to 2.51 THz (corresponding to the Stokes wavelength from 1068.18 nm to 1072.81 nm). In comparison to [53], the overall frequency tuning range is wider (1.2 THz vs 0.8 THz) and have a similar shape, with dips in the spectrum due to absorption by water vapour in the laboratory of atmosphere [1, 164].

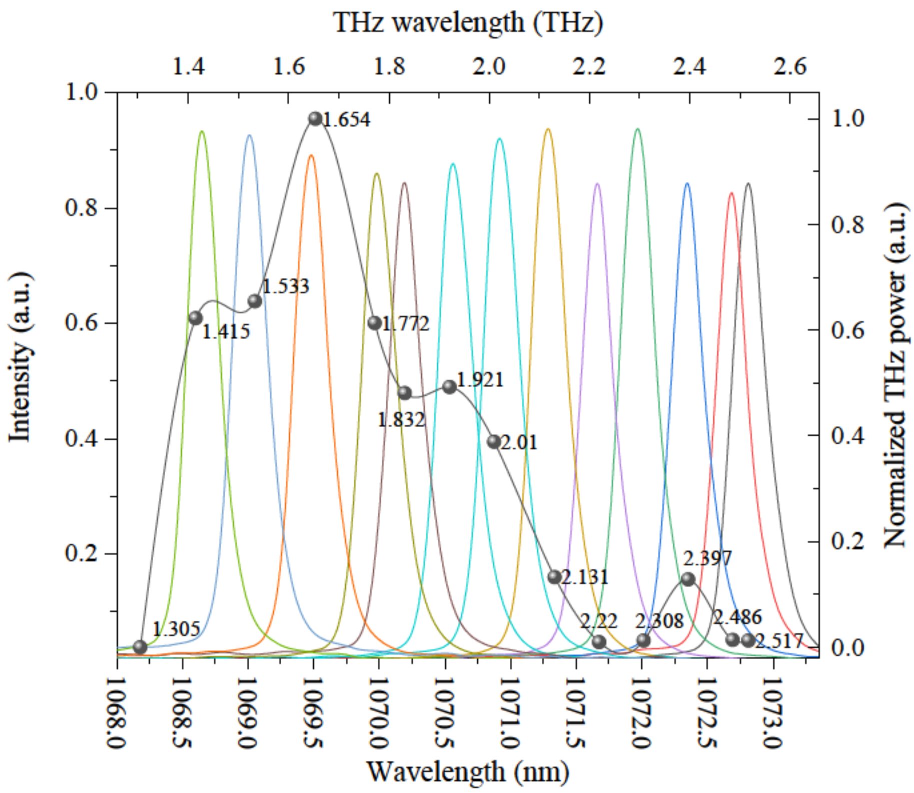


Figure 3.16: Stokes spectra (coloured plots) and THz signal (black curve) as a function of Stokes wavelength/THz wavelength at the incident diode pump power of 6 W.

There are a number of interesting features to note. The detected THz power depends most strongly on the phase matching angle and THz frequency. Based on this laser design, the smallest angle between the fundamental and Stokes cavities is 1.5°, so that the system cannot lase at the Stokes / THz wavelength shorter than 1068 nm (1.3 THz) because of clipping of the fundamental field by the Stokes cavity mirrors which are D-shaped in order to minimise this problem. When the angle is increased, the detected THz emission increases rapidly and reaches the maximum at 1.654 THz. This is consistent with the increase in gain due to SPS process [49]. The SPS gain increases rapidly in the range of 0 THz to 1.9 THz, and then decreases as the polariton frequency increases towards 3 THz. This decrease in THz output at higher frequencies, is due to a significant increase in frequency-dependent absorption in the $MgO:LiNbO_3$ crystal [67] and the decreased interaction regions between two fields as the angle between the cavities increases.

## 3.5 Discussion

Compared to [53], the laser performances have been greatly improved and summarised in Table 3.3. The results highlight that several key factors limiting THz power scaling and overall output from this system. The major differences between the two system are the pump scheme and the SPS crystal. The biggest challenges are the thermal effect and photofreactive effect. To manage these, a new pump scheme was used in this thesis and as a result, the residual pump is reduced and the laser slope efficiency is improved.

In [53], the pump wavelength was 808 nm, unpolarised, whith no chopping of the pump. The maximum pump power was 6.2 W, which was only half of the power was absorbed by the laser crystal. Then the residual pump power went through to SPS crystal and some of them were absorbed by a factor of $10^{-3}$ $cm^{-1}$ at pump wavelength in $MgO:LiNbO_3$ crystal [165]. The absorbed pump could be converted into heat in $MgO:LiNbO_3$ crystal and cause photorefractive effects. In contrast, in this thesis, the residual pump power is 5 times lower due to use the polarisation of the high absorption of pump. Therefore, reducing the residual pump originates from fundamental resonator can alleviate the photofreactive effect caused by refractive index changes and then enhance output THz power.

The fundamental threshold in two pumping schemes were 0.9 W and 0.2 W, respectively. The system presented here had the lower fundamental threshold indicating low losses in the fundamental resonator. The SPS thresholds kept the similar values (2.3 w vs 2.5 W). The maximum detected THz power using new pumping scheme was 23.1 $\mu$W, an order of magnitude higher than that of 2014 CW THz laser (2.3 $\mu$W), corresponding to maximum depletion of 42.7% vs 36%. The THz tunable range was 1.3 - THz, 0.4 THz wider, this may be due to the fine adjustment of the resonator angle of fundamental and Stokes field, or the improved THz power could be detectable at the edge of the tunable range. No beam distortion was observed in this system, which was a problem in the 2014 CW THz laser.

Table 3.3: Comparison between the intracavity CW THz laser in [53] and this thesis

| **Laser performance** | **2014 CW THz laser** [53] | **This thesis** |
|---|---|---|
| Pumping wavelength | 808 nm | 879 nm |
| Maximum pump power | 6.2 W | 7.5 W |
| Polarised pumping | No | Yes |
| Chopped pumping | No | Yes |
| Fundamental threshold | 0.9 W | 0.2 W |
| SPS threshold | 2.3 W | 2.5 W |
| Maximum detected THz power | 2.3 $\mu$W @ 1.83 THz | 23.1 $\mu$W @ 1.66 THz |
| Maximum depletion | 36% | 42.7% |
| Tunability | 1.5-2.3 THz | 1.3-2.5 THz |
| Beam distortion | Yes | No |

## 3.6 Summary

In this chapter, the improvements of the intracavity CW THz laser have been described and characterised.

The comparison with Lee's work in 2014 shows the advantage of the new pump scheme, specifically, pumping at 879 nm brings less residual pump and thermal loading. Significant enhancements of THz output power have been achieved and 23.1 $\mu$W THz output (10 times higher than the power reported [53]) could be the highest CW output power based on SPS process to generate THz emission.

The thermal effects and photorefractive effects of the CW source have been investigated. No beam distortions were observed in the fundamental and Stokes field. The cause of the distortion of the fundamental field mentioned was solved, and this included contributions from reducing free-carrier-induced photorefractve effects within the MgO:$LiNbO_3$ using the new pumping scheme and an aperture before the SPS crystal. The use of the new pumping scheme was effective at reducing the residual pump power through the SPS crystal, which minimised the possibility of refractive index changes due to heating the SPS crystal. The beam profiles in fundamental and Stokes fields were shown to be Gaussian-like and of good quality.

The spectral properties of fundamental and Stokes fields were investigated in the free-running case. The fundamental and Stoked linewidths in the "free-running" case were 0.39 nm (102 GHz) and 0.28 nm (72 GHz), respectively. These values will be used to evaluate the level of linewidth reduction in the following chapters as the reference for comparison.

The improved intracavity CW THz system lays the groundwork for the linewidth narrowing study in the following chapters.

# 4

# Linewidth-narrowing using tilted etalons

## 4.1 Introduction

The linewidth of the terahertz field generated by the basic intracavity source described in the previous chapter was around 100 GHz [160]. This is adequate for a wide variety of spectroscopic measurements of solids and liquids, as spectral lines these substances exhibit are generally very broad [166]. However, some applications such as THz spectroscopy of water vapour require narrower linewidths. Therefore, developing a narrow linewidth THz laser source is of key importance for high resolution spectroscopy.

The intracavity SPS approach lends itself well to line narrowing strategies which are more traditionally implemented in the fundamental laser, due to the conservation of energy between fundamental and down-converted THz and Stokes photons involved in the SPS process. The control of the linewidths of the two resonant optical waves (fundamental and Stokes) by necessity controls the linewidth of the terahertz wave. Limiting the linewidth of the fundamental and Stokes fields leads to a concomitant reduction in THz linewidth. As the fundamental and Stokes fields are simply optical fields resonant within their respective Fabry-Perot cavities, a host of established linewidth narrowing technologies can be brought to bear in order to realise a narrow linewidth THz system.

Solid etalons act as mode selecting elements and have been widely used to achieve narrow linewidth output in lasers [126, 167–170]. In this system, the idea is to insert an etalon into the fundamental cavity to obtain narrow bandwidth output both in fundamental and Stokes fields and thus the THz field can be narrowed as well.

Etalons can act in two different ways depending whether they are on its aligned to the laser cavity or not. In this chapter, the etalon is tilted at an angle to the axis of the laser cavity, so that it acts as an intracavity bandpass filter (This would be considered the "traditional" way of using an etalon). This chapter concerns the investigation of an intracavity CW THz laser using tilted solid etalons for the purpose of linewidth narrowing.

This chapter starts with describing how the angle at which the etalon is tilted affects its response, in theory. This part includes the transmission properties with wavelength resonance at normal incidence or at gain max, spectral bandwidth, transmission with tilt angle and how to calculate losses associated with etalon tilt. Several experiments using different etalons are described following the theoretical study. The terminology "free-running" will be used to describe the laser system when no etalon is present. Power transfer characteristics, and SPS thresholds will be compared for the case of with and without etalons ("free-running" case) and specifically the impact of tilted etalons. Further investigations using a 100 $\mu$m uncoated etalon will be presented for an intracavity CW THz laser due to the excellent performance attained. The impact of the spectral linewidth on effective SPS threshold will be analysed, and experiments to access the benefits of controlling the spectral behaviour of the laser with an etalon will be presented.

## 4.2 Experimental setup

The experimental setup was consistant with the one described in Chapter 3, but with the additon of an etalon inserted in front of output coupler $M_2$, shown in Figure 4.1.

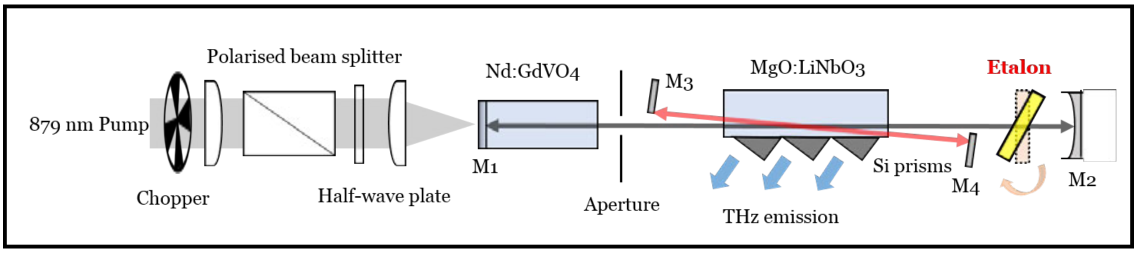


Figure 4.1: Experimental setup with tilted etalon in the fundamental cavity.

The etalon was positioned a small angle ($\theta_{gmax}$) to the laser beam in the fundamental resonator so that a transmission peak occurred at a wavelength close to the wavelength of maximum gain in the Nd:GdVo$_4$ crystal. The etalons ideal position was at the laser beam waist. However, the laser beam waist position is in the middle of the laser crystal and the system is highly compact, so it is not enough space was available to put the etalon at the laser beam waist point or closer. Based on the modelling using LASCAD, the laser beam size was only increased 0 - 50 $\mu$m so it would not be strongly effected by the etalon position in the system.

## 4.3 How does tilt effect etalon response?

### 4.3.1 Effects of etalon tilt on wavelength response

The linewidth of a laser is determined by how many longitudinal modes are able to oscillate. An optical etalon restricts the number of oscillating longitudinal modes in the cavity. Different etalons have different transmission properties, so the transmission properties for each etalon mentioned in Table 2.4 are also considered. The theoretical transmission curves of etalons are calculated using the equations given in Koechner [115]:

$$T = [1 + \frac{4R}{(1-R)^2} \sin^2(\frac{\delta}{2})]^{-1}, \tag{4.1}$$

where

$$\delta = (\frac{2\pi}{\lambda}) 2nd \cos\theta_{int}. \tag{4.2}$$

R is the reflectivity of each etalon surface, assumed equal for both surfaces, $\lambda$ is the wavelength, n is the refractive index of the etalon, d is the thickness of the etalon and $\theta_{int}$ is the angle of the beam to the surface normal inside the etalon. In Figure 4.2 is plotted the transmission of the nine examined etalons.

We can see that the thinner the etalon, the greater the free spectral range; the higher the reflectivity of the surfaces, the higher finesse and the narrower the transmission peaks. These curves were calculated assuming perfect surface quality and flatness.

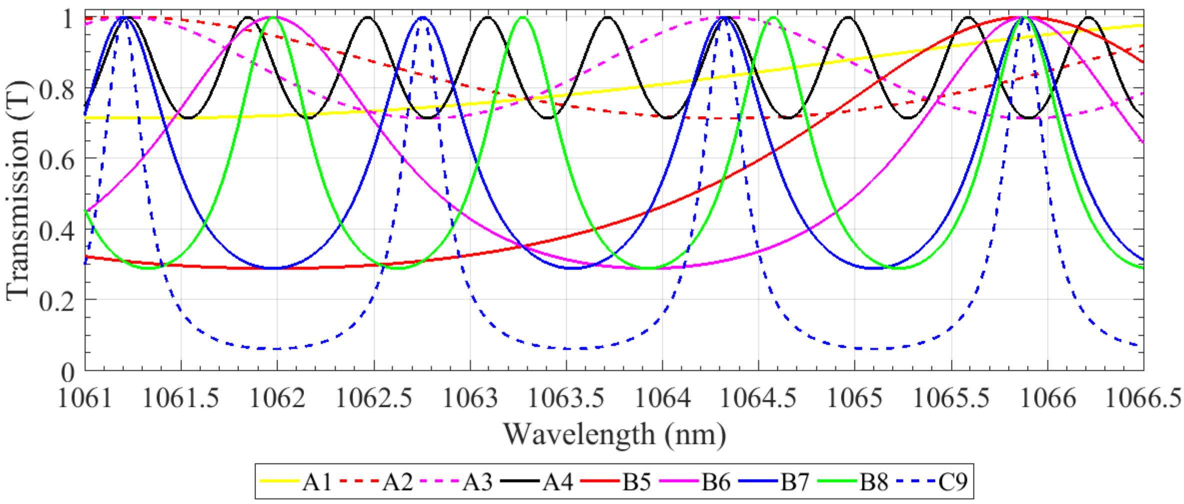


Figure 4.2: Different etalon transmission curves as a function of wavelength, when at normal incidence. Refer to Table 2.4 to see the properties of each etalons.

Ideally an etalon would be configured, by tilting, such that one of its transmission peaks coincides with the peak wavelength of the Nd:$GdVO_4$ stimulated emission cross section. The maximum of the Nd:$GdVO_4$ stimulated emission cross section is at 1062.8 nm [112] from here-on, this wavelength will be referenced to as $\lambda_{gmax}$. The maximum transmission of each etalon is not at the central wavelength of 1062.8 nm when the etalon is used at normal incidence, and several degrees of tilt are required for a transmission peak to coincide with maximum gain. This is considered in the next step.

### i. Calculations of tilt angles with wavelength resonance at gain max

In this section, the etalon tilt angle has been calculated and the effect on transmission peaks is discussed. The optimal tilt angles for the various etalons range from 2° to 10° in order to achieve highest transmission at 1062.8 nm. Figure 4.3 shows the transmission curves of each etalon and the required tilt angles, to achieve maximum transmission at $\lambda_{gmax}$.

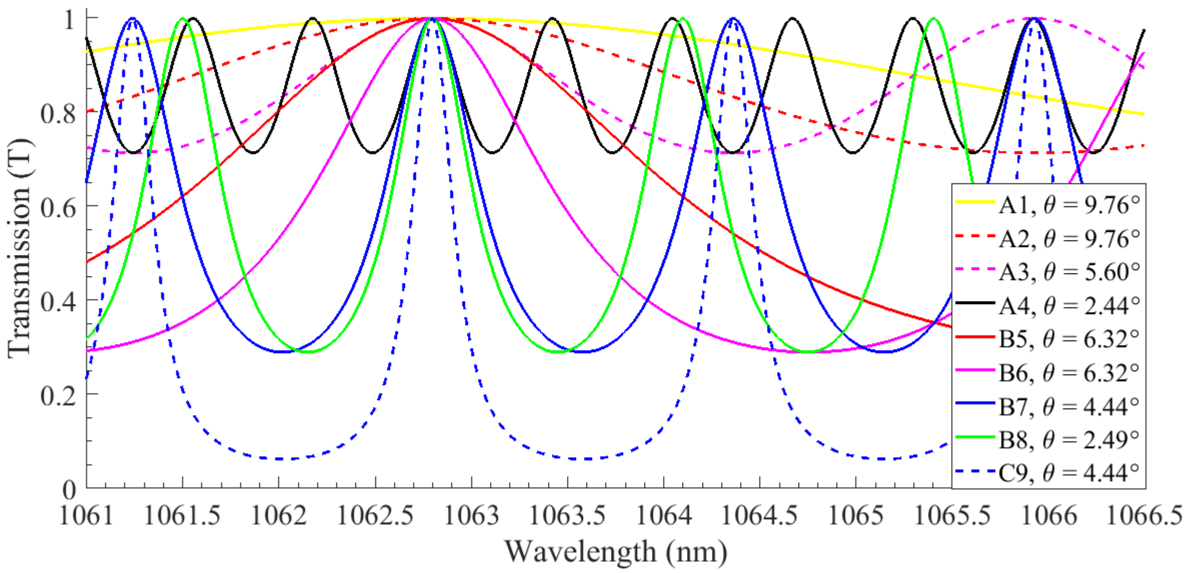


Figure 4.3: Etalon transmission curves as a function of wavelength, when the etalon tilt angle is optimised for maximum transmission at gain max. The corresponding angles of tilt for each etalon are shown in the Figure 2.4.

Based on the theoretical modelling, some of these etalons have been chosen to use in our CW THz laser to investigate spectral properties which will be mentioned in this chapter. Very high intensity fundamental and Stokes fields are required to build an intracavity THz laser, so the transmission properties, spectral properties and losses should be considered and then in doing so, it is anticipated that some trade offs will be made. Therefore, in the next step, the relationships of tilted etalon angle with transmission, wavelength shifts in etalon resonance as a function of tilt angle, and walk-off losses will be considered.

### ii. Full width at T=98%

The extent to which an etalon in the fundamental resonator will narrow the fundamental linewidth is indicated by the spectral linewidth of the etalon transmission peak. In our intracavity CW SPS THz laser, in order to reach SPS threshold, extremely high intensity in the laser cavity is required, and relatively modest losses of a few percent can prevent the SPS process. Therefore, in this part, the full width at T=98% is used as a metric to select etalons for the CW THz laser system. The full width at T=98% for each etalon is listed in Table 4.1. In other words, this is the spectral bandwidth of one of the etalons passband over which 98% transmission is maintained.

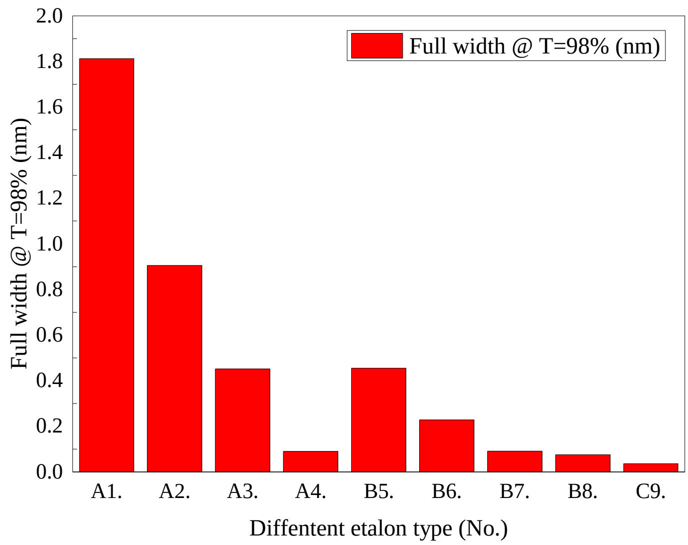


Figure 4.4: Summary of full width @ T=98% for the different etalons.

We can see that the 250 $\mu$m, R=60%, FS (C9) provides the smallest full width @T=98% (0.036 nm) centred at 1062.8 nm for a tilt angle of $\theta$ = 4.44°. On the other hand, among these etalons, the 25 $\mu$m, R=8.4%, YAG (A1) has the highest full width @ T=98% value (1.81nm) for a tilt angle of $\theta$= 9.76°. The 300 $\mu$m, R=30%, FS (B8) has the second narrowest bandwidth of 0.075 nm, similar to the value for the 500 $\mu$m, R=8.4%, YAG (A4) and the 250 $\mu$m, R=30%, FS (B7). With the goal of narrowing linewidth, it would hence be assumed that etalon C9 would be the ideal choice, as it offers the smallest full width. However, one must also consider the FSR of the etalon and how this interacts with the emission bandwidth of the fundamental field.

The etalons were chosen, from the limited range that were available to us, on basis of free spectral range and surface reflectivity demonstrated in Chapter 2.2. The free spectral range was selected large enough to ensure only one resonant mode, also the surface reflectivity determines finesse: too low a finesse would not narrow sufficiently, and too high would cause unacceptably high round-trip losses. The etalons were chosen from a set of 30% surface reflectivity in different thicknesses (fused silica)and some uncoated YAG etalons (the details of etalons can be seen in Table 2.4). In Section 4.4, the laser performance of using different etalons were analysed and comparisons were made.

Table 4.1: Summary of full width @ T=98% for different etalons

| No. | Etalon type | Full width @ T=98% (nm) | $\theta_{ext}$ | FSR (nm) |
|---|---|---|---|---|
| A1. | 25 $\mu$m, R=8.4%, YAG | 1.812 | 9.73° | 12.17 |
| A2. | 50 $\mu$m, R=8.4%, YAG | 0.90535 | 9.73° | 6.12 |
| A3. | 100$\mu$m, R=8.4%, YAG | 0.4518 | 5.59° | 3.07 |
| A4. | 500 $\mu$m, R=8.4%, YAG | 0.0903 | 2.44° | 0.62 |
| B5. | 50 $\mu$m, R=30%, FS | 0.45475 | 6.32° | 7.67 |
| B6. | 100 $\mu$m, R=30%, FS | 0.2275 | 6.318° | 3.85 |
| B7. | 250 $\mu$m, R=30%, FS | 0.0908 | 4.435° | 1.54 |
| B8. | 300 $\mu$m, R=30%, FS | 0.07522 | 2.485° | 1.29 |
| C9. | 250 $\mu$m, R=60%, FS | 0.0364 | 4.436° | 1.54 |

**iii. Wavelength tuning of peak transmission as a function of tilt angle**

In this part, the tuning characteristics of an etalon as it is tilted, will be considered at the price of transmission change. In the following, transmission at 1062.8 nm as a function of tilt angle are plotted in Figure 4.5 It is assumed that a perfectly collimated beam is incident on the etalon.

The condition that light at wavelength $\lambda$ has a transmission maximum for a given value of $\theta_{ext}$ is $2nd\cos\theta_{int} = m\lambda$, $\theta_{int} \cong \theta_{ext}/n$, where m is an integer; for small $\theta_{ext}$,

$$2nd(1 - \theta_{ext}^2/n^2) = m(\lambda_0 - \Delta\lambda), \tag{4.3}$$

Where $\lambda_0$ is the resonant wavelength for $\theta_{ext} = 0$; $\Delta\lambda$ is the shift in the resonant wavelength due to tilt $\theta_{ext}$. From this expression and the definition of $\lambda_0$, we may express $\Delta\lambda$ explicitly;

$$\Delta\lambda = -\lambda\theta_{ext}^2/2n^2, or \Delta\nu = \nu\theta_{ext}^2/2n^2. \tag{4.4}$$

Thus, the tuning curve of a tilted etalon (resonant wavelength or frequency vs angle of tilt) depends only on the refractive index of the etalon, and not on its thickness (d). In contrast, the frequency selectivity, depends on both the etalon thickness and the reflectivity of its surfaces. The transmission of the tilted etalon is approximately given by [170]:

$$T = [1 + (2F/\pi)^2 \sin^2 \frac{2\pi nd \cos\theta_{ext}/n}{\lambda}]^{-1}, \tag{4.5}$$

where we assume, that absorption and scattering losses within the bulk of the etalon are negligible.

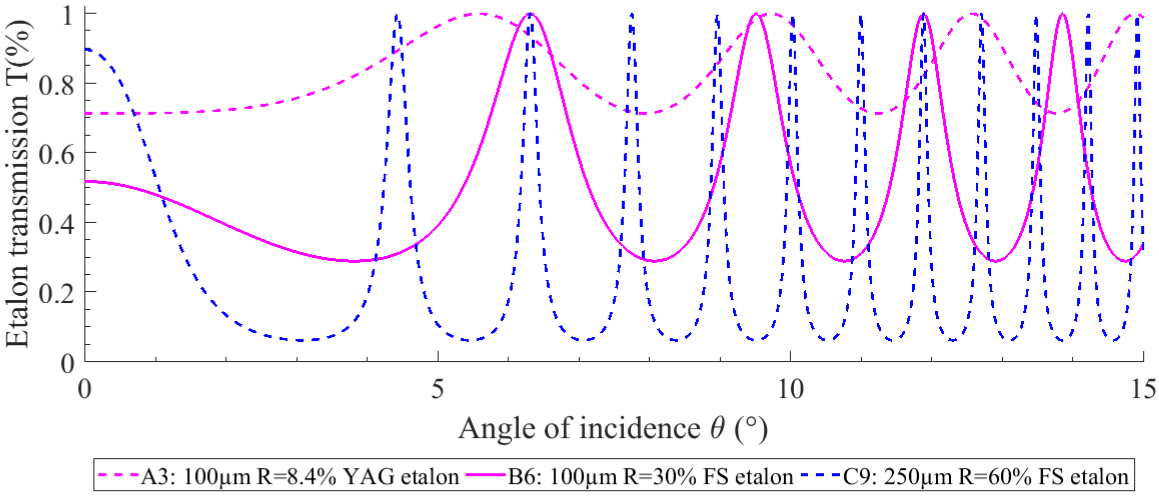


Figure 4.5: Theoretical plot of the etalon transmission at 1062.8 nm as a function of angle of tilt for i). 100 $\mu$m, uncoated YAG (A3); ii). 100 $\mu$m, R=30% FS (B6); iii). 250 $\mu$m, R=60% FS (C9).

When a collimated beam of finite diameter is transmitted by a tilted etalon, the peak transmission at normal incidence is not unity. From Figure 4.5, we can see that the higher finesse (R=60%) etalon (C9) with sharp transmission changes and is more sensitive to tilt angle. The transmission at 1062.8 nm as a function of angle varies from T=90% to T=6% within 2° tilt angle and is hence quite sensitive to angle. In contrast, the 100 $\mu$m, YAG etalon both uncoated and coated, have a region of 3° with lowest transmission in the curves which correspond to $T_{min}$ = 70% and $T_{min}$ = 30% respectively. For the FS etalon, a broad transmission region has been observed at small angles (less than 4°), and has maximum transmission of T=50%. This study highlights a number if features; i) thicker, higher reflectivity etalons exhibit greater sensitivity to angle, moving off its transmission peak more quickly than the 100 $\mu$m etalons,

ii) the change in transmission is significantly higher than the 100 $\mu$m etalons. Both of these factors are of critical importance when considering a practical system.

In this work, three etalons were studied as they offered the best transmission at central wavelength and narrower bandwidth in the fundamental field. The walk-off losses is a key factor with tilted etalons, and this plays a key role in the operation of intracavity, CW SPS lasers.

### 4.3.2 Losses etalons introduce into a laser cavity

While etalons can benefit laser resonators by acting as an intracavity band-pass filter, they do introduce additional losses within the resonator, which must be considered, especially in the case of CW systems which rely on non-linear effects such as SPS.

#### i. Fixed insertion losses

The etalon is assumed to have no losses in modeling, but a perfect etalon with no losses or imperfections is impossible to achieve in practice, so insertion losses must be considered in a practical system. The insertion losses include etalon surface flatness, surface defects, surface damage and surface cleanness. If the etalon surfaces are not parallel, this causes light to leak out of the etalon, while the etalon material may also absorb light during each pass, so material scattering and absorption losses also need to be added into the insertion losses consideration. According to the suppliers that we purchased our etalon from, fixed insertion losses of up to 0.5% (@1063 nm) could be possible.

#### ii. Angle-dependent insertion loss: walk-off losses

Because of multiple internal reflections and finite beam diameter, tilting an etalon causes a transmitted beam to walk-off and this manifests as tilt losses. Walk-off losses are absent when an etalon is used at normal incidence, however in that case, it would interact with one of the resonator mirrors, resulting in a three-mirror (coupled-cavity) configuration. Such a configuration is extremely sensitive to related movements and has absolutely different filter characteristic than when using an etalon itself and tilted, which will be discussed in detail in chapter 5. In this section, we consider how to calculate the walk-off losses induced by a tilted intracavity etalon and it is influence on CW THz laser performance. We follow the approach to calculating walk-off losses presented in [171].

In the following calculations, a lossless etalon is assumed, with perfect surfaces and no absorption in either substrate or the reflective surfaces. It is assumed, that only a beam with a Gaussian beam profile has enough gain to overcome the losses in the laser cavity and that a plane-parallel etalon is placed at the beam waist. Based on these assumption, to get numerical results one has to start with the equation:

$$\gamma = T\frac{2\frac{w_1}{w_0}}{1+(\frac{w_1}{w_0})^2}\sum_{p=0}^{\infty} R^p exp\left[-\frac{(\frac{h}{w_0}-\frac{\Delta x}{w_0}p)^2}{1+(\frac{w_1}{w_0})^2}\right], \tag{4.6}$$

Where $\gamma$ is the expansion coefficient, $w_1$ is the beam radius after going through the etalon, h is the vertical shift based on $w_0$, Δx is the beam displacement.

$$\Delta x = 2d\tan\theta_{int}\cos\theta_{ext}, \frac{\sin\theta_{ext}}{\sin\theta_{int}} = n, c = \frac{\Delta x}{w_0}. \tag{4.7}$$

The value of $\gamma$ has been maximised, varying $w_1$, and h. This gives $\gamma_m$, $w_m$ and $h_{(m)}$, and the beam radius and the position for the best fitting Gaussian mode. The round trip loss l can be obtained through the equations 4.6, 4.7, 4.8:

$$\varepsilon = \frac{2Tw_0w_m}{w_0^2+w_m^2}\sum_{p=0}^{\infty} R^p exp\left[-\frac{(h_m+p\Delta x)^2}{w_0^2+w_m^2}\right], \tag{4.8}$$

$$l = 1-(\gamma_m\varepsilon)^2. \tag{4.9}$$

Therefore, the equations yield the round-trip power loss l as a function of R and c.

Reference [171] considers the dependence of the loss on various parameters and identifies several regimes. In particular when losses are low, it can be shown that $l$ is proportional to $c^2$, to a good approximation, but only in the low-losses region when the correct absolute values are about a factor of 4 lower. One can also show that the dependence of $l$ and R (for constant c) can be approximated quite well by a $R/(1-R)^2$ function. Both would correspond to the equation given by:

$$l = \frac{8R}{(1-R)^2}c^2. \tag{4.10}$$

Applying into our CW THz system, and considering the high Q laser cavity, the etalon round-trip power losses with the small tilt angle should in the low-losses region. The beam waist of this laser is 300 $\mu$m in radius; d is the etalon thickness; and $\theta_{int} and \theta_{ext}$ are the etalon tilted angle of internal and external. Therefore, the intracavity round-trip losses as a function of tilted etalon angle can be obtained by equation 4.10 and is shown in Figure 4.7. The round-trip losses increase with the growing tilt angle and the minimum round-trip losses can be achieved at normal incidence no matter which etalon we use. For the 100 $\mu$m uncoated YAG etalon, the round-trip walk-off losses are 0.1% when the etalon is tilted at 5.59° to coincide with maximum gain of 1062.8 nm. In comparison, the walk-off loss value is 1.25% at 6.3° for the 100 $\mu$m R=30% FS etalon. However, the 250 $\mu$m R=60% FS etalon has very high round-trip losses (23.67%) at 4.4° tilt angle. It should be noted that the tilt angle referenced here is the external angle of incidence.

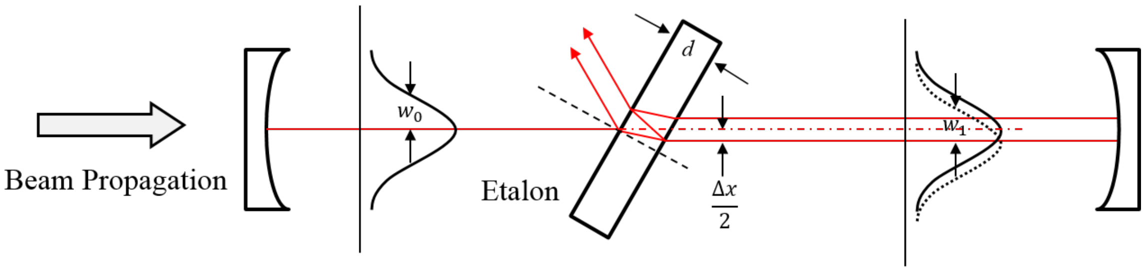


Figure 4.6: Resonator and etalon geometry.

It is obvious that the 250 $\mu$m R=60% FS etalon has the greatest round-trip losses (23.67%) with tilt angle, and this makes reaching SPS threshold impossible. Compared to other etalons used in the CW THz laser system, the 100 $\mu$m uncoated etalon with the lowest round-trip losses (0.1%) has smallest effect on the laser gain, and should enable the laser to reach SPS threshold with different tilt angles. The corresponding experimental results can be seen in Section 4.4. It is questionable whether the 100 $\mu$m R=30% FS etalon will work at small tilt angles (smaller than 6.3°) with 1.5% walk-off losses. Walk-off losses, transmission and full width at T=98% (which has been discussed in section 4.3.1) are all factors which must be considered to obtain the smallest total losses with optimised tilted etalon angle.

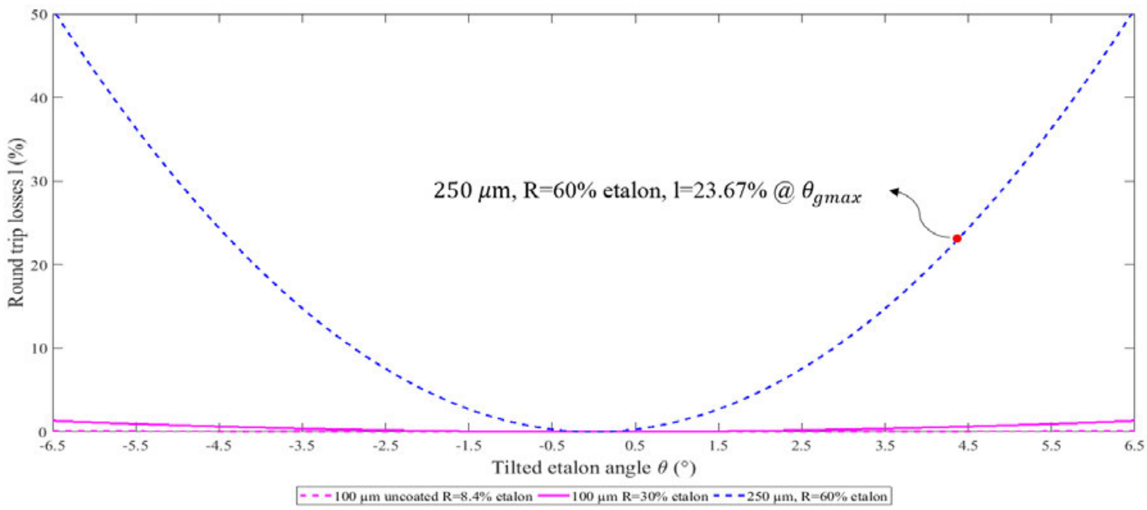


(a)

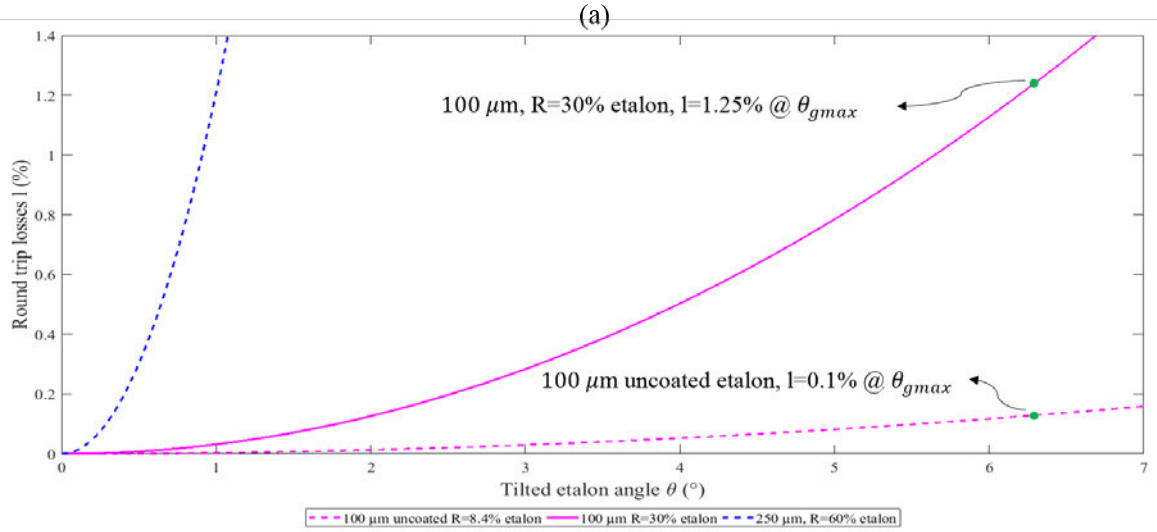


(b)

Figure 4.7: Round-trip walk-off losses calculated as a function of etalon tilt angle for three different etalons (A3, B6, C9). Note the expanded scale for (b).

What is the maximum round-trip losses with tilted etalon angle our THz laser can sustain? What kind of compromise needs to be made considering the etalon insertion losses and round-trip losses? To establish the level of loss the fundamental field resonator can sustain, and still reach threshold, the high reflectively (HR>99.995%) mirror was replaced with a T=1% output coupler. Unfortunately, we were unable to reach SPS threshold so we therefore conclude that etalon losses of 1% would also prevent the laser from reaching SPS threshold. In addition, the intracavity power and the SPS threshold can be estimated by measuring the leaking fundamental power and mirror coatings. No etalon was inserted to do this measurement.

In summary, the total losses induced by tilting intracavity etalons consist of two part: fixed insertion losses and angle-dependent walk-off losses. The fixed insertion losses is determined by the etalon quality and the walk-off losses include contributions from the etalon thickness, reflectivity, beam waist and tilting angle. The modelling results show that the greater tilting etalon angle leads to stronger walk-off losses. Among the total losses, the walk-off losses are dominated in the THz laser system, because they are relevant to the SPS threshold.

## 4.4 Experimental results

Different etalons were selected to be used in our laser based on the theoretical modelling. Considering the transmission at gain max, each different etalon needs to be tilted with different angle when it is inserted into the cavity according to specified requirements. Based on the theoretical modelling talked about in Section 4.2, the results show that inserting an etalon at an angle $\theta_{gmax}$ will give rise to maximum transmission compared to other tilt angles based on the numerical results of the etalon theory, however, tilting the etalon results in walk-off losses. Therefore, in this part, the experimental results will be presented using the etalons selected based on combining the theoretical study of etalons. The laser properties of power transfer and spectral properties were examined in detail at the condition that when each different etalon was inserted with tilt angle $\theta_{ext}@\theta_{gmax}$ calculated in Table 2.4. And the effects of inserting an etalon into the fundamental cavity of an intracavity CW THz laser were investigated in depth.

It is worthy to mention that most of the results were measured with the laser operating under the condition of 50% duty cycle chopping of the input pump radiation, because thermal loading can be relieved (refer to Section 3.2.2). Spectral characterization was performed under 50% duty-cycle chopping of the pump, in cases where the grating spectrometer was used, and in CW pumping when measuring with the Bristol Wavementer and FP interferometer.

### 4.4.1 Power scaling using different etalons at tilt angle $@\theta_{gmax}$

**i. Uncoated YAG etalons**

When an etalon acts as an intracavity bandpass filter, the ideal situation is tilting the etalon insertion angle to achieve maximum transmission at the laser gain peak ($\lambda_{gmax}$) while minimising the associated losses. Walk-off loss and insertion loss are two dominant losses which highly influence whether the SPS threshold can be reached or not when an etalon is used for linewidth narrowing. Therefore, the first step is to establish whether SPS threshold can be achieved, and to understand how the power transfer curve changes when a tilted etalon is used in the laser.

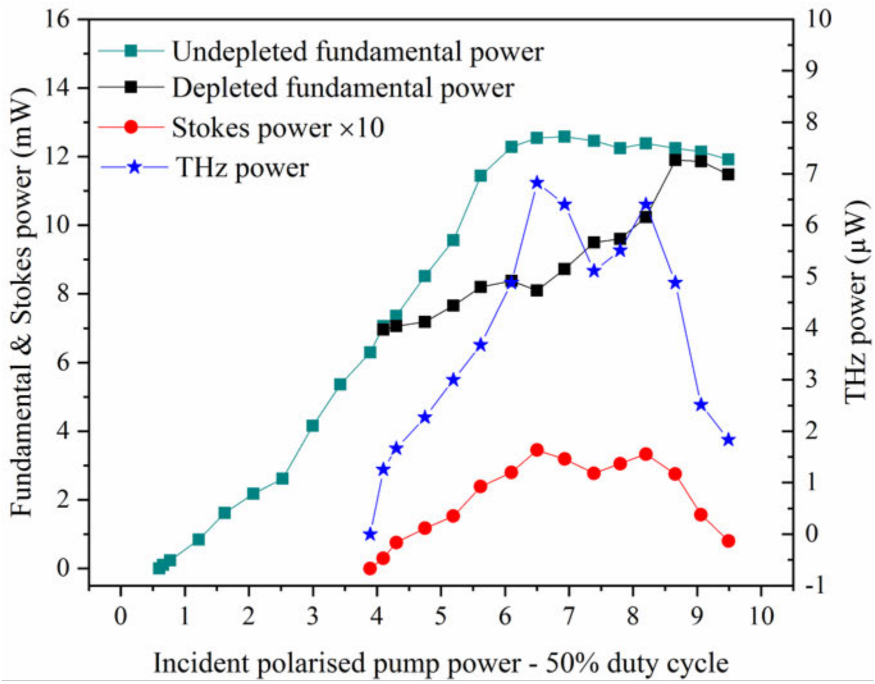


(a)

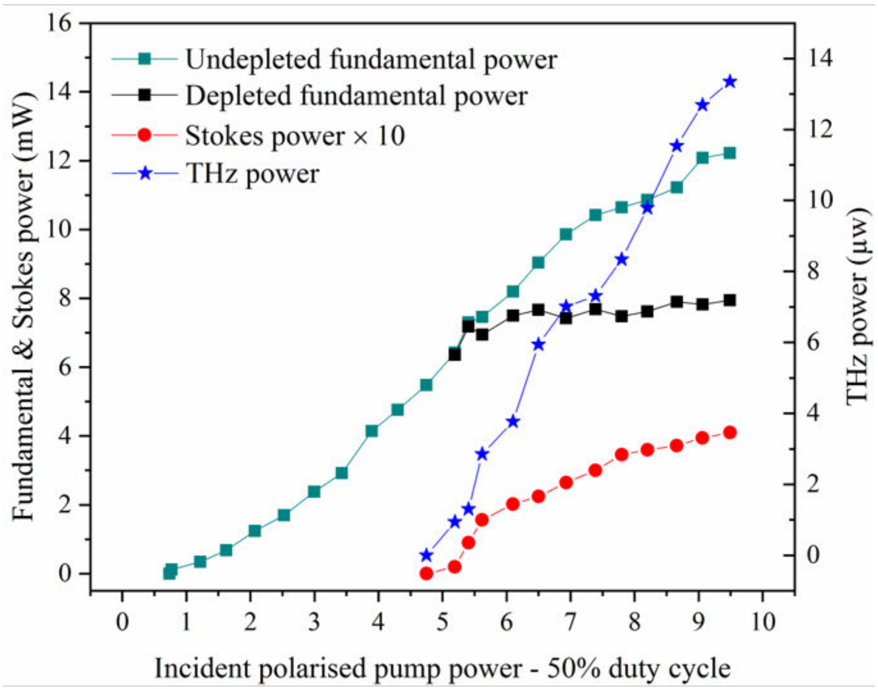


(b)

Figure 4.8: Output powers plotted for fundamental, Stokes and THz fields as a function of incident pump power in an intracavity CW THz laser for the (a) "free-running" laser (no etalon) and (b) the laser incorporating the 100 $\mu$m uncoated YAG etalon (A3).

The power-scaling properties of the laser in each case of (a) no etalon and (b) with 100 $\mu$m uncoated etalon (A3) with 6° insertion angle are shown in Figure 4.8. The power of the residual fundamental and Stokes fields through mirrors $M_2$ and $M_4$, respectively, are plotted, along with the detected THz power as a function of incident diode pump power with 50% duty cycle. In this case, the angle between the Stokes and fundamental field resonators was fixed so as to generate THz emission at 1.8 THz.

Without an etalon in the fundamental cavity, a maximum average output power of 6.8 $\mu$W was detected at 6.5 W incident diode pump power. From the graph in Figure 4.8 a, a fundamental field depletion in excess of 35.4% can be calculated. The results show that the average THz output power dropped at higher pump level and there was some evidence of saturation of the undepleted fundamental, Stokes and THz fields when pumping beyond 6.5 W. These performances are consistent with the observations mentioned in Chapter 3.

When a 100 $\mu$m, uncoated YAG etalon (A3) at 6° incidence was inserted into the fundamental cavity, a significant finding is observed, in that the THz power does not roll-over, and continues to increase at high pump power level. The SPS threshold was reached at 4.6 W (compared to 3.9 W when no etalon is used). The slight increase in threshold may originate from the insertion losses (such as imperfect surface flatness, defects, and walk-off loss, etc.). An increase in the measured THz output was observed, and a maximum average output power of 13.7 $\mu$W was detected at 9.5 W incident diode pump power. From the graph Figure 4.9 b a fundamental field depletion in excess of 35.2% can be calculated in this case at 9.5 W pump. Comparing these two power-scaling results, we can see that the output power of the laser behaves more linearly when a 100 $\mu$m, uncoated YAG etalon was used. If the laser is pumped harder when it has this etalon in the resonator, there is potential to generate more THz output. However, due to concerns about of damaging the SPS crystal ($MgO:LiNbO_3$ crystal), the incident diode pump power was limited to 10 W.

Depletion indicates the conversion of fundamental photons to Stokes photons, and polaritons. High depletion contributes to high THz power in theory. When the 100 $\mu$m, uncoated YAG etalon at 6° incidence is inserted, the depletion over the incident pump power scale appears roughly linear, however, the relationship between depletion and THz power is not obvious, as is shown in Figure 4.9 a for the case where no etalon is used.

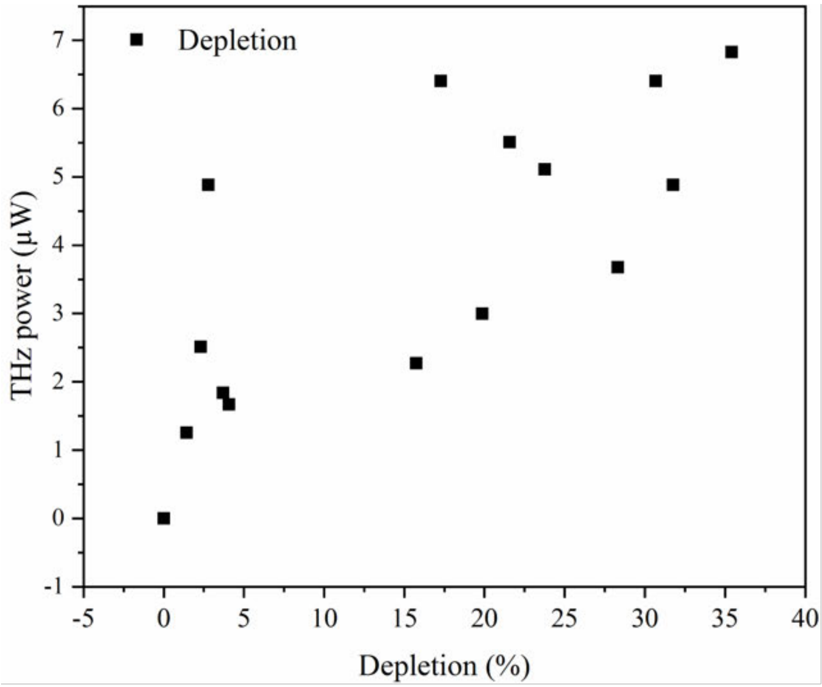


(a)

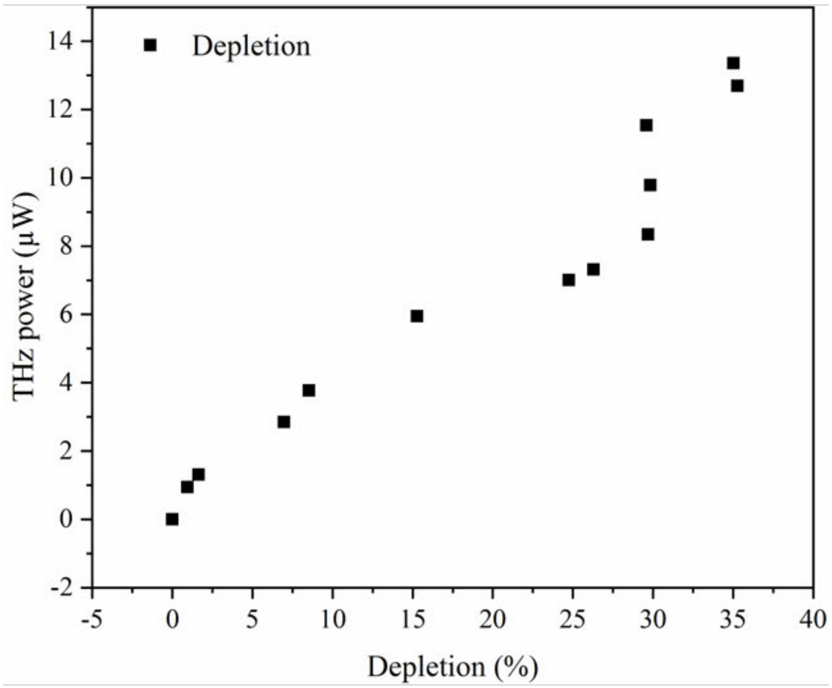


(b)

Figure 4.9: THz output power plotted as a function of fundamental depletion for the (a) "free-running" laser (no etalon) and (b) the laser incorporating the 100 $\mu$m un coated YAG etalon (A3).

Next, the other uncoated etalons were inserted into the fundamental cavity at the appropriate tilt angles $\theta_{gmax}$. The results show that SPS threshold could be reached using the

100 $\mu$m, uncoated YAG etalon with 6° incidence and the 500 $\mu$m, uncoated YAG etalon with 2.4° incidence. The corresponding SPS thresholds were 4.6 W and 9.5 W, respectively.

Table 4.2: Summary of key uncoated etalons with tilt angle

| Etalon type | SPS threshold | Fundamental power (Leaking) |
|---|---|---|
| No etalon ("free-running" laser) | 3.9 W | 12.1 mW @ 9 W |
| 50 $\mu$m, uncoated YAG (A2) with 9.7° | Could not reach | 0.89 mW @ 9 W |
| 100 $\mu$m, uncoated YAG (A3) with 6° | 4.6 W | 12.2 mW @ 9 W |
| 500 $\mu$m, uncoated YAG (A4) with 2.4° | 9.5 W | 3.67 mW @ 9 W |

What is more, using the 500 $\mu$m, uncoated YAG etalon with 2.4° incidence, given concerns about damaging the laser crystal, SPS threshold could just be reached. The Stokes and THz signals are quite weak, and hard to maintain long-time operation. The difficulty in using this etalon effectively is most likely due to high insertion losses arsing from poor surface quality and pallelism. The rest of the uncoated etalons listed in Table 4.2 could not reach the SPS threshold at the maximum incident pump power.

**ii. Coated FS etalons**

Several coated etalons sourced from Light Machinery Inc. are tested in this CW THz system as well. The coated etalons are inserted into the fundamental cavity individually and aligned at the appropriate tilt angle. Unfortunately, it was not possible to reach SPS threshold using any of them. In each case, the fundamental power leaking through mirror $M_2$ dropped to very low levels as shown in Table 4.3. The results indicate that the intracavity fundamental intensity is not sufficiently high to reach SPS threshold and we ascribe these to the relatively high walk-off losses (ranging from 0-40%) that were estimated in Section 4.3.2. Therefore, as anticipated, the experimental and theoretical results both indicate that losses prevent THz lasing and coated etalons with reflectivities of R=30% and higher cannot work as a band-pass filter in this laser when tilted at the appropriate angle.

Table 4.3: Summary of key coated etalon with tilt angle

| Etalon type | SPS threshold | Fundamental power (Leaking) |
|---|---|---|
| 100 $\mu$m, R=30% FS (B6) with 6.3° | Could not reach | 2.05 mW @ 9 W |
| 250 $\mu$m, R=30% FS (B7) with 4.4° | Could not reach | 4.66 mW @ 9 W |
| 300 $\mu$m, R=30% FS (B8) with 2.5° | Could not reach | 1.56 mW @ 9 W |
| 250 $\mu$m, R=60% FS (C9) with 4.4° | Could not reach | 0.03 mW @ 9 W |

### 4.4.2 Spectral properties using different etalons, at tilt angle $@\theta_{gmax}$

The spectral data of the THz laser without an etalon and using the 100 $\mu$m uncoated YAG etalon at 6° incidence and at three different pump powers (6 W, 7.5 W and 9 W) are shown in Figure 4.10. Note that the "free-running" (no etalon) case spectra were measured, shown in Figure 4.10 (left) for comparison. The spectra of the laser in the two cases were measured using an Ocean Optics HR4000 spectrometer, with an optical resolution of 0.08 nm. The fundamental and Stokes spectra were measured simultaneously.

The fundamental linewidth did not broaden significantly (broadening of the fundamental spectrum may occur as the SPS process may act as a spectrally-dependent loss mechanism, akin to what occurs in Raman lasers [167]) as the power increases without the etalon, but the Stokes linewidth did increase from 0.28 nm to 0.37 nm without the etalon.

The fundamental linewidth became narrower when the etalon was inserted. As indicated in Figure 4.10, the fundamental spectra FWHM can be narrowed from 0.38 nm to 0.23 nm and the Stokes spectra FWHM can be slightly narrowed from 0.28 nm to 0.22 nm at the incident pump of 6.0 W. Indeed, the Stokes linewidth is broader at high pump level when 100 $\mu$m uncoated etalon was inserted, and as expected, the linewidth is narrowed to 0.27 nm compared to 0.37 nm without an etalon.

The linewidths measured with the etalon was present are close to or below the instrument limit of the Ocean Optics HR4000. Therefore, a Bristol Wavemeter (model 771A) with the resolution of 2 GHz (0.007 nm) was used to measure the spectra. As described in Section 2.3.5, the Bristol Wavemeter requires a CW or higher than 100 KHz repetition rate input signal, so the laser must be operated under CW pumping. Accordingly, the chopper used to chop the diode pump light was not used.

We note that the intracavity CW THz laser suffered from strong thermal effects, and removing chopping made it worse. The SPS threshold could not be reached. Accordingly, we investigated the effects of the etalon on the fundamental spectra, but not in the presence of SPS, using the Bristol Wavementer. Spectral structures and their effects on the linewidth when an etalon was involved are analysed here.

Different etalons were used at their optimal tilt angle, and the corresponding fundamental spectra traces were shown in Figure 4.11. The FWHM and Full width at 10% intensity were measured to give a reference of linewidth changes, as seen in the plot, the structure contains several peaks and each peak includes many longitudinal modes.

Five different etalons, both coated and uncoated were used in this experiment and it is clear to see that the spectra obtained with the HR4000 were indeed instrument limited. The linewidth of the fundamental field could be narrowed in every case. It is noteworthy that the fundamental spectra show two peaks when the 500 $\mu$m uncoated YAG etalon was used. This is consistent with calculation, since the free spectral range of this etalon is smaller than the laser crystal gain bandwidth, so two regions close to laser gain bandwidth can oscillate and the separation between these two oscillating wavelengths is 0.5 nm, which is the slightly broader than the FSR of this 500 $\mu$m uncoated etalon. Note that it was possible to angle this etalon to achieve emission at a single fundamental wavelength. This is shown as the dotted grey trace in Figure 4.11(c).

In Section 4.4.1, it was found that using the 100 $\mu$m uncoated etalon (A3) at $\theta_{gmax}$ provides good power transfer performance so in this stage, it is particularly interesting to examine the spectra when using that etalon using a high resolution instrument. The results show that the fundamental linewidth at FWHM is 0.0068 nm, 35 times narrower compared to the value measured using HR4000 and 57 times narrower than the "free-running" linewidth. The spectra exhibited multiple peaks and over time, it was observed that these peaks competed each other, and the amplitude of each peak varied with time. The FWHM value was determined by the positions of these over 50% intensity peaks, but this measurement was not sufficient to describe the spectra, therefore, the full width at 10% intensity was also given. The general spectral characteristics were used to investigate the effects and trends rather than the FWHM values alone, and distinguish the spectra differences measured by instruments with different resolution. When the etalon was inserted into the fundamental cavity (see Figure 4.10 b and Figure 4.11 b). We can see that the spectra measured using HR4000 is limited by the instrument and does not reflect the actual spectral bandwidth. Using the Bristol Wavemeter has revealed that the fundamental linewidth did narrow. To obtain more accurate measurement, several spectral traces were recorded and Figure 4.12. shows five typical spectra recorded in a minute time period. It can be seen from Figure 4.12 that the central wavelength is hopping around and each peak intensity is varying with time, most likely due to mode competition in say a 0.1 nm spectral slice or a "peak" as recorded, but the overall bandwidth does not change significantly, as represented by the shaded region.

It should be noted, that when operating at high incident pump power ($\geqslant$ 6 W), an additional fundamental emission line @ 1066 nm would develop. This line is an orthogonal emission line in the Nd:$GdVO_4$ laser crystal [112]. This line does not contribute to the polariton / THz generation process, and is therefore undesirable as it is effectively an energy loss path way. It was found that as the pump power increased, the intensity of the desirable 1063 nm line decreased, and that of the 1066 nm line, increased. It could be found that the 1066 nm line could be suppressed by slightly adjusting the end-mirror and etalon alignment, this having the effect of tweaking the oscillating modes. Once this adjustment was made, the system would operate on the single, desired 1063 nm wavelength.

The spectral characteristics of the system when using different etalons, and under high incident pump power are summarised in Table 4.4. What is notable is that the fundamental field linewidth broadness when "free-running", while in the case where etalons are used, this is not observed. Also, the etalons effectively restrict the linewidth of the fundamental field. Also, note that in the case of the coated etalons, the 1066 nm line is never observed. This is due to the additional intracavity loss the etalon introduces, making it impossible for this line to reach threshold.

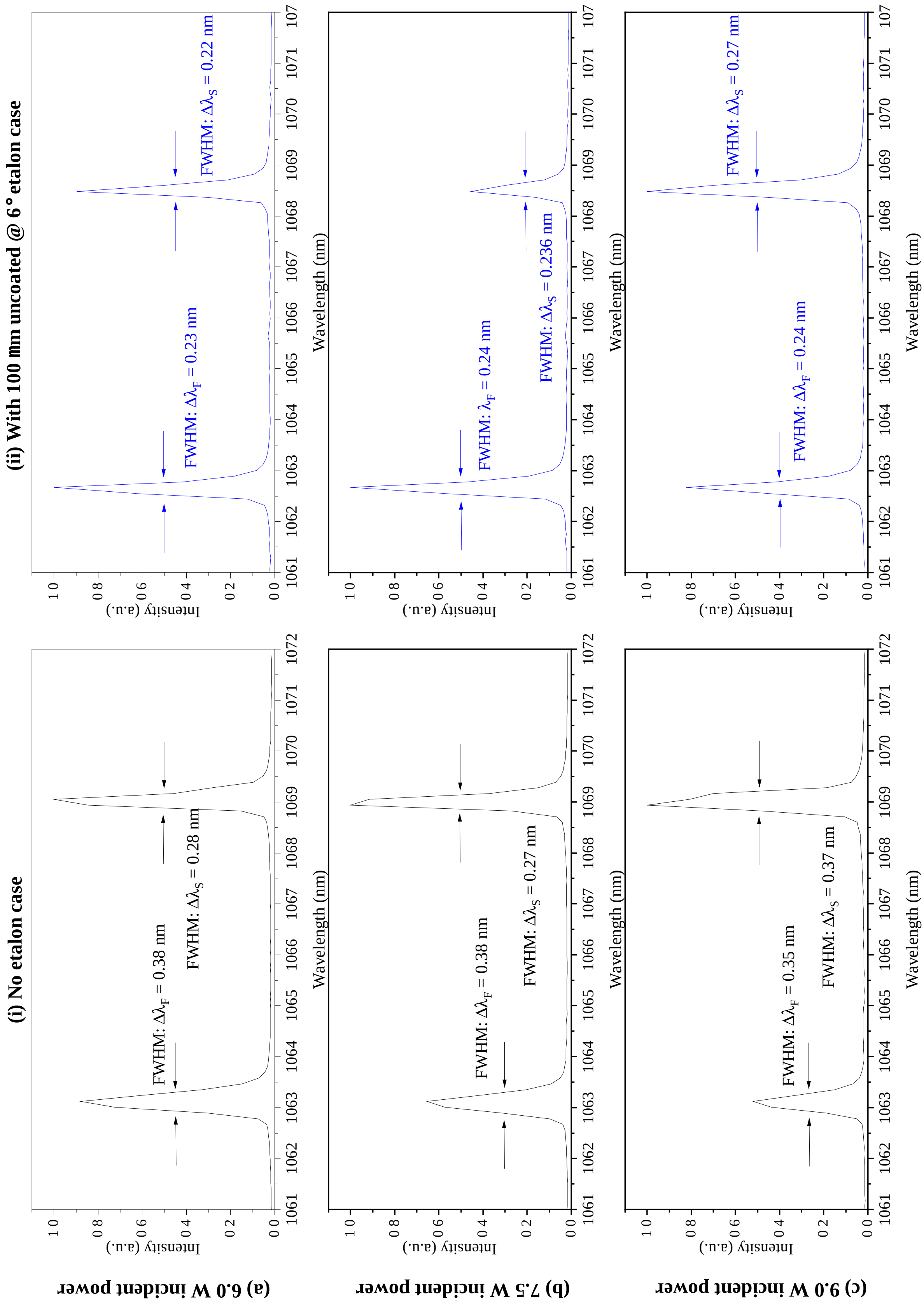


Figure 4.10: Spectra of fundamental and Stokes at different incident pump of (a) 6.0 W, (b) 7.5 W, (c) 9.0 W.

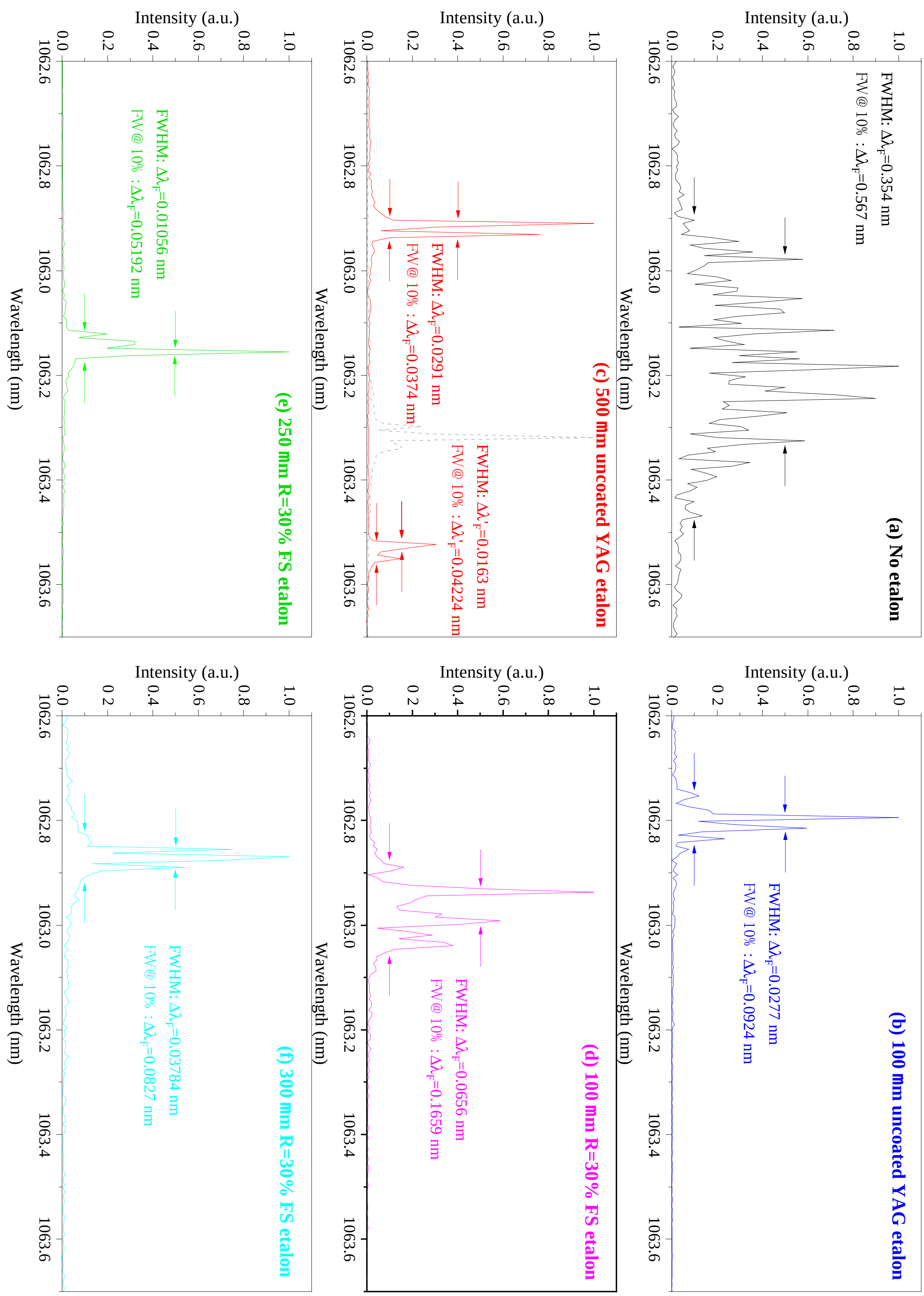


Figure 4.11: Fundamental spectra at 7.5 W incident power (a) without etalon, with etalon of (b) 100 $\mu$m uncoated, (c) 500 $\mu$m uncoated, (d) 100 $\mu$m, R=30%, (e) 250 $\mu$m, R=30% and (f) 300 $\mu$m, R=30%.

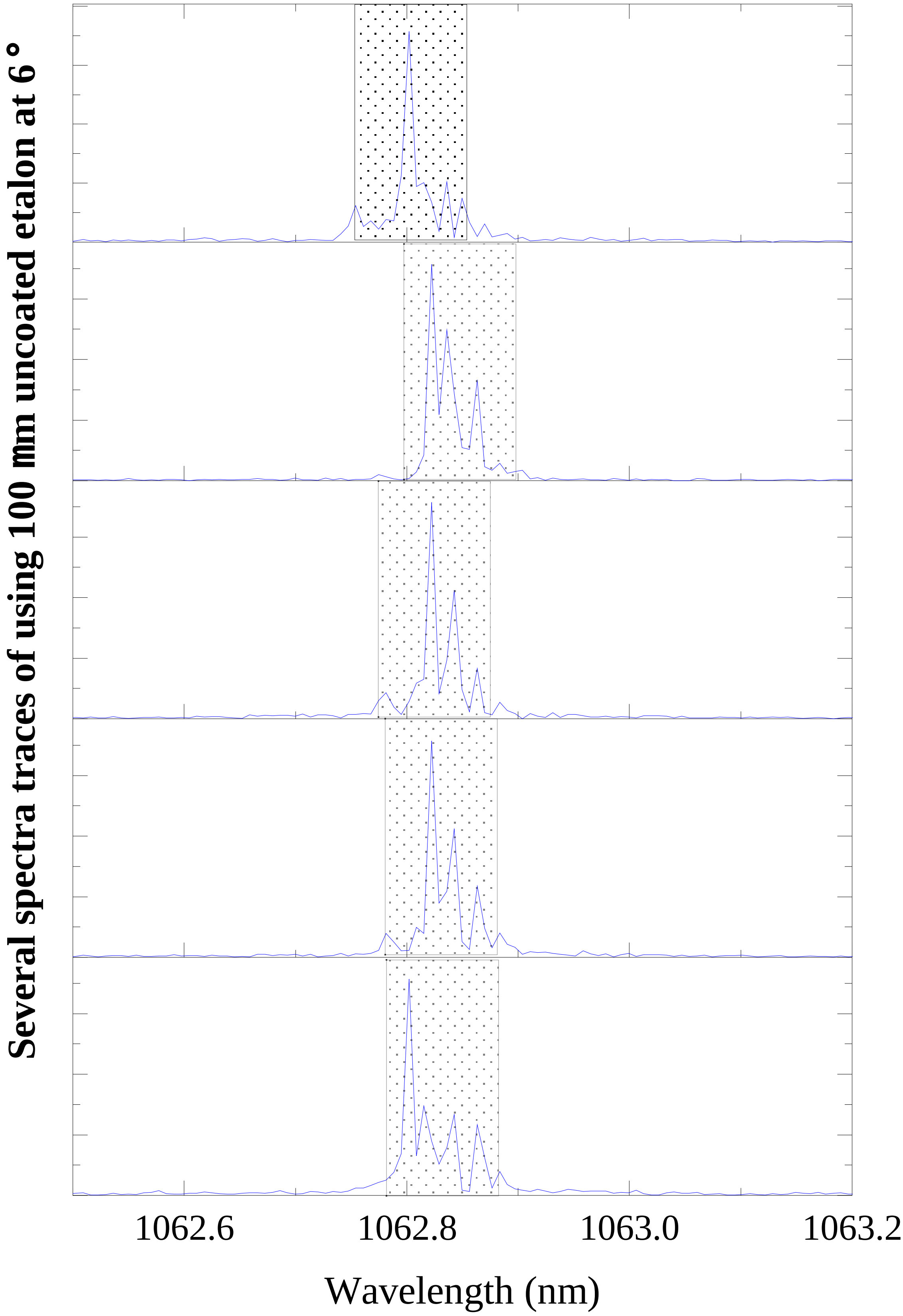


Figure 4.12: Several fundamental spectra traces of obtained using Bristol Wavemeter with the 100 $\mu$m uncoated YAG etalon .

Table 4.4: Summary of linewidth and central wavelength using different etalons.

| | Oscillating wavelength | Linewidth (nm) | Measured at 9.0 W incident power |
|---|---|---|---|
| No etalon | 1063 nm present | Average FW @ 10% intensity | 0.42922 |
| | | Average FWHM | 0.35425 |
| | | Central wavelength | 1063.19013 |
| | 1066 nm present | Average FW @ 10% intensity | 0.23265 |
| | | Average FWHM | 0.21211 |
| | | Central wavelength | 1065.63597 |
| A3. 100 $\mu$m uncoated etalon | 1063 nm present | Average FW @ 10% intensity | 0.07488 |
| | | Average FWHM | 0.0068 |
| | | Central wavelength | 1062.78051 |
| | 1066 nm present | Average FW @ 10% intensity | 0.06161 |
| | | Average FWHM | 0.00684 |
| | | Central wavelength | 1065.79246 |
| A4. 500 $\mu$m uncoated etalon | 1063 nm present | Average FW @ 10% intensity | 0.08851 |
| | | Average FWHM | 0.02724 |
| | | Central wavelength | 1062.93904 |
| B6. 100 $\mu$m R=30% etalon | 1063 nm present | Average FW @ 10% intensity | 0.11577 |
| | | Average FWHM | 0.07491 |
| | | Central wavelength | 1062.97029 |
| B7. 250 $\mu$m R=30% etalon | 1063 nm present | Average FW @ 10% intensity | 0.04768 |
| | | Average FWHM | 0.01362 |
| | | Central wavelength | 1063.17053 |
| B8. 300 $\mu$m R=30% etalon | 1063 nm present | Average FW @ 10% intensity | 0.06808 |
| | | Average FWHM | 0.03404 |
| | | Central wavelength | 1062.89015 |

### 4.4.3 Effects of etalon tilt angle on laser performance

In this section, some laser performances are investigated in detail by using the 100 $\mu$m uncoated etalon because the lowest SPS threshold can be obtained among all the tested etalons. What is more, excellent power transfer and linewidth narrowing by a factor of 10 have been achieved when the 100 $\mu$m YAG uncoated etalon was inserted into the system.

#### i. Effects on SPS threshold

The diode pump power required to reach threshold was measured as a function of the etalon tilt angle, as shown in Figure 4.13.

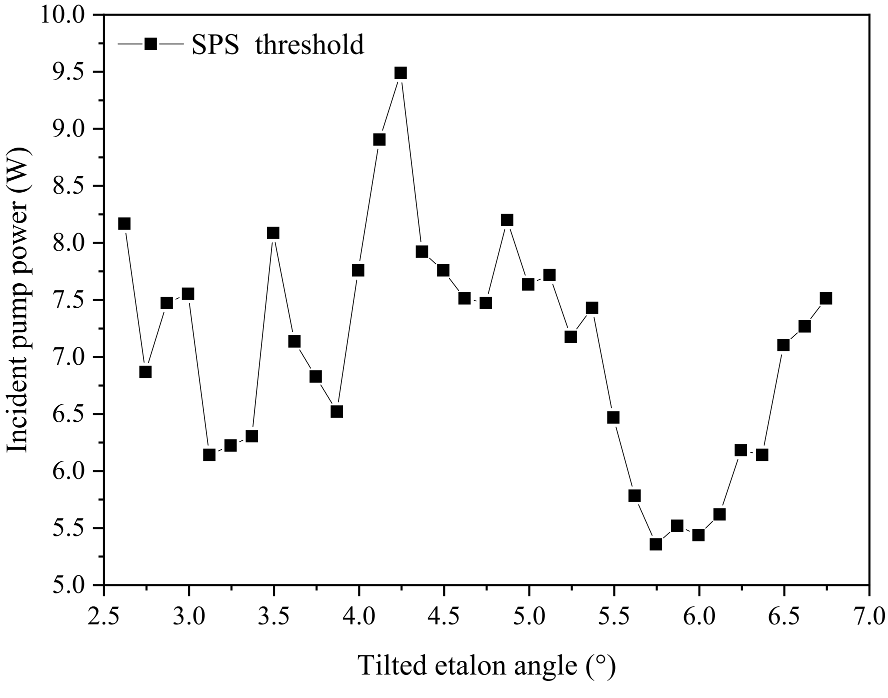


Figure 4.13: Diode pump power required to reach SPS threshold as a function of etalon tilt angle using the 100 $\mu$m uncoated etalon (A3).

It should be noted that the etalon tilt angle listed in the following figures are absolute angle relative to normal incidence (0°). The 0° position was determined by measuring the back-reflected signal from He-Ne laser at a distance of 1 m from the etalon. The data points were collected by adjusting mirror mount screws with a step size of 0.125°, which is a quarter turn of the micrometer mirror mount. The starting point of tilt angle was 6.5°, and the uncertainty of calculation is around ±0.2°.

The SPS threshold is an important factor which is determined by the difference between SPS gain and losses in the Stokes cavity. When the SPS gain is greater than the Stokes cavity loss, SPS threshold can be reached. The SPS gain scales with the intracavity fundamental intensity in the SPS crystal. Therefore, relationships between the SPS threshold and etalon tilt angle were investigated and the results are shown in Figure 4.13. Compared to the "no etalon case", additional losses are caused by the etalon insertion losses. In Section 4.3.2, the insertion losses were analysed. Transmission and walk-off losses are two main insertion losses have strong influences intracavity intensity and fundamental leaking power through $M_2$, as seen in Table 4.2. However, the actual situation is more complicated during the experiment. The etalon transmission and walk-off losses both depend on the tilt angle, and so we can expect that the SPS threshold to vary with etalon tilt angle in a complex way. The plot in Figure 4.13 shows that the SPS threshold varies markedly with etalon tilt angle, in this case, the lowest threshold is achieved at angles between 5.75° and 6°, which is close to the theretical angle (5.6°) at which the etalon has maximum transmission at the wavelength gain max. As the tilt angle changes from this value, the SPS threshold increases. This is being a consequence of the transmission of the etalon changing from that at gain max, and the intracavity losses also evolving.

**ii. Effects on fundamental and THz powers for different pump power**

To further investigate the effect of etalon tilt, the powers of the undepleted- (SPS off), depleted- (SPS on) fundamental fields, and the THz field, are investigated as a function of etalon tilt angle, for three fixed incident pump powers: 7.5 W, 6.0 W and 5.3 W. These plots offer insight into the dynamics ans response of the system to angling of the etalon.

We can see that the THz power can be detected over a broader range of etalon tilt angles for higher incident pump (eg. 7.5 W). The more depletion give rises to the more THz power with tilt etalon angle. The THz power fluctuated from 5.5 $\mu$W to 1.2 $\mu$W with the tilt angle changing between 2.5° and 4.0°. No THz signal was detected at the etalon tilt angle of 4-4.5°. Based on the modelling result shown in Figure 4.5, the transmission starts to increase with the increased tilt angle and reaches the maximum transmission at the tilt etalon of 5.6°.

The experimental result at the same condition shows increased THz power which is consistent with the modelling result. It is also can be seen that the fundamental power and THz power is inversely proportional to SPS threshold, so the trend is similar to the results observed in Figure 4.13.

At lower incident pump powers of 6.0 W and 5.3 W, shown in Figure 4.14 (b) and (c) respectively, it is obvious that both fundamental and THz power decreases. Over the range of etalon tilt angles of 2.5-7.0°, the range of angles over which THz enission/SPS threshold is observed progressively decreases, this becoming more confide to the region near 5.6°, corresponding to the angle at gain max.

The results indicate that THz generation and SPS threshold is very sensitive to etalon tilt angle and the insertion losses. If narrow linewidth output is required by using an optical etalon in the laser cavity, it is clearly necessary to minimise insertion losses. This study highlights that using the etalon at the angle corresponding to gain max, will maximise system performance. It also highlights the difficulty in using coated etalons when tilted, as the induced walk-off losses are so high that they prevent the system from reaching SPS threshold.

**iii. Effects on fundamental and Stokes wavelength for different pump power**

By inserting an etalon into the laser cavity, spectral tuning can be achieved by changing its tilt angle thus effectively shifting the band-pass of the etalon. Therefore, the spectral tunability with 100 $\mu$m uncoated etalon was measured at different incident pump power, shown in Figure 4.14 (right).

The data points were collected with the step size of 0.25°. The wavelength varies from 1063.6 nm to 1062.8 nm in the fundamental field and 1069.8 nm to 1069.6 nm in the Stokes field, with variation of ±0.1 nm. Note the "steps" between wavelengths are due to the pixel spacing of the HR4000 CCD. Thus, there are some gaps when the wavelength shifts, due to the spectrometer resolution.

It is can be confirmed that the Stokes wavelength changes simultaneously with fundamental wavelength and the shifts of different data points are similar, which is corresponding to SPS shifts of 69 $cm^{-1}$. This difference in fundamental and Stokes wavelength is fixed by the phase matching angle of the SPS process (angle between the fundamental and Stokes cavities). The change in fundamental and Stokes wavelength with etalon tilt angle match well with the characteristics observed in Figure 4.14 (right) in that angling of the etalon shifts the transmission peak from gain max, and promotes oscillation of different fundamental wavelengths.

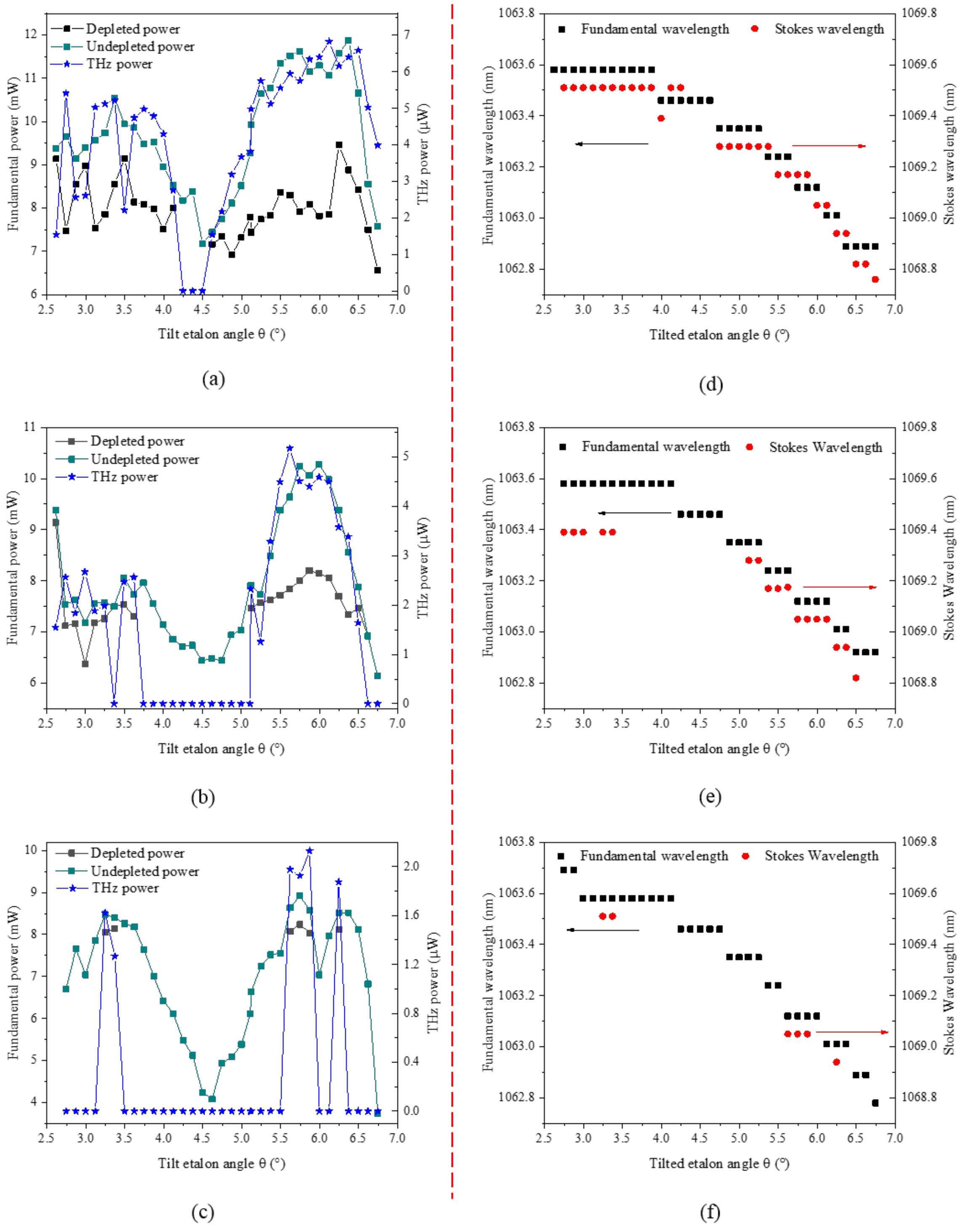


Figure 4.14: Fundamental and Stokes wavelength with etalon tilt angle at the incident pump powers of (a) 7.5 W, (b) 6.0 W, and (c) 5.3 W, and fundamental and Stokes wavelength with etalon tilt angle at the incident pump powers of (d) 7.5 W, (e) 6.0 W, and (f) 5.3 W.

## 4.5 Discussion

We investigated an approach to generate narrow band THz output without sacrificing output power in a CW THz laser, by placing a single etalon into the fundamental field cavity. The etalons used in this chapter were tilted at their $\theta_{ext}$ @ $g_{max}$, which act as the "traditional" use of intracavity bandpass filter. Two important findings are found and these contribute to the development of CW THz.

### 4.5.1 Linewidth narrowing

The use of the etalon has enabled us to narrow the linewidth of the fundamental and Stokes fields which should also lead to narrow THz output. The use of a 100 $\mu$m thick, uncoated etalon (A3) successfully achieved linewidth narrowing, leading to the fundamental linewidth of 0.0068 nm, 57 times narrower than that of "free-running" laser. The rest of etalons used in this chapter did narrow the fundamental linewidth to different degrees, but SPS cannot be achieved in the THz system. This is due to the losses, mainly walk-off losses induced by the intracavity etalon were too high to prevent the laser reaching SPS threshold. For the 100 $\mu$m, uncoated etalon, the losses were around 0.1% at the $\theta_{ext}$ @ $g_{max}$, and these losses were tolerated with our system. Therefore, this etalon was used in the "traditional" way in the CW THz laser, as the first way of etalon usage: Etalon acts as an intracavity bandpass filter when the etalon is tilted in the cavity.

### 4.5.2 Enhancement of THz output power

In the "free-running" CW THz laser [53], the THz power increased to maximum power and then started to drop with the increasing incident pump power, however, this phenomenon was not observed in this laser, when the etalon was inserted.

Instead, it was consistently found that the use of etalons in the fundamental field was effective in preventing the decline in THz power. Inserting an etalon in the fundamental laser resonator not only narrows the linewidth, but improves the THz output power. This is a particularly exciting and significant finding, as it paves the way for further power and efficiency scaling of this type of THz laser.

Similar observation was reported in [167] for an intracavity near-IR Raman laser. In that work, using etalons were effective in controlling the fundamental linewidth and increasing the Stokes output power. The reason behind this is due to the spectral broadening of the fundamental, which occurs as a consequence of the nonlinear SRS process and reduces the effective Raman gain. Therefore, control the spectral broadening of fundamental field in the Raman laser can improve the Raman output power.

Although the SPS process is similar to the SRS process, they still have some differences. In this thesis, it was found that no spectral broadening of the fundamental field was observed. The lack of spectral broadening of the fundamental field, when SPS-shifting, may be attributed to the fact that the SPS crystal used in this thesis is lithium niobate. Lithium niobate crystal is one of the Raman crystal to minimise or prevent spectral broadening because the Raman line or SPS line (21.4 cm$^{-1}$ [172]) is broad compared to the laser gain (8.8 cm$^{-1}$ [112]). Therefore, this may not the reason to well explain that the finding has resulted in substantially enhanced THz output power. Insight into this effect is offered in Chapter 6 as it is strongly related to a reduction in phase mismatch, offered by narrowing the fundamental linewidth. This is in contrast to prior studies on Raman lasers [167].

### 4.5.3 Comparison to other similar research work

The use of one or more etalons in pulsed SPS lasers was previously reported in [107] where Stokes linewidths as low as 5 GHz were achieved. However, linewidth narrowing of CW SPS lasers has not previously been reported.

Some similarities and differences are compared. Both studies have used etalons in the intracavity THz laser to achieve the linewidth narrowing and the etalon was used as intracavity bandpass filter, which means the etalon was tilted in the cavity. However, the etalons were used in two laser operation regimes. In paper [107], the laser was pulsed and here, it was CW regime. D. Stothard *et al.* reported that two etalons were used in the fundamental and Stokes cavity, respectively. Two etalons have the thickness of 600 $\mu$m, finesse of 3 in the fundamental field and finesse of 14 in the Stokes field. The linewidth achieved was around 5 GHz. By comparison, in this thesis, only one etalon was used in the fundamental field to achieve linewidth narrowing. The etalon used in the fundamental resonator was 100 $\mu$m thick, uncoated, and the fundamental linewidth was around 2 GHz. What is more, the THz output power has been enhanced with the substantial reduction of fundamental linewidth. This finding was not demonstrated in the 2008 paper [107].

## 4.6 Summary

In this chapter, we have demonstrated a milestone in the development of an intracavity CW THz laser source with narrow linewidth and high power output by using an etalon in the fundamental cavity and acting as an intracavity bandpass filter. An etalon and its effects on an intracavity CW THz laser have been fully studied.

There is no doubt that the fundamental spectrum can be narrowed when the etalon (both coated and uncoated) was inserted with tilt angle at gain maximum compared to free running case. However, only a few select etalons can work in an intracavity CW THz laser, because of the associated insertion losses owing to walk-off, these losses can be very high in the case of coated etlons, and limits their effectiveness as tilted elements in these systems.

The experimental results shows that the fundamental power significantly dropped when the coated etalon was used. In the case of the uncoated etalon, the walk-off losses are lower compared to coated one, and it was found that a number of uncoated etalons can reach SPS threshold despite the etalon tilt angle being large. Among all uncoated etalons used, laser threshold can be reached only using the thickness of 100 $\mu$m and 500 $\mu$m YAG etalon. The use of 500 $\mu$m uncoated etalon was not pursued because of its non-ideal spectral properties.

A significant finding is that by using an appropriate etalon, the THz output power can be improved, and the spectra of fundamental and Stokes field can be narrowed around by 15 times. SPS threshold, fundamental and THz power, wavelength shifts with tilt etalon angle have been investigated in detail.

The in depth investigation of the use of the 100 $\mu$m uncoated etalon (A3) revealed that angling of the etalon has a dramatic effect in the laser performance. It suggests the fact that angling of the etalon to maintain oscillation at gain max is essential to maintain high

THz emission. It highlights that there are significant caveats to using angled etalons within these laser resonators. In the next chapter an investigation of the e of etalon in an alternative configuration is offered.

# 5

# Linewidth narrowing using etalons at normal incidence

## 5.1 Introduction

Etalons acting as a band-pass filter in the CW THz laser have been demonstrated in Chapter 4. In this chapter, the investigation focuses on etalons working in another way, when the etalon is inserted into the laser resonator at normal incidence. In this case, the etalon interacts with the laser resonator to form a coupled cavity.

This chapter starts with an experimental investigation of the influence an etalon inserted at normal incidence deliberately, has on the power-scaling, and spectral properties of the CW SPS laser. This is followed by a theoretical investigation of the characteristics of the coupled cavities which are formed. Both experimental and theory results are discussed and the opportunities for using etalons at normal incidence are presented.

## 5.2 Experimental arrangement

The experimental setup was slightly different to the experimental setup described in Chapter 4. In this chapter, the etalon was inserted into the fundamental cavity at normal incidence, shown in Figure 5.1, just before the end mirror $M_2$. This position was chosen to be consistent with the work presented in Chapter 4. Both coated and uncoated etalons are investigated in this work.

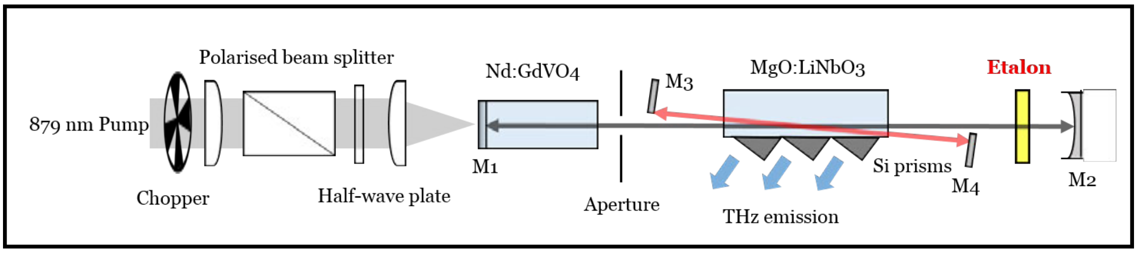


Figure 5.1: Experimental setup with an etalon inserted at normal incidence.

## 5.3 Experimental results

The etalons used in this body of work are described in detail in Chapter 2 Table 2.4. Specifically etalons A3, A4, B5, B6, B7, B8 were studied. These were consistent with those investigated in chapter 4.

### 5.3.1 Power scaling using different etalons at normal incidence (0°)

To avoid damaging the laser and SPS crystal, the highest incident pump power was limited to 9 W, so all the results were obtained under the incident pump power of 9 W. It should also be noted that the THz output power dropped over the course of these experiments due to progressive damage of the laser crystal, mirrors and SPS crystal, so the detected THz output power in this chapter is lower than the previous chapter. However, the purpose of this study is the physical insights of the etalon effect on the CW THz laser, more specifically, the power-scaling trend, spectral performance, and stability of the laser are more important than the overall THz output power. Therefore, the laser system was often characterised in a regime where it produced stable THz output. This refered to as the "well-performed" area.

### i. The "free-running" case

The experimental characterisation of this system was started with the "free-running" THz laser where no etalon is inserted into the laser. The laser performance of the CW THz laser in the "free-running" case is shown in Figure 5.2. The detected THz power was also plotted as a function of the fundamental-field depletion, and is shown in Figure 5.3.

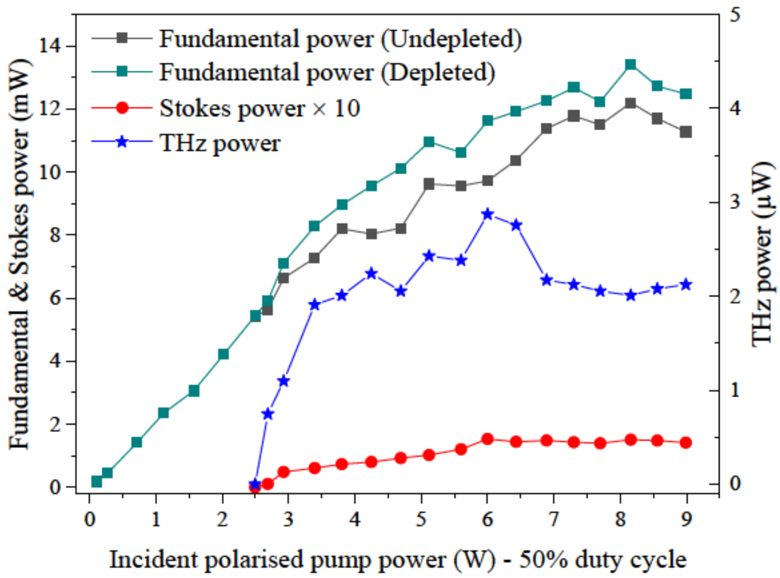


Figure 5.2: Power-transfer curves in the "free-running" case, showing plots for the fundamental, Stokes and THz fields.

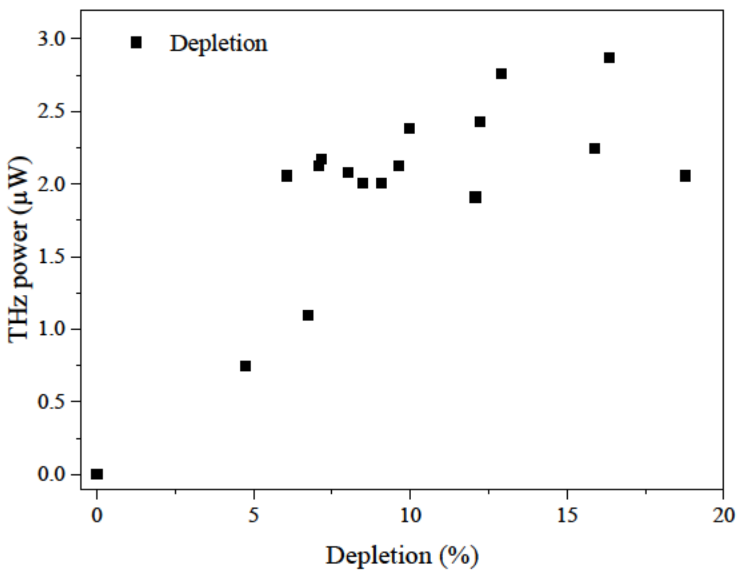


Figure 5.3: Plot of THz power vs fundamental field depletion, in the "free-running" case.

The system was power-scaled under the condition of chopped pumping, producing quasi-CW THz output. The trend of the power transfer in the fundamental, Stokes and THz fields was similar to those observed in Chapter 3. With the increase of the incident pump power, the THz power was increased to the highest incident pump power of 6 W and then dropped at higher incident pump powers. The SPS threshold was 2.5 W, and the maximum THz power was 2.88 $\mu$W. The percentage of depletion in the fundamental field can indicate the SPS conversion efficiency. The THz output power versus the fundamental depletion is plotted in Figure 5.3. The depletion is under 20% throughout the whole pump range (up to 9 W), suggesting a low SPS conversion efficiency.

**ii. Uncoated YAG etalons**

In this section, the study focuses on an investigation of inserting an uncoated YAG etalon into the fundamental cavity at normal incidence, at the position shown in Figure 5.1.

To make sure the etalon was inserted at 0° (normal incidence), a He-Ne laser was used as a guide laser to align the etalon in the fundamental field. In the fundamental field, the fundamental wavelength of 1063 nm presents all the time with any inserted etalon listed in Table 2.4, different from the result presented in Chapter 4. It should be noted that in this work, SPS threshold could be readily achieved when using etalons at normal incidence. This is in contrast to the work in Chapter 4, where angling the etalons had a significant influence on the ability to reach SPS threshold.

Two uncoated etalons 100 $\mu$m (A3) and 500 $\mu$m (A4) made from YAG were studied. As shown in Figure 5.4 a and Figure 5.4 b, the power scaling of the CW THz laser by using these different thickness etalons was measured in fundamental, Stokes and THz fields as a function of incident pump power.

The fundamental laser (1063 nm) using 100 $\mu$m and 500 $\mu$m YAG etalons had similar threshold pump power of 0.18 W, slightly higher compared to the required pump power of 0.1 W in a "free-running" laser. The SPS threshold was around 2.9 W when 100 $\mu$m uncoated etalon (A3) was inserted into the laser resonator. Using the uncoated 500 $\mu$m YAG etalon (A4), the SPS threshold to the incident pump power was around 2.5 W, which was similar to the "free-running" case. The insertion losses of the uncoated etalons were not high, which is indicated by the THz laser threshold (SPS threshold of with and without etalon).

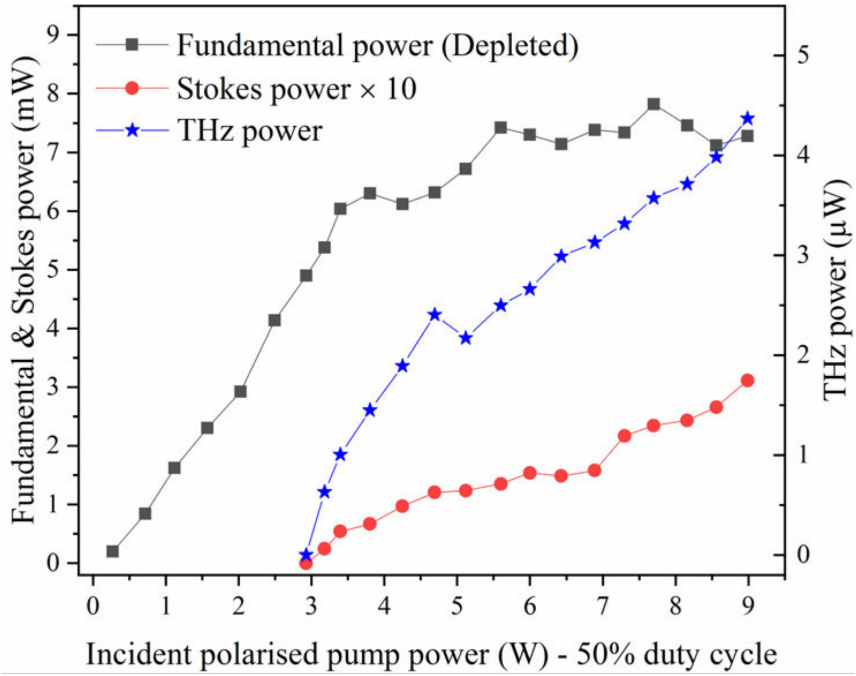


(a)

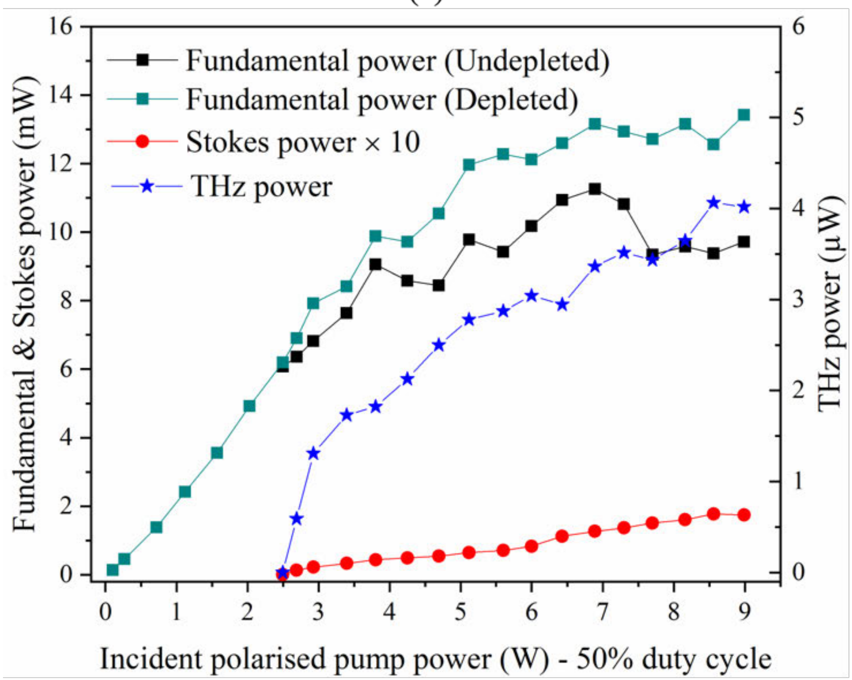


(b)

Figure 5.4: Output powers for fundamental, Stokes and THz fields in an intracavity CW THz laser with the uncoated etalons of (a) 100 $\mu$m thickness (A3); (b) 500 $\mu$m thickness (A4) at normal incidence.

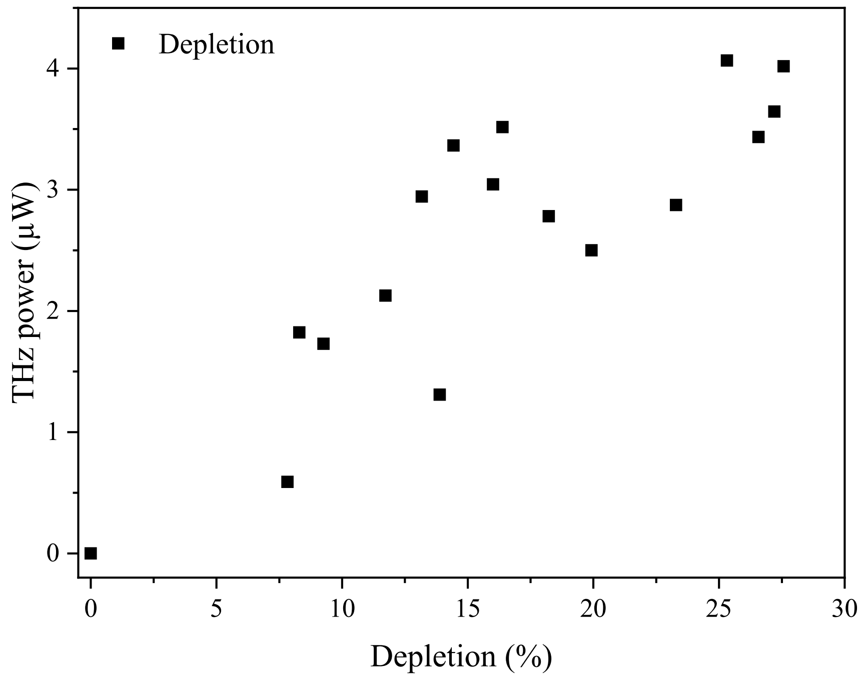


Figure 5.5: 500 $\mu$m uncoated etalon at normal incidence: THz output power as a function of fundamental depletion.

In the "free-running" laser, it is noticed that the THz output power dramatically increased to the maximum power of 2.88 $\mu$W at 6.0 W pump power and then dropped to 2.1 $\mu$W within the increase of 3.0 W pump power. Using the 100 $\mu$m YAG uncoated etalon (A3), the detected THz power was 4.5 $\mu$W at the incident pump power of 9 W, and 4.1 $\mu$W of maximum THz power (at 9 W incident pump power) was obtained using the 500 $\mu$m uncoated YAG etalon (A4). The results show that the maximum THz power continued to increase with the increase of incident pump power when the uncoated YAG etalons (A3 and A4) were inserted into the fundamental cavity in contrast to that of the "free-running" case. This finding is very promising, as it can provide an opportunity to obtain more THz output power. This is similar to the observation found in Chapter 4, where it was found that this improvement may be due to a reduction in phase mismatch due to linewidth narrowing.

To investigate this phenomenon, an uncoated 500 $\mu$m YAG etalon was used to measure the depleted and undepleted (the Stokes was unblocked and blocked) fundamental power together with Stokes and THz power to characterise the down-conversion performance of the intracavity cavity SPS process.

The down-conversion efficiency of the system using the 500 $\mu$m thick etalon is also investigated. Shown in Figure 5.5 is a plot of THz power as a function of fundamental field depletion. In comparison to the "free-running" case (Figure 5.3), greater depeletion is achieved (up to 27% c.f. 17%), and consequently higher THz power is generated. The overall increase in depletion is discussed later in this chapter, within the context of enhanced spectral performance.

Table 5.1: Summary of SPS threshold and maximum THz power, when using YAG etalons at normal incidence

| Etalon type | SPS threshold | Maximum THz power |
|---|---|---|
| No etalon ("free-running" laser) | 2.5 W | 2.88 $\mu$W @ 6.0 W |
| 100 $\mu$m, uncoated YAG etalon (A3) | 2.9 W | 4.5 $\mu$W @ 9.0 W |
| 500 $\mu$m, uncoated YAG etalon (A4) | 2.5 W | 4.1 $\mu$W @ 9.0 W |

### iii. Coated fused silica (FS) etalons

This section presents the performance of a THz laser that generates high output power with different finesse etalons. Most of studies are focused on R=30% reflectivity FS etalons with thicknesses of 50 $\mu$m (B5), 100 $\mu$m (B6), 250 $\mu$m (B7), and 300 $\mu$m (B8) (specific etalons are shown in Table 2.4).

For each of these etalons, the power scaling curves of the fundamental, Stokes and THz power as a function of incident pump power were obtained under the same conditions; ie. same resonator configurations and ambient lab conditions; These plots are shown in Figures 5.6 a, b, c and d, using etalons B5, B6, B7 and B8, respectively, at normal incidence. The maximum THz output powers were 5.14 $\mu$W (5.6 W pump power), 4.68 $\mu$W (9 W pump power), 2.03 $\mu$W (6 W pump power), 4.44 $\mu$W (7.3 W pump power) respectively (Summarised in Table 5.2). Not all the THz powers were at maximum pump power. An obvious exception was observed that the detected THz power was only 2.03 $\mu$W (lower than "free-running" case) by using the 250 $\mu$m, R=30% FS etalon (B7), at 6.0 W incident pump power. Compared to the SPS threshold with and without an etalon in the laser system, the 250 $\mu$m, R=30% FS etalon (B7) has the highest SPS threshold (4.25 W); a summary of system thresholds can be seen in Table 5.2. It was noted that the B7 etalon had a significant number of surface scratches and likely induced a significant insertion loss.

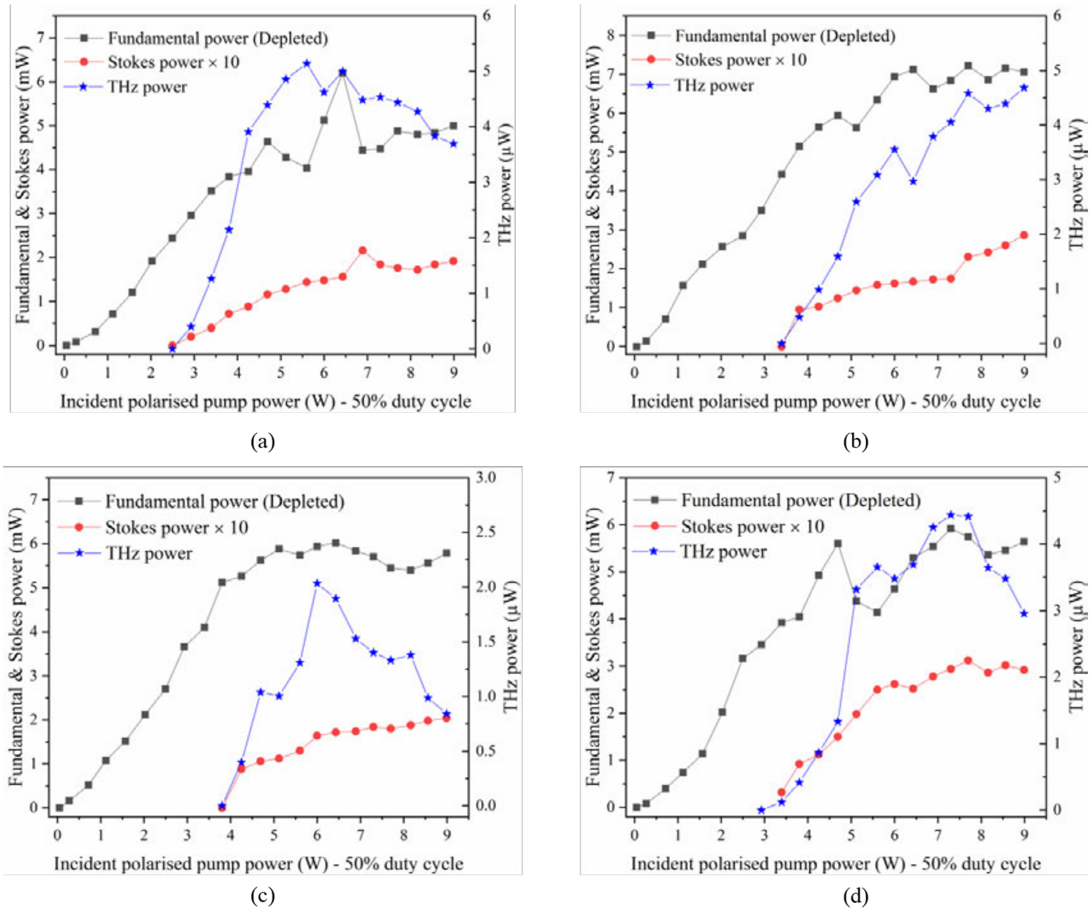


Figure 5.6: Output powers for fundamental, Stokes and THz fields in an intracavity CW THz laser with the etalon of (a) 50 $\mu$m R=30% coated (B5) (b), 100 $\mu$m R=30% coated (B6), (c) 250 $\mu$m R=30% coated (B7), and (d) 300 $\mu$m R=30% coated (B8) at normal incidence.

It is interesting to observe that most of the coated etalons used at the normal incidence give rise to improvement of THz output power. With the exception of the 100 $\mu$m, R=30% etalon (B6), the power scaling trends using the rest of the etalons (B5, B7, B8) are similar to that of the "free-running" laser, where the THz output power exhibits an "up and down" trend. It is noted that a largely linear increase in the THz output power with increased incident pump

Table 5.2: Summary of SPS threshold and maximum THz power, when using coated FS etalons at normal incidence

| Etalon type | SPS threshold | Maximum THz power |
|---|---|---|
| 50 $\mu$m, R=30% FS etalon (B5) | 2.9 W | 5.14 $\mu$W @ 5.6 W |
| 100 $\mu$m, R=30% FS etalon (B6) | 3.4 W | 4.68 $\mu$W @ 9.0 W |
| 250 $\mu$m, R=30% FS etalon (B7) | 4.25 W | 2.03 $\mu$W @ 6.0 W |
| 300 $\mu$m, R=30% FS etalon (B8) | 3.39 W | 4.44 $\mu$W @ 7.3 W |

power was achieved using the 100 $\mu$m, R=30% etalon (B6).

In summary, a steady increase in THz output power over the range of pump powers was achieved using all of the uncoated YAG etalons, and the 100 $\mu$m, R=30% FS etalon inserted at normal incidence in the fundamental laser. It is interesting to note that the performance of the 100 $\mu$m thickness, coated and uncoated etalons are similar, and yet they have the same free spectral range but different finesse. The reasons for this similar performance are discussed in Section 5.3.2 and 5.3.3.

### 5.3.2 Spectral properties using different etalons at normal incidence

This section is focused on the investigation of the fundamental field linewidth, using etalons at normal incidence, and in particular, the possibility to obtain a narrower spectrum. To investigate the relationship between the THz output power and the spectral bandwidth, the fundamental spectrum, when using each etalon was analysed. Considering the promising power scaling result obtained in Section 5.3.1, the spectral output of the lasers were investigated, especially for the use of etalons: A3, A4 and B6.

The fundamental spectra with different etalons were measured using the same spectrometer (Bristol Wavemeter 771A) as used in Chapter 4. Note that the instrument requires pure CW laser input operation and so the lasers were characterised without chopping of the pump. The results can still be used to analyse the spectral changes with and without an etalon in the cavity.

The spectra of the fundamental field for the various etalons are shown in Figure 5.8. Note that the spectra were measured at the same time as the power scaling measurements at a fixed incident pump power of 6.0 W. At this pump power, the lasers were well above the SPS threshold, and produced stable output. The fundamental spectra have each been normalised.

It can be seen that the fundamental spectrum changes significantly as the different etalons are used, ranging from multiple peaks to only one peak, which corresponding to a changing bandwidth of 1.25 nm to 0.025 nm (the latter is the instrument limit). The spectrum of the "free-running" case was also taken for comparison, and this is shown in Figure 4.11. The full width at half maximum (FWHM) of the fundamental spectra with the different etalons were measured, and are shown in Figure 5.7 b. The irregular shape of the spectral peaks makes it difficult to define a measure of the widths that is appropriate for all cases. The FWHM can give deceptively small values for the width of the fundamental spectrum of the THz laser with and without etalons in the cavity, because those spectra contain significant structure below the half maximum level.

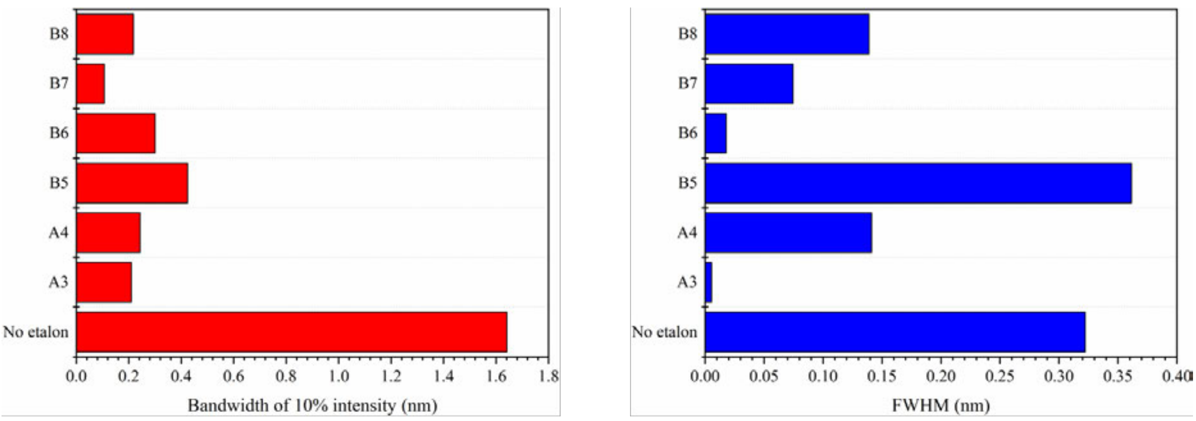


(a) (b)

Figure 5.7: The fundamental spectra for the CW THz laser (a) Bandwidth of 10% intensity (b) FWHM.

The possibility of using the widths at the 10% of the peak value of the normalised spectra was also considered, and this metric is shown in Figure 5.7 a. Low signal to noise ratio of the spectra in these different cases was considered when using this parameter as a measure of the peak width. The most important point of this work was to identify general trends in the spectral behaviour, rather than determining an accurate, absolute measurement of the spectral width, and therefore, instead of measuring the FWHM, the bandwidth at 10% of intensity was selected in case that it can give misleading values for individual spectra which have a particularly complex structure. in the ideal case, both the FWHM and 10% widths would both be small.

No matter which etalon was selected for use, the fundamental linewidth was narrower than that of in the "free-running" THz laser, demonstrating that using an etalon at normal incidence can be effective at narrowing the fundamental field linewidth. This is in contrast to using a tilted etalon as examined in Chapter 4. The peculiarities and theory behind the effectiveness of this unconventional use of etalons are examined in the following section. In particular, the 250 $\mu$m thick, R=60% etalon provides very narrow linewidth, and the properties of the laser making use of this etalon will be studied in-depth in Chapter 6.

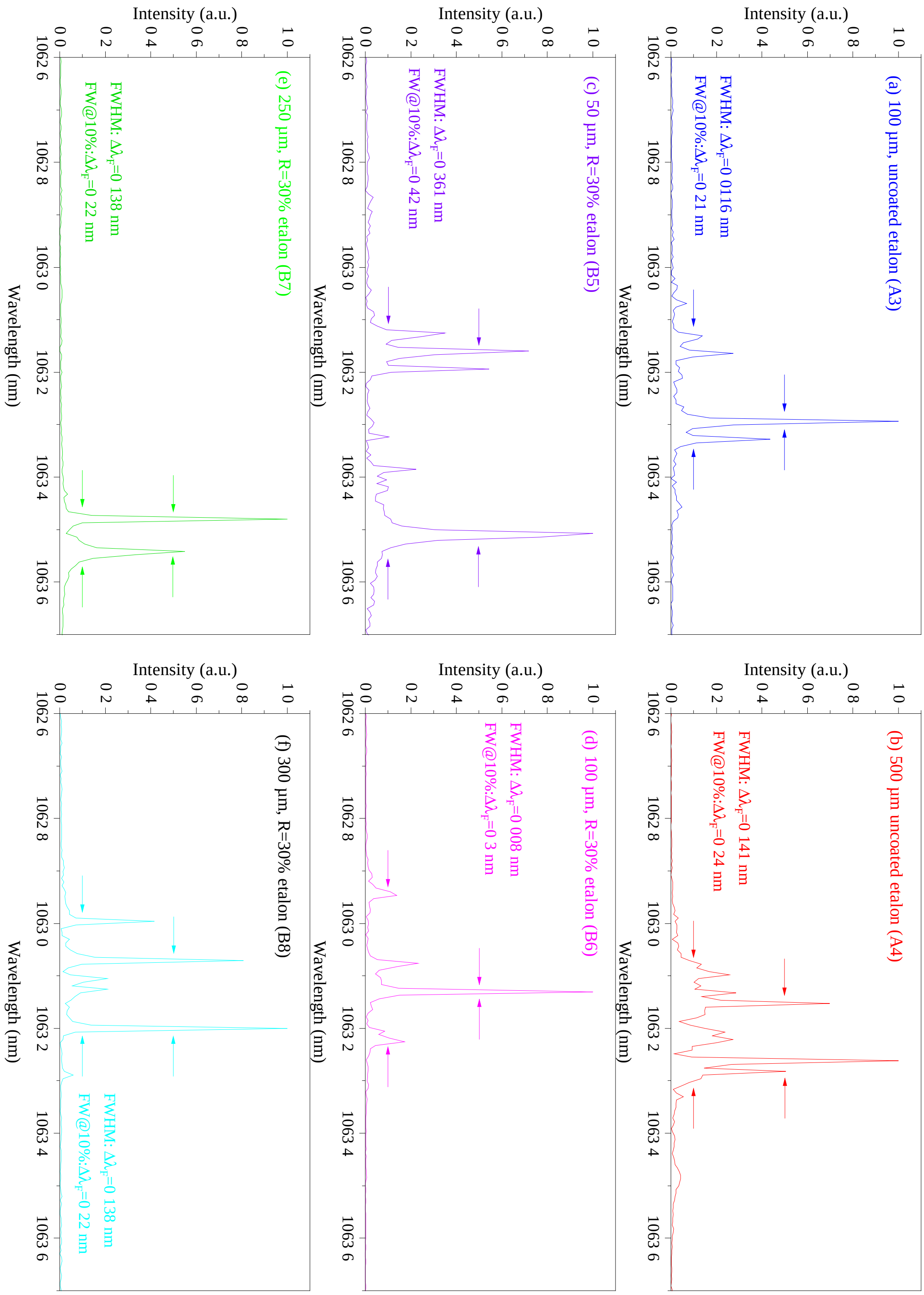


Figure 5.8: Fundamental spectra at 6.0 W incident power with etalon at normal incidence for (a) 100 $\mu$m uncoated (A3), (b) 500 $\mu$m uncoated (A4), (c) 50 $\mu$m, R=30% (B5), (d) 100 $\mu$m, R=30% (B6), (e) 250 $\mu$m, R=30% (B7) and (f) 300 $\mu$m, R=30% (B8).

### 5.3.3 Effects of etalon at normal incidence on laser performance

The power scaling and spectral properties measured using each etalon were discussed in Section 5.3.1 and 5.3.2. The results show that beneficial effects using an etalon in the THz laser was achieved, especially using the 100 $\mu$m thick uncoated and coated etalons. The linewidth of the fundamental was narrowed, and more THz power was generated at the higher incident pump power. In this part, the effect on the Stokes spectral properties, SPS threshold, fundamental, THz power and wavelength shifts, due to tilt etalon angle (angling away from normal incidence) are investigated in some detail.

#### i. Stokes spectral properties

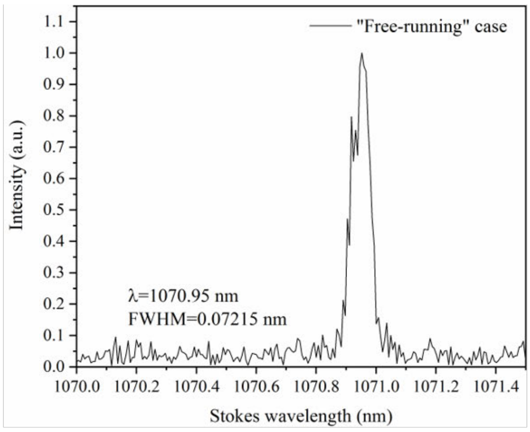


(a)

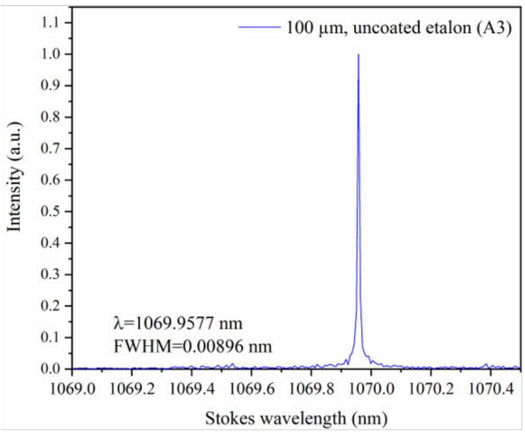


(b)

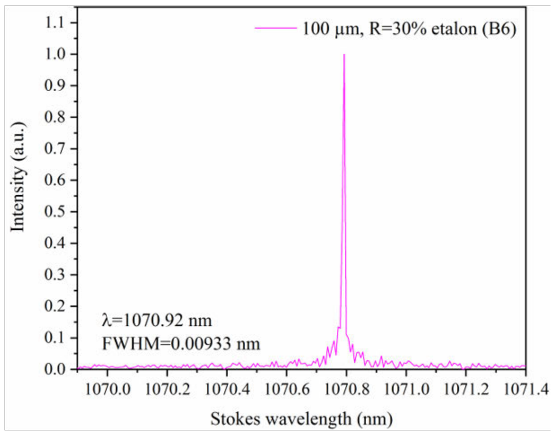


(c)

Figure 5.9: Stokes field spectra measured by laser spectrum analyser with 6.0 W incident pump ower in the case of (a) "free-running" case (no etalon) (b) 100 $\mu$m, uncoated etalon (A3) and (c) 100 $\mu$m, R=30% etalon (B6).

The Stokes spectra have been fully characterised using the Bristol Wavemeter (771A), and the representative spectra for the three different cases: (a) "free-running" case, (b) with 100 $\mu$m uncoated etalon (A3) and (c) with 100 $\mu$m, R=30% etalon (B6) are shown in Figure 5.9, respectively. All of these spectra were measured at the same incident pump power (6.0 W) as used to measure the fundamental spectra shown in Figure 5.8.

The 1063 nm fundamental had a "free-running" linewidth of 0.423 nm FWHM prior to inserting etalons, and substantial narrowing was observed when any of the two etalons were inserted. A narrowing up to was achieved a factor of 53 was achieved, and the linewidths at FWHM were 0.0116 nm and 0.008 nm for the uncoated (A3) and R=30% (B6) etalons respectively (refer to Figure 5.7). As a consequence of the narrowing of the fundamental, the Stokes spectra also showed substantial narrowing by a factor of 8, from around 0.072 nm when no etalon was present, to 0.009 nm when either etalon was used. Although we have not measured the linewidth of the THz field directly, we can predict that it would be narrowed as well, by a similar order as the Stokes and fundamental fields, following conservation of energy.

**ii. Effects on SPS threshold**

Since the insertion of an etalon only in the fundamental field can significantly narrow the linewidth of fundamental and Stokes spectra, the dependence of SPS threshold on etalon tilt angle was investigated using the etalons mentioned above in the CW THz laser. Angling of the etalon in this case is also important as it effectively diminishes the strength of coupled cavity effects within the resonator, and presumably brings the system more in-line with that examined in Chapter 4.

The SPS threshold with etalon tilt angle in the case of 100 $\mu$m uncoated YAG etalon (A3) is shown in Figure 5.10 a, and SPS threshold in the same situation with 100 $\mu$m, R=30% coated FS etalon (B6) is shown in Figure 5.10 b. It can be seen that the SPS process can only occur in a small range of angles ( 0.08°), and the lowest SPS threshold was 5.2 W at a normal incident angle and then rapidly increases with increased angle until SPS process would not take place when the 100 $\mu$m, R=30% YAG etalon was inserted. In contrast, in the case of 100 $\mu$m uncoated YAG etalon was inserted, the laser performance can be maintained across a broad range of tilt angles. The SPS threshold keeps lower values over an angle range of

0.6°-1.85°, and gradually increases on the positive side limited clipping of the mirror mount; and rapidly raising on the other side. Overall, the SPS process can be generated stably across a greater tilt range. Note that the 100 $\mu$m thick uncoated YAG etalon used here has different FSR and broader transmission peaks than the coated one (owing to the different substrate types).

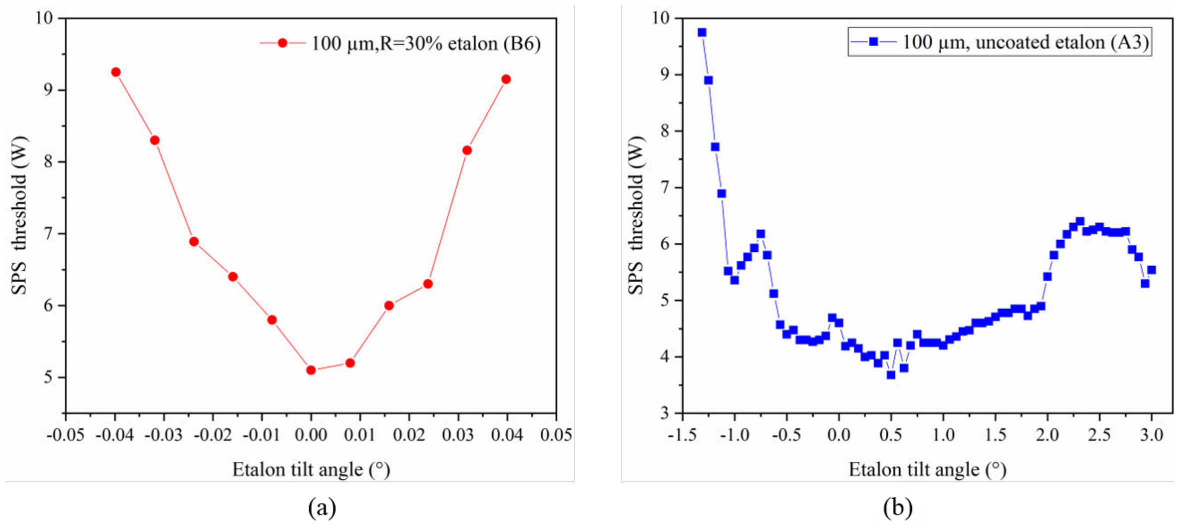


Figure 5.10: Diode pump power required to reach SPS threshold, as a function of etalon tilt angle for (a) 100 $\mu$m, uncoated YAG etalon (A3); and (b) 100 $\mu$m, R=30% FS etalon (B6).

### iii. Effects on fundamental and THz powers

The fundamental and THz powers were recorded as a function of etalon tilt angle. Traces are shown in Figure 5.11 a and 5.11 b in the cases of etalons A3 and B6 respectively. In case of etalon B6, the SPS process can be generated only in a very small range of angles close to 0°. This characteristic is likely due to the high finesse of the etalon, and the high insertion loss that results from angling (as per the study in Chapter 4 given that for etalon B6, $\theta_{gmax}$ = 6.32°). It may also be due to a change in the spectral behaviour of the coupled cavity.

From side by side comparison, in the cases of A3 high fundamental power is maintained across a wide band of tilt angles. Consequently, THz output is also maintained. In the case of B6, high fundamental power is only achieved across a very narrow range of angles.

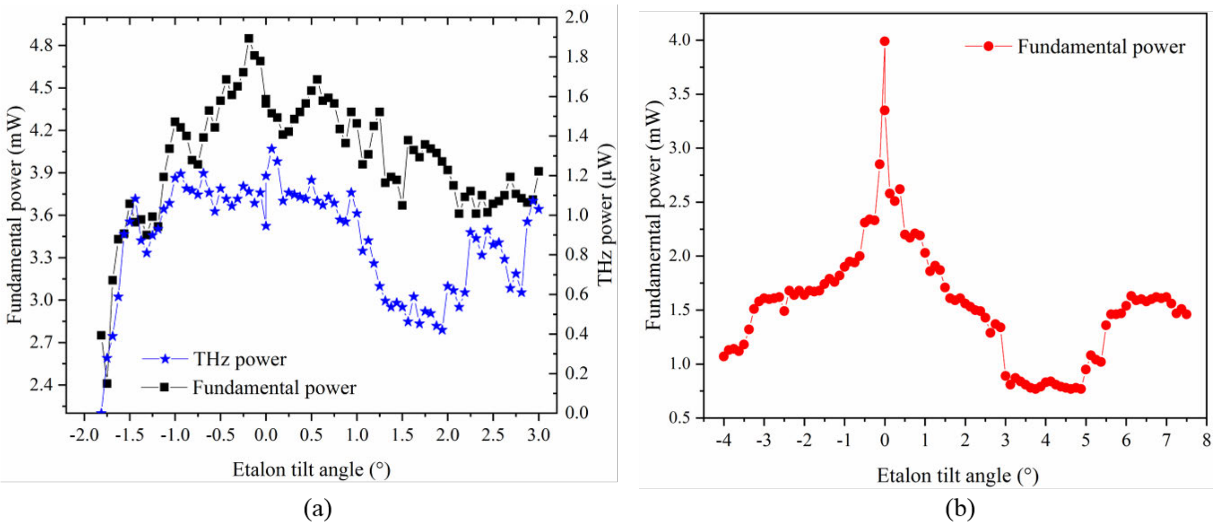


Figure 5.11: Properties of output power with tilt etalon angle, for the system (a) with SPS process, 100 $\mu$m, uncoated YAG etalon (A3) and (b) without SPS process, 100 $\mu$m, R=30% FS etalon (B6).

### iv. Effects on fundamental and Stokes wavelength

As explored in Chapter 4, by tilting the etalon, the fundamental wavelength can be tuned. The fundamental wavelength changes with angling of etalons A3 and B6 was recorded, and are shown in Figure 5.12 a and 5.12 b. The fundamental wavelength can be tuned from 1063.45 nm to 1063.9 nm with the uncoated etalon, but less tunability is achieved for the R=30% etalon because the losses is too high to reach SPS threshold , a trend supported by Figure 5.10 b. If the SPS process is ignored, the fundamental wavelength can cover the range of total lasing emission gain of Nd:$GdVO_4$, which is from 1062 nm to 1066 nm. It is interesting to note that the THz power dropped rapidly from 1° to 2° and then continue to increase with the uncoated 100 $\mu$m etalon. The THz power with etalon tilt angle exhibits similar performance from the tilted angle of 2-3°, to that observed in Section 4.4.3. This may indicate that from this point, the etalon acts as bandpass filter instead of forming coupled cavity due to the etalon tilt angle.

It is interesting to note that the tuning of the fundamental wavelength achieved through tilting of the etalon, may offer a method of also fine-tuning the generated THz frequency. This is by virtue of the fixed fundamental-Stokes resonator angle ($\theta$, refer to Figure 2.2), and the consequent change to the phase matching curve.

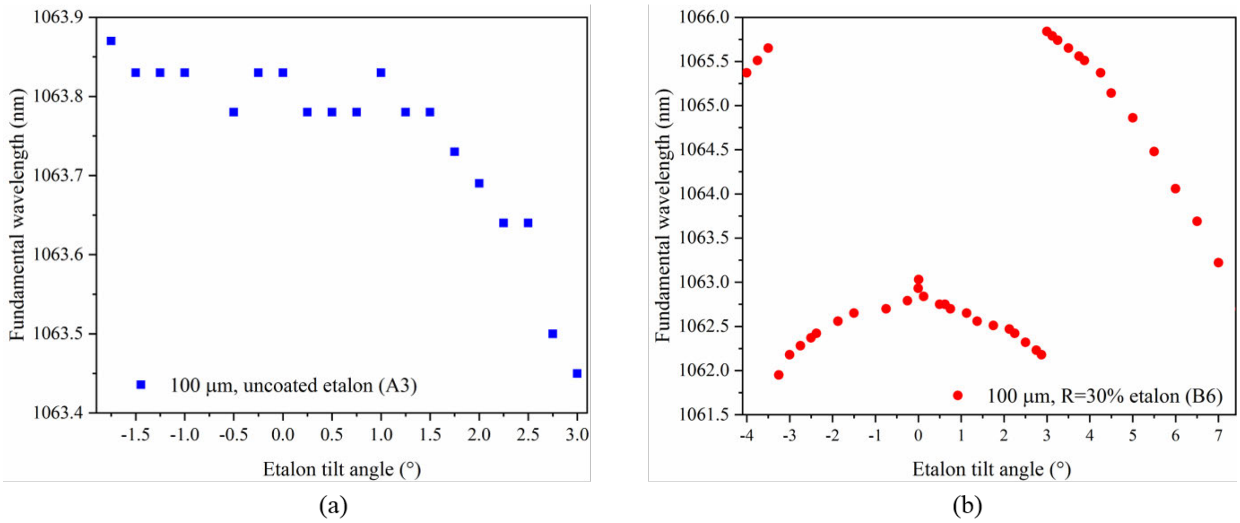


Figure 5.12: Change in fundamental wavelength with etalon tilt angle, for the system (a) with SPS process, 100 $\mu$m, uncoated YAG etalon (A3) and (b) without SPS process, 100 $\mu$m, R=30% FS etalon (B6).

## 5.4 Coupled cavity effects

The basis for linewidth narrowing in this chapter is that etalons at normal incidence interact with the laser resonator mirrors to effectively form a "coupled cavity" with unique pass-band properties. This is distinctly different to using angled etalons. In this section, the theory of coupled cavities is given along with modelling specific to the configurations investigated experimentally.

### 5.4.1 How to form coupled cavities

If the gain profile of a laser is wider than the axial-mode spacing of the laser cavity, the laser can oscillate simultaneously over a broad spectrum of multiple axial modes. It is common practice, provided the laser gain is not too small, to insert a short, tilted intracavity such etalons, inside the laser cavity as shown in Figure 5.1, so that the narrow-band frequency transmission of these etalons near resonance can provide frequency tuning and axial mode selection in the laser. The transmission properties of such simple passive etalons have been analysed in Chapter 4, where it was found that the tilt of the intracavity etalon must be kept small enough that it does not seriously reduce the transmission of the etalon through transverse walk-off, yet is large enough that the reflected waves from each side of the etalon pass out of the cavity and do not set up additional resonances with the other mirrors of the laser cavity [171].

Sometimes additional mirrors added to laser cavities may be deliberately aligned in resonance with the existing cavity mirrors to obtain multimirror laser cavities [173]. The resonance frequency properties of such cavities then become coupled, and the net resonator characteristics is more complicated. In this chapter, to induce coupled effects into our laser system, the etalon was inserted in the fundamental cavity at normal incidence.

### 5.4.2 Theory of coupled cavities

The simplest form of the multimirror cavity is the three-mirror cavity shown in Figure 5.13. The properties of such a resonant cavity with three or more mirrors are in general complex, and it may be useful to introduce briefly some of these complexities using a simple analytical model.

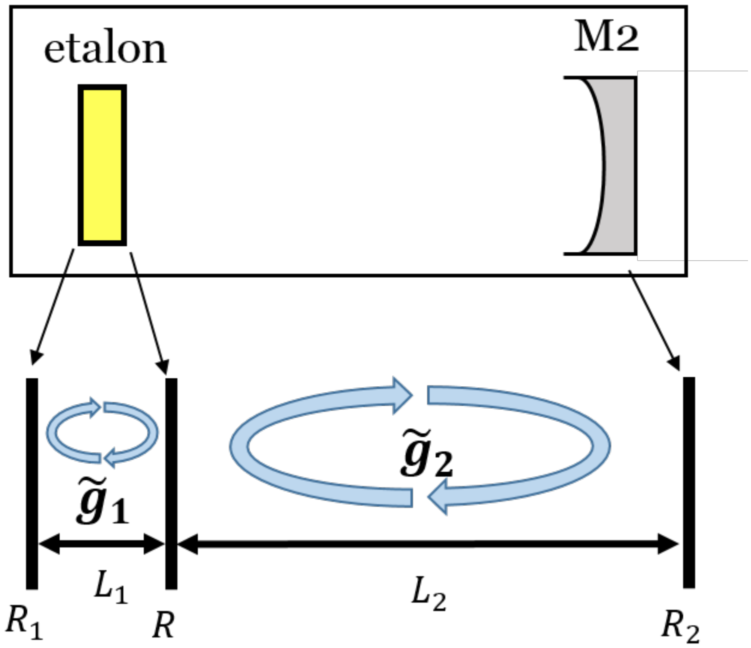


Figure 5.13: Analytical model for the general three-mirror laser cavity [174].

The theoretical study of coupled cavity effects presented here has followed the method presented in [174]. Suppose first a general three-mirror cavity was considered as shown in Figure 5.13. Such a cavity if two of the mirrors are closely enough spaced, can also be viewed as a two-mirror resonator with an etalon mirror on one end or the other. As shown in Figure 5.13, assuming this resonator has mirror reflectivities $R_1$, $R_2$, and R, and use $\tilde{g_1}$ and $\tilde{g_2}$ to describe the round-trip gains inside the two cavity segments, leaving out the mirror reflectivities, so that

$$\tilde{g_1} \equiv exp\,(-\alpha_1 p_1 - j\omega p_1/c) \equiv exp\,(l_1 - \frac{4\pi L_1}{\lambda} j) \tag{5.1}$$
$$\tilde{g_2} \equiv exp\,(-\alpha_2 p_2 - j\omega p_2/c) \equiv exp\,(l_2 - \frac{4\pi L_2}{\lambda} j) \tag{5.2}$$

with $\alpha_1 p_1$ and $\alpha_2 p_2$ representing the round-trip laser losses, if any, inside each segment of the laser cavity. $\lambda$ is the wavelength and c is the speed of light.

$l_1$ and $l_2$ are the round trip loss items for the two segments, which can be expressed as:

$$l_1 = -\alpha_1 2L_1 \tag{5.3}$$
$$l_2 = -\alpha_2 2L_2 \tag{5.4}$$

The loss item is determined by the absorption coefficient ($\alpha$) and cavity length (L). One simple way to analyse such a cavity is to use our earlier results to write down the complex amplitude reflectivity, call it $r_2^{'}$, looking into the R, $R_2$ section of this interferometer (of length $L_2$) from the left. We can then use this result for $r_2^{'}$ as the effective end reflectivity to write down the total reflectivity, call it $r_1^{'}$, look into the $R_1$, R cavity segment (of length $L_1$) again from the left. The end result of this is that the total reflectivity R*, as observed by looking into the three-section cavity from outside the $R_1$ mirror can be written as

$$R^* = [\frac{\sqrt{R_1}(1 - \sqrt{RR_2}\tilde{g_2}) - \tilde{g_1}(\sqrt{R} - \sqrt{R_2}\tilde{g_2})}{1 - \sqrt{RR_1}\tilde{g_1} - \sqrt{RR_2}\tilde{g_2} + \sqrt{R_1R_2}\tilde{g_1}\tilde{g_2}}]^2 \tag{5.5}$$

Here, the total relative reflectivity R* can be obtained as a function of wavelength $\lambda$, so that the model of the three-mirror laser cavity can be considered as a "new output coupler". This "new output coupler" is similar to the output coupler ($M_2$) used in our system but with different reflectivity R*.

Depending on the relative reflectivity R* and spacing of the cavity mirrors, one used in our fundamental laser views a three-mirror cavity as a single long cavity of total length $L_2$ with an etalon mirror of length $L_1$ on one end. The analytic approximations can then be used to calculate the cavity resonant frequencies from Equation 5.5.

As a general rule, however, the resonance properties of the three-mirror cavity are sufficiently complex that the use of numerical solutions and computer display techniques can be beneficial in finding and understanding the resulting total reflectivity. Thus, the total reflectivity R* is calculated to illustrate the behaviour that can result.

### 5.4.3 Coupled cavity effects on linewidth narrowing

In the Appendix A.4, the total reflectivity R* has been calculated using a self-programmed GUI application implemented in MATLAB. The coupled cavity effects on linewidth narrowing will be analysed in this section.

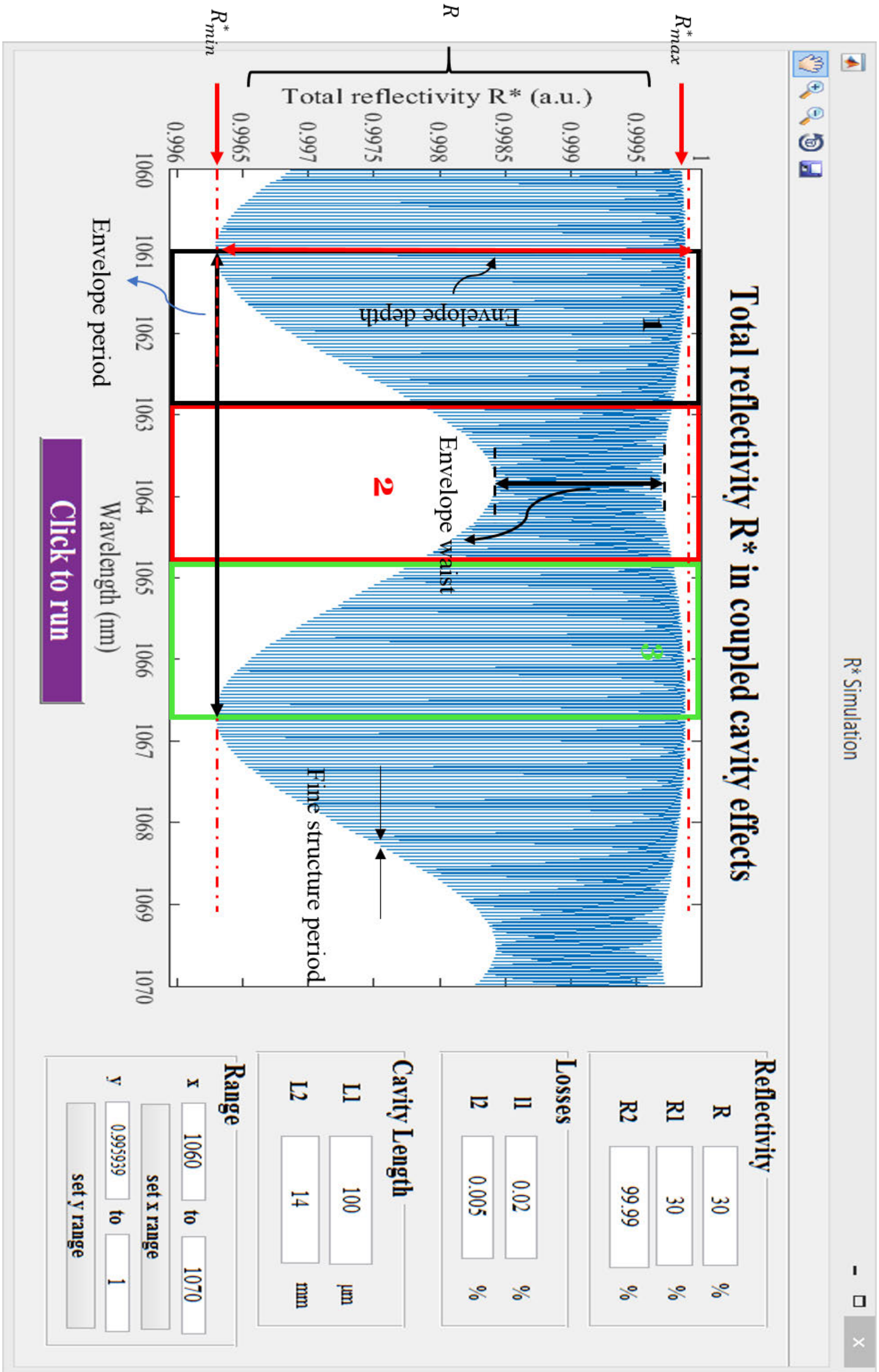


Figure 5.14: Key features labelled affects the modelling results.

The total reflectivity can be obtained using Equation 5.5, so the $R^*$ represents the reflectivity of the three mirrors coupled cavity. This means the fundamental laser is formed by $M_1$ and new $M_2^{'}$ with reflectivity $R^*$. The fundamental laser resonator with the new output coupler $M_2^{'}$ has a variable reflectivity $R^*$, so it is important to analyse how it affects to our laser system compared to the laser with constant reflectivity R for output coupler $M_2$ in the "free running" case.

With this model, we can play with parameters of reflectivity, losses and cavity length and understand how these parameters affect the total reflectivity $R^*$. Here, to discuss the results, the etalon of 100 $\mu$m thick, uncoated (A3) and R=30% (B6) etalons were used in this section as examples. Look at the Equation 5.5, the four groups of parameters which affect the total reflectivity $R^*$ are presented and discussed individually in Table 5.3. An example of these factors implemented in the GUI, and the resultant $R^*$ plot is shown in Figure 5.14.

In the experimental part, the use of 100 $\mu$m A3 and B6 etalons enable yielded the best performance so here, the modelling results using these etalons are shown in Figures 5.15 a and 5.15 b. The parameters used in the model are as follows: R and $R_1$ equal to 8.4% and 30%, respectively; $R_2$ is the original reflectivity of output coupler with the value of 99.99%. For reflectivity items R and $R_1$, they are determined by the particular etalon used in the system. These values affect the total reflectivity of the coupled cavity. The minimum total reflectivity ($R^*_{min}$) is 0.99964 with etalon reflectivity of 8.4% and 0.9988 with that of 30% (shown in Figure 5.15) for comparison. The lower etalon reflectivity gives rise to the higher minimum total reflectivity $R^*$ under the same values of other parameters involved in this setup.

Coupling effects manifest themselves as etalon effects from intracavity components. As a result, the coupling between different optical components should either be avoided or carefully controlled. Referring to Figure 5.13, the design consists of two coupled resonators. One resonator is considered plane parallel and is formed by etalon itself. Since the etalon has formed this resonator, it is referred to as being active. The second resonator is hemispherical and is formed by the plane mirror and concave mirror, which also serve as an output coupler, so this cavity is passive. In the experimental system, losses in each component cannot be ignored, so the cavity losses are estimated in order to obtain the reasonable simulation results. The losses for cavity 1 is assumed to be $l_1$=0.02% and for cavity 2 is $l_2$ = 0.005%.

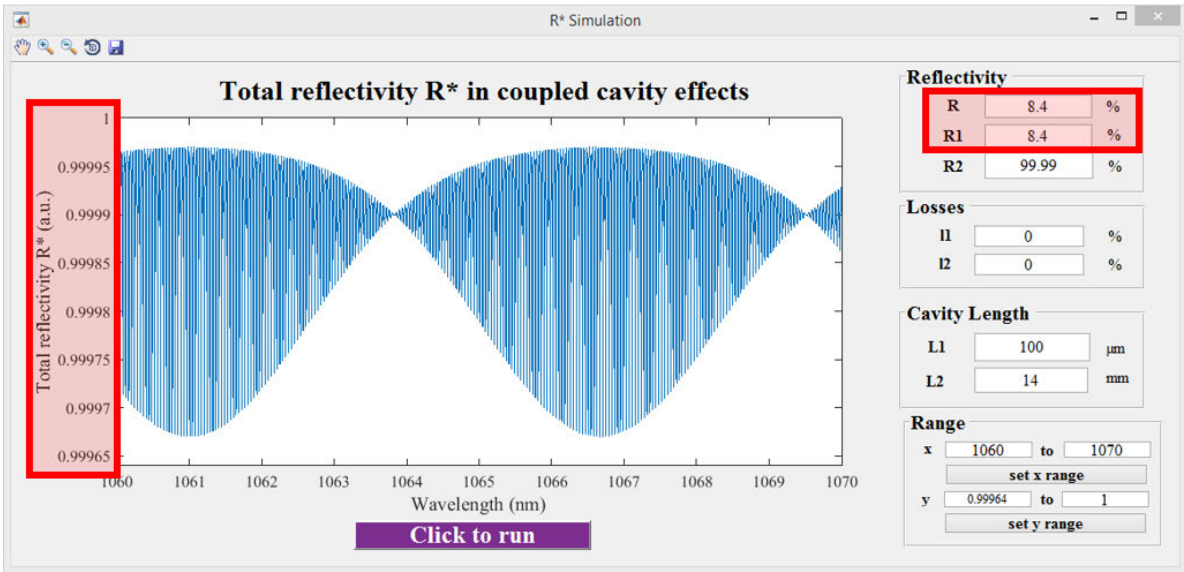


(a)

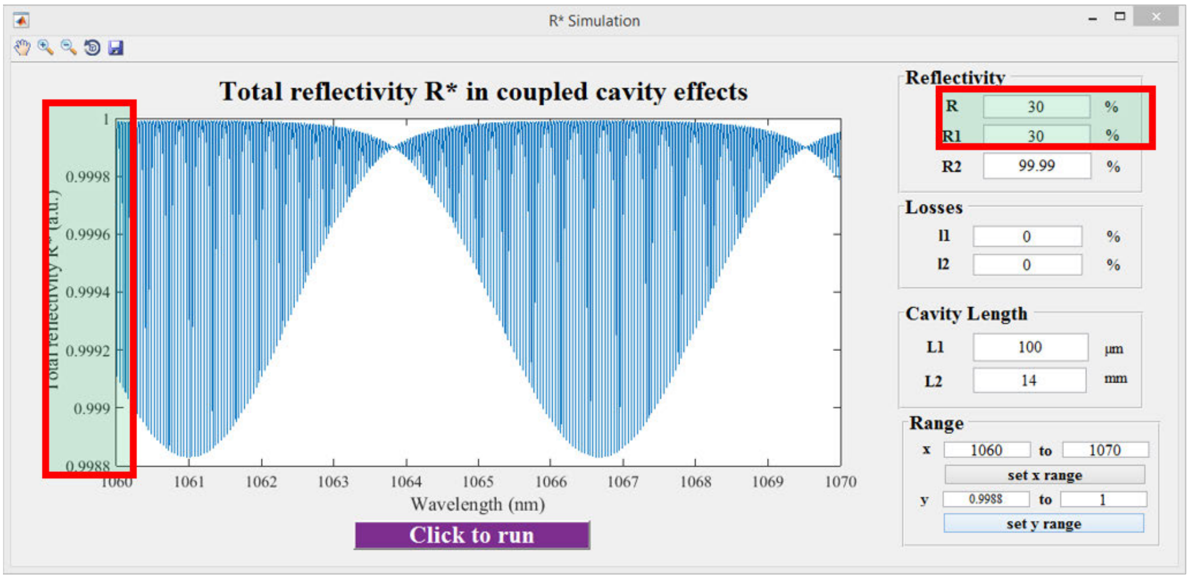


(b)

Figure 5.15: Simulation results of using etalon at normal incidence (a) 100 $\mu$m, uncoated etalon: A3, (b) 100 $\mu$m, R=30% etalon: B6.

Applying into the simulation application, the results for there two etalons is shown in Figures 5.16 and 5.17. The parameters of reflectivity and loss affect the total transmission of the coupled cavity. With the inclusion of these assumed losses, the minimum total reflectivity with the use of A3 etalon, drops to 0.9985, and that of B6 drops to 0.996. Both of the results have a fairly complex structure.

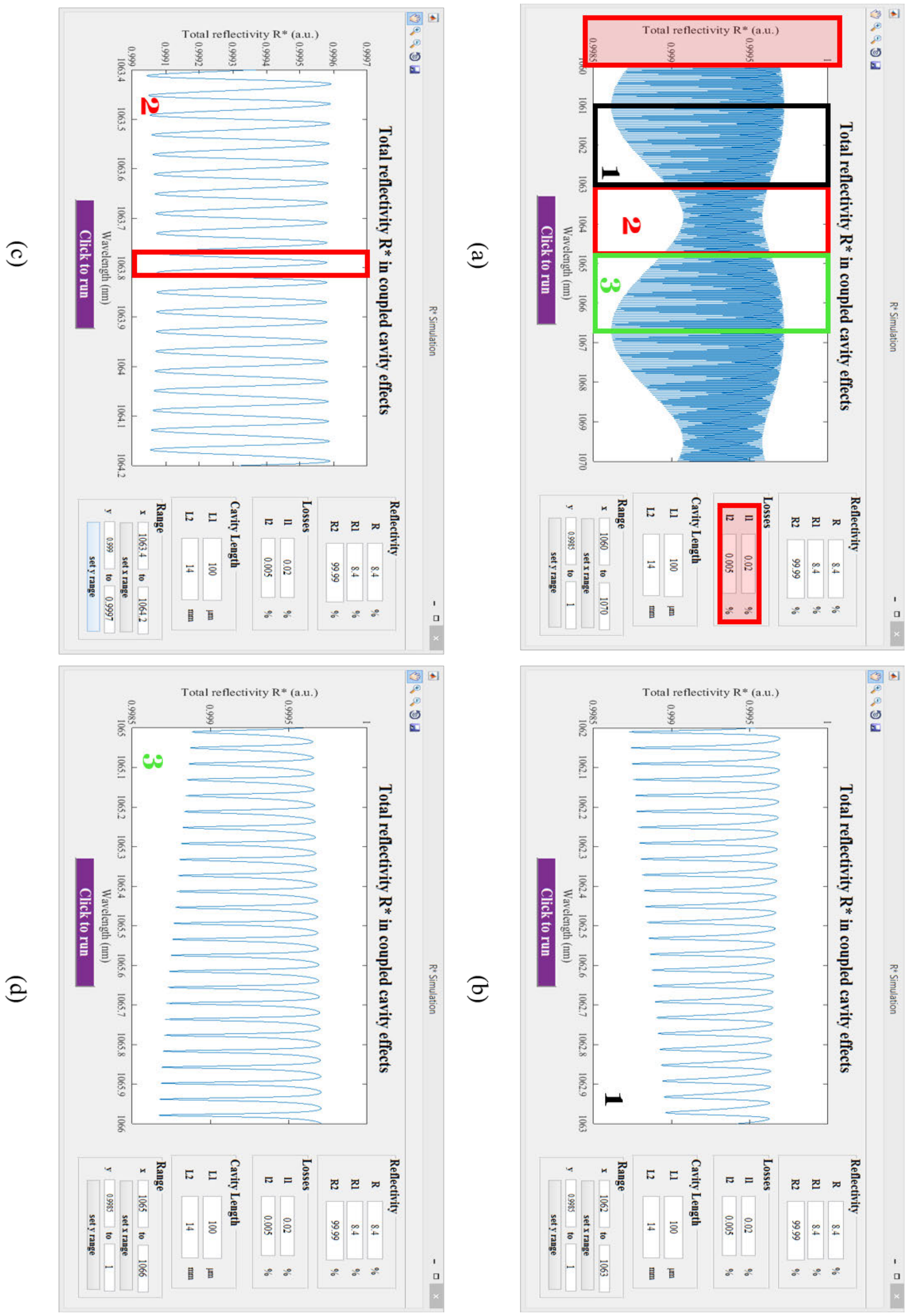


Figure 5.16: Simulation results of using 100 $\mu$m, uncoated A3 etalon at normal incidence (a) overall modelling results, (b) zone 1, (c) zone 2, and (d) zone 3.

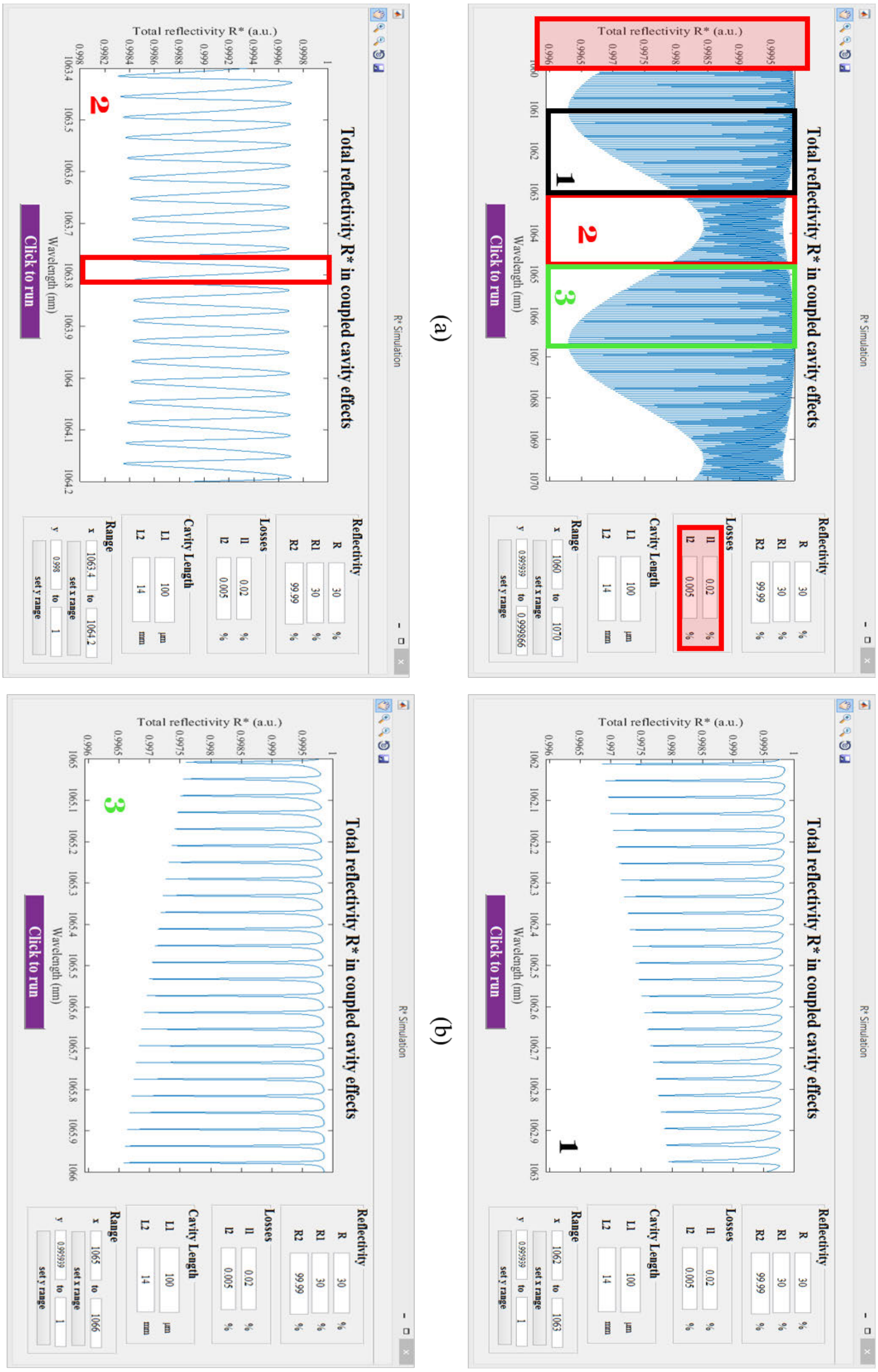


Figure 5.17: Simulation results of using 100 $\mu$m R=30% B6 etalon at normal incidence (a) overall modelling results, (b) zone 1, (c) zone 2, and (d) zone 3.

Table 5.3: Summary of key factors in coupled cavity model

| Feature | Factors which affect the features |
|---|---|
| Envelope period | etalon thickness, $L_1$ |
| Fine structure period | $L_2$ |
| $R^*_{max}$ | $R=R_1$, $R_2$, $l_1$, $l_2$ (mainly); $\lambda$, $L_1$ (minor) |
| $R^*_{min}$ | $R=R_1$, $R_2$, $l_1$, $l_2$ (mainly); $\lambda$, $L_2$ (minor) |
| Envelope depth: $R^*_{max}$-$R^*_{min}$ | $R=R_1$, $R_2$, $l_1$, $l_2$ (mainly); $\lambda$, $L_1$, $L_2$ (minor) |
| Envelope waist | $l_1$, $l_2$ |
| Fine structure: zone 1, 2, 3 | all factors |

To analyse the structure, which is influenced by the cavity length $L_1$ and $L_2$, we can consider that it was three zones and zoomed in, as illustrated in each case. The results are shown in Figures 5.16 a, b, c, d, and Figures 5.17 a, b, c, d, respectively. It is found that cavity lengths affect the wavelength response of coupled cavity. $L_1$ impacts broad-range structure, and $L_2$ impacts fine structure. This is because of the FSR of each cavity, the longer cavity length, the broader FSR, in contrast, the shorter cavity length, the narrower FSR. In the laser system, $L_2$ is smaller than $L_1$, so the two cavities affect the wavelength response in the different ranges. Each of the zoomed spectra represent different zones of response of the coupled cavity. The characteristic of each zone is discussed in detail.

The structure response to wavelength shows that the changes of total reflectivity $R^*$ are asymmetric in distinct zones 1 and 3, and the lowest peak varies with the shape of FSR of cavity $L_2$. It is not expected that the laser will oscillate in the distinct zones 1 and 3, because the severe changes of total reflectivity $R^*$ with wavelength. Rather, it is most likely expected to lase in zone 2, with symmetric total reflectivity $R^*$ change, which is highlighted in Figures 5.16 c and 5.17 c for the 100 $\mu$m, uncoated and R=30% etalon. This is the zone we are primarily interested because the temporal coupling of the two cavities is associated with constructive or destructive interference that arises from multiple reflections for $M_2'$. The overall effect can be described as that of a wavelength-dependent output coupler, which in turn leads to a loss discrimination between the longitudinal eigenmodes. This therefore selects the oscillating longitudinal modes in the fundamental resonator. In the highlighted range, the total reflectivity $R^*$ has a distinguishable range from 0.9997 to 0.9984 with B6 etalon, as across a wavelength span of 0.04 nm (shown in Figures 5.18 b). It is found that using A3 etalon, the wavelength span is the same due to $L_2$=14 mm both in the two cases. $L_2$ is a factor which affects the fine structure period. However, in the case of A3, the maximum and minimum $R^*$ values in zone 2 are 0.9996 and 0.9991, respectively, illustrated in Figure 5.18 a.

The position of zone 2 (with respect to wavelength) is heavily influenced by the etalon thickness $L_1$. Indeed, by changing the thickness by 1 $\mu$m, the centre of the range can be shifted to from 1063.83 nm to 1063.18 nm. This correlates better with the central wavelengths observed in Figure 5.18. Note that the manufacturer quotes a thickness error of ±5 $\mu$m so it is conceivable that is conceivable that shifts of this order maybe expected. The relative plots are shown in Figure 5.19.

The differences using the etalons A3 and B6 are the total reflectivity $R^*$ maximum and minimum values of the spectra, especially in zone 2. The overall $R^*$ ranges with wavelength response is from 0.999 to 0.9996 using the etalon A3. However, that of etalon (B6) is from 0.9984 to 0.9996. In the simulation results, they show that several constructive peaks appear in the laser gain range and the total reflectivity $R^*$ difference means it is hard to suppress the adjacent longitudinal modes under the laser gain in a high Q cavity. Therefore, more than one peak is likely to be observed, and this is seen experimentally in Figures 5.8a and 5.8d. Because of the total reflectivity structure in the coupled cavity, the central experimentally observed wavelength was dancing around the laser gain maximum, and the central wavelength is 1063.1 nm with the etalon (B6). More peaks oscillate using etalon (A3) because the minimum total reflectivity $R^*$ is 0.999, so more longitudinal modes can reach SPS threshold.

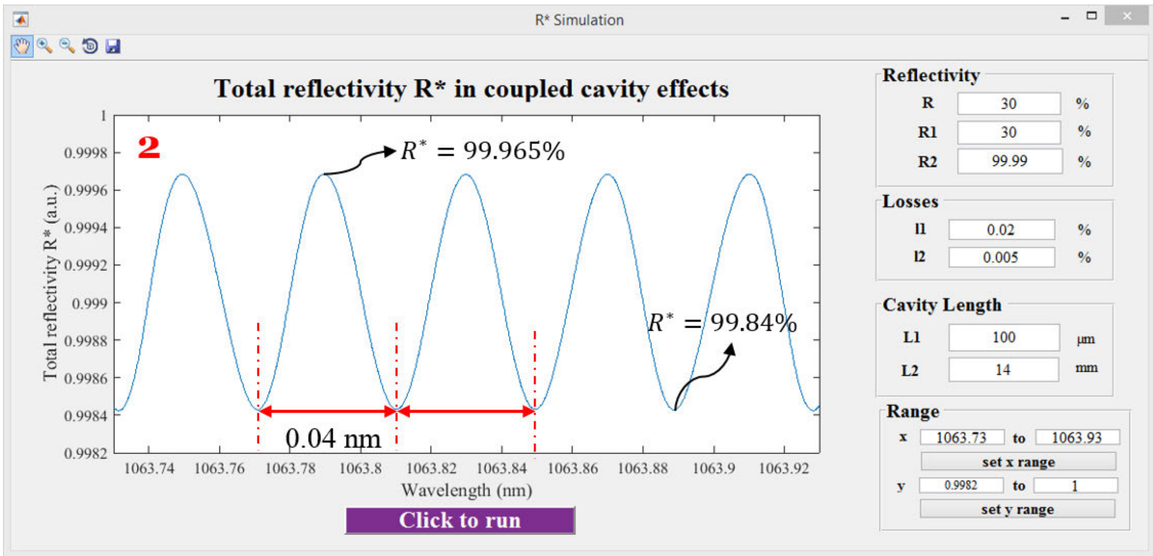


(a)

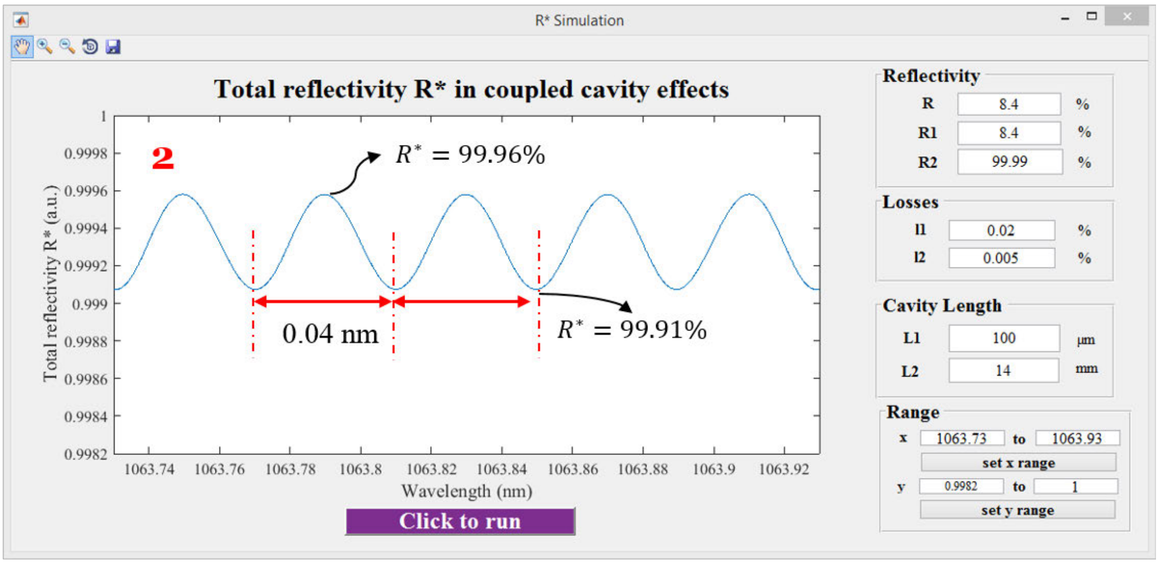


(b)

Figure 5.18: Detailed simulation results for each etalon in zone 2 (a) 100 $\mu$m, uncoated etalon: A3, (b) 100 $\mu$m, R=30% etalon: B6.

In summary, etalons inserted at normal incidence in a CW THz laser system achieves linewidth narrowing because the etalon forms coupled cavity effects and the effects with a complex reflectivity can achieve mode selection. Notably with the coupled cavity, the laser operates in zone 2. The physics at play in coupled cavities are complex, and our analysis is ongoing.

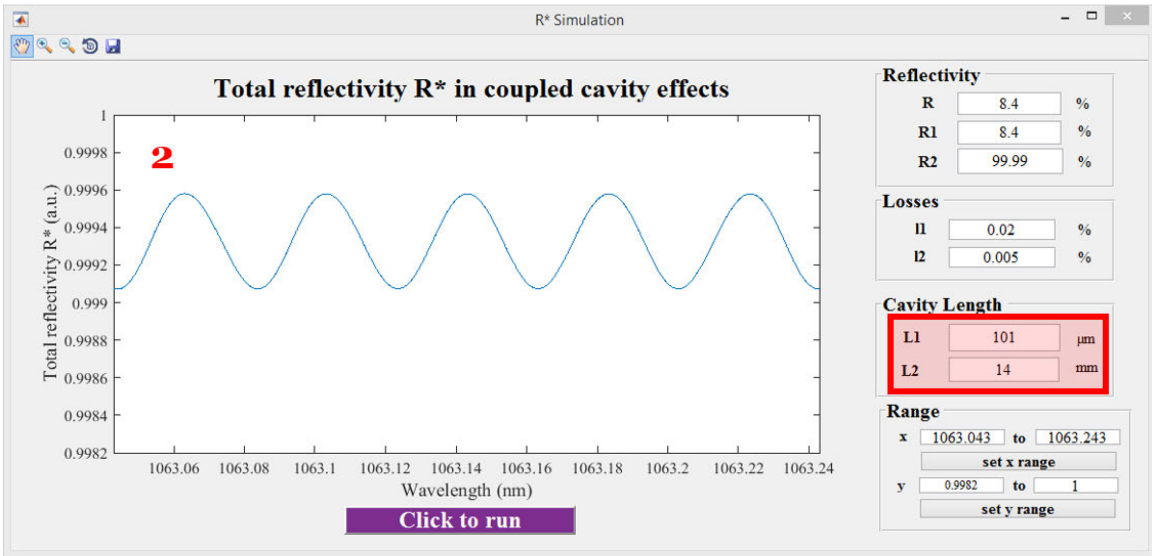


(a)

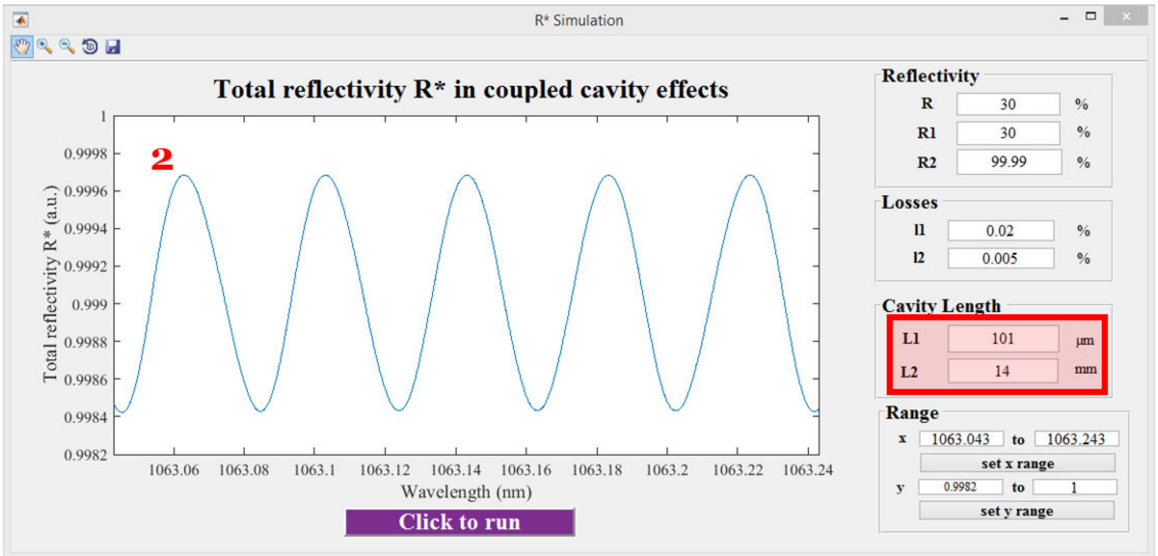


(b)

Figure 5.19: Simulation results in zone 2 when using etalons A3 and B6 with a 1 $\mu$m increase in thickness (a) 100 $\mu$m, uncoated etalon: A3, (b) 100 $\mu$m, R=30% etalon: B6.

## 5.5 Analysis of spectra using the A3 and B6 etalons

In this chapter, the study focused on the investigation of using an etalon to deliberately form coupled cavity, to achieve linewidth narrowing. The spectral properties were studied both experimentally and theoretically. The theory study indicated that the etalon spectral response located in the distinct zone 2 is the likely region having the most influence on the laser spectral properties because this zone is symmetric. The modelling has shown that the coupled cavity response is strongly influenced by $L_1$ and $L_2$. The response of the coupled cavity is so fine in wavelength spacing that it will significantly influence the longitudinal modes of the laser. To investigate this, the measured fundamental spectra both using A3 and B6 etalons were compared with the modelling results.

Figures 5.20 and 5.21 show the $R^*$ response of the coupled cavities for zones 1, 2 and 3 (note that the response of zones 1 and 3 are identical due to symmetry, and are plotted on the same plot), when using etalons A3 and B6 respectively. Overlaid on these plots are the fundamental output spectrum as measured from the laser cavity. The spectral response at the fundamental wavelength is governed by the emission cross section of the Nd:GdVO4 crystal, and hence, emission is centred in the range 1063.0-1063.4 nm. What is interesting is that the output spectrum takes on fine-structure which correlates very well to the $R^*$ characteristic of the coupled cavity. This clearly shows that the coupled cavity impacts the range of longitudinal modes which can oscillate within the laser, and this is the source of linewidth narrowing of the laser output.

While it was stipulated that zone 2 would be the dominant region in which the coupled cavity affects the laser response, it is clear that regions 1 or 3 (Figure 5.20 b and 5.21 b) may also be responsible for the apparent mode selection/limiting within the system. We have also shown that the $R^*$ response is heavily influenced by subtle changes to etalon thickness and cavity length. While effort was made to reduce the overall amount of vibration within the lab/system environment, a level of vibration was still present, along with dynamic heating of the system components (including the intracavity etalon). As a result, it is conceivable that the response of the coupled cavity will shift dynamically and influence the spectral response of the system. While this does impart a level of spectral instability, the laser can still maintain narrow linewidth emission owing to operation across each of the regions 1, 2 and 3.

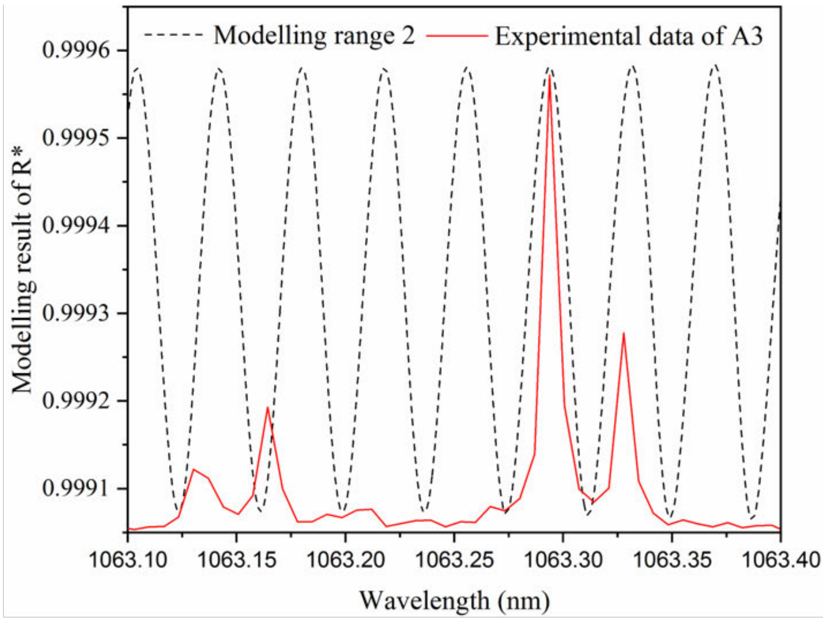


(a)

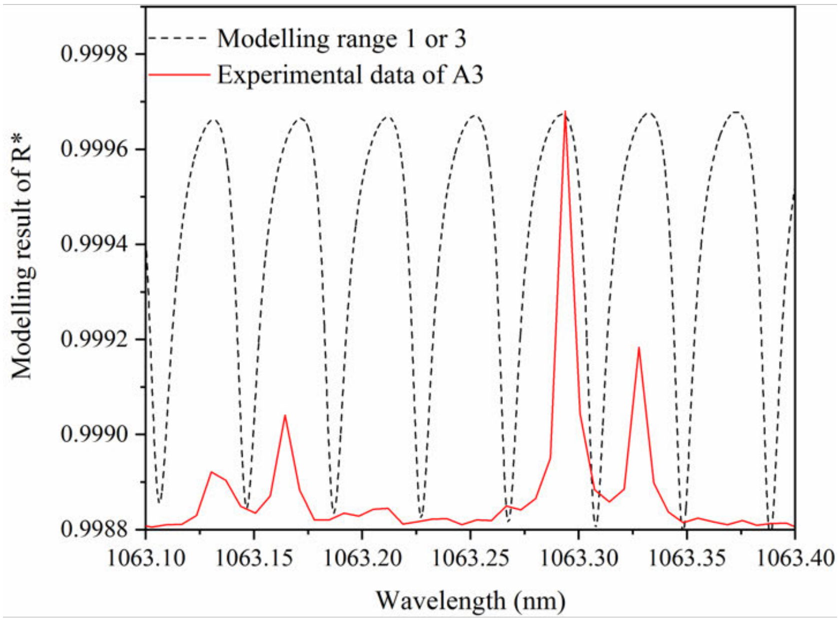


(b)

Figure 5.20: Simulation results of using A3 etalon at normal incidence, combined with experimental data: (a) zone 2 or 3, and (b) zone 1 or 3.

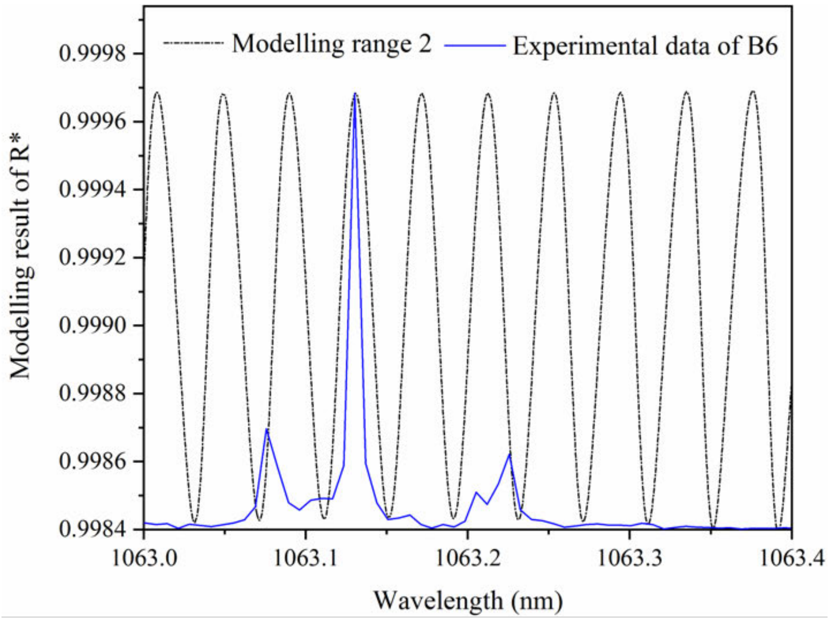


(a)

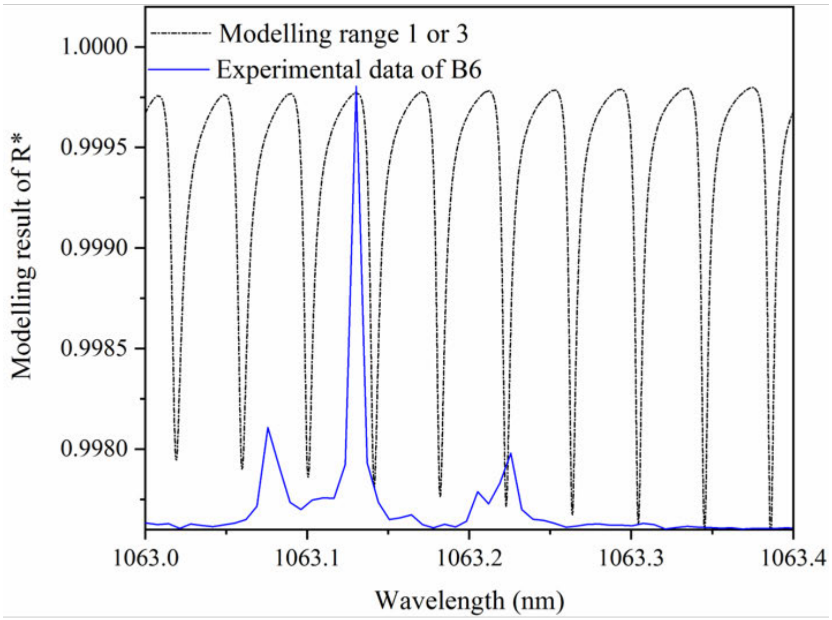


(b)

Figure 5.21: Simulation results of using B6 etalon at normal incidence, combined with experimental data: (a) zone 2 or 3, and (b) zone 1 or 3.

## 5.6 Conclusion

In this chapter, etalons used at normal incidence within the fundamental laser cavity was investigated. This led to the formation of complex coupled cavity resonators within the laser. It was found that the linewidth of the fundamental field can be narrowed significantly by forming a coupled cavity when an etalon is inserted at normal incidence. In this case, the fundamental FWHM reached a value of 0.008 nm with etalon (B6). Etalons, both uncoated and coated were effective in narrowing the linewidth in this configuration. When a 100 $\mu$m thick, uncoated YAG etalon (A3) was used in the fundamental laser, both the fundamental and Stokes fields were narrowed. A similar characteristic was observed when the coated etalon (B6) was used. Interestingly, with all tested etalons, when inserted at normal incidence, it was possible to observe an increase in the maximum THz power, in comparison to the "free-running" case. The net result was that the fundamental field linewidth could be narrowed, but in some cases, multiple resonance were observed. In all cases, an improvement in THz power scaling was observed.

The theoretical study focused on how the etalon used at normal incidence, formed a coupled cavity, with three distinct spectral response regions. This study revealed that the spectral response had very fine structure, which could be easily influenced by etalon thickness and cavity length. This supporting the experimental observation of high sensitivity to vibration. This comes with compromises in angular sensitivity and susceptibility to vibration. But it is a distinct way of using an etalon to linewidth narrow. Theoretical modelling of the coupled cavity spectral characteristics revealed a very complex structure, which could be separated into 3 regions of operation. Based on consideration of the laser emission cross-section, region 2 is the one most likely to influence the spectral characteristics of the laser. This is supported by the spectral characteristics of the coupled cavity being most sensitive to the etalon thickness.

The linewidth narrowing of the fundamental field yields an improvement in the THz output power due to reduced phase mismatch along the same lines as discussed in Chapter 4. The work presented in this chapter determines that an unconventional used of etalons at normal incidence, to form a coupled cavity, can be highly effective at linewidth narrowing in our intracavty THz lasers. While the effectiveness is clear, further experimental work and modelling is required to fully understand the mechanisms at play.

# 6

# Single longitudinal mode operation in an intracavity CW THz laser

## 6.1 Introduction

The properties of etalons and their application in the CW SPS laser have been investigated in depth in Chapter 4 and 5. The linewidth both in the fundamental and Stokes fields (and consequently, the THz field) can be narrowed using an etalon in the fundamental cavity. The possibility of better linewidth narrowing thus motivated the investigation of using a high finesse etalon in the fundamental field. Using etalons to form a coupled cavity indicated that the etalon with high finesse could give rise to very narrow band linewidth output in a laser. In this chapter, further linewidth narrowing is investigated using a high finesse etalon inserted at normal incidence.

In this chapter, linewidth narrowing down to a single longitudinal mode is investigated in detail, using a 250 $\mu$m, R=60% etalon (C9). Substantial improvements in the performance of THz output power and linewidth are described. These results achieved in this chapter have been reported in the 2016 AIP conference and this publication is included in the Appendix.

In addition, an investigation of phase mismatching is undertaken, and this sheds significant insight into the improved power scaling enabled by narrowing the fundamental field linewidth using etalons.

## 6.2 Experimental setup

The laser setup is similar to that used in Figure 5.1 except that a high finesse 250 $\mu$m, R=60%, fused silica (FS) etalon was used. The specific etalon properties can be found in Table 2.4. Fine control of the cavity length was necessary for narrow linewidth operation as for the results of Chapter 5, and was achieved using a translation stage with fine adjustment on the output coupler.

## 6.3 Power transfer characteristics

When the 250 $\mu$m, R=60% FS etalon was inserted, it was found that it increased the loss to the fundamental field, but this could be compensated by increasing the diode pump power. This behavior was expected given the already substantial fundamental cavity round-trip loss. Fine tuning of the etalon position was therefore critical to achieving SPS threshold.

### 6.3.1 Quasi-CW operation

For comparison, the system without an etalon was power scaled and plots of the fundamental, Stokes and THz field under the same condition as with the high finesse etalon are shown in Figure 6.1. The system power transfer characteristics for the fundamental and SPS fields with the etalon inserted, is plotted in Figure 6.2 for the SPS generation at 1070.7 nm (1.99 THz) under quasi-CW (chopped pump) conditions.

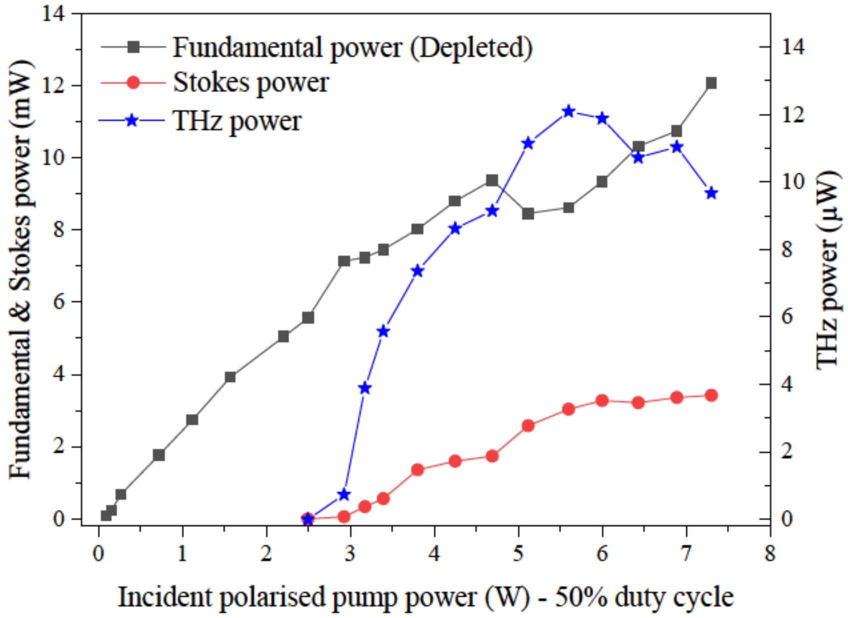


Figure 6.1: No etalon in the fundamental cavity; output powers for fundamental, Stokes and THz fields.

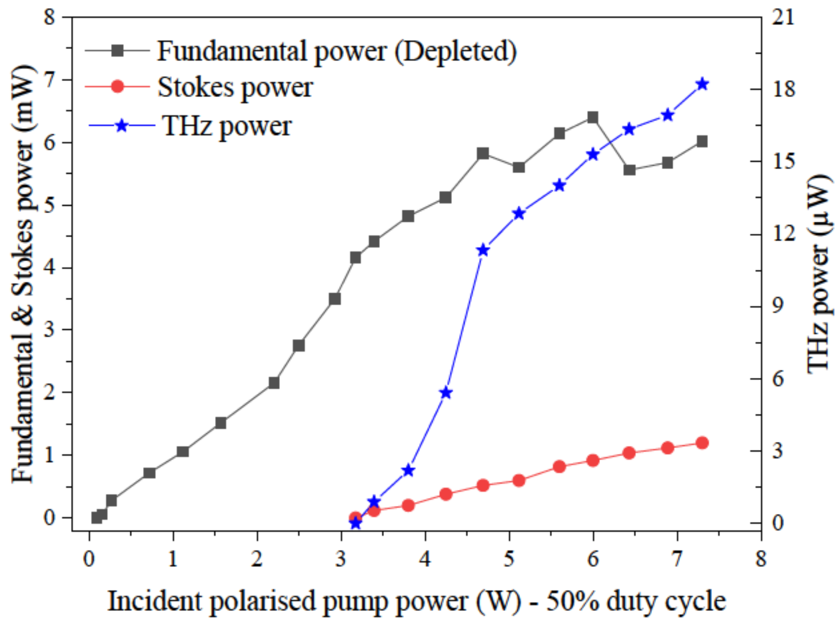


Figure 6.2: With 250 $\mu$m R=60% etalon inserted into the fundamental cavity, at normal incidence: output powers for fundamental, Stokes and THz fields in an intracavity CW THz laser.

As expected, the THz laser performed better when the etalon was present, and more THz power was detected with no roll-over evident. The threshold for the fundamental field was very slightly affected by the insertion of the etalon. The SPS threshold however, increased to 3.2 W (22%) compared to the value of 2.5 W (no etalon case). The reason behind this is from the losses induced by the etalon, which is analysed in Chapter 5. The possibility of pumping the system harder enabled an increase in the THz output power, as anticipated. The maximum THz output power was 18.2 $\mu$W at 1.99 THz for 7.3 W diode pump power. This is 1.5-times higher in maximum THz power, in comparison to 12.0 $\mu$W obtained under the same condition but with no etalon involved. This result is similar to that reported using other etalons in Chapter 4 and 5.

Worth noting is that this THz frequency (1.99 THz) does not correspond to where we expected the highest THz power to be achieved (1.65 THz), suggesting that the efficiency of the THz output power could be increased [60].

### 6.3.2 Pure CW operation

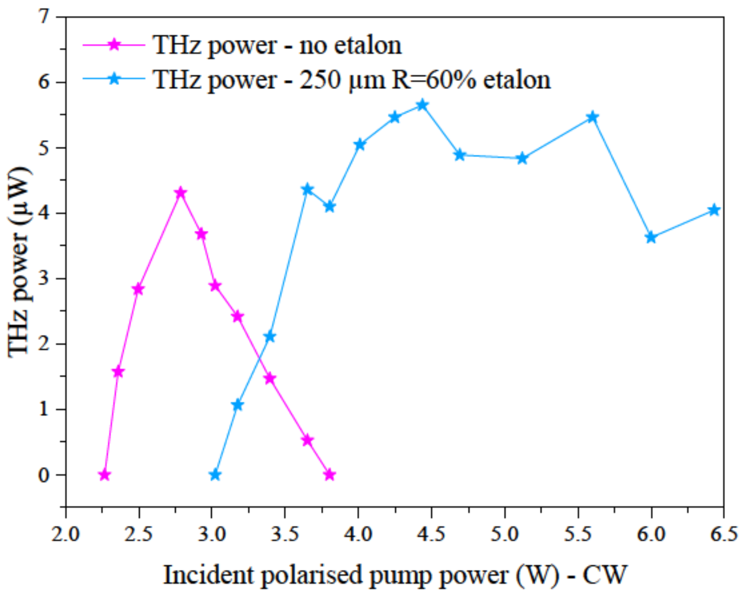


Figure 6.3: Power scaling properties of the THz output with and without the 250 $\mu$m, R=60% etalon under CW pumping.

The power transfer of the THz field under true-CW pumping conditions is shown in Figure 6.3. Due to the operational limitations of some of the characterisation equipment used in this work, pure CW regime operation is required. The requirements for each optical spectrometer are shown in Table 2.5. Thus, laser performance of THz power in the pure CW regime with and without the 250 $\mu$m, R=60% etalon are shown in Figure 6.3. Threshold for THz generation was 2.3 W in the free running case and 3 W with the insertion of the etalon. The advantage of using the 250 $\mu$m, R=60% etalon is that the THz laser was easy to lase and the THz power is maintained over a wider range of pump powers. The reasons for the difference in THz power in these two cases may be explained by the difference of the characteristics which will be discussed in next section.

## 6.4 Spectral control

Due to energy conservation in the SPS process, narrowing the frequency band of the fundamental and Stokes fields results in associated constraint on the linewidth of the generated THz field [107].

### 6.4.1 Spectral characteristics

The spectral characteristics of fundamental and Stokes fields were examined and from this, the spectral characteristics of the THz field were inferred. The longitudinal mode structure of SPS laser was characterised using a scanning Fabry-Perot interferometer (FPI) (Thorlabs, model SA210) with a free spectral range (FSR) of 10 GHz and a spectral resolution of about 70 MHz. Simultaneously, the fundamental central wavelength was monitored by using a laser spectrum analyser (Bristol Instruments, model 771A-NIR), which provided an accuracy of 2 GHz in the 1 $\mu$m spectral range. The details of these devices have been presented in Chapter 2.

To verify the linewidth both in fundamental and Stokes fields, the results are shown in Figure 6.4a and Figure 6.5a, respectively. The central wavelength of fundamental wavelength was 1063.14 nm, and the Stokes wavelength was 1070.77 nm. From these figures, it is observed that the spectra both in fundamental and Stokes fields were close to instrument limit, so the 10 GHz scanning F-P interferometer weas used to examine the actual linewidths without

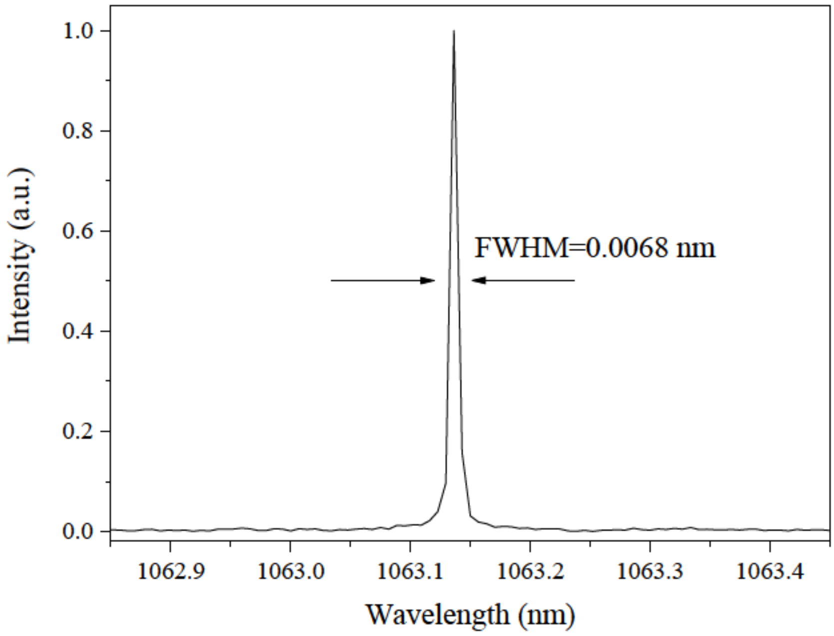


(a)

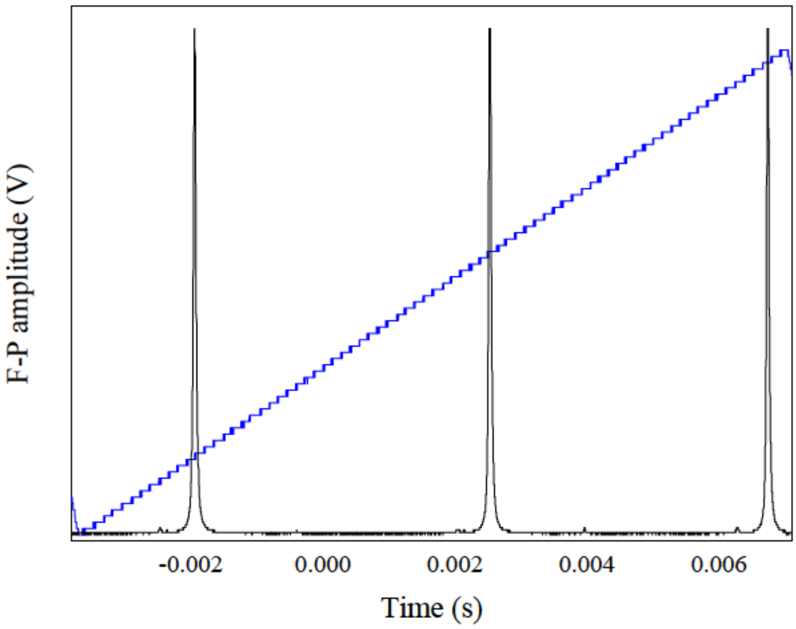


(b)

Figure 6.4: Fundamental field spectrum measured by (a) laser spectrum analyser and (b) scanning Fabry-Perot interferometer.

the limitation of the Bristol Wavemeter. The measured fundamental FWHM linewidth was 70 MHz which is closed to the instrument limit again (Figure 6.4b), and the Stokes FWHM linewidth was 400 MHz (Figure 6.5b).

The free spectral range of the fundamental cavity is calculated to be 0.69 GHz (optical cavity length = 185 mm, including 13 mm long Nd:$GdVO_4$ crystal with refractive index at 1063 nm n=2.19, and 20 mm MgO:$LiNbO_3$ crystal with refractive index at 1070 nm n=2.23.). Therefore, approximately 148 longitudinal modes fit within the FWHM of the *free-running* fundamental laser spectrum of 102 GHz (Ref. 3.12 a). Using the same calculation, the free spectral range of the Stokes cavity is 1.1 GHz with the cavity length of 130 mm, so around 45 longitudinal modes oscillate within in the FWHM of the Stokes laser spectral width of 72 GHz (Ref. 3.12 b).

The linewidth of etalon-narrowed fundamental field is 70 MHz and that of Stokes field is 400 MHz, so only one longitudinal mode was present under the laser gain both in fundamental and Stokes fields. Hence, both fundamental and Stokes fields operated with a single longitudinal mode. Based on the linewidths measured, it is anticipated that the THz linewidth should be less than 400 MHz.

The fundamental linewidth measured by the 10 GHz F- P interferometer is 70 MHz, which is close to the instrument limit, so another high resolution scanning Fabry-Perot interferometer (FPI) (Thorlabs, model SA200-8B) was used to better resolve the fundamental linewidth. The resolution of this 1.5 GHz Fabry-Perot interferometer is around 7.5 MHz. The resolved fundamental linewidth was 6.68 MHz (Shown in Figure 6.6). The fundamental linewidth measurement was 10 times narrower compared to that of 10 GHz F-P interferometer measurement result. It is because the limitation of the instrument. It should be noted that the laser is extremely unstable and one trace was recorded to show that the laser linewidth can be obtained to 6.68 MHz albeit with instability. It was hard to measure Stokes linewidth because the leaking Stokes power was too small to be measured using the interferometer. Therefore, unfortunately, no corresponding Stokes linewidth is recorded with the fundamental linewidth of 6.68 MHz.

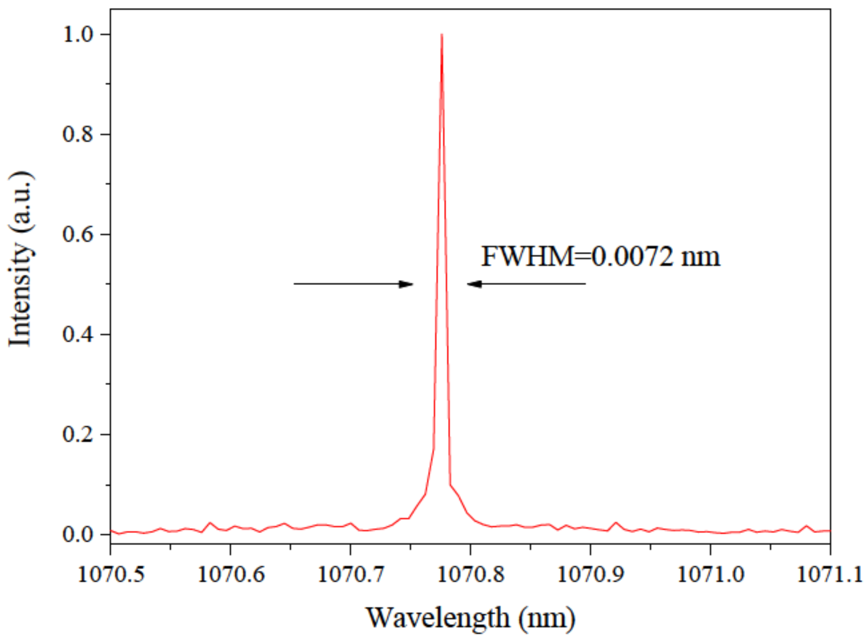


(a)

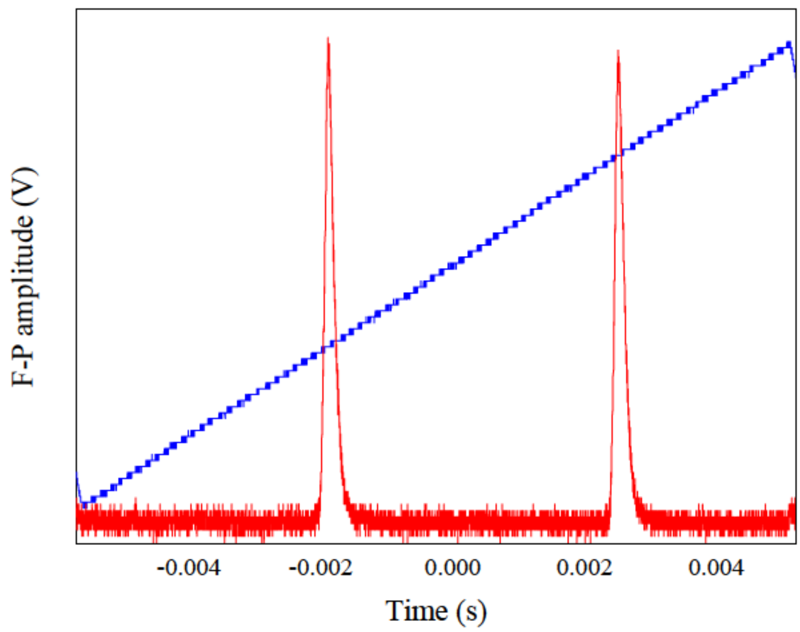


(b)

Figure 6.5: Stokes field spectrum measured by (a) laser spectrum analyser and (b) scanning Fabry-Perot interferometer.

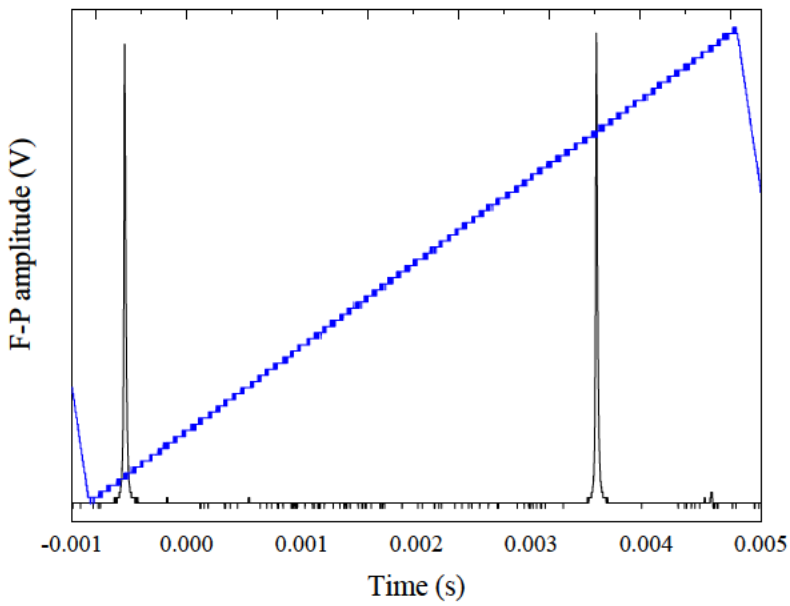


Figure 6.6: Fundamental field spectrum measured by (b) 1.5 GHz scanning Fabry-Perot interferometer.

## 6.5 Laser stability

For a narrow linewidth laser, especially single longitudinal laser, laser stability is very important factor, so the laser stability is analysed and optimised in this section. To understand the causes of mode instability in the THz lasers is challenging in the present system as the spectral dynamics are very complex.

### 6.5.1 Observation of laser instability

The dynamics of the CW THz laser is analysed under different pump power regimes, and using the 10 GHz scanning F-P interferometer. This enabled analysis of both the fundamental and Stokes fields.

The SPS threshold for the system was 3.2 W of incident pump power. Using the 10 GHz scanning F-P interferometer, in examining either fundamental or Stokes fields, at near SPS threshold (3.5 W), single longitudinal mode was observed. For incident pump power higher, between 3.5-4.5 W, the single longitudinal mode output was stable (Figure 6.7) apart from occasional mode hops caused by mode competition and thermal drift. At a higher power (4.5-6.0 W), the single longitudinal mode output was for less stable. Mode hopping was observed and subsequently the appearance of multiple lasing cavity modes, as shown in Figure 6.8. With increased incident pump power up to 7.3 W, the output tended to be highly multi-mode, and the SPS process fluctuated with time because of the accumulated thermal load in the laser crystal. This thermal effect was so dramatic that the Stokes cavity would not lase for a few seconds and lase again momentarily, and then stop.

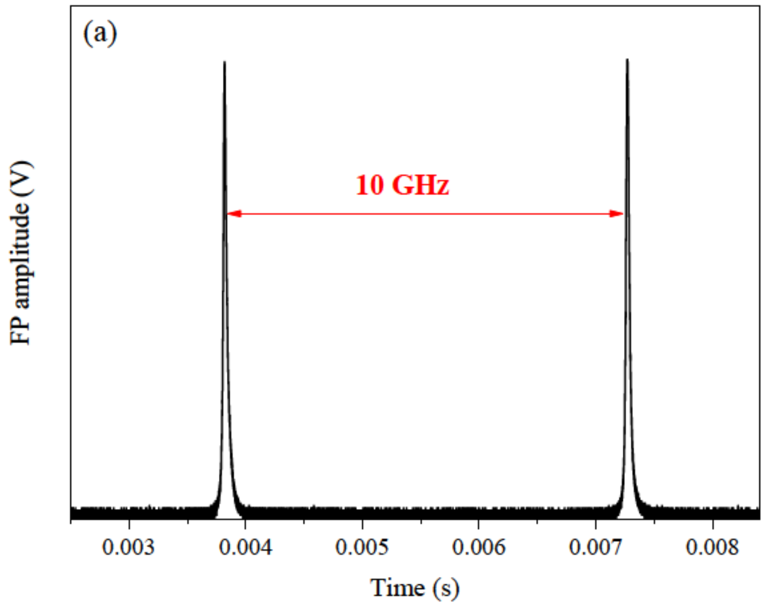


Figure 6.7: Fundamental field scans by F-P 10 GHz interferometer with (a) incident power of 4.5 W.

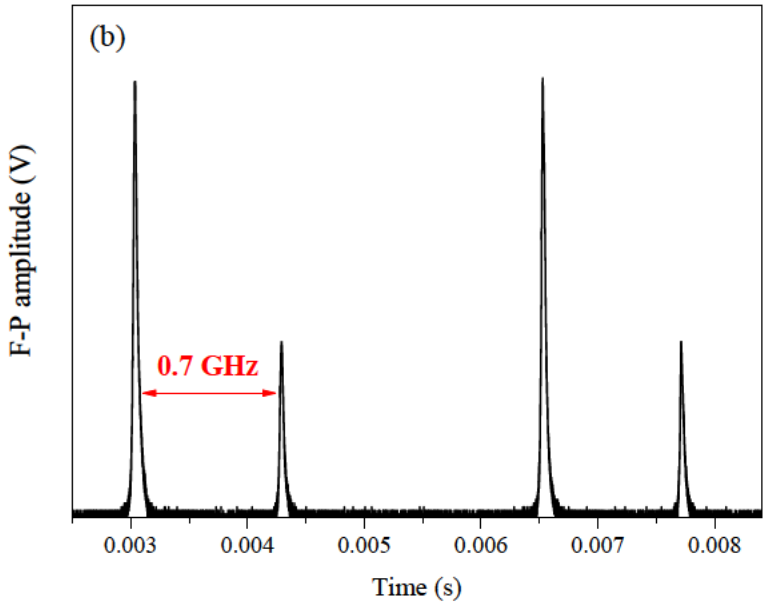


Figure 6.8: Fundamental field scans by F-P 10 GHz interferometer with (b) incident power of 6.0 W.

The FPI spectra showed that single longitudinal mode outputs were obtained at incident pump power up to 6.0 W both in fundamental and Stokes fields. Single longitudinal mode operation was only observed for pump power up to 53% over the SPS threshold, depending on the precise alignment of the end mirror at certain incident pump power.

### 6.5.2 Reasons for laser instability

From the laser behaviour described above, the single longitudinal mode operation in CW SPS laser was limited by the system instability. Notably, this instability becomes worse as the pump power increases. These might be caused by multiple aspects such as coupled cavity effects, mode competition, and thermal loading in the CW THz laser.

### 6.5.3 Coupled cavity effect

As detailed in Chapter 5, the overall effect of linewidth narrowing using the coupled cavity approach relies on interaction between different cavities which are generated in the laser, especially when the etalon is at normal incidence to the cavity mode. The modeling showed very high sensitivity to fluctuations in etalon position, and this is even more apparent when using a high reflectivity etalon, as is the case of the R=60% etalon used here. In this case, the overall reflectivity of a three mirrors system (as modeled in Chapter 5), as a function of fundamental wavelength response in the coupled cavity, is shown in Figure 6.9. What is especially apparent is that small fluctuations of 0.018 nm can make a significant change in overall reflectivity (99.99%-99.65%). This has the ability to drive laser modes above and below threshold, and hence degrade the stability of the system. Changes in etalon position of this order are easily driven by mechanical vibrations and thermal gradients within the system. Rising incident pump power (and increasing unabsorbed pump power) has the prospect of heating up resonator components.

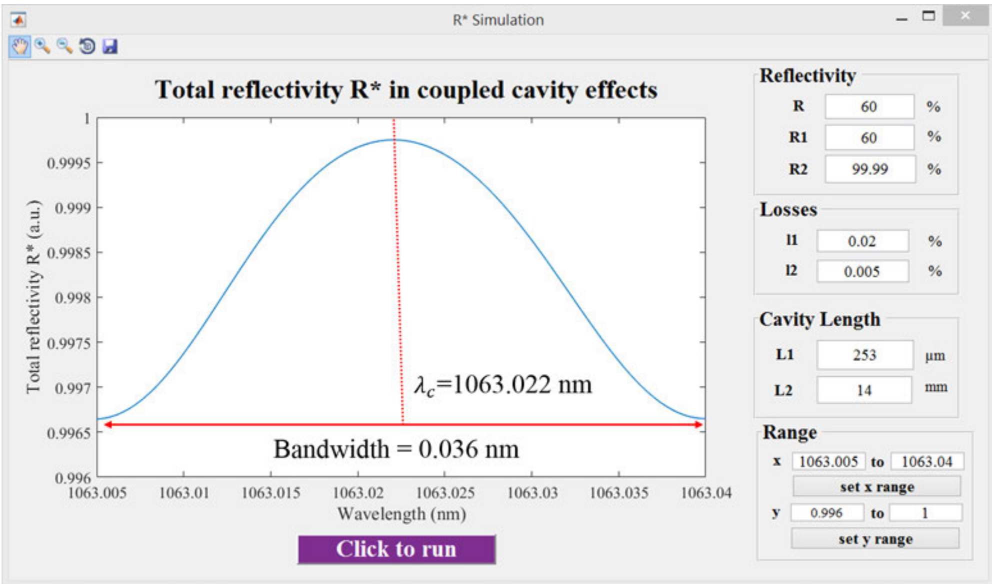


Figure 6.9: Simulation result of using C9 etalon at normal incidence.

### 6.5.4 Thermal effects

The heating of the laser crystal and impurity absorption leads to changes in the optical cavity length ΔL through the thermo-optic effect and thermal expansion, and is given by:

$$\Delta L/\Delta T = d(\frac{dn}{dT} + n\alpha) \tag{6.1}$$

The values of the thermo-optic coefficient ($dn/dT$=13.8 $\times$ 10$^{-6}$ K$^{-1}$) and thermal expansion coefficient ($\alpha$ =7.3$\times$ 10$^{-6}$) are taken from Table 2.1. Therefore, $\Delta L/\Delta T$ =301 nm/K for the Nd:$GdVO_4$ crystal of length d=13 mm. Given that laser action alters $\Delta L$ through heating, it is reasonable to expect that there is coupling between the fundamental and cavity resonance as the cavity is tuned.

In order to compensate $\Delta L$ because of heating and to improve the stability property of THz system, precise control of laser crystal temperature is crucial when aiming at high wavelength stability of the SPS laser output. In addition, the fine control translation stage (resolution: 25 $\mu$m, Model: Thorlabs MT1A) was used to slightly adjust the fundamental cavity length. While heating may have a role in the instability, it is anticipated that it will reach a steady-state after a certain period. Following each increase in pump power, the system was allowed to settle, and slight adjustment to the fundamental field end mirror angle, and the etalon angle were made, to improve power stability at the pump power.

### 6.5.5 Physical environment

What is more, the physical background noise also affected on the laser stability. It is observed that the THz laser suffered with the vibration caused such us tapping the table, closing the door, vibration of air conditioner and associated air current.

Consequently, the stabilisation technique was introduced into this system, using an anti-vibration optical table (Thorlabs PTS601) to minimise the physical background, as well as housing the complete laser system in a custom-built perspex box.

### 6.5.6 Use of anti-vibration table to optimise laser stability

An anti-vibration optical table was used and the laser was covered by a plastic box to reduce the airflow. It is aiming to improve the laser stability by optimising the physical environment. The stability of both fundamental and Stokes fields were monitored for five minutes using the laser spectrum analyser (Wavemeter 771A). This device enabled tracking of the peak wavelength over periods of many minutes.

For comparison, the laser stability was recorded before and after using the anti-vibration optical table. The central wavelength of the fundamental and Stokes fields were monitored and recorded for 300 seconds to show the effects of laser stability. It is clear to see that

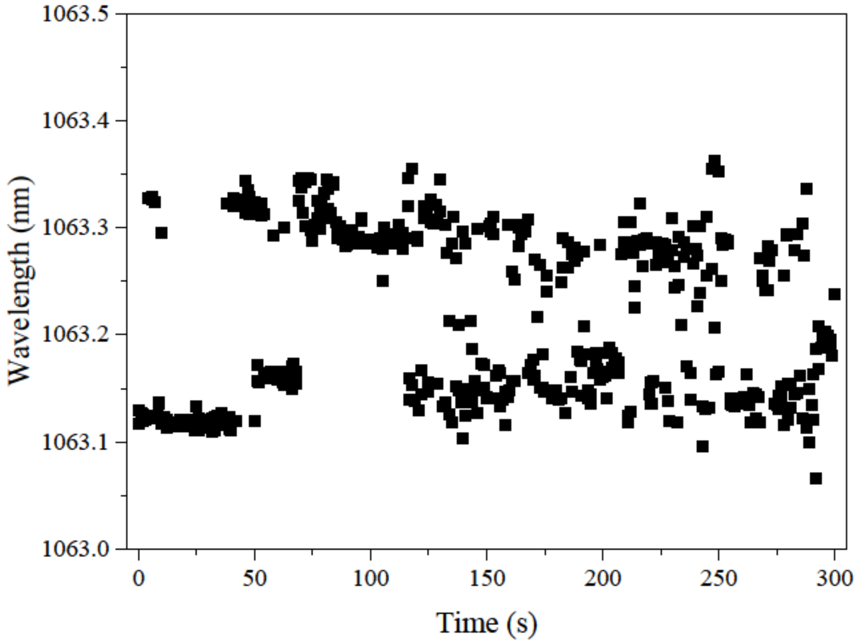


(a)

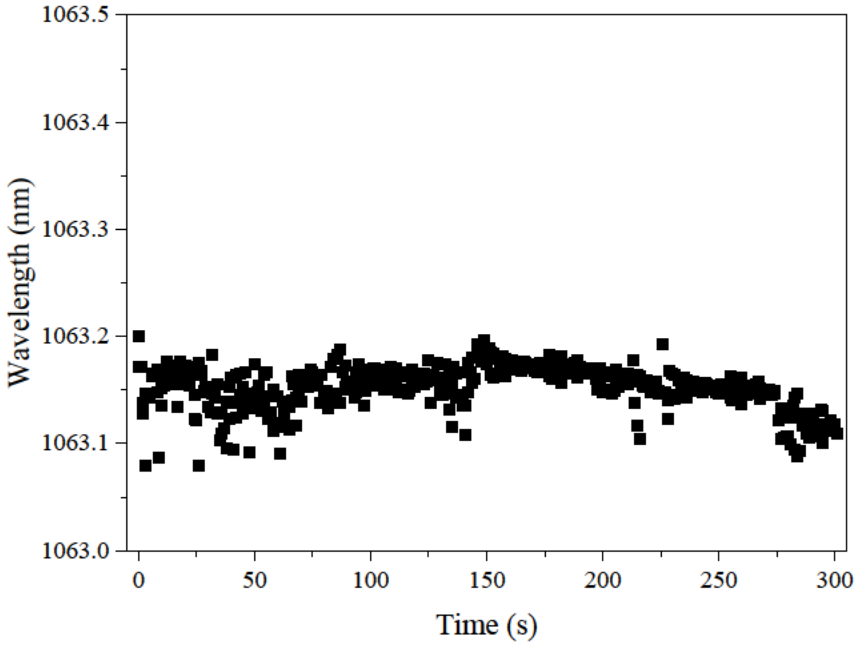


(b)

Figure 6.10: Fundamental wavelength stability (a) without (b) with anti-vibration table.

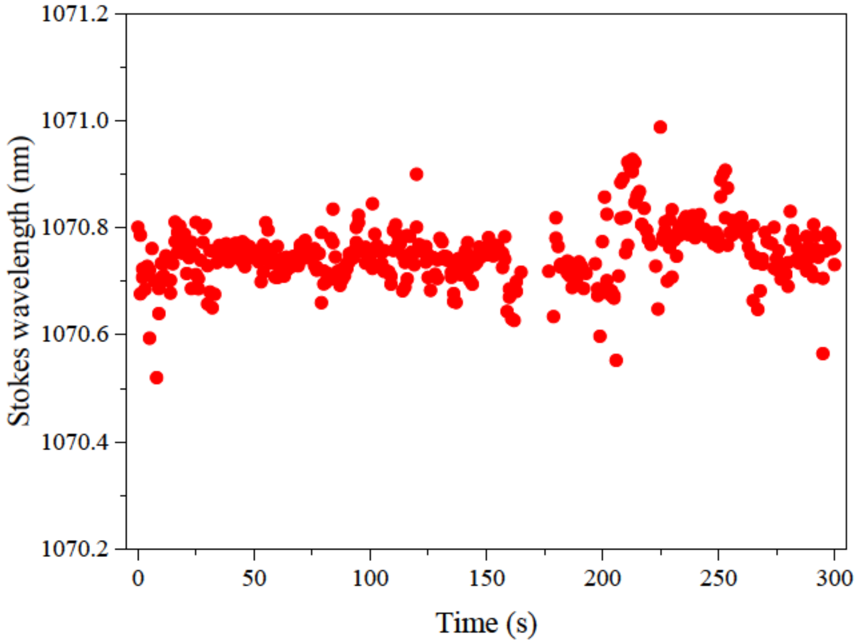


(a)

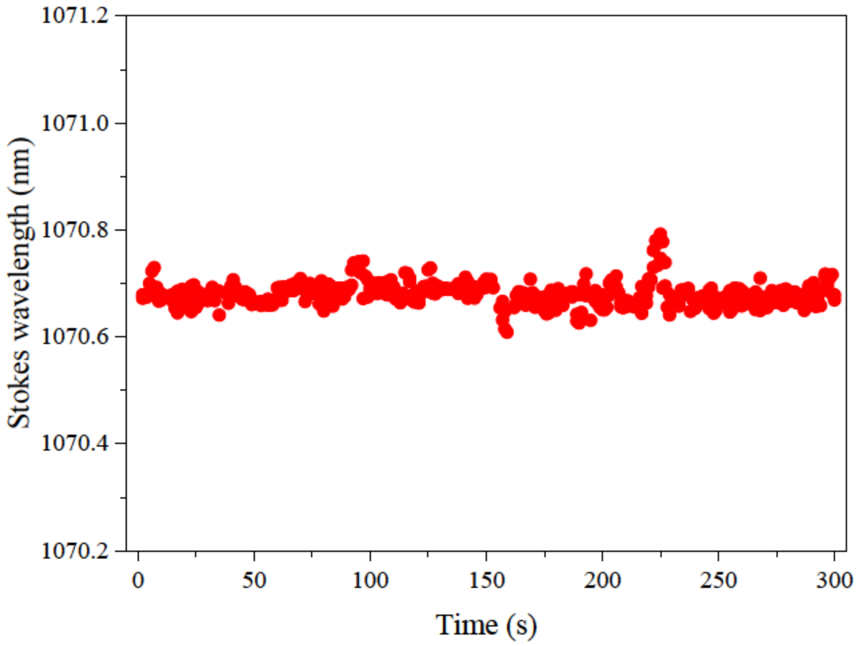


(b)

Figure 6.11: Stokes wavelength stability (a) without (b) with anti-vibration table.

the laser stability was improved by incorporating the anti-vibration table in Figure 6.10b, and 6.11b.

In the fundamental field, the wavelength fluctuated around ±0.25 nm without using anti-vibration table, however, it was improved to ±0.12 nm after using anti-vibration table.

Compared to the fundamental field, the stability of the Stokes field is better. The same observation is that the wavelength stability has been improved using the anti-vibration optical table. In this case, the simple change causes the Stokes wavelength fluctuated by only ± 0.03 nm, compared to ± 0.2 nm fluctuation with no anti-vibration, an order of magnitude improvement.

In summary, it is found that the laser stability has been improved by making effective use of an anti-vibration table, and perspex box, to minimise the influence of external factors. With these in place,the laser could operate stably for periods in excess of 5 minutes.

## 6.6 Analysis of spectral narrowing and improvements to power scaling

The linewidth of fundamental and Stokes fields has been substantially narrowed to a single longitudinal mode, with the insertion of high finesse etalon. No roll over in the THz power was observed and 1.5 times higher THz power was detected compared with the free running case under quasi-CW pumping. Under true, CW pumping, this etalon enabled sustained power scaling over a broad pump power range.

It is found that the THz output power continues to increase when the etalon was inserted into the cavity. The paper [175] shows that the effective area for Raman interaction and the effective Raman gain, impacts the Raman threshold and slope efficiency. The SPS process is similar to SRS process, so the interaction area in the CW intracavity laser was investigated along with phase mismatching, and the effects on THz output was studied in this section.

In the SPS process, phase matching is an essential requirement to satisfy, and the phase matching efficiency affects the overall output power of the system. Therefore, the phase matching efficiency was evaluated in this section. In the intracavity CW THz laser, the Stokes resonator will select the phase matching solution that experiences the highest SPS gain, and so narrowing of spectral output will be observed compared to the fundamental field. In the low gain limit, as the phase mismatch Δk builds up, SPS efficiency decreases roughly as

$$\eta = 4\sin^2(\frac{\vec{\Delta k} l}{2})/(\vec{\Delta k}^2 l^2) \tag{6.2}$$

where l is the interaction length of three waves and

$$\vec{\Delta k} = \vec{k_f} - \vec{k_S} - \vec{k_{THz}} \tag{6.3}$$

There is hence a range of frequencies, which do not perfectly to phase match. This range of frequencies lies within the phase matching bandwidth, which is over 1/2 bandwidth, defined as the overall gain bandwidth. In terms of phase matching bandwidth, its value of relate to the fundamental field. In this chapter, the fundamental linewidth can be narrowed from 102 GHz to 7 MHz ($1.4\times10^4$ times narrower). Phase matching contributes to this.

If the Stokes wave direction was taken as fixed by the Stokes resonator as shown in Figure 6.12, a phase mismatching occurs when, the fundamental wavelength changes slightly (as per its finite linewidth), generating Stokes and THz fields with slightly different wavelength.

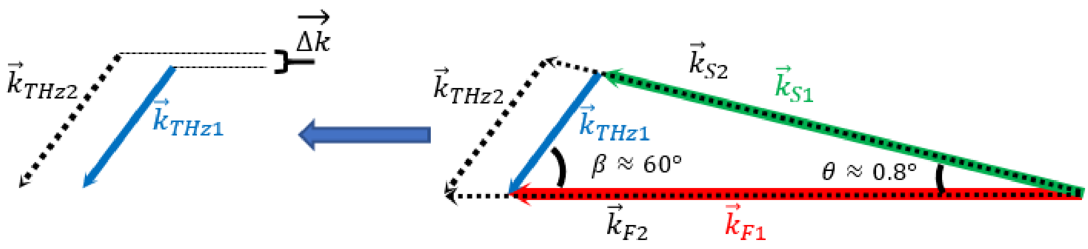


Figure 6.12: $\vec{k}$ vector diagram illustrating the origin of the phase mismatch that can build up in the non-collinear scheme when the Stokes angle is fixed by a resonant cavity. For a pair of fundamental wavelengths ($\vec{k_{F1}}$ and $\vec{k_{F2}}$), a corresponding pair of Stokes ($\vec{k_{S1}}$ and $\vec{k_{S2}}$) and THz fields ($\vec{k_{THz1}}$ and $\vec{k_{THz2}}$) are generated for a fixed angle $\theta$. We define the difference between the THz frequencies, $\vec{\Delta k}$.

The effect of phase mismatch induced by the finite linewidth of the fundamental field was analysed by taking the phase matching angle between fundamental and Stokes fields used in the experiment and then scanning through the Stokes - terahertz frequency pairs allowable by the conservation of energy, calculating the associated phase mismatch, given by

$$\vec{\Delta k} = \left|\vec{k_F} - \vec{k_S}\right| - \left|\vec{k_{THz}}\right| \tag{6.4}$$

This was then used to determine the decrease in SPS gain according to equation 6.2. The interaction length can be expressed by:

$$l = \frac{\omega_f}{\tan\theta} \tag{6.5}$$

where $\omega_f$ is the fundamental beam diameter and $\theta$ is the angle between the fundamental and Stokes waves.

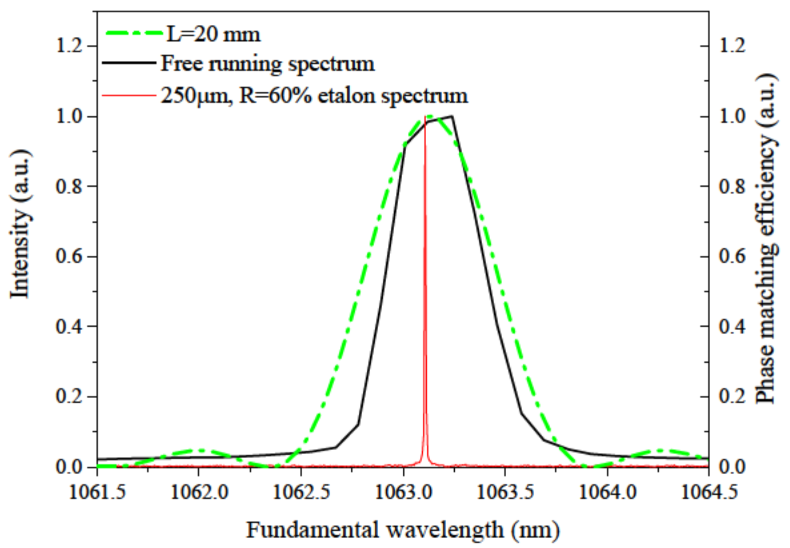


Figure 6.13: Phase matching in the fundamental field.

For the laser system described in this chapter, the phase matching angle is $\theta$=0.8°, and the fundamental beam diameter is $\omega_p$=600 $\mu$m (as stimulated in LASCAD), so the calculated interaction length based on equation 6.5 is $l = 42.96\ mm$. Considering the SPS crystal length of lithium niobate (20 mm) used in the experiment, the interaction length is limited by the length of SPS crystal, so the effective interaction length is the length of SPS crystal. Here, the interaction length was 20 mm in the analysis of SPS gain determined by the phase matching. The phase mismatch ($\vec{\Delta k}$) was determined for a range of wavelengths over the span 1061.5 nm-1064.5 nm, centred at 1063.1 nm. This was done through solution of the polariton dispersion curve and phase matching curves following the approach of Sussman [60].

Using equation 6.2, the phase matching efficiency is plotted in Figure 6.13 as a function of fundamental wavelength. This plot shows that wavelengths within a band of 0.75 nm, centred about 1063,1 nm will have phase matching efficiency of >50%.

The spectral bandwidth of the fundamental field when free-running, and with the 250 $\mu$m, R=60% etalon are shown overlayed on Figure 6.13. It is clear to see that the phase matching efficiency depends on the "effective" bandwidth of free running case and with etalon case. If the linewidth or bandwidth of fundamental field is narrow (single longitudinal mode operation), the whole linewidth falls into the range close to phase matching efficiency=1, meaning that it is well phase matched. In contrast, if the linewidth of the fundamental field is broader, the phase matching efficiency is distributed between 0-1.

The modelling shows that narrowing linewidth of the fundamental field gives rise to higher phase matching efficiency, and hence improved system efficiency as more photons in the fundamental field are converted to the THz field.

## 6.7 Conclusion

A CW THz laser with single longitudinal mode operation has been achieved through the use of a 250 $\mu$m thick, R=60% etalon in the fundamental cavity at normal incidence, forming a coupled cavity. The linewidth of the resultant fundamental field and Stokes fields are 70 MHz and 400 MHz, respectively. The THz linewidth is also narrowed because the control of the linewidths of two resonant optical waves by necessity, controls of the linewidth of the terahertz waves. This is because the highest THz frequency generated cannot exceed the largest difference between the fundamental and Stokes frequencies, and the lowest cannot be lower than the least difference. Therefore, limiting the linewidth of the fundamental and Stokes fields leads to a concomitant reduction in the THz linewidth.

In addition, it is highlighted that THz output power continues to increase and has the potential to generate more THz with the use of etalons. To better understand this, the impact of fundamental field linewidth on the phase matching efficiency was examined. It was found that broad linewidth fundamental fields suffer from phase mismatch and hence lower overall conversion across its entire width. Narrow linewidths (single frequency), however can experience perfect phase matching across their entire bandwidth. This is why we observe improved power scaling in laser which use intracavity etalons, and where linewidth narrowing has been observed.

The laser stability is quite challenging, especially when only one mode oscillated in the laser cavity. Mode competition and coupled cavity effects are main reasons to cause laser instability. Apart from the laser dynamics the physical consideration of laser and the environment can also not be ignored. An anti-vibration table was incorporated, along with a confinement box, and had significant improvements on laser stability. Mode hopping was reduced to a small range and the laser become less sensitive to air-flows and noise. Unfortunately, time constraints did not enable me to demonstrate this.

In conclusion, single longitudinal mode operation CW THz laser has been demonstrated with excellent THz output power. It is anticipated that such a narrow line, high power CW THz source, may be used for high resolution spectroscopy.

# 7

# Conclusion and future work

Narrow linewidth, continuous wave intracavity terahertz lasers via stimulated polariton scattering process have been developed in this thesis, sources which have the potential to contribute significantly in closing the "THz Gap". Continuous wave terahertz lasers based on the SPS technique are difficult to build because of the threshold of the SPS process. The beauty of the intracavity design is that it can achieve SPS threshold with low pump power requirements and makes it possible to achieve CW operation. Since Lee *et al.* demonstrated the first CW intracavity THz laser source in 2014, no further work has been reported in the field despite its great potential applications. Due to the immature development of CW SPS THz lasers, this thesis is heavily motivated by a keen desire to investigate the fundamental characteristics of CW SPS lasers and to exploit knowledge to achieve narrow linewidth CW THz laser sources with high power levels.

## 7.1 Improvements on laser performances of the intracavity CW SPS laser

Many challenges need to be overcome in order to improve the laser performance reported in [53]. Since the THz output power was only 2.3 $\mu$W, it still has potential to bring the THz output power to a higher level. Notably, distortion of the fundamental field was observed, possibly arising from pyroelectrically-induced photorefractive damage. The core technique to reach the SPS threshold is to keep very low resonator losses, so high resonator Q-factors were utilised for both the fundamental and Stokes resonators. Thermal problems often limit the performance of intracavity polariton lasers, and these effects are generally more severe in the CW regime. A new pumping scheme using polarised pumping at 879 nm has been implemented into the intracavity CW THz laser. The advantages of using this new pumping scheme are improved pump absorption efficiency up to 90% and reduced residual pump radiation (5 times lower) reaching the laser crystal and SPS crystal. These improvements resulting in higher THz power and better beam quality. Photorefractive effects in this system were greatly reduced through the use of this pumping scheme.

Significant enhancement of THz output power has been achieved, and 23.1 $\mu$W THz output power, an order of magnitude increase compared to the first CW polariton laser, the highest ever reported from a CW THz polariton source. Furthermore, through smart laser design, thermal effects within the system were managed, and the beam profiles of both fundamental and Stokes were shown to be Gaussian-like. This work detailed in Chapter 3 set a good starting point for the subsequent thesis work.

## 7.2 Application of intracavity etalons for THz linewidth narrowing

Etalons work in two ways depending on whether they are aligned to the cavity or not. In Chapter 4, the etalon was inserted with a tilted orientation ($\theta_{max}$) in the intracavity CW THz polariton laser, so the etalon acted as an intracavity band-pass filter. In Chapter 5, the etalon was inserted at normal incidence in the fundamental cavity, so coupled cavity effects were formed. The use of an etalon in two distinct ways, has been studied in depth, both theoretically and experimentally, in the context of a CW intracavity THz laser. In particular, deliberately aligning the etalon to the cavity to form a coupled cavity has been well understood in this thesis, with the assistance of theoretical simulations. Comparisons have been made, and some similarities and differences in the way these systems operated, were found.

### 7.2.1 Similarities

The common finding is no matter which way the etalons were used (as a band-pass filter, or to induce a coupled cavity), linewidth narrowing of both the fundamental and Stokes fields was observed. Only one etalon needs to be inserted in the fundamental resonator. The level of linewidth narrowing is dependent on the etalon properties (FSR, FWHM, finesse), the position of the etalon (tilted or not), and the laser gain. The higher finesse gives rise to narrower FWHM, and the thicker etalon gives broader FSR.

In the case of etalons as a tilted bandpass filter, the combination of high finesse and thickness have the most impact on the spectral properties of the laser. In the case where etalons are used at normal incidence to form a coupled cavity, the thickness of the etalon has the most impact.

The THz output power was found to increase if the linewidths of fundamental field is narrowed, in comparison to the "free-running" polariton laser under the same condition. This is an important experimental observation because it indicates that more of the fundamental field is converted to Stokes and THz photons. As discussed in Chapter 6, this was explained through an investigation of a phase mismatch with finite linewidth fundamental fields. Generally, a linear increase in output power is observed when the system is (as a function of input diode pump) effectively linewidth narrowed when using an etalon, whereas it rolls over when free-running.

Uncoated etalons, can work in both ways as a tilted band-pass filter, or to form a coupled cavity. The linewidth of the fundamental, Stokes fields could be narrowed, not to an extreme value. Using a 100 $\mu$m thick, uncoated etalon (A3), the CW polariton laser delivers the THz power of 13.7 $\mu$W at 9.5 W diode pump power, and the fundamental linewidth of

0.0068 nm, when the etalon used as bandpass filter. In the case of a coupled cavity configuration, the THz power of 4.5 $\mu$W has been obtained with the fundamental linewidth of 0.0116 nm and the Stokes linewidth of 0.009 nm at FWHM.

In the case of coated etalons, they can only be used at normal incidence due to the large walk-off losses, so that the laser cannot reach SPS threshold when it tilted. The benefit of using an etalon in this way is that the linewidth can be greatly reduced. When using the 100 $\mu$m, R=30% etalon (B6), which a resulting linewidth of 0.008 nm (close to the instrument limit) both in the fundamental and Stokes fields were observed. Linewidth can be further narrowed by selecting the 250 $\mu$m thick, R=60% etalon to form a coupled cavity, and single longitudinal mode could be achieved.

### 7.2.2 Differences

Examining the results achieved in Chapter 4 and 5, it is clear that not all the etalons give rise to excellent performance in the CW THz laser, and this is associated with the etalon properties, discussed in Section 4.3. The quality of the etalon is also quite important because it associates with losses which can stop reaching SPS threshold in the CW polariton laser. Different from the pulsed THz laser system, the losses in the CW system are far more critical.

It is found that the laser can reach SPS threshold for all examined etalons when inserted at normal incidence, (presented in Chapter 5). However, only uncoated etalons (A3) and (A4) can be used as an intracavity band-pass filter in Chapter 4, with the laser reaching SPS threshold. The reasons behind these observations are due to the losses induced by the etalon in these two ways. If the losses induced by the etalon, plus the general cavity round trip losses are greater than the SPS gain, the laser cannot reach the THz laser threshold. Therefore, the important finding is that the losses induced by etalon itself in the CW THz laser are critical to understanding if the laser can work or not. It is noted that all the etalons used in Chapter 4 are the same as that of in Chapter 5, assuming that the fixed insertion losses are the same. When an etalon is used as an intracavity bandpass filter, walk-off losses are unavoidable because the etalon is inserted at an angle, this dictating the band-pass filter characteristics. The analysis of walk-off losses is described in detail in Section 4.3.2, and walk-off losses are calculated.

Meanwhile, when the etalon is used to form a coupled cavity, there are no walk-off losses involved because the etalon is inserted at normal incidence. Instead of inducing walk-off losses, the etalon together with the output coupler in the fundamental field forms three mirror cavities, and this effect impacts on the laser output through the generation of multiple closely - spaced transmission features. The total reflectivity has been calculated and analysed as a function of wavelength with the wavelength response in Chapters 5. In chapter 4 and 5, the laser performance has been fully investigated using a 100 $\mu$m thick, uncoated etalon (A3). It indicates that the laser performance has been improved using the 100 $\mu$m uncoated etalon (A3) no matter which method of application. However, for the 100 $\mu$m, R=30% etalon (B6), it only works in a coupled cavity regime. The losses induced by the method of application, for these different etalons are compared in Table 7.1.

Table 7.1: Summary of losses induced by etalon (excluded fixed losses) in two ways (a) bandpass filter (b) coupled cavity effect

| Etalon type | losses induced in (a) | losses induced in (b) |
|---|---|---|
| 100 $\mu$m, uncoated etalon (A3) | 0.1% | 0.1% |
| 100 $\mu$m, R=30% etalon (B6) | 1.25% | 0.16% |
| 250 $\mu$m, R=60% etalon (C9) | 23.67% | 0.35% |

For the 100 $\mu$m, uncoated etalon (A3), the losses induced by the etalon are quite low, only 0.1% in both ways. The losses are low enough to tolerate, so the laser easily reaches SPS threshold. Notably, the fundamental spectrum is broader when the etalon is used tilted, because the longitudinal modes are only influenced by a single pass-band by one etalon. In contrast, when the etalon forms a coupled cavity, the spectral response is influenced by multiple, narrow resonances.

For a coated etalon, the walk-off losses are greater than the losses caused by coupled cavity effects, so only when using such an etalon at normal incidence, can the laser reach SPS threshold. For the 100 $\mu$m, R=30% etalon (B6), the losses induced by the etalon in two ways are 1.25% and 0.16%, respectively. This effect of walk-off loss is even more apparent in the case of etalon C9.

## 7.3 Single longitudinal mode operation

Taking advantage of a coupled cavity configuration formed by deliberately inserting an etalon at normal incidence, single longitudinal mode operation both in the fundamental and Stokes fields has been successfully achieved using a high finesse etalon "C9". The THz linewidth has been estimated to be less than 400 MHz, based on the measured fundamental and Stokes linewidth of 70 MHz and 400 MHz, respectively. A maximum THz power of 18.2 $\mu$W at 1.99 THz with the diode pump power of 7.3 W has been detected in this system. The observation of continuing increase in THz power was more prominent under this single longitudinal mode operation.

The question as to why the output power of the THz laser improved when an etalon was used, has been well explained with the investigation of phase mismatch in the SPS process. This study shows that the phase matching efficiency approaches 1 (perfect phase matching) when the fundamental linewidth is single longitudinal mode. On the country, if the linewidth of the fundamental field is broader, the phase matching efficiency is distributed in the range of 0-1, and the actual maximum phase matching efficiency value determined by fundamental linewidth. In the "Free-running" laser, the overall fundamental bandwidth is 1.5 nm, but only half of the entire bandwidth falls into phase matching efficiency over 50%.

The techniques used for narrowing the THz wave output by restricting the fundamental and Stokes linewidths proved successful, and has led to single longitudinal mode operation. The significant linewidth narrowing of CW intracavity SPS sources has also led to excellent THz power levels which can be used for high resolution spectroscopy.

## 7.4 Summary

In summary, this thesis consists of two key parts: the first is improvement to laser performance of CW intracavity SPS laser. Here, an order of magnitude increase in THz output power has been achieved from this source design. The second part details the achievement of narrow linewidth, high output power from CW SPS lasers, with most emphasis on the use of etalons in two ways.

Ultimately, the etalons have been proven to work in two ways in the CW THz laser; either as a band-pass filter or to form a coupled cavity. Both ways can achieve the goal of linewidth narrowing.

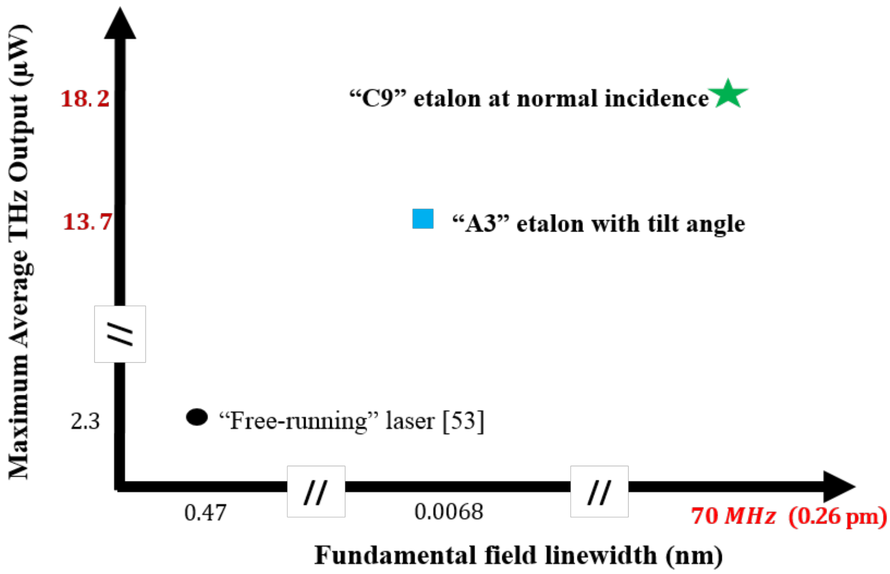


Figure 7.1: Summary of the THz power and the fundamental field linewidth using an etalon as (a) band-pass filter (blue square) (b) in a coupled cavity (green star). (Data from the "free-running" laser prior to this PhD candidature is presented in black [53].)

The significant linewidth narrowing of CW intracavity SPS sources resulting from this project is summarised in Figure 7.1. The figure shows the key results in terms of the maximum THz power and the corresponding fundamental linewidth when the best etalons are used in the two distinct ways.

It is hoped that the development of the narrow linewidth, frequency tunable, continuous wave, intracavity, polariton lasers, that has been presented in this thesis holds high potential for applications in areas like imaging, telecommunications or high-resolution spectroscopy, and contributes substantially to understand, and closing the "THz Gap".

## 7.5 Future work

While extensive investigations have been carried out in this thesis both experimentally and theoretically, there remains scope for future work in several areas. The results of this thesis directly impacts the design and operation of narrow linewidth, CW intracavity SPS laser technology. Many of the outcomes indicate interesting directions for further study, and opportunities include.

### 7.5.1 Selecting the optimal etalon

Further work is also merited on narrowing the linewidth in CW intracavity THz lasers. The use of etalon in two ways has been proven an effective method. However, the etalons used in this thesis may not be optimal. The modelling for coupled cavity effects in Chapter 5.4 provides guidance on how to design cavity configurations using etalons, regarding to the etalon position, thickness and coating. It would be useful to try a very high quality etalon with a sufficiently large free spectral range and reasonable finesse. A 300 $\mu$m thick YAG etalon coated to 30% reflectivity would likely be suitable.

It is difficult to draw conclusion whether it would be better to place a high finesse etalon only in the fundamental cavity or to put two low finesse etalons in the fundamental and Stokes cavities separately. This would be a worthy area of study.

### 7.5.2 Frequency stability

The CW intracavity THz laser with single longitudinal mode operation in this thesis suffered from mode competition between adjacent modes in the laser cavity, leading to frequency instability. The laser instability is undesirable for many applications. Several reasons for this instability has been preliminaryly discussed in Section 6.5.2. An anti-vibration optical table has been implemented in the system, and this helps reduce the vibrations from the physical environment to make laser stable in a short time. However, it can not grantee the long-time operation. In order to improve the laser stability, further understanding the reasons may benefit to solve this problem. Stabilisation techniques such as Hänsch-Couillaud technique is an option which may provide the necessary stability, particularly when operating single longitudinal mode.

### 7.5.3 THz linewidth measurement

A consequence of the instability of the THz sources in this thesis, is that the THz linewidth could not be directly measured. Therefore, measuring the THz linewidth directly will be ongoing work. The THz linewidth can be measured directly, in a number of ways including utilising a THz F-P interferometer, or through measuring water vapour spectral features. This work is interesting as it gives a way of quantifying how narrow the linewidth of the CW THz source is. In addition, this approach may also demonstrate that the CW THz source is able to resolve the narrowest water absorption feature in the THz frequency range. Precise tracking the frequency of the CW source will be the key consideration. Here, accurate control may be achieved through the use of high-prescision rotation stages. Once this has been accomplished the construction of a THz spectrometer would then allow a critical comparison of this method with that of THz-TDS and FTIR techniques.

### 7.5.4 Understanding the theoretical factors that affect the linewidth of the THz laser

In general, beyond this thesis work, the study of CW intracavity polariton lasers is immature, so there is scope for future work in several areas. The theoretical factors that affect the linewidth are not particularly well understood for SPS systems. Obvious comparison can be drawn from Raman and OPO systems to interpret our observations and measurements. These will give us some insight into the process within an SPS system because this system can be thought of as a combination of both SRS and OPO processes. What is happening within our systems is not fully understood. The dynamics of the CW SPS system would be worth to investigating.

### 7.5.5 Developing CW SPS sources with novel design

In the pulsed regime, the surface-emitted configuration has been applied to the SPS laser as a technique to avoid the intrinsic limitations of the linear geometry. And the design of using a fundamental wavelength of 1342 nm to completely avoid the negative effect of free-carrier generation within silicon prisms was demonstrated, enhancing terahertz wave extraction. It would be useful to transfer these strategies into the CW SPS system, improving the power scaling.

# A

# An Appendix

## A.1 Early work on CW THz lasers based on intracavity SPS by this research group at Macquarie University.

Paper by Andrew Lee and Helen Pask. "Continuous wave, frequency-tunable terahertz laser radiation generated via stimulated polariton scattering." Optics Letters 39(3), 442 (2014).

The work reported in this paper was completed at Macquarie University prior to the starting of this research project, but it is a very important for the work studied during this PhD research and for this reason is related in this thesis.

**Pages 166-169 of this thesis have been removed as they contain published material under copyright. Removed contents published as:**

Lee, A. J., & Pask, H. M. (2014) Continuous wave, frequency-tunable terahertz laser radiation generated via stimulated polariton scattering, *Optics Letters*, Vol. 39, no.3, pp. 442-445. https://doi.org/10.1364/OL.39.000442

## A.2 Summary of Mirror coatings

The transmission spectra for the laser mirrors which used in the fundamental and Stokes cavities are attached. The mirror specifications are presented in Section 2.1.2.

Fundamental resonator end mirror M2

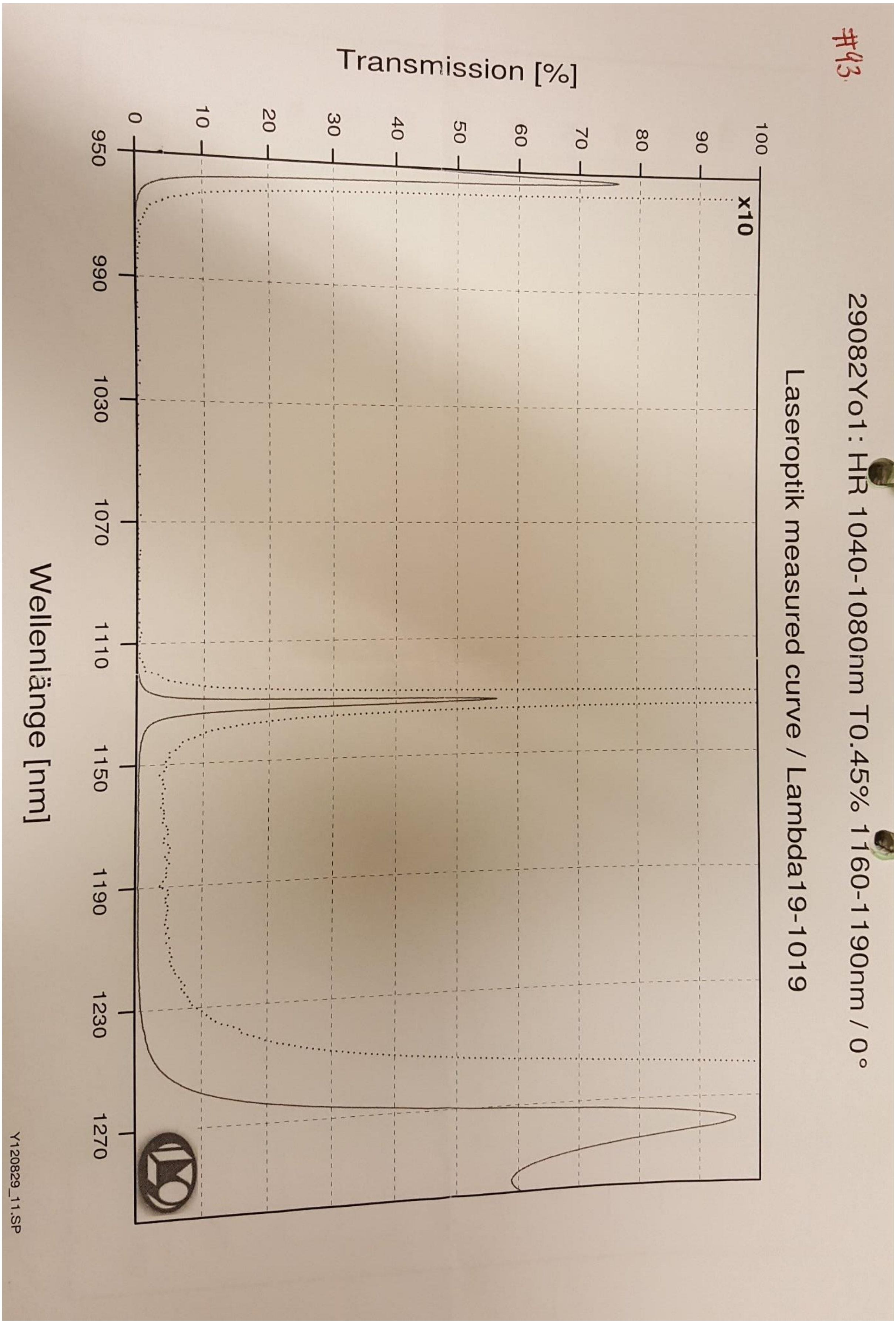

LiNbO3 AR coatings

CASTECH®

**CASTECH INC.**
Leading Manufacturer of Crystals and Optics for Laser Applications

## Coating Inspection Report

**P/N:**

**Batch Number:** I2168-2

**Description:**

Product Name:

Dimension: 5x5x25mm³

Coating: S1,S2:AR-(1064-1085)nm.

**Coating Lot**: S1:07V-111118-01,S2:07V-111118-02;

**Quantity**: 2pcs.

**Product No.:** 0-77532 -0001、0003

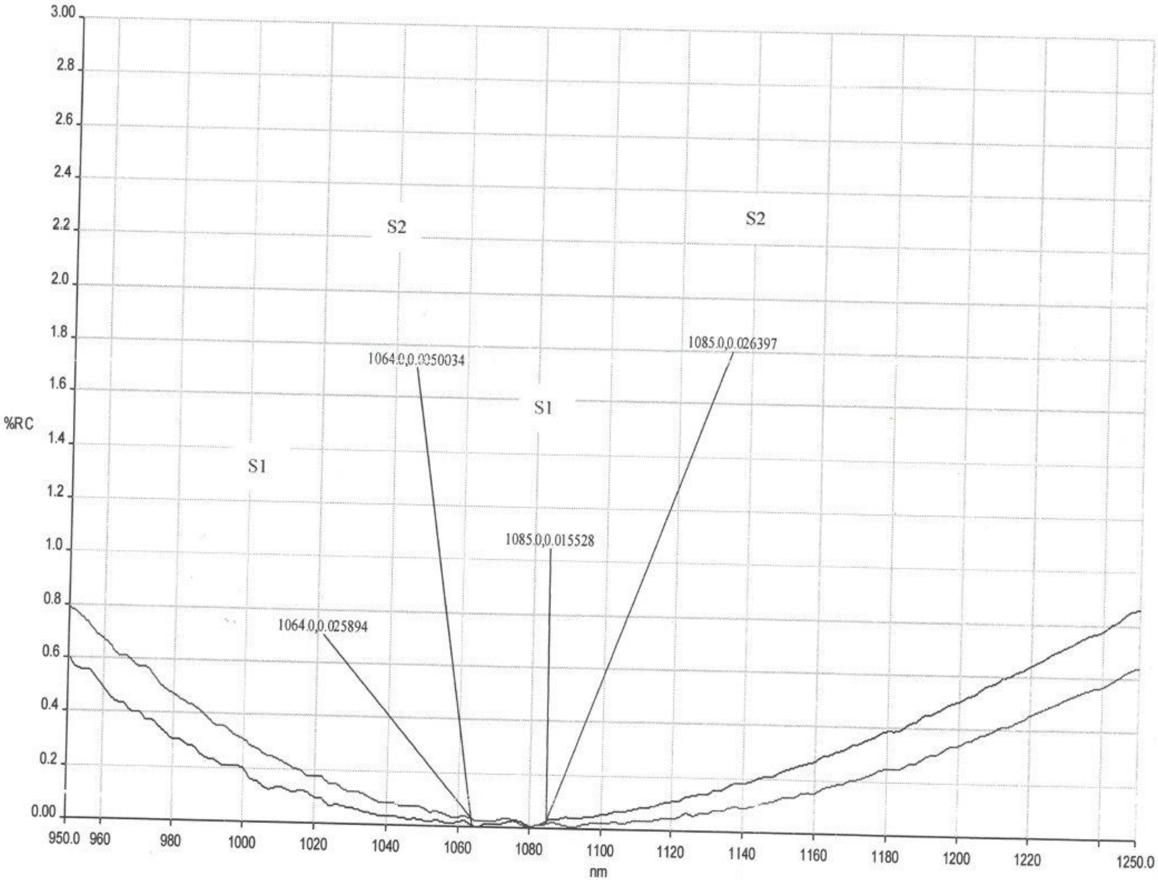


Reflection Curve

**Operator**: *Fang Wang*

**Date:** 24 November 2011

**Approved by:** Xiuli Fang

**Date:** 24 November 2011


Add:155 Yangqiao West Road, Fuzhou Fujian 350002,P.R.China.
Fax:+86-591-83711593
E-mail:sales@castech.com
Tel:+86-591-83710533
Http://www.castech.com

Nd:GdVO4 crystal coating M1

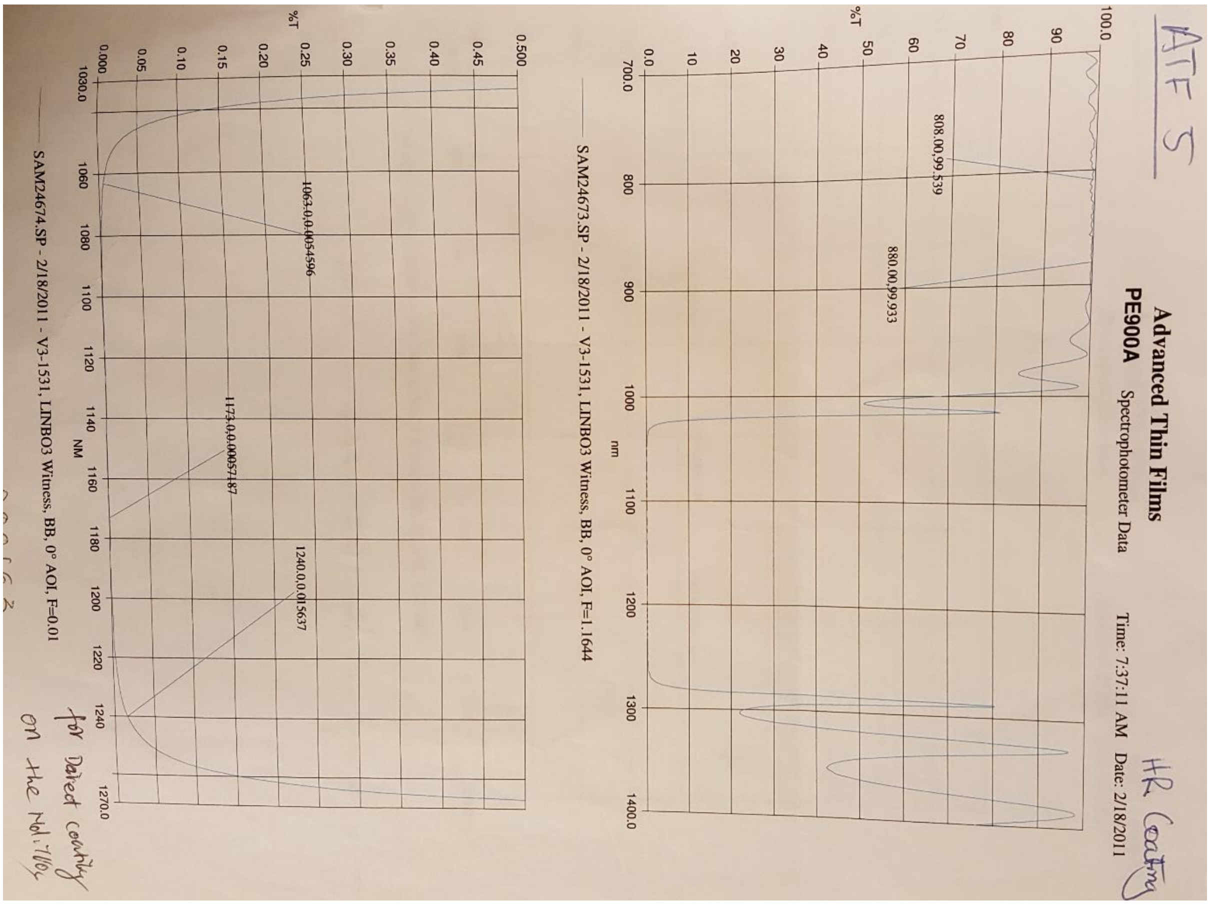


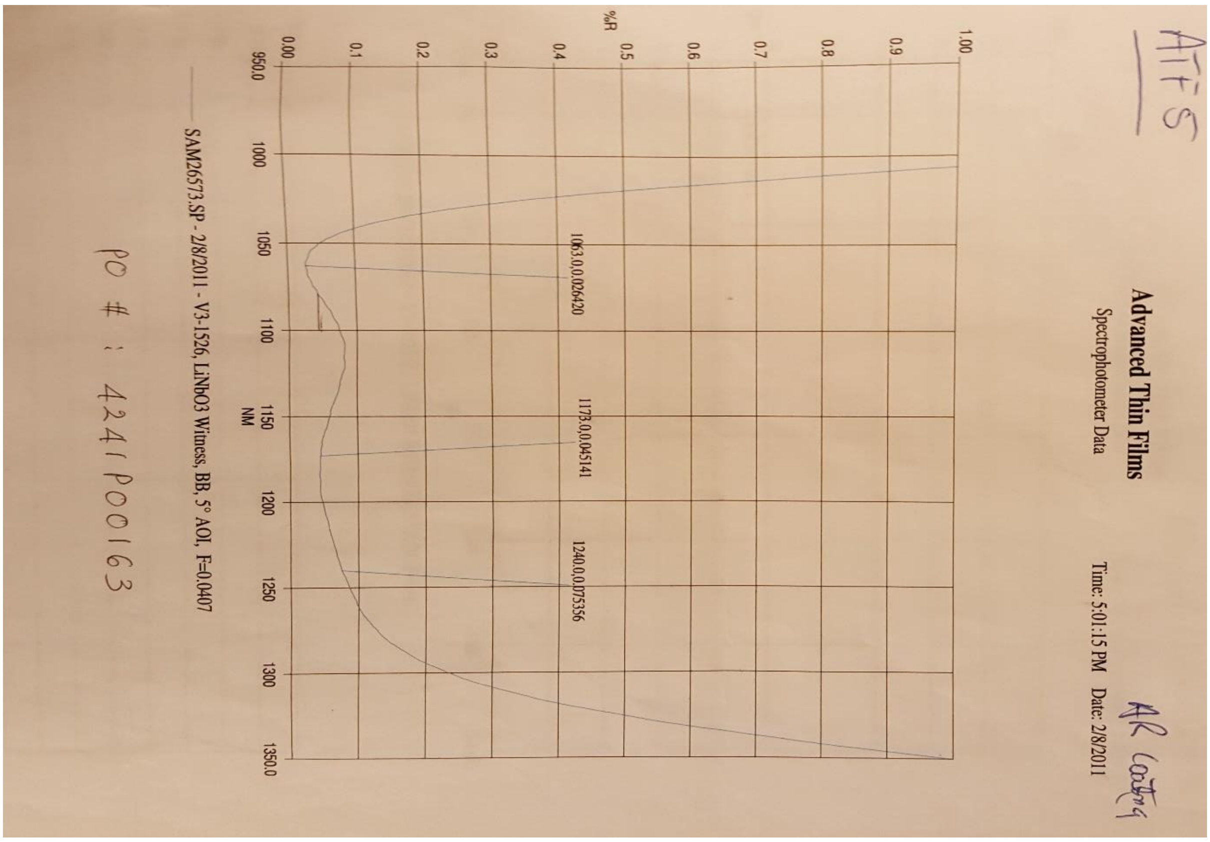

Stokes cavity mirror M3

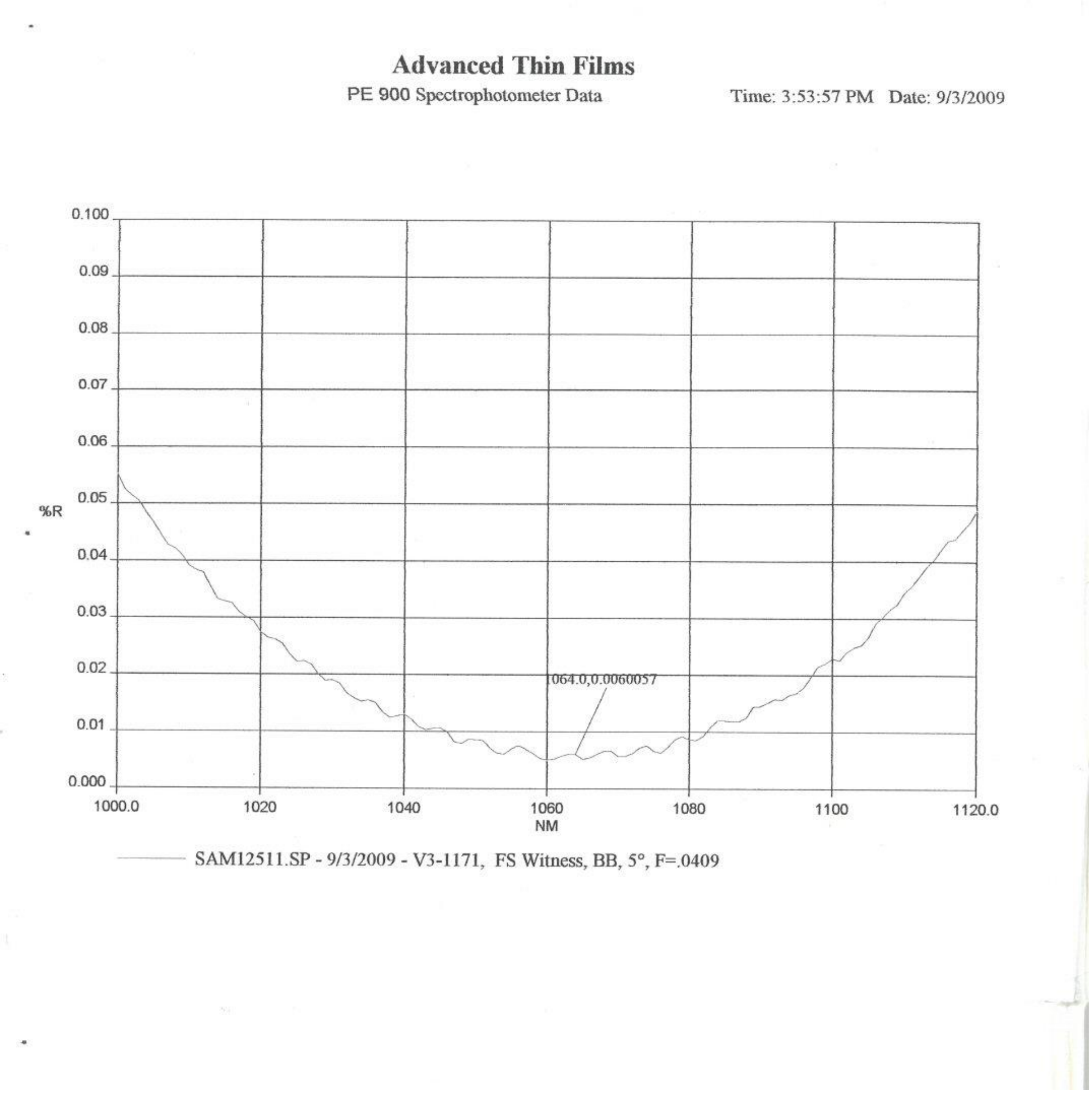

Stokes cavity mirror M4

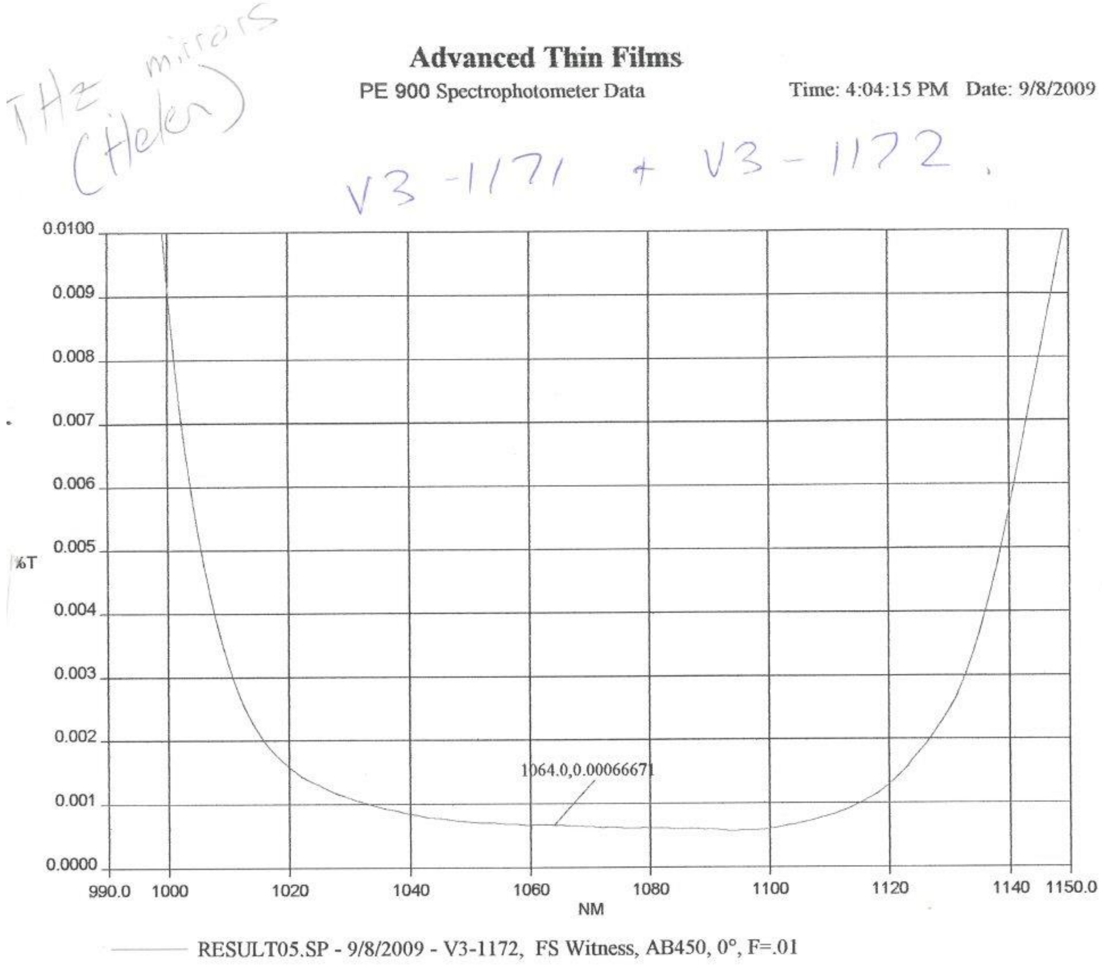

## A.3 Summary of etalon specifications

The specifications for the etalons used in this thesis are attached. The detail of etalons are summarised in Table 2.4.

**LightMachinery**

# *Test Report*

Customer: Macquarie University
Customer P.O.: 4241P00736
Work Order: 76760, 79873, 70790, 72156 — Sales Order: 63614
Part No.: OP-3167-50 , -100, -250, -500 — Serial No.: [various]

Part **OP-3167-50**: YAG Etalon, 5mm diameter, thickness 50um

| (WO #76760) S/N: | Target | #3 | #4 |
|---|---|---|---|
| Thickness variation (nm): | <60 | 24 | 23 |
| Thickness (µm): | 50±2.5 | 50.1 | 50.1 |

Part **OP-3167-100**: YAG Etalon, 5mm diameter, thickness 100um

| (WO #79873) S/N: | Target | #4.1 | #5.1 |
|---|---|---|---|
| Thickness variation (nm): | <60 | 5 | 6 |
| Thickness (µm): | 100±2.5 | 100.8 | 100.8 |

Part **OP-3167-250**: YAG Etalon, 5mm diameter, thickness 250um

| (WO #70790) S/N: | Target | #4 |
|---|---|---|
| Thickness variation (nm): | <60 | 13 |
| Thickness (µm): | 250±2.5 | 251.6 |

Part **OP-3167-500**: YAG Etalon, 5mm diameter, thickness 500um

| (WO #72156) S/N: | Target | #6 |
|---|---|---|
| Thickness variation (nm): | <60 | 16 |
| Thickness (µm): | 500±2.5 | 498.8 |

Notes:

- Thickness data was measured at 1.55 µm. A map of thickness variation over the clear aperture is attached.

Reviewed by:
2015 December 4

LightMachinery Inc.
80 Colonnade Rd., Nepean, Ontario
K2E 7L2 Canada

Tel: (613) 749-4895
Fax: (613) 749-8179
www.lightmachinery.com

Etalon Thickness Report, LightMachinery Inc. 2015.07.24 10:03:15 AM
Measurement Program: SW-3583 ver.13.exe (2015.06.01 1:12:50 PM) on EQ-1861
Material: YAG. Work Order: WO76760 YAG pc3 Decontacted - 2, 4mm 25.0℃, w1=1100, slow
Thickness (micron): Average: 50.1052 Min: 50.0900 Max: 50.1139 Variation: 0.0239 Standard RMS: 0.005349
Grid size: 16X16. Step size: 0.25 mm. Center position: X= 70.7 mm, Y= 29.7 mm
Temperature Compensation: Relative. Reference thickness variation: +0.10 nm. Measurement time= 25:39
Power= -8.4 nm. Radius= -237.1 m. Wedge= 0° 0' 0.941" [-117°]

Thickness Variation (nm) from Minimum (50.0900 um):

| | | | | | | | | | | | | | | | |
|---|---|---|---|---|---|---|---|---|---|---|---|---|---|---|---|
| - | - | - | - | - | 3 | 4 | 4 | 5 | 3 | 1 | - | - | - | - | - |
| - | - | - | 6 | 7 | 7 | 7 | 8 | 9 | 8 | 6 | 4 | 0 | - | - | - |
| - | - | 9 | 10 | 11 | 10 | 10 | 11 | 11 | 10 | 9 | 7 | 5 | 1 | - | - |
| - | 10 | 12 | 13 | 13 | 12 | 12 | 12 | 12 | 12 | 11 | 10 | 8 | 5 | 1 | - |
| - | 13 | 14 | 15 | 15 | 15 | 14 | 14 | 14 | 14 | 13 | 12 | 10 | 8 | 4 | - |
| 13 | 15 | 16 | 17 | 17 | 16 | 15 | 16 | 16 | 15 | 15 | 14 | 12 | 9 | 7 | 4 |
| 15 | 16 | 17 | 17 | 18 | 17 | 17 | 18 | 18 | 16 | 16 | 14 | 13 | 11 | 9 | 6 |
| 16 | 17 | 18 | 18 | 18 | 18 | 18 | 20 | 19 | 17 | 16 | 15 | 13 | 12 | 11 | 8 |
| 17 | 17 | 19 | 19 | 19 | 19 | 19 | 20 | 18 | 17 | 17 | 16 | 14 | 13 | 12 | 9 |
| 17 | 19 | 20 | 20 | 20 | 22 | 21 | 21 | 21 | 19 | 19 | 17 | 15 | 14 | 12 | 9 |
| 18 | 19 | 20 | 20 | 21 | 23 | 22 | 22 | 22 | 22 | 20 | 19 | 16 | 14 | 12 | 9 |
| - | 19 | 20 | 20 | 20 | 22 | 21 | 21 | 24 | 22 | 19 | 19 | 16 | 14 | 12 | - |
| - | 18 | 20 | 21 | 21 | 21 | 22 | 23 | 24 | 22 | 20 | 18 | 16 | 15 | 12 | - |
| - | - | 19 | 21 | 21 | 22 | 22 | 22 | 23 | 21 | 20 | 18 | 17 | 14 | - | - |
| - | - | - | 19 | 21 | 21 | 21 | 21 | 20 | 19 | 18 | 18 | 17 | - | - | - |
| - | - | - | - | - | 19 | 19 | 20 | 19 | 19 | 18 | - | - | - | - | - |

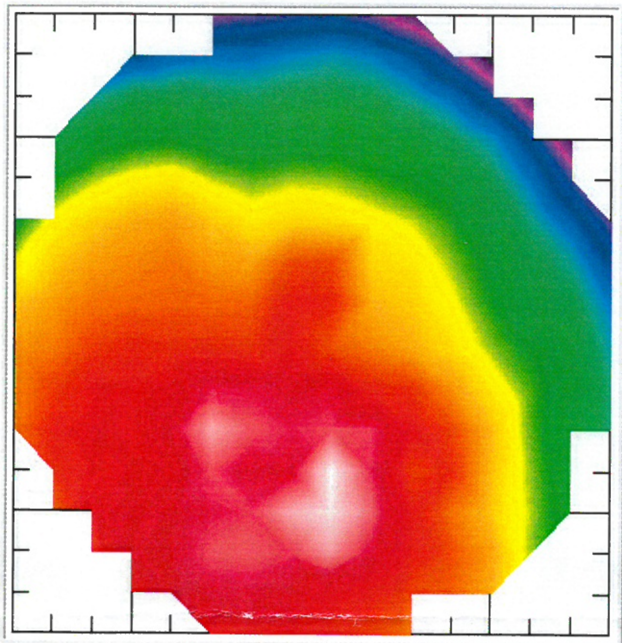

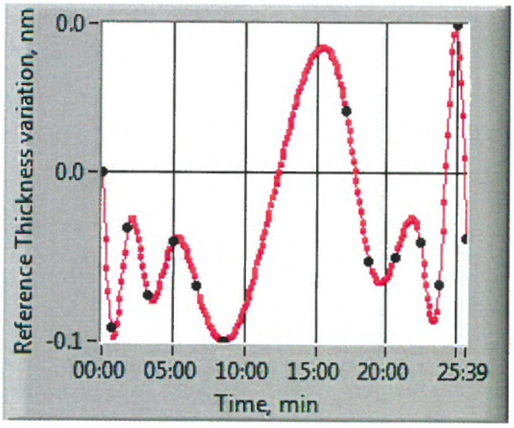


Mapping data loaded from: W:\WO76760\YAG pc3 Decontacted - 2, 4mm.txt

Etalon Thickness Report, LightMachinery Inc. 7/15/2015 1:38:05 PM
Measurement Program: SW-3583 ver.13.exe (6/15/2015 10:48:46 AM) on EQ-1861
Material: YAG. Work Order: WO72156 YAG pc6 Decontacted - 1, 3mm 24.8℃
Thickness (micron): Average: 498.8482 Min: 498.8385 Max: 498.8543 Variation: 0.0158 Standard RMS: 0.004154
Grid size: 12X12. Step size: 0.25 mm. Center position: X= 154.0 mm, Y= 30.2 mm
Temperature Compensation: Relative. Reference thickness variation: -0.05 nm. Measurement time= 12:36
Power= -8.8 nm. Radius= -128.1 m. Wedge= 0° 0' 0.889" [-142°]

Thickness Variation (nm) from Minimum (498.8385 um):

| | | | | | | | | | | | |
|---|---|---|---|---|---|---|---|---|---|---|---|
| – | – | – | – | 3 | 2 | 1 | 0 | – | – | – | – |
| – | – | 7 | 7 | 6 | 5 | 4 | 3 | 2 | 0 | – | – |
| – | 9 | 10 | 10 | 9 | 8 | 7 | 6 | 4 | 3 | 1 | – |
| – | 11 | 12 | 12 | 12 | 11 | 10 | 8 | 7 | 5 | 3 | – |
| 11 | 12 | 13 | 14 | 15 | 14 | 12 | 10 | 8 | 6 | 4 | 2 |
| 12 | 13 | 14 | 15 | 16 | 15 | 14 | 12 | 10 | 7 | 5 | 3 |
| 12 | 13 | 14 | 15 | 16 | 15 | 14 | 12 | 10 | 8 | 6 | 3 |
| 11 | 13 | 14 | 14 | 15 | 15 | 14 | 13 | 11 | 8 | 6 | 3 |
| – | 12 | 13 | 14 | 14 | 14 | 14 | 13 | 11 | 8 | 6 | – |
| – | 11 | 12 | 13 | 13 | 13 | 13 | 12 | 10 | 8 | 5 | – |
| – | – | 11 | 12 | 12 | 12 | 12 | 11 | 9 | 6 | – | – |
| – | – | – | – | 11 | 10 | 10 | 9 | – | – | – | – |

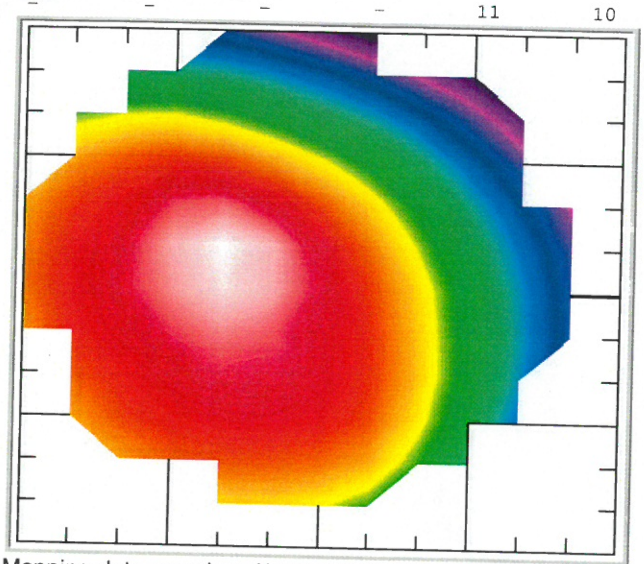

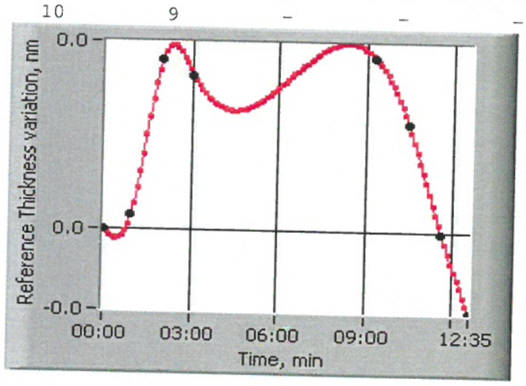


Mapping data saved at: W:\WO72156\YAG pc6 Decontacted - 1, 3mm.txt

Etalon Thickness Report, LightMachinery Inc. 2015.07.24 2:12:37 PM
Measurement Program: SW-3583 ver.13.exe (2015.06.01 1:12:50 PM) on EQ-1861
Material: YAG. Work Order: WO76760 YAG pc4 Decontacted - 3, 4mm 25.0℃, w1=1100, slow
Thickness (micron): Average: 50.1050 Min: 50.0896 Max: 50.1127 Variation: 0.0231 Standard RMS: 0.005297
Grid size: 16X16. Step size: 0.25 mm. Center position: X= 61.0 mm, Y= 29.7 mm
Temperature Compensation: Relative. Reference thickness variation: +0.05 nm. Measurement time= 25:48
Power= -6.7 nm. Radius= -296.4 m. Wedge= 0° 0' 0.973" [8°]

Thickness Variation (nm) from Minimum (50.0896 um):

| | | | | | | | | | | | | | | | |
|---|---|---|---|---|---|---|---|---|---|---|---|---|---|---|---|
| - | - | - | - | - | 10 | 12 | 13 | 14 | 14 | 15 | - | - | - | - | - |
| - | - | - | 8 | 10 | 12 | 14 | 15 | 16 | 16 | 17 | 18 | 19 | - | - | - |
| - | - | 6 | 10 | 12 | 13 | 14 | 16 | 18 | 18 | 19 | 20 | 21 | 21 | - | - |
| - | 4 | 8 | 10 | 12 | 14 | 15 | 17 | 19 | 20 | 21 | 21 | 22 | 23 | 22 | - |
| - | 6 | 9 | 11 | 13 | 15 | 16 | 17 | 18 | 20 | 22 | 23 | 23 | 23 | 23 | - |
| 3 | 7 | 10 | 12 | 14 | 15 | 16 | 17 | 18 | 20 | 22 | 23 | 23 | 23 | 22 | 21 |
| 4 | 8 | 11 | 13 | 15 | 16 | 17 | 17 | 18 | 19 | 21 | 22 | 22 | 22 | 22 | 21 |
| 3 | 8 | 11 | 13 | 15 | 16 | 17 | 17 | 18 | 19 | 21 | 21 | 22 | 22 | 21 | 20 |
| 2 | 8 | 11 | 13 | 14 | 15 | 16 | 17 | 18 | 19 | 20 | 21 | 22 | 22 | 21 | 20 |
| 1 | 7 | 9 | 12 | 14 | 15 | 16 | 17 | 17 | 18 | 19 | 21 | 22 | 22 | 21 | 20 |
| 0 | 6 | 9 | 11 | 14 | 15 | 16 | 16 | 17 | 18 | 19 | 20 | 21 | 22 | 21 | 19 |
| - | 4 | 8 | 11 | 13 | 14 | 15 | 16 | 17 | 18 | 19 | 20 | 20 | 21 | 20 | - |
| - | 1 | 7 | 10 | 12 | 13 | 14 | 15 | 16 | 18 | 19 | 19 | 20 | 20 | 18 | - |
| - | - | 4 | 8 | 10 | 11 | 13 | 14 | 16 | 17 | 18 | 19 | 19 | 18 | - | - |
| - | - | - | 4 | 8 | 10 | 11 | 13 | 15 | 16 | 17 | 17 | 17 | - | - | - |
| - | - | - | - | - | 6 | 9 | 11 | 13 | 14 | 15 | - | - | - | - | - |

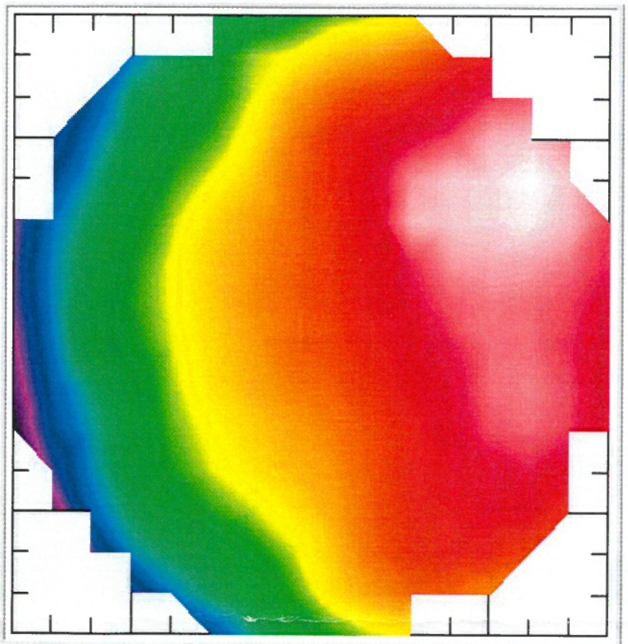

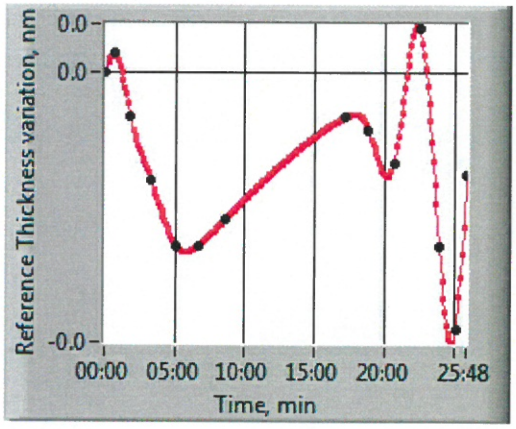


Mapping data loaded from: W:\WO76760\YAG pc4 Decontacted - 3, 4mm.txt

Etalon Thickness Report, LightMachinery Inc. 5/1/2015 10:05:31 AM
Measurement Program: SW-3583 ver.13.exe (3/10/2015 3:36:59 PM) on EQ-1861
Material: YAG. Work Order: WO79873 YAG pc4.1 Edged - 1, 3mm 22.8℃, w1=300, slow
Thickness (micron): Average: 100.8058 Min: 100.8032 Max: 100.8084 Variation: 0.0052 Standard RMS: 0.001415
Grid size: 12X12. Step size: 0.25 mm. Center position: X= 154.5 mm, Y= 29.8 mm
Temperature Compensation: Relative. Reference thickness variation: +0.26 nm. Measurement time= 13:19
Power= 0.0 nm. Radius= -130433.7 m. Wedge= 0° 0' 0.387" [-80°]

Thickness Variation (nm) from Minimum (100.8032 um):

| | | | | | | | | | | | |
|---|---|---|---|---|---|---|---|---|---|---|---|
| – | – | – | – | 0 | 0 | 0 | 0 | – | – | – | – |
| – | – | 0 | 1 | 0 | 0 | 1 | 1 | 1 | 1 | – | – |
| – | 1 | 1 | 1 | 1 | 1 | 1 | 1 | 1 | 1 | 1 | – |
| – | 1 | 1 | 1 | 1 | 1 | 1 | 1 | 1 | 1 | 2 | – |
| 1 | 2 | 2 | 2 | 2 | 2 | 2 | 2 | 2 | 2 | 2 | 2 |
| 2 | 2 | 2 | 2 | 2 | 2 | 2 | 2 | 2 | 3 | 3 | 3 |
| 2 | 2 | 3 | 3 | 3 | 3 | 3 | 3 | 3 | 3 | 4 | 3 |
| 3 | 3 | 3 | 3 | 3 | 3 | 3 | 3 | 4 | 4 | 4 | 4 |
| – | 4 | 4 | 4 | 4 | 4 | 4 | 4 | 4 | 4 | 4 | – |
| – | 4 | 4 | 4 | 4 | 4 | 4 | 4 | 5 | 5 | 4 | – |
| – | – | 4 | 4 | 4 | 4 | 5 | 5 | 5 | 5 | – | – |
| – | – | – | – | 5 | 5 | 5 | 5 | – | – | – | – |

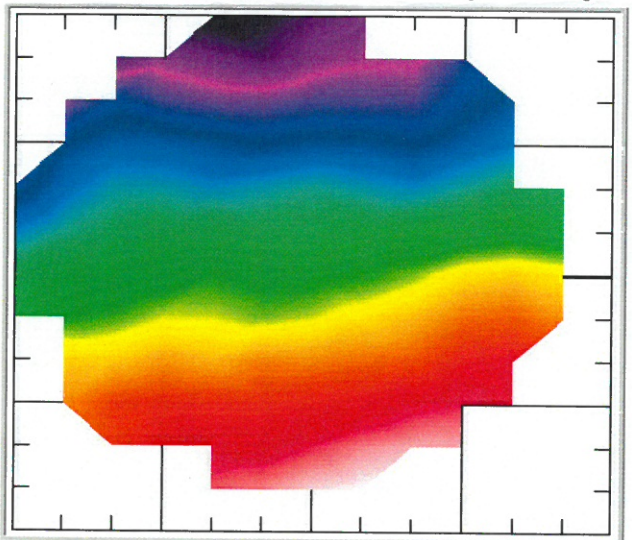

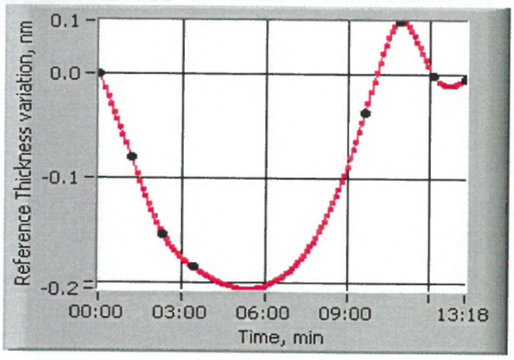


Mapping data saved at: W:\WO79873\YAG pc4.1 Edged - 1, 3mm.txt

Etalon Thickness Report, LightMachinery Inc. 5/1/2015 10:47:18 AM
Measurement Program: SW-3583 ver.13.exe (3/10/2015 3:36:59 PM) on EQ-1861
Material: YAG. Work Order: WO79873 YAG pc5.1 Edged - 1, 3mm 22.7℃, w1=300, slow
Thickness (micron): Average: 100.7992 Min: 100.7965 Max: 100.8024 Variation: 0.0059 Standard RMS: 0.001733
Grid size: 12X12. Step size: 0.25 mm. Center position: X= 154.5 mm, Y= 29.8 mm
Temperature Compensation: Relative. Reference thickness variation: +0.34 nm. Measurement time= 13:19
Power= 0.6 nm. Radius= 1736.0 m. Wedge= 0° 0' 0.468" [-122°]

Thickness Variation (nm) from Minimum (100.7965 um):

| | | | | | | | | | | | |
|---|---|---|---|---|---|---|---|---|---|---|---|
| – | – | – | – | 1 | 1 | 0 | 0 | – | – | – | – |
| – | – | 2 | 2 | 1 | 1 | 1 | 0 | 0 | 0 | – | – |
| – | 3 | 2 | 2 | 2 | 1 | 1 | 1 | 0 | 0 | 0 | – |
| – | 3 | 3 | 2 | 2 | 2 | 1 | 1 | 0 | 0 | 0 | – |
| 4 | 3 | 3 | 3 | 3 | 2 | 1 | 1 | 1 | 0 | 0 | 0 |
| 4 | 4 | 4 | 3 | 3 | 2 | 2 | 2 | 1 | 1 | 1 | 1 |
| 5 | 4 | 4 | 3 | 3 | 3 | 2 | 2 | 2 | 2 | 1 | 1 |
| 5 | 5 | 4 | 4 | 3 | 3 | 3 | 3 | 3 | 2 | 2 | 2 |
| – | 5 | 5 | 4 | 4 | 4 | 4 | 4 | 3 | 3 | 2 | – |
| – | 5 | 5 | 5 | 5 | 5 | 5 | 5 | 4 | 4 | 3 | – |
| – | – | 6 | 6 | 6 | 5 | 5 | 5 | 5 | 4 | – | – |
| – | – | – | – | 6 | 6 | 6 | 6 | – | – | – | – |

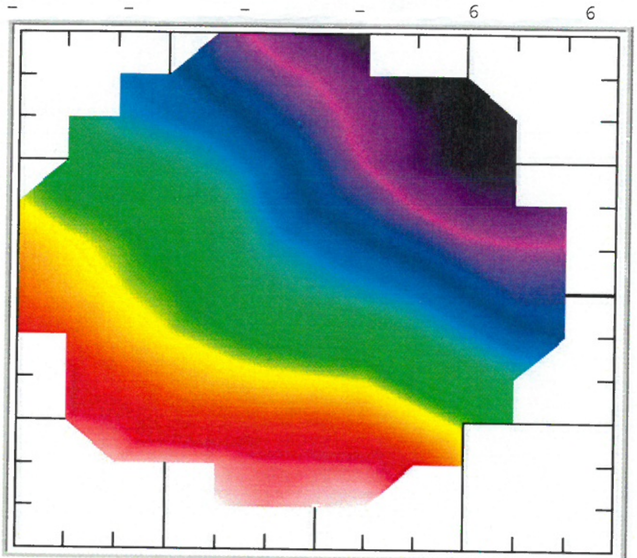

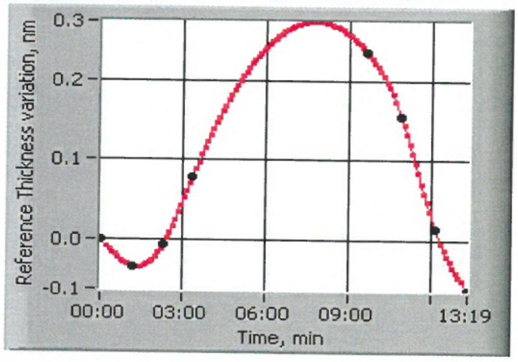


Mapping data saved at: W:\WO79873\YAG pc5.1 Edged - 1, 3mm.txt

Etalon Thickness Report, LightMachinery Inc. 2015.07.20 9:15:37 AM
Measurement Program: SW-3583 ver.13.exe (2015.06.01 1:12:50 PM) on EQ-1861
Material: YAG. Work Order: WO70790 YAG pc4 Decontacted - 2, 4mm 25.0℃
Thickness (micron): Average: 251.6490 Min: 251.6413 Max: 251.6543 Variation: 0.0130 Standard RMS: 0.002984
Grid size: 16X16. Step size: 0.25 mm. Center position: X= 61.0 mm, Y= 29.7 mm
Temperature Compensation: Relative. Reference thickness variation: -0.05 nm. Measurement time= 23:20
Power= -2.0 nm. Radius= -1025.4 m. Wedge= 0° 0' 0.538" [131°]

Thickness Variation (nm) from Minimum (251.6413 um):

| | | | | | | | | | | | | | | | |
|---|---|---|---|---|---|---|---|---|---|---|---|---|---|---|---|
| - | - | - | - | - | 11 | 11 | 11 | 10 | 9 | 8 | - | - | - | - | - |
| - | - | - | 11 | 12 | 13 | 13 | 13 | 12 | 11 | 10 | 8 | 6 | - | - | - |
| - | - | 11 | 13 | 13 | 13 | 13 | 13 | 12 | 12 | 11 | 9 | 8 | 6 | - | - |
| - | 11 | 13 | 13 | 12 | 12 | 12 | 12 | 11 | 11 | 10 | 9 | 8 | 6 | 4 | - |
| - | 11 | 12 | 12 | 11 | 11 | 11 | 11 | 11 | 10 | 9 | 8 | 7 | 6 | 5 | - |
| 11 | 12 | 12 | 11 | 10 | 10 | 10 | 10 | 10 | 9 | 8 | 7 | 6 | 6 | 5 | 3 |
| 11 | 12 | 11 | 10 | 9 | 9 | 9 | 9 | 9 | 9 | 8 | 6 | 6 | 6 | 5 | 3 |
| 11 | 12 | 11 | 9 | 8 | 8 | 8 | 8 | 8 | 8 | 7 | 6 | 5 | 5 | 5 | 2 |
| 11 | 12 | 11 | 9 | 8 | 7 | 7 | 8 | 8 | 7 | 7 | 6 | 6 | 5 | 4 | 2 |
| 9 | 10 | 10 | 9 | 8 | 7 | 6 | 7 | 7 | 7 | 7 | 6 | 6 | 6 | 4 | 1 |
| 7 | 9 | 9 | 9 | 8 | 7 | 6 | 6 | 6 | 6 | 6 | 6 | 6 | 6 | 4 | 0 |
| - | 8 | 8 | 8 | 8 | 7 | 6 | 6 | 6 | 6 | 6 | 7 | 6 | 5 | 2 | - |
| - | 5 | 7 | 7 | 7 | 7 | 7 | 6 | 6 | 6 | 6 | 6 | 6 | 4 | 1 | - |
| - | - | 4 | 6 | 6 | 6 | 7 | 7 | 7 | 7 | 6 | 5 | 4 | 1 | - | - |
| - | - | - | 2 | 3 | 4 | 5 | 6 | 7 | 6 | 5 | 3 | 0 | - | - | - |
| - | - | - | - | - | 1 | 2 | 3 | 4 | 3 | 2 | - | - | - | - | - |

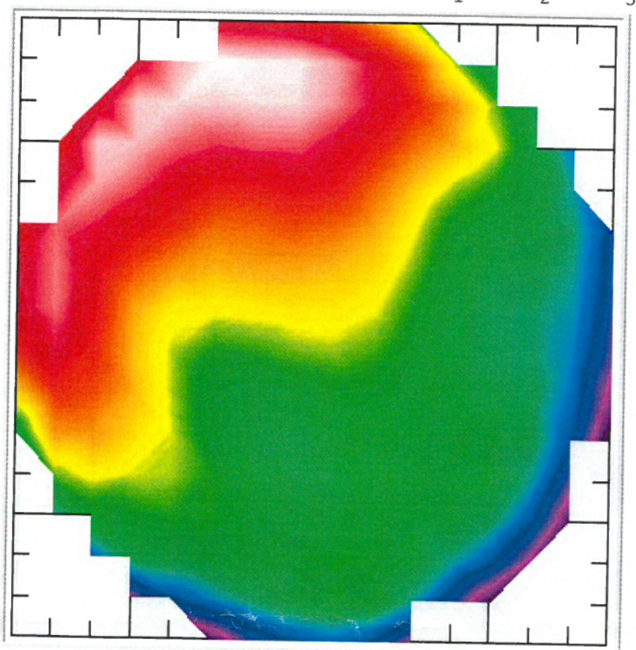

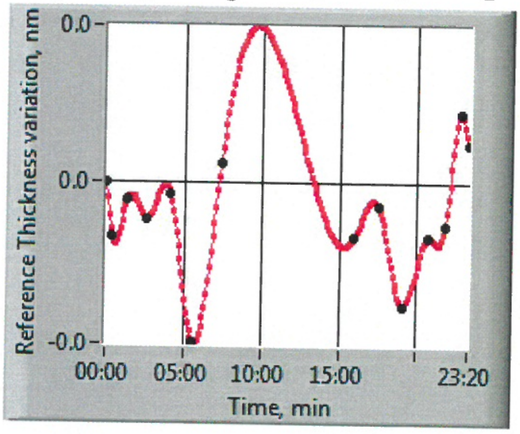


Mapping data loaded from: W:\WO70790\YAG pc4 Decontacted - 2, 4mm.txt

## A.4 Program for modelling total reflectivity $R^*$ in coupled cavity effects

Matlab is a powerful and convenient tool for data calculation, modelling and viewing. Besides that, this software supports creating GUI Applications, so Matlab was chosen to develop the framework for "Coupled Cavity Effects Simulation GUI Application".

### A.4.1 Setting key parameters

After analysing the parameters for calculating and simulating the process for the cavity effects and concerning the visibility, flexibility and usability of the software application, the design of our "Couple Cavity Effects Simulation GUI Application" is finalised, and the function scope is listed below:

- Building the parameters:

□ Reflectivity: R, $R_1$, and $R_2$

□ Lossess: Loss1 ($l_1$), and Loss2 ($l_2$)

□ Cavity length: Length1 ($L_1$), and Length2 ($L_2$)

- Axises range adjustment
- Graphics showing the result
- Graphic drag, zoom in/out and rotation.
- Graphics file save and package to "xxx.exe" application format

### A.4.2 Procedures to build GUI application for $R^*$ in coupled cavity effects

Open MATLAB software and click the "New" button and select "GUIDE", then choose "Blank GUI (default)", then a black GUI project was obtained, as shown below in Figure A.1:

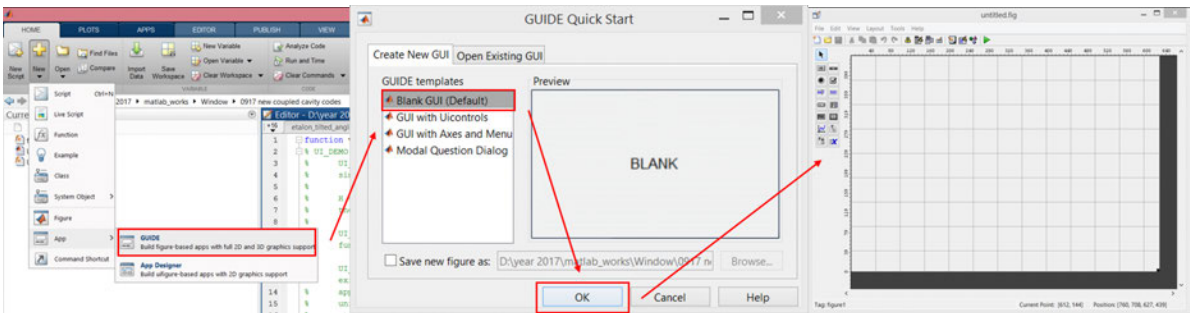


Figure A.1: Procedures to build a GUI application.

After that, according to the functional parameters are finalised above, creating the components and the widgets, including the input editors for all the parameters related to total reflectivity R* in the coupled cavity effect calculation and axis adjustment, graphic view panel and one button "Run" for executing the process. The final "GUI application" is shown in Figure A.2 below. After the GUI components are finished, start implementing all functions of the GUI application:

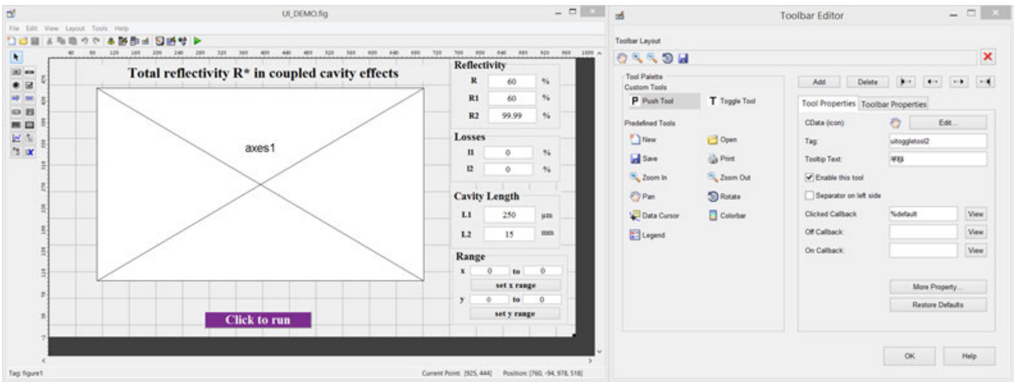


Figure A.2: Procedures to build a GUI application.

- Add the function of graphics move, zoom in/out, rotation and file save through the "Toolbar Editor" as the Figure A.2 shown below.

To better retrieve the parameter, set the labels for each component and widgets, i.e. the Figure A.3 showed below.

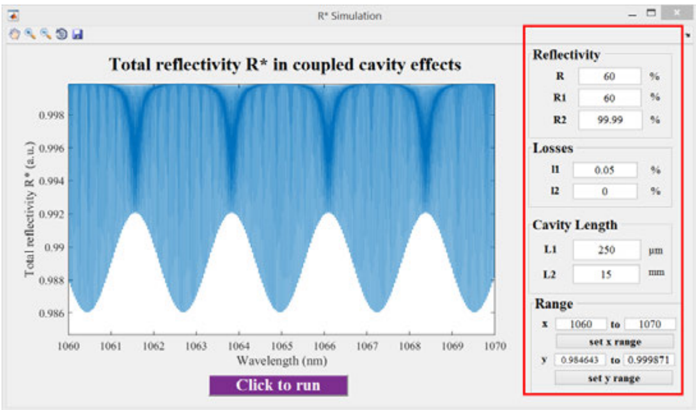


Figure A.3: Procedures to build a GUI application.

• Create to call back functions for the axis range update buttons: "set x range" and "set y range", then implement the function of update axis range inside the functions.

• Create the call back function for the "Execution" button. Leveraging the call back function, implement the function of reading the parameters from the input component and widgets, calculating the couple cavity effect, and updating the graphic view component.

All the functional program code is attached in the appendix A. After all the above procedures are completed, run the application and click the "Execution" button to verify the result, and test each function works as expected. The running and testing results of the "GUI application" in different axis scales are shown in Figure A.3.

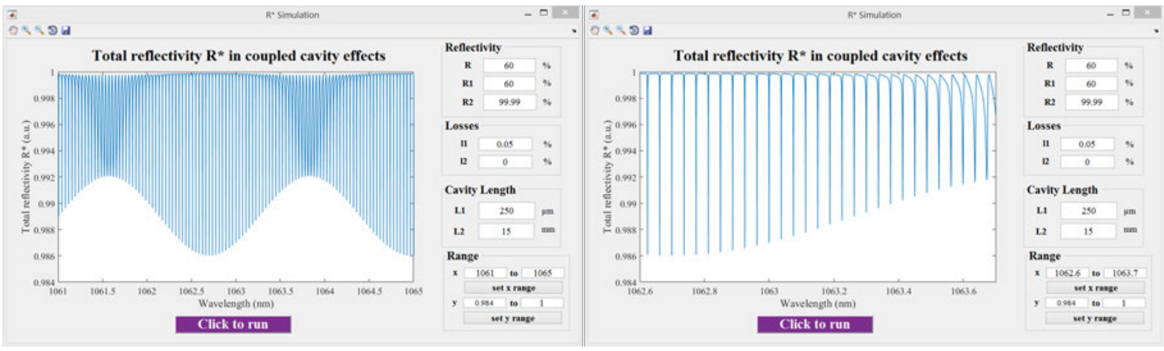


Figure A.4: Procedures to build a GUI application.

## A.4.3 Saving files and package to "xxx.exe" application format

A "Save" button is created to save the generated results in this "GUI application", so the results can be saved as different formats to the destination. Besides, an "xxx.exe" application

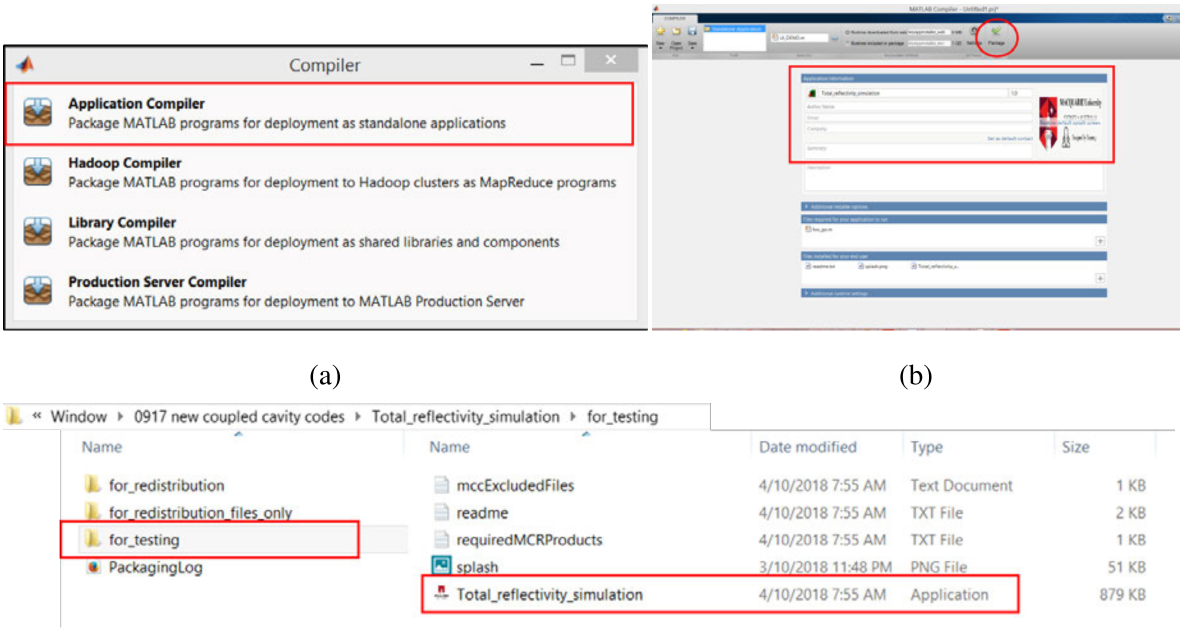


(a) (b)

(c)

Figure A.5: Procedures to build a GUI application.

format of this design is packaged via the following procedures, shown in Figure A.5.

- Type "deploytool" in the "Command Window", and the show up the "Compiler" window, choose the "Application Compiler".

- Add Matlab code file in the "MATLAB Compiler" window, and optional the "Application Information", to change or use the default setting.

- Click "Package" button and the "GUI application" is generated.

## A.5 Journal paper 1

Journal paper resulting from this work: Ran Li, Yameng Zheng, David J. Spence, Helen Pask, and Andrew Lee, Intracavity THz polariton source using a shallow-bounce configuration," accepted on 29th, Jan, 2018 (minor revision) for publication in Transactions on Terahertz Science and Technology.

# Intracavity THz polariton source using a shallow-bounce configuration

Ran Li, Yameng Zheng, David J. Spence, Helen M. Pask and Andrew J. Lee

***Abstract*—We demonstrate a frequency-tunable THz polariton source based on stimulated polariton scattering (SPS) in MgO:LiNbO$_3$. The system produces THz emission using an intracavity, shallow-bounce configuration. Continuously-tunable THz emission across the frequency range 1.05 – 2.89 THz is demonstrated, and a maximum average THz power of 67.5 µW is detected at 1.34 THz, when pumped with 15.1 W from a continuous-wave laser diode at 880 nm. In contrast to conventional linear configurations, this shallow-bounce configuration offers enhanced THz output power across the systems entire THz frequency-tuning range, and especially at higher frequencies. This is achieved through careful consideration of the THz generation volume, and locating it as close as possible to the emitting surface of the polariton-active crystal, thereby minimizing the deleterious effect of absorption within the SPS crystal. In addition to experimental data, the degree of THz enhancement offered using this configuration, in contrast to a linear configuration is also investigated mathematically.**

***Index Terms*—Laser cavity resonators, nonlinear optics, solid-state lasers, stimulated polariton scattering (SPS), Terahertz generation, parametric generation, parametric oscillator**

## I. Introduction

Terahertz generation in the range of frequencies from 0.3 to 10 THz is attracting attention for a wide variety of applications in defense and security [1], life sciences and medicine [2], non-destructive sensing [3] and ultra-high bandwidth communication [4]. Over the last five years, frequency-tunable THz sources based on stimulated polariton scattering (SPS) have been demonstrated in both continuous-wave (CW) [5], and pulsed (nanosecond [6], and picosecond [7]) modalities. The interest in these THz sources stem from their robust solid-state design, low pump-power requirements, and their ability to be frequency-tuned across a very broad frequency range, through the use of different nonlinear, SPS-active crystals. These include magnesium oxide-doped lithium niobate (MgO:LiNbO$_3$) [5-10], potassium titanyl phosphate (KTiOPO$_4$ or KTP) [11], potassium titanyl arsenate (KTiOAsO$_4$ or KTA) [12] and rubidium titanyl phosphate (RbTiOPO$_4$ or RTP) [13, 14]. This has led to frequency-tunable THz radiation, with frequency ranging from 0.8 to 6.3 THz, with sub-milliwatt-level average powers. In these sources, an Nd-based fundamental laser field (i.e. emitting at 1064 nm) is typically utilized to generate the Stokes and THz fields via SPS in an appropriate crystal. SPS frequencies generated must lie on the dispersion curve as well as on the phase-matching curve, that depends upon the intersection angle between fundamental and Stokes fields. Extracavity [15, 16] and intracavity [8, 9] configurations have been reported, however in this work, our focus is on intracavity configurations as they offer a compact, standalone approach to THz generation.

In terms of intracavity SPS designs, two geometries have been demonstrated in the literature, the so-called linear configuration, and the surface-emitting configuration, with the latter implementing total-internal-reflection of both the fundamental and Stokes fields within a trapezoidal SPS crystal [10,14]. By far, the most dominant intracavity configuration has been the linear configuration (depicted in Fig. 1(a)), whereby a conventional cuboid crystal is used, through which the fundamental- and Stokes-fields resonate in a linear fashion [5, 8, 9]. The popularity of this design stems from its relative simplicity, and similarity to conventional end-pumped solid state laser designs.

Within these laser systems, the THz field is produced through the SPS process, and its frequency and direction are dictated by the conservation of momentum of the fundamental ($k_f$), Stokes ($k_S$) and polariton fields ($k_{THz}$) (see Fig. 1). In MgO:LiNbO$_3$, the external intersection angle ($\theta_{ext}$ shown in Fig. 1 (a)) between fundamental and Stokes fields is typically adjusted from 1° to 3° and the corresponding THz field is generated at angles of around 63° to 65°, relative to the fundamental field. Because the emitting angle of the THz field exceeds the critical angle for total internal reflection (TIR) at the MgO:LiNbO$_3$-air interface, high-resistivity silicon (Si)-prisms are typically bonded to the crystal side face to couple the THz field from the crystal into the air.

Within the context of linear resonator geometries, two absorption losses impact the extracted THz power and frequency tuning range. One is the high absorption of THz radiation within the SPS crystal itself, especially when the system is tuned to a higher THz frequency (the absorption coefficient increases with THz frequency). The other is free-carrier absorption [17] which occurs when scattered near-infrared (e.g. fundamental and Stokes) fields induce free carriers via the photoelectric effect, which absorb the THz

Manuscript received June xx, 2018. This work was supported by the Australian Research Council (ARC) Linkage Project Scheme. (LP140100724). The authors thank M Squared Lasers Inc. for their support. (Corresponding author: Ran Li)

The authors are with the MQ Photonics Research Centre, Department of Physics and Astronomy, Macquarie University, Sydney, N.S.W. 2109, Australia (e-mail: ran.li@mq.edu.au; yameng.zheng@students.mq.edu.au; david.spence@mq.edu.au; helen.pask@mq.edu.au; andrew.lee@mq.edu.au).

radiation, in the Si-prisms. The opportunity to overcome the latter source of loss was demonstrated in [18], when a fundamental-field wavelength of 1342 nm was used to circumvent the generation of free carriers within the Si prisms, as the photon energy is below the band-gap of Si. Little attention has however, been given to addressing the former source of loss, the inherent absorption within the SPS crystal.

The impact that SPS crystal absorption has on the extraction of generated THz photons, is principally determined by the distance these photons must propagate through the SPS crystal, before reaching the surface of the crystal. In the case of a linear resonator, this distance is governed by how close the interaction, or overlap region of the fundamental and Stokes fields, can be located to the emitting surface of the SPS crystal. As depicted in Fig. 1(a), this must also accommodate for angling of the Stokes field within the SPS crystal, to achieve frequency-tuning; here clipping of the Stokes field becomes an issue at large intersection angles ($\Theta_{ext}$). Given the typical fundamental and Stokes-field mode diameters used in these intracavity systems, and the range of intersection angles, the fundamental field mode is typically located at ~ 0.5 mm from the emitting surface of the SPS crystal.

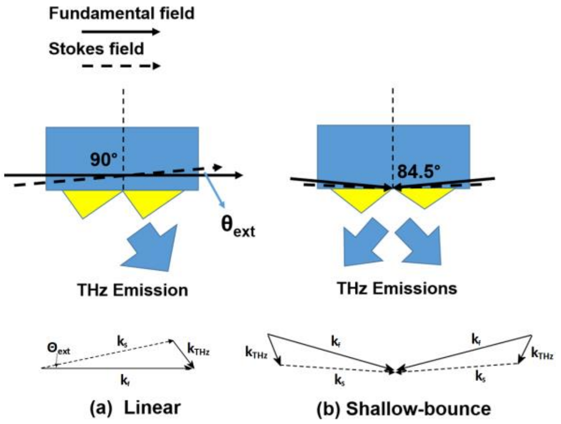


Fig. 1. Schematic diagram of a) a linear configuration; and b) a shallow-bounce configuration. Wavevectors of the fundamental ($k_f$), Stokes ($k_S$), and THz ($k_{THz}$) fields (exaggerated for clarity), are shown for each configuration.

While it may seem that this is a “hard limitation” encountered when using linear resonator geometries and cuboid crystals, this is not the case. To minimise the THz field propagation distance, and hence impact of THz absorption within the SPS crystal, it is necessary to locate the interaction zone as close as possible to the emitting surface of the crystal. This can be achieved by shallow-bouncing both the fundamental and Stokes fields [6], as sown in Figure 1(b). This configuration also facilitates the generation of two THz beams, as is required for many applications.

In this letter, we present an experimental demonstration of a shallow-bounce, intracavity SPS THz system, and discuss its relative merits in comparison to conventional linear resonator designs. A mathematical investigation of the enhancement that this geometry offers over linear resonators is also given.

## II. Experiment Details

The experimental setup is shown schematically in Fig. 2. It comprised two shallow-bounce resonators, one for the fundamental, and one for the Stokes field. A 0.3 at. % Nd:$YVO_4$ laser crystal with dimensions 4×4×10 mm$^3$, with both end surfaces anti-reflection (AR) coated for 880 nm (R < 0.5 %) and 1342 nm (R < 0.2 %), was utilized to generate the fundamental wavelength at 1342 nm. The crystal was end-pumped by a fiber-coupled diode laser (100 µm core diameter, NA ~ 0.22), capable of producing up to 30 W pump power at 880 nm. Two plano-convex lenses were used to obtain a ~ 150 µm pump beam radius inside the Nd:$YVO_4$ crystal. A flat end-mirror (M1, R < 0.25 % at 880 nm and R > 99.9 % at 1342 nm), an x-cut 5 at. % MgO:$LiNbO_3$ SPS crystal (HC Photonics Corp.) and a concave high reflectivity (HR) mirror (M2, radius of curvature (ROC) = 1000 mm; R = 99.9 % at 1342 nm) defined the fundamental field resonator, which had a length of 260 mm. The MgO:$LiNbO_3$ crystal had dimensions of 5×5×20 mm$^3$, and was AR coated on both end surfaces (R < 0.2 % at 1340 – 1380 nm at normal incidence). The fundamental field beam entered the crystal at an angle of 12°, relative to the normal of the crystal end-face. A protective Teflon layer with ~ 150 nm thickness (AF Amorphous Fluoroplastic Solutions; AF 2400; Chemours) was applied (spin-coated) to the bounce surface, to prevent laser damage at high pump power, the effect of which has been detailed in [10]. An intracavity acousto-optic Q-switch (NEOS, 33027-25-2-1-1.3) was used to achieve pulsed operation at a repetition rate of 5 kHz.

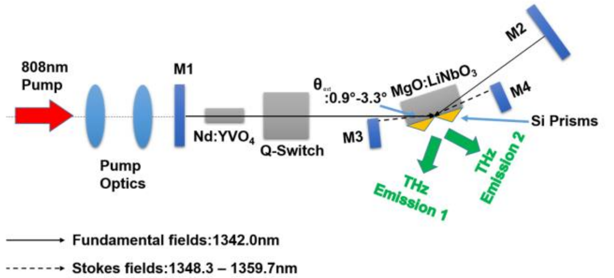


Fig. 2. Intra-cavity shallow-bounce configuration layout, angles are exaggerated for clarity.

A separate pair of HR mirrors (M3 and M4, ROC = 1000 mm; R = 99.9 % from 1340 – 1380 nm) were used to construct a 95 mm-long Stokes resonator which oscillated and bounced the Stokes field at the same TIR surface and position as the fundamental field. Two high-resistivity Si-prisms with angles of 33°/33°/114° (dimensions 6×6×10 mm$^3$) were placed in close proximity to the Teflon-coated, polished x-z surface of the MgO:$LiNbO_3$ crystal. These prisms extracted two THz beams at angles of ~ ± 30° relative to the SPS crystal bounce surface. Both Stokes mirrors were D-shaped to avoid clipping of the fundamental field, and were mounted on independent rotation stages. THz frequency tuning was achieved by rotating two Stokes mirrors (M3 and M4) to tune the intersecting angle (θ shown in Fig. 2) between the fundamental and Stokes field resonator axes. In this work, the fundamental field bounce angle was 84.5°.

Inspection of white-light interference fringes produced by the gap between the Si-prisms and MgO:LiNbO$_3$ crystal indicated a gap that varied between 0.5 µm and 2 µm. The performance of the THz emission was not sensitive to the precise value of the gap, however the presence of the gap, which comprises 150 nm Teflon and the remainder of air, is essential to enabling low loss TIR of the fundamental and Stokes beams within the MgO:LiNbO$_3$ crystal, and high transmission of the THz beam from the MgO:LiNbO$_3$ into the Si-prism. Our calculations, taking into account the evanescent waves which extend into the gap [19], show that for the fundamental and Stokes (wavelength ~ 1340 – 1360 nm), low loss TIR (i.e. R > 99.9 %) can be achieved for gaps in excess of 450 nm. In other words, there is minimal frustration of the TIR for the near-infrared fields. For the THz radiation (wavelength ~ 100 – 300 µm), TIR is strongly frustrated, and the transmission is in excess of 85 % for gaps below 2 µm. The maximum THz transmission, limited by Fresnel reflection at the MgO:LiNbO$_3$/Si interface is ~ 91 %.

The THz output beam was chopped by a mechanical chopper (Thorlabs MC2000B) at a frequency of 10 Hz (50 % duty cycle), and was detected by a Golay cell (Tydex, GC-1P), while the leakage powers of the fundamental and Stokes fields were measured using a thermal power meter (Thorlabs S310C) after M2 and M3 respectively. A long pass filter (Tydex, LPF 14.3) was put in front of the Golay cell detector (which includes a TPX window) to block any scattered signals, except for the THz radiation. The spectra of both near-infrared wavelengths from the fundamental and Stokes field resonators were monitored using a calibrated Ocean Optics grating spectrometer (NIRQuest 512). The frequency of the generated THz radiation was calculated from the difference in frequency of the fundamental and Stokes field wavelengths.

## III. RESULTS AND DISCISSION

In this work, the combined maximum average THz power of the two emitted THz beams was 67.5 µW, for an incident CW pump power of 15.1 W, with the system generating emission at 1.34 THz. The power transfer curves for the fundamental, Stokes and THz fields are shown in Fig. 3. The threshold pump power for oscillation of the fundamental field was 1.6 W, and the SPS threshold was reached for an incident diode pump power of 7.2 W. Up to 35 % depletion of the fundamental field was observed at the maximum detected THz power, as determined by blocking/unblocking the Stokes resonator to disable/enable SPS.

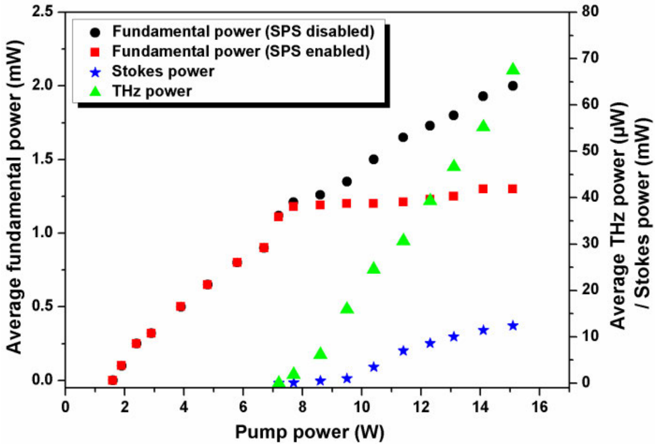


Fig. 3. Power transfer curves for the fundamental (SPS disabled and SPS enabled), Stokes, and THz fields under CW pumping at 1.34 THz

The temporal profiles of fundamental and Stokes fields were investigated using two photodiodes (Thorlabs, PDA10CS). For an incident pump power of 15 W, the fundamental pulse width decreased from 74 ns to 57 ns at full width at half-maximum as a consequence of SPS, when the Stokes field cavity was blocked and unblocked, and the Stokes pulse width was typically 29 ns. The spatial profiles of the dual-beam THz emission were also explored. The horizontal and vertical beam profiles were each measured at positions of 1 mm, 6 mm and 20 mm from the surface of the Si-prisms using a 10 % to 90 % knife-edge method. A high divergence, full-angle of ~ 11° was measured in the vertical plane while the horizontal beam profile showed a much lower divergence of ~ 0.5°.

The THz frequency tuning range was characterized at the maximum incident pump power and is shown in Fig. 4 (black dots). The dips in the spectrum are due to water vapor absorption features in the laboratory atmosphere. The intersection angle between fundamental and Stokes axes was adjusted by M3 and M4 with an external rotation angle from 0.9° to 3.3°. The corresponding tuning range of the Stokes wavelengths and THz frequencies were from 1348.3 to 1359.7 nm, and 1.05 to 2.89 THz, respectively. Also shown (red dots) is the frequency-tuning characteristic of a linear-configuration resonator [18].

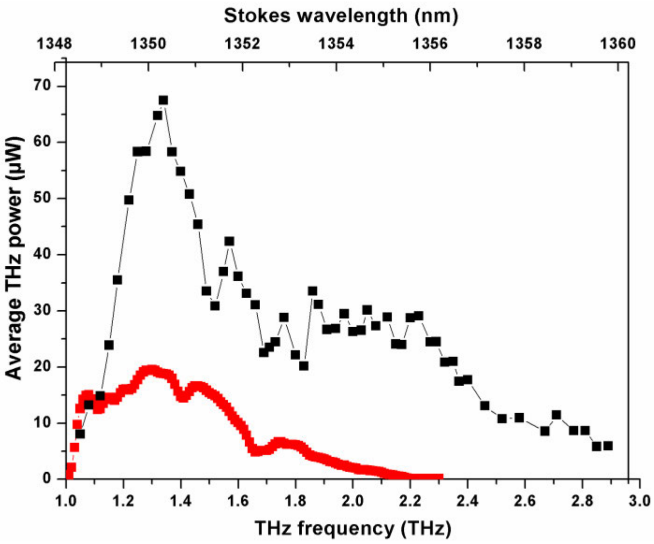


Fig. 4. THz frequency tuning characteristics of the shallow-bounce (black dots) and linear configurations (red dots, replicated from [18])

We mathematically compared the generation volume and overall THz extraction efficiency of both the linear and shallow-bounce geometries depicted in Fig. 1. In the traditional linear resonator, there is a compromise between minimizing the THz field propagation distance and maintaining broad frequency-tunability; this is not a compromise in a shallow bounce configuration.

In a commonly-used model of SPS THz lasers [20], the exponential Stokes field gain is proportional to the fundamental field intensity. The THz field is assumed to be in steady-state with the local fundamental and Stokes fields, and the THz losses (due to the infinite plane wave assumption). This leads to a THz photon generation rate proportional to the local fundamental and Stokes fields. In these intracavity lasers, the fundamental and Stokes beams are both resonated and change slowly during each round trip, and the beams radii do not significantly change through the cavity. We assume top-hat beam profiles, such that all regions of overlap between the fundamental and Stokes beams within the crystal contribute equally to Stokes gain and to THz generation.

We first calculate the overlap region $V_G$ between the fundamental and Stokes beams, which provides a measure of the *generated* THz power (for a given fundamental and Stokes power). THz photons generated near the surface of the crystal have a much higher probability of exiting the crystal without absorption, given by $e^{-\alpha x}$, where $\alpha$ is the absorption coefficient, and $x$ is the distance the THz photons must propagate to the crystal edge, from their generation location. Accordingly, we can calculate an extraction-weighted overlap volume $V_E$, as the sum of overlap elements, each weighted by the $e^{-\alpha x}$. The ratio $\eta_1 = V_E / V_G$ quantifies the fraction of generated photons that reach the exit surface of the $MgO:LiNbO_3$, for a particular geometry. The output coupling efficiency ($\eta_2$) represents how many of these THz photons can be coupled from the $MgO:LiNbO_3$ into the air, and takes account of the various Fresnel losses, frustrated-total-internal-reflection losses (in the case of the shallow-bounce cavity), and Si-prism absorption [21]. We can then compare the overall THz extraction efficiencies ($\eta_1 \times \eta_2$) for the resonator designs.

In these calculations, we modelled a 5×5×25 mm$^3$ cuboid $MgO:LiNbO_3$ crystal. In the linear configuration, a 0.5 mm distance was assumed between the THz-emitting edge of the $MgO:LiNbO_3$ crystal, and the bottom edge of the internally propagating fundamental field mode, consistent with our experiments in [9,18]. The fundamental and Stokes fields are assumed to be two top-hat beams with diameters of 0.4 mm and 0.3 mm respectively. The calculations were performed across a THz frequency tuning range of 1.3 to 2.2 THz.

TABLE I

MATHEMATICALLY-DETERMINED GENERATION AND EXTRACTION-WEIGHTED VOLUMES FOR LINEAR, SHALLOW-BOUNCE, AND SURFACE-EMITTING CONFIGURATIONS, ALONG WITH EXTRACTION EFFICIENCIES.

| | | Shallow-bounce cavity | Linear cavity |
|---|---|---|---|
| 1.3THz | $V_G$ (mm$^3$) | 1.56 | 1.56 |
| | $V_E$ (mm$^3$) | 0.60 | 0.54 |
| | $\eta_1$ | 38.5% | 34.6% |
| | $\eta_2$ | 63.8% | 60.9% |
| | $\eta_1 \times \eta_2$ | 24.5% | 21.1% |
| 2.2THz | $V_G$ (mm$^3$) | 1.18 | 1.18 |
| | $V_E$ (mm$^3$) | 0.26 | 0.05 |
| | $\eta_1$ | 22.0% | 4.2% |
| | $\eta_2$ | 62.4% | 58.1% |
| | $\eta_1 \times \eta_2$ | 13.7% | 2.5% |

Table I shows that the shallow-bounce cavity exhibits the highest overall extraction efficiencies ($\eta_1 \times \eta_2$) at both 1.3 THz and 2.2 THz. A plot comparing the fraction of THz photons that reach the exit surface ($\eta_1$), in both the linear and shallow-bounce configurations, as a function of generated THz frequency is shown in Figure 5.

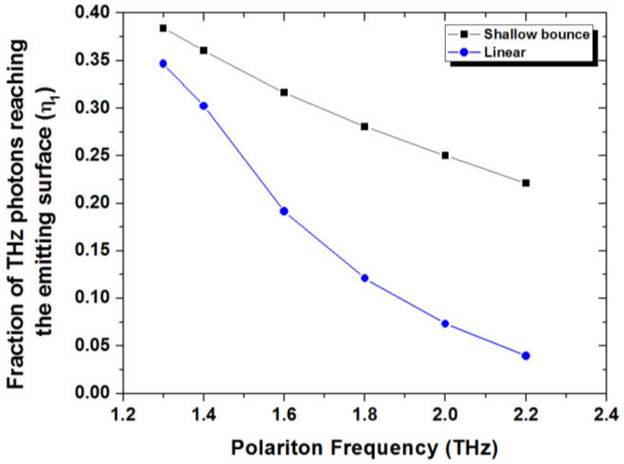


Fig. 5. Plot of the fraction of THz photons reaching the emitting surface ($\eta_1$) for the linear (blue) and shallow-bounce (black) configurations, as a function of generated THz frequency.

These calculations show that while mode overlap and THz generation volumes are a key consideration in these laser designs, ultimately, careful thought must be given to the overall effect of THz absorption at different THz frequencies, along with output coupling efficiency. These results show that the shallow-bounce configuration maintains the highest overall THz extraction efficiency across modelled THz frequencies, and holds promise as the configuration which will yield the highest overall THz power.

Data exists for a reasonable comparison to be made between the performance characteristics of a linear [18], and a shallow-bounce configuration (this paper), and this is summarized in Table. II.

TABLE. II
SUMMARY OF INTRACAVITY SPS THz PERFORMANCE USING MgO:LiNbO$_3$, COMPARING LINEAR AND SHALLOW-BOUNCE CONFIGURATIONS

| | Linear configuration at 1.3 THz | Shallow-bounce configuration at 1.3 THz |
|---|---|---|
| SPS threshold | 5.0 W | 7.2 W |
| Max fundamental field depletion | 33 % | 35 % |
| Max THz power (CW pumping) | 23.6 µW @ 12.5 W diode pumping | 67.5 µW @ 15.1 W diode pumping; ~39 µW @ 12.5 W diode pumping |
| Frequency tuning | 1.00 – 2.30 THz | 1.05 – 2.89 THz |

Both linear and shallow bounce configurations are based on a Nd:YVO$_4$ laser crystal generating a 1342 nm fundamental field wavelength, and a MgO:LiNbO$_3$ crystal as the SPS medium. Higher average THz output power and extended THz frequency tuning range are both observed in the shallow-bounce configuration. Indeed, following the ratio of overall extraction efficiencies, one would anticipate a 48 % increase (35 %/23.6 %) in overall THz power comparing the shallow bounce design to the linear design.

As shown in Fig. 4, the THz signal in the linear configuration drops much faster than the shallow-bounce case for frequencies above 1.8 THz. This is consistent with the modelling shown in Figure 5, where in the linear case, the fraction of generated THz photon reaching the emitting surface, decreases dramatically as THz frequency increases, in comparison with the shallow bounce configuration. The shallow-bounce configuration has a higher threshold for SPS than the linear configuration, and this is attributed to reflection losses at the SPS crystal end-faces for the non-normal (~ 12°) angle of incidence of the fundamental and Stokes beams.

It should be noted that this study is focussed on improving the geometry of linear-configuration systems utilising cuboid crystals. There is no surface emitting configuration performance data to which our calculations can be fairly compared. The most similar source is reported in [10], but the laser crystal (Nd:YAG vs Nd:YVO$_4$), pumping scheme (50 % duty cycle pumping vs CW pumping) and fundamental field wavelength (1064 nm vs 1342 nm) are different, leading to different laser and SPS gains. It should be highlighted however, that while surface-emitting configurations such as those detailed in [10], do not require the use of Si prisms for out-coupling the generated THz field, the fundamental and Stokes fields inherently have very steep bounce angles. As as-such, much of the interaction zone between the fundamental and Stokes fields is located further away from the exit surface of the SPS crystal, and many of the generated THz photons will suffer absorption loss as they propagate to the exit surface.

## IV. CONCLUSION

In conclusion, a shallow-bounce configuration has been demonstrated in an intracavity Q-switched SPS THz source using MgO:LiNbO$_3$, combined with a fundamental wavelength at 1342 nm. Dual-beam THz emission (with similar output powers and beam profiles) was achieved with a combined, maximum average power of 67.5 µW for an incident CW pump power of 15.1 W, which is a major advance on the previous best power of 23.6 µW, obtained using a conventional linear cavity design under 12.5 W CW pumping. THz frequency coverage ranged from 1.05 to 2.89 THz, which is broader than that achieved from a linear design (i.e. from 1.00 to 2.30 THz). We have modelled the generation and extraction efficiency of this configuration, and have found that it has the greatest potential for high THz output power, across a broad THz frequency range. The dual-beam THz emission is unique and may suit self-referenced experiments/applications, and THz interferometry [22], without the need for THz beam splitters.

## References


1. M. C. Kemp, “Explosives Detection by Terahertz Spectroscopy—A Bridge Too Far? ” IEEE Trans. Terahertz Sci. Technol. **1**(1), 282-292 (2011).
2. B. Ferguson and X. Zhang, “Materials for terahertz science and technology,” Nat. Mater. **1**, 26-33 (2002).
3. S. Krimi, J. Klier, J. Jonuscheit, G. V. Freymann, R. Urbansky, and R. Beigang, “Highly accurate thickness measurement of multi-layered automotive paints using terahertz technology,” Appl. Phys. Lett. **109**, 021105 (2016).
4. I. F. Akyildiz, J. M. Jornet, C. Han, “Terahertz band: Next frontier for wireless communications,” Phys. Commun. **12**, 16-32 (2014).
5. A. J. Lee and H. M. Pask, “Continuous wave, frequency-tunable terahertz laser radiation generated via stimulated polariton scattering,” Opt. Lett. **39**(3), 442-445 (2014).
6. R. Zhang, Y. Qu, W. Zhao, C. Liu, and Z. Chen, “Si-prism-array coupled terahertz-wave parametric oscillator with pump light totally reflected at the terahertz-wave exit surface,” Opt. Lett. **41**(17), 4016-4019 (2016).
7. A. M. Warrier, R. Li, J. Lin, A. J. Lee, H. M. Pask, and D. J. Spence, “Tunable terahertz generation in the picosecond regime from the stimulated polariton scattering in a $LiNbO_3$ crystal,” Opt. Lett. **41**(18), 4409-4412 (2016).
8. T. J. Edwards, D. Walsh, M. B. Spurr, C. F. Rae, M. H. Dunn, and P. G Browne, “Compact source of continuously and widely-tunable terahertz radiation,” Opt. Express **14**(4), 1582-1589 (2006).
9. A. Lee, Y. He, and H. Pask, “Frequency-Tunable THz Source Based on Stimulated Polariton Scattering in $Mg:LiNbO_3$,” IEEE J. Quantum Electron. **49**(3), 357-364 (2013).
10. T. A. Ortega, H. M. Pask, D. J. Spence, and A. J. Lee, “THz polariton laser using an intracavity $Mg:LiNbO_3$ crystal with protective Teflon coating,” Opt. Express **25**(4), 3991-3999 (2017).
11. W. Wang, Z. Cong, X. Chen, X. Zhang, Z. Qin, G. Tang, N. Li, C. Wang, and Q. Lu, “Terahertz parametric oscillator based on $KTiOPO_4$ crystal,” Opt. Lett. **39**(13), 3706-3709 (2014).
12. W. Wang, Z. Cong, Z. Liu, X. Zhang, Z. Qin, G. Tang, N. Li, Y. Zhang, and Q. Lu, “THz-wave generation via stimulated polariton scattering in $KTiOAsO_4$ crystal,” Opt. Express **22**(14), 17092-17098 (2014).
13. F. Gao, X. Zhang, Z. Cong, Z. Qin, X. Chen, Z. Liu, J. Lu, Y. L, J. Zang, D. Wu, C. Jia, Y. Jiao, S. Zhang, “Terahertz parametric oscillator with the surface-emitted configuration in $RbTiOPO_4$ crystal,” OPT. LASER. TECHNOL. **104**, 37-42 (2018).
14. T. A. Ortega, H. M. Pask, D. J. Spence, and A. J. Lee, “Tunable 3–6 THz Polariton Laser Exceeding 0.1 mW Average Output Power Based on Crystalline $RbTiOPO_4$,” IEEE J. Sel. Top. Quantum Electron. **24**(5), 5100806 (2018).
15. K. Kawase, J. Shikata, and I. Hiromasa, “Terahertz wave parametric source,” J. Phys. D **35**, R1-R14 (2002).
16. T. Ikari, X. Zhang, H. Minamide, and H. Ito, “THz-wave parametric oscillator with a surface-emitted configuration,” Opt. Express **14**(4), 1604-1610 (2006).
17. T. Nozokido, H. Minamide, and K. Mizuno, “Modulation of Submillimeter Wave Radiation by Laser-Produced Free Carriers in Semiconductors,” Electron. Commun. Jpn. Part II Electron. **80**(6), 1-8 (1997).
18. A. J. Lee, D. J. Spence, and H. M. Pask, “Tunable THz polariton laser based on 1342 nm wavelength for enhanced terahertz wave extraction,” Opt. Lett. **42**(14), 2691-2694 (2017).
19. S. Zhu, A. W. Yu, D. Hawley, and R. Roy, “Frustrated total internal reflection: A demonstration and review,” Am. J. Phys. **54**(7), 601-606, (1986).
20. S. Sussman, “Tunable Light Scattering from Transverse Optical Modes in Lithium Niobate,” Microw. Lab. Rep. No1851, Stanford Univ. (1970).
21. J. Dai, J. Zhang, W. Zhang, and D. Grischkowsky, “Terahertz time-domain spectroscopy characterization of the far-infrared absorption and index of refraction of high-resistivity, float-zone silicon,” J. Opt. Soc. Am. B, **21**(7), 1379-1386 (2004).
22. J. E. Allnutt and J. A. Staniforth, “A Mach-Zehnder interferometer for the measurement of the complex permittivity of lossy dielectrics at submillimeter wavelengths,” J. Phys. E: Sci. Instrum. **4**, 730-732 (1971).



**Ran Li** received the M.Sc and the Ph.D degrees in Electronic & Electrical Engineering from the University of Strathclyde, Glasgow, UK, in 2011 and 2016, respectively.
He is currently a Post-doctoral Research Associate in MQ Photonics Research Centre, Macquarie University. His current research interests include development of compact and frequency-tunable THz sources and their applications and development of solid-state Raman lasers.

**Yameng Zheng** received the M.S. degree in Optical Engineering from Shanghai Institute of Optics and Fine Mechanics (SIOM), Chinese Academy of Science, China in 2014. Currently, she is working toward the Ph.D. degree at Macquarie University, Australia. She is the recipient of International Macquarie University Research Excellence Scholarship (iMQRES). Her research interests include development of frequency-tunable, continuous wave THz polariton lasers and development of near-infrared fiber lasers.

**David J. Spence** was born in Birmingham, U.K., in 1975. He received the M.Phys. and D.Phil. degrees in physics from Oxford University, Oxford, U.K., in 1997 and 2001, respectively. After a year in the industry and two years as a Research Assistant at Oxford, he moved to Sydney, Australia, in 2004. Following an Australian Research Council Postdoctoral Fellowship, he won a Lectureship at Macquarie University, Sydney, N.S.W., Australia, where he is currently an Associate Professor. His research interests include lasers and nonlinear optics, including Raman lasers and frequency conversion, and visible and ultraviolet laser materials.

**Helen M. Pask** received the Ph.D. degree in physics from Macquarie University, Sydney, N.S.W., Australia, in 1992. She currently holds an Australian Research Council Future Fellowship at Macquarie University, with research interests in crystalline Raman lasers, THz generation and applications, remote sensing, and Raman spectroscopy.

**Andrew J. Lee** received the Bachelor’s degree (Honors First Class) in optoelectronics and the Ph.D. degree in physics from Macquarie University, Sydney, N.S.W., Australia, in 2001 and 2007, respectively.
He is currently a Macquarie University Co-Funded Fellow with Macquarie University and M Squared Lasers. His current research interests include development of high-power THz sources and their applications, development of high-power continuous wave Raman lasers, and vortex lasers.

## A.6 Conference paper 1

Conference paper resulting from this work: "Power improvement in a CW THz polariton laser," Frontiers in Optics (FiO) conference, Washington DC, USA, September 2018.

This paper is related to the work reported in Chapter 3.

# Power improvement in a CW THz polariton laser

**Yameng Zheng**, **Andrew Lee, Helen Pask**
*MQ Photonics, Department of Physics and Astronomy, Macquarie University*
*Author e-mail address* yameng.zheng@hdr.mq.edu.au

**Abstract:** An enhancement in the performance of an intracavity CW THz polariton laser is reported. THz output power of up to 23.1 µW was detected at 1.66 THz, frequency tunability across 1.30 - 2.51 THz was achieved.

**OCIS codes:** (140.3550) Lasers; (190.5890) Scattering, stimulated; (190.4410) Nonlinear optics, parametric processes.

## 1. Introduction

CW terahertz (THz) sources are well suited for imaging and high-resolution spectroscopy [1]. Recently Lee et. al.[2] demonstrated the first CW, frequency tunable THz source based on the stimulated polariton scattering (SPS) process [3], but the output power only had 2.3 µW, which limited its useful applications. Here we report on a system with similar overall architecture, but makes use of polarized, 880 nm pumping to reduce thermal loading both in the laser and polariton crystals. An order of magnitude increase in THz power to 23.1 µW is achieved.

## 2. Experimental setup and results

The THz laser setup is shown in Fig. 1. The output from an 880 nm laser diode passed through a polarizing beam splitter to select polarization parallel to the c-axis of the 13 mm long $Nd:GdVO_4$ crystal. The fundamental field resonator was formed using a coated $Nd:GdVO_4$ crystal M1 and mirror M2. A resonator for the Stokes field which is generated through the SPS process, was formed around the 5% a.t MgO-doped LiNbO3 crystal (20 mm long and oriented such that the fundamental field was polarized parallel to the crystal z-axis) using mirrors M3 and M4, and oriented at an angle (ranging from 1.4°-2.7° external angle) to the fundamental field resonator. The mirror coating details are listed in Tab. 1. An aperture was placed after the laser crystal to eliminate high-order laser modes and block residual pump light.

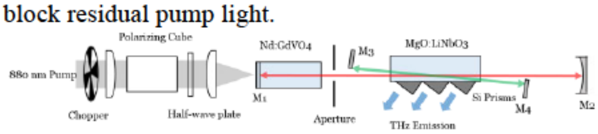


Fig.1 Experimental setup

| | |
|---|---|
| $M_1$ | HT@ 880 nm, HR @ 1063-1173 nm (R~99.99 %) |
| $M_2$ | R=99.995 %@1063 nm, ROC=500 mm |
| $M_3$ & $M_4$ | R>99.999% @ 1060-1180 nm, ROC=1m |

Tab. 1 Coating details of mirrors

Fig. 2 shows a) power transfer, b) tunability and c) beam profiles. The threshold for the SPS laser occurred for just 2.5 W incident pump power. The overall efficiency and power scaling capacity of the system are 10 times greater than that reported [2], and the maximum instantaneous THz power of 23.1 µW at 1.66 THz with the depletion of 42.7% was generated. The detected THz tuning range was from 1.30 to 2.51 THz, corresponding to Stokes wavelengths from 1068.18 to 1072.81 nm. No beam distortion was observed in the fundamental and Stokes fields through whole pump power. The THz power was improved due to reduced thermal loading of the laser and SPS crystals. The reasons for this improvement have been investigated and will be presented later.

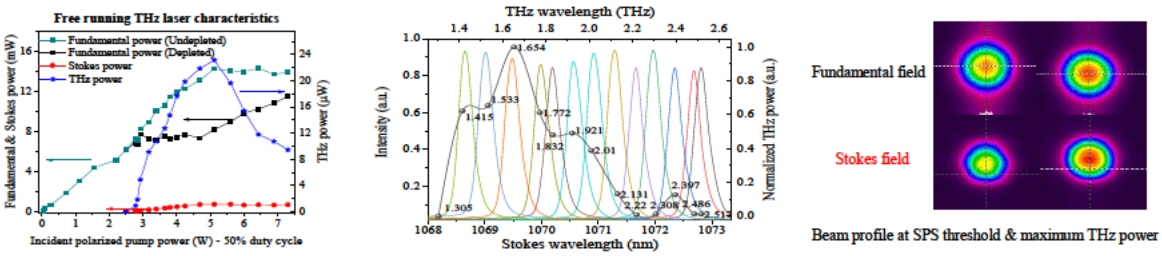


Fig.2 a) Power transfer curves under 50% - duty cycle pump, b) tunability and c) beam profiles both in fundamental and Stokes fields.

## 3. Summary

In summary, significant improvements in laser performance have been achieved by managing thermal loading and photorefractive effects, using the scheme of polarized and chopped pump at 880 nm.

## References

[1] M. Tonouchi, "Cutting-edge terahertz technology," *Nat. Photonics*, vol. 1, pp. 97–105, 2007.
[2] A. J. Lee and H. M. Pask, "CW, frequency-tunable THz laser radiation generated via SPS," Opt. Lett.,39(3), 442, 2014.
[3] D. L. Mills and E. Burstein, "Polaritons: the electromagnetic modes of media," *Reports Prog. Phys.*, vol. 37, no. 7, pp. 817–926, 2001.

## A.7 Conference paper 2

Conference paper resulting from this work: "Beneficial effects of using etalons in an intracavity CW THz polariton laser," Advanced Solid-State Lasers (ASSL) Conference, Nagoya, Japan, October 2017.

This work was awarded the "outstanding poster presentation".

**Pages 198-200 of this thesis have been removed as they contain published material under copyright. Removed contents published as:**

Zheng, Y., Lee, A., Spence, D., & Pask, H. (2017) Beneficial effects of using etalons in an intracavity CW THz polariton laser, in Laser Congress 2017 (ASSL, LAC), OSA Technical Digest (online) (Optical Society of America, 2017), paper JM5A.40. https://doi.org/10.1364/ASSL.2017.JM5A.40

## A.8 Conference paper 3

Conference paper resulting from this work: "Narrow linewidth continuous wave intracavity THz laser source," 21st Australian Institute of Physics (AIP) Congress, Brisbane, Australia, December 2016.

This paper is related to the work reported in Chapter 6. This work was also presented in the 2016 "KOALA" conference and was awarded "Best poster presentation".

# Narrow linewidth continuous wave intracavity THz laser source

Yameng Zheng[1], Andrew Lee[1] and Helen Pask[1]

[1]*MQ Photonics Research Centre, Department of Physics and Astronomy, Macquarie University, NSW 2109, Australia*

A technique for line-narrowing terahertz (THz) radiation is reported in a continuous wave (CW) intracavity laser which utilises stimulated polariton scattering in a $MgO:LiNbO_3$ crystal. By inserting an etalon into the fundamental laser cavity, the linewidth of the fundamental laser field is narrowed to 80 MHz, and the linewidth of the corresponding Stokes field is also narrowed to 400 MHz.

Stimulated polariton scattering (SPS) is a non-linear process which has been successfully applied to generation of THz laser emission [1]. CW THz sources have the characteristics of being interfaced with simple detectors such as Golay cells and pyroelectrics, and their linewidth can be made very narrow, which could be utilized for high resolution THz spectroscopy [2]. In this work, we examine the effect of intracavity etalons on the linewidth of the THz emission we can generate from a CW intracavity SPS laser based on $MgO:LiNbO_3$ crystal.

The CW THz laser setup is shown in Fig.1. The laser pump source was an 880 nm, fibre-coupled laser diode. The diode output was focussed to a spot with 400 µm diameter, onto the surface of a 0.3% a.t. doped $Nd:GdVO_4$ laser crystal which had dimensions of 5 mm×5 mm×13 mm, and was coated high-reflecting (HR) R~99.994% at 1063-1173 nm and with T> 99.930% at 880 nm [3]. The fundamental resonator was formed using coated surface of the $Nd:GdVO_4$ as the input mirror $M_1$ and output mirror $M_2$ which had a radius of curvature (ROC) of 500 mm and HR coating with R>99.995% at 1063 nm.

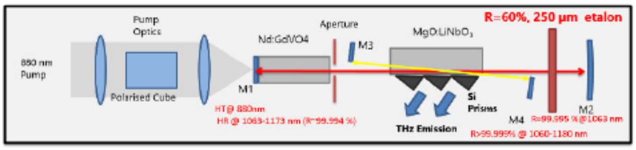


**Fig. 1 Experimental setup**

An x-cut 5% a.t. MgO-doped $LiNbO_3$ crystal with dimensions 5 mm×5 mm×20 mm was used in the THz system. Two 1 m radius of curvature D-shaped mirrors ($M_3$ and $M_4$) were used for the Stokes cavity. Both of the mirrors were HR coated R~99.999% from 1060-1080 nm. A 250 µm thickness, R=60% reflectivity etalon was inserted directly into the fundamental cavity, positioned close to the output coupler $M_2$. High resistivity silicon prisms were adhered to the emitting surface of the $MgO:LiNbO_3$ crystal to enable out-coupling of the THz field.

The power scaling characteristics of the THz emission with and without (free-running) the 250 µm thickness, R=60% etalon is shown in Fig. 2. The power of out-coupled THz field was measured using a calibrated Golay cell (Tydex, GC-1T), with a mechanical chopper (10 Hz with 50% duty-cycle). Threshold for THz generation was 2.3 W in the free-running case, and 3W with insertion of the etalon. The THz output is maintained over a wider range of pump powers when the etalon is used. We are currently investigating the reason for this effect.

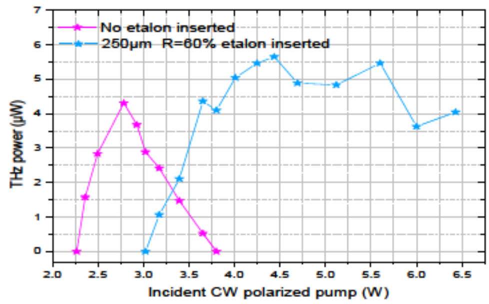


**Fig. 2 Power scaling properties of the THz output with and without the 250µm, R=60% etalon**

Based on energy conservation in the SPS process, constraining the frequencies of the fundamental and Stokes fields, results in associated constraint on the linewidth of the generated terahertz field [4]. The 250 µm thick etalon used in this work has a free spectral range of 409GHz and a finesse of 6. We examined the linewidth of the fundamental and Stokes field emission from the system using both a Bristol Wavemeter (model 771) and a Thorlabs 10 GHz Fabry-Perot Interferometer (SA210). Scans of the fundamental and Stokes field emission taken using the Fabry-Perot interferometer are shown in Fig. 3.

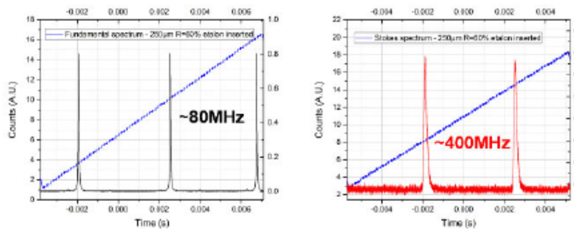


**Fig. 3 Fundamental (left) and Stokes (right) linewidths measured using the F-P interferometer**

By using the intracavity etalon, linewidth reduction of the fundamental (1063 nm) and Stokes (1070 nm) fields was achieved, going from 100 GHz to 80 MHz, and from 4 GHz to 400 MHz, respectively. The cavity lengths of the fundamental and Stokes resonators were 185 mm and 130 mm respectively, which correspond to adjacent mode spacing in each cavity of 0.69 GHz and 1.1 GHz. Our current efforts are focused on directly measuring the linewidth of the THz field.

In summary we present a linewidth narrowed CW THz laser source based on SPS in $MgO:LiNbO_3$ crystal, enabled through the use of an intracavity etalon.

**References**

[1] J. Gebwachs, R. H. Pantell, H. E. Puthoff, Appl. Phys. Lett., vol.14, No.9, pp. 258 (1969).

[2] K. Kawase, J.-i. Shikata, and H. Ito. J. Phys. D Appl. Phys. 34, R1-R14 (2001).

[3] A. Lee, H. Pask, Opt. Lett., vol. 39, No.3, pp. 442-445, (2014).

[4] D. J. M. Stothard, T. J. Edwards, D. Walsh, C. L. Thomson, et.al., Appl. Phys. Lett. 92, 141105 (2008).

# References

[1] I. Hosako, N. Sekine, M. Patrashin, S. Saito, K. Fukunaga, Y. Kasai, P. Baron, T. Seta, J. Mendrok, S. Ochiai, *et al.* *At the dawn of a new era in terahertz technology*. Proceedings of the IEEE **95**(8), 1611 (2007).

[2] J. Chamberlain. *Where optics meets electronics: recent progress in decreasing the terahertz gap*. Philosophical Transactions of the Royal Society of London A: Mathematical, Physical and Engineering Sciences **362**(1815), 199 (2004).

[3] S. Withington. *Terahertz astronomical telescopes and instrumentation*. Philosophical Transactions of the Royal Society of London A: Mathematical, Physical and Engineering Sciences **362**(1815), 395 (2004).

[4] P. H. Siegel. *THz instruments for space*. IEEE Transactions on Antennas and Propagation **55**(11), 2957 (2007).

[5] P. de Maagt. *Terahertz technology for space and earth applications*. In *2007 International workshop on Antenna Technology: Small and Smart Antennas Metamaterials and Applications*, pp. 111–115 (IEEE, 2007).

[6] T. W. Crowe, T. Globus, D. L. Woolard, and J. L. Hesler. *Terahertz sources and detectors and their application to biological sensing*. Philosophical Transactions of the Royal Society of London A: Mathematical, Physical and Engineering Sciences **362**(1815), 365 (2004).

[7] E. Pickwell and V. Wallace. *Biomedical applications of terahertz technology*. Journal of Physics D: Applied Physics **39**(17), R301 (2006).

[8] J. F. Federici, B. Schulkin, F. Huang, D. Gary, R. Barat, F. Oliveira, and D. Zimdars. *THz imaging and sensing for security applications-explosives, weapons and drugs*. Semiconductor Science and Technology **20**(7), S266 (2005).

[9] M. C. Kemp. *Millimetre wave and terahertz technology for detection of concealed threats-a review*. In *Infrared and Millimeter Waves, 2007 and the 2007 15th International Conference on Terahertz Electronics. IRMMW-THz. Joint 32nd International Conference on*, pp. 647–648 (IEEE, 2007).

[10] T. Kleine-Ostmann and T. Nagatsuma. *A review on terahertz communications research*. Journal of Infrared, Millimeter, and Terahertz Waves **32**(2), 143 (2011).

[11] H.-J. Song and T. Nagatsuma. *Present and future of terahertz communications*. IEEE Transactions on Terahertz Science and Technology **1**(1), 256 (2011).

[12] D. Zimdars, J. S. White, G. Stuk, A. Chernovsky, G. Fichter, and S. Williamson. *Large area terahertz imaging and non-destructive evaluation applications*. Insight-Non-Destructive Testing and Condition Monitoring **48**(9), 537 (2006).

[13] J. Jackson, M. Mourou, J. Whitaker, I. Duling III, S. Williamson, M. Menu, and G. Mourou. *Terahertz imaging for non-destructive evaluation of mural paintings*. Optics Communications **281**(4), 527 (2008).

[14] J. Qin, Y. Ying, and L. Xie. *The detection of agricultural products and food using terahertz spectroscopy: a review*. Applied Spectroscopy Reviews **48**(6), 439 (2013).

[15] Z. Yan, Y. Ying, H. Zhang, and H. Yu. *Research progress of terahertz wave technology in food inspection*. In *Terahertz Physics, Devices, and Systems*, vol. 6373, p. 63730R (International Society for Optics and Photonics, 2006).

[16] G. P. Williams. *Filling the THz gap-high power sources and applications*. Reports on Progress in Physics **69**(2), 301 (2005).

[17] S. Wietzke, C. Jansen, C. Jördens, N. Krumbholz, N. Vieweg, M. Scheller, M. Shakfa, D. Romeike, T. Hochrein, M. Mikulics, *et al. Industrial applications of THz systems*. In *International Symposium on Photoelectronic Detection and Imaging 2009: Terahertz and High Energy Radiation Detection Technologies and Applications*, vol. 7385, p. 738506 (International Society for Optics and Photonics, 2009).

[18] E. Linfield. *Terahertz applications: A source of fresh hope*. Nature Photonics **1**(5), 257 (2007).

[19] P. H. Siegel. *Terahertz technology*. IEEE Transactions on Microwave Theory and Techniques **50**(3), 910 (2002).

[20] P. H. Siegel. *Terahertz technology in biology and medicine*. IEEE Transactions on Microwave Theory and Techniques **52**(10), 2438 (2004).

[21] B. B. Hu and M. C. Nuss. *Imaging with terahertz waves*. Optics Letters **20**(16), 1716 (1995).

[22] D. Mittleman. *Terahertz imaging*. In *Sensing with Terahertz Radiation*, pp. 117–153 (Springer, 2003).

[23] S. Nakajima, H. Hoshina, M. Yamashita, C. Otani, and N. Miyoshi. *Terahertz imaging diagnostics of cancer tissues with a chemometrics technique*. Applied Physics Letters **90**(4), 041102 (2007).

[24] A. Dobroiu, M. Yamashita, Y. N. Ohshima, Y. Morita, C. Otani, and K. Kawase. *Terahertz imaging system based on a backward-wave oscillator*. Applied Optics **43**(30), 5637 (2004).

[25] T. Shibuya and K. Kawase. *THz tomography*. In *Terahertz Spectroscopy and Imaging*, pp. 433–449 (Springer, 2012).

[26] M. Tonouchi. *Cutting-edge terahertz technology*. Nature photonics **1**(2), 97 (2007).

[27] B. Gorshunov, A. Volkov, I. Spektor, A. Prokhorov, A. Mukhin, M. Dressel, S. Uchida, and A. Loidl. *Terahertz bwo-spectrosopy*. International Journal of Infrared and Millimeter Waves **26**(9), 1217 (2005).

[28] M. Yalandin, G. Smirnov, V. Shpak, and S. Shunailov. *High-power repetitive millimeter range back-wave oscillators with nanosecond relativistic electron beam*. In *IEEE Pulsed Power Conference*, vol. 9, pp. 388–388 (Institute of Electrical Engineers Inc (IEEE), 1993).

[29] Q.-L. Liu, Z.-C. Wang, P.-K. Liu, C.-H. Du, H.-Q. Li, and A.-Y. Xu. *A THz backward-wave oscillator based on a double-grating rectangular waveguide*. IEEE Transactions on Electron Devices **60**(4), 1463 (2013).

[30] E. Grosse. *THz radiation from free electron lasers and its potential for cell and tissue studies*. Physics in Medicine & Biology **47**(21), 3755 (2002).

[31] A. G. Stepanov, J. Hebling, and J. Kuhl. *Efficient generation of subpicosecond terahertz radiation by phase-matched optical rectification using ultrashort laser pulses with tilted pulse fronts*. Applied Physics Letters **83**(15), 3000 (2003).

[32] J. Hebling, A. Stepanov, G. Almási, B. Bartal, and J. Kuhl. *Tunable THz pulse generation by optical rectification of ultrashort laser pulses with tilted pulse fronts*. Applied Physics B **78**(5), 593 (2004).

[33] S.-G. Park, Y. Choi, Y.-J. Oh, and K.-H. Jeong. *Terahertz photoconductive antenna with metal nanoislands*. Optics Express **20**(23), 25530 (2012).

[34] X. Ropagnol, F. Blanchard, T. Ozaki, and M. Reid. *Intense terahertz generation at low frequencies using an interdigitated ZnSe large aperture photoconductive antenna*. Applied Physics Letters **103**(16), 161108 (2013).

[35] J. Faist, F. Capasso, D. L. Sivco, C. Sirtori, A. L. Hutchinson, and A. Y. Cho. *Quantum cascade laser*. Science **264**(5158), 553 (1994).

[36] B. S. Williams. *Terahertz quantum-cascade lasers*. Nature photonics **1**(9), 517 (2007).

[37] J. Faist, L. Ajili, G. Scalari, M. Giovannini, M. Beck, M. Rochat, H. Beere, A. G. Davies, E. H. Linfield, and D. Ritchie. *Terahertz quantum cascade lasers*. Philosophical Transactions of the Royal Society of London A: Mathematical, Physical and Engineering Sciences **362**(1815), 215 (2004).

[38] S. Kumar. *Recent progress in terahertz quantum cascade lasers*. IEEE Journal of Selected Topics in Quantum Electronics **17**(1), 38 (2011).

[39] Y. J. Ding. *Progress in terahertz sources based on difference-frequency generation*. Journal of the Optical Society of America B **31**(11), 2696 (2014).

[40] A. J. Deninger, T. Göbel, D. Schönherr, T. Kinder, A. Roggenbuck, M. Köberle, F. Lison, T. Müller-Wirts, and P. Meissner. *Precisely tunable continuous-wave terahertz source with interferometric frequency control*. Review of Scientific Instruments **79**(4), 044702 (2008).

[41] M. Tang, H. Minamide, Y. Wang, T. Notake, S. Ohno, and H. Ito. *Tunable terahertz-wave generation from DAST crystal pumped by a monolithic dual-wavelength fiber laser*. Optics Express **19**(2), 779 (2011).

[42] Y. Jiang, Y. J. Ding, and I. B. Zotova. *Power scaling of widely-tunable monochromatic terahertz radiation by stacking high-resistivity GaP plates*. Applied Physics Letters **96**(3), 031101 (2010).

[43] W. Shi and Y. J. Ding. *Continuously tunable and coherent terahertz radiation by means of phase-matched difference-frequency generation in zinc germanium phosphide*. Applied Physics Letters **83**(5), 848 (2003).

[44] P. Zhao, S. Ragam, Y. J. Ding, and I. B. Zotova. *Compact and portable terahertz source by mixing two frequencies generated simultaneously by a single solid-state laser*. Optics Letters **35**(23), 3979 (2010).

[45] A. Angeluts, V. Bezotosnyi, E. Cheshev, G. Goltsman, M. Finkel, S. Seliverstov, M. Evdokimov, M. Gorbunkov, G. K. Kitaeva, A. Koromyslov, *et al. Compact 1.64 THz source based on a dual-wavelength diode end-pumped Nd:YLF laser with a nearly semiconfocal cavity*. Laser Physics Letters **11**(1), 015004 (2013).

[46] T. Tanabe, K. Suto, J. Nishizawa, T. Kimura, and K. Saito. *Frequency-tunable high-power terahertz wave generation from GaP*. Journal of Applied Physics **93**(8), 4610 (2003).

[47] K. Vodopyanov and Y. H. Avetisyan. *Optical terahertz wave generation in a planar GaAs waveguide*. Optics Letters **33**(20), 2314 (2008).

[48] J. Kiessling, I. Breunig, P. Schunemann, K. Buse, and K. Vodopyanov. *High power and spectral purity continuous-wave photonic THz source tunable from 1 to 4.5 THz for nonlinear molecular spectroscopy*. New Journal of Physics **15**(10), 105014 (2013).

[49] K. Kawase, J.-i. Shikata, and H. Ito. *Terahertz wave parametric source*. Journal of Physics D: Applied Physics **35**(3), R1 (2002).

[50] W. Wang, Z. Cong, X. Chen, X. Zhang, Z. Qin, G. Tang, N. Li, C. Wang, and Q. Lu. *Terahertz parametric oscillator based on KTiOPO$_4$ crystal*. Optics letters **39**(13), 3706 (2014).

[51] T. Edwards, D. Walsh, M. Spurr, C. Rae, M. Dunn, and P. Browne. *Compact source of continuously and widely-tunable terahertz radiation*. Optics Express **14**(4), 1582 (2006).

[52] A. Lee, Y. He, and H. Pask. *Frequency-Tunable THz Source Based on Stimulated Polariton Scattering in Mg:LiNbO$_3$ crystal*. IEEE Journal of Quantum Electronics **49**(3), 357 (2013).

[53] A. J. Lee and H. M. Pask. *Continuous wave, frequency-tunable terahertz laser radiation generated via stimulated polariton scattering*. Optics Letters **39**(3), 442 (2014).

[54] T. A. Ortega, H. M. Pask, D. J. Spence, and A. J. Lee. *Frequency-tunable THz polariton laser based on intracavity RbTiOPO$_4$ crystal*. In *Infrared, Millimeter, and Terahertz waves (IRMMW-THz), 2016 41st International Conference on*, pp. 1–2 (IEEE, 2016).

[55] D. Walsh, D. Stothard, T. Edwards, P. G. Browne, C. Rae, and M. Dunn. *Injection-seeded intracavity terahertz optical parametric oscillator*. Journal of the Optical Society of America B **26**(6), 1196 (2009).

[56] A. J. Lee and H. M. Pask. *Cascaded stimulated polariton scattering in a Mg: LiNbO$_3$ terahertz laser*. Optics Express **23**(7), 8687 (2015).

[57] C. Yan, Y. Wang, D. Xu, W. Xu, P. Liu, D. Yan, P. Duan, K. Zhong, W. Shi, and J. Yao. *Green laser induced terahertz tuning range expanding in KTiOPO$_4$ terahertz parametric oscillator*. Applied Physics Letters **108**(1), 011107 (2016).

[58] J. Gelbwachs, R. Pantell, H. Puthoff, and J. Yarborough. *A tunable stimulated Raman oscillator*. Applied Physics Letters **14**(9), 258 (1969).

[59] J. Yarborough, S. Sussman, H. Purhoff, R. Pantell, and B. Johnson. *Efficient, tunable optical emission from $LiNbO_3$ without a resonator*. Applied Physics Letters **15**(3), 102 (1969).

[60] S. S. Sussman. *Tunable light scattering from transverse optical modes in lithium niobate*. Tech. rep., STANFORD UNIV CA MICROWAVE LAB (1970).

[61] M. Piestrup, R. Fleming, and R. Pantell. *Continuously tunable submillimeter wave source*. Applied Physics Letters **26**(8), 418 (1975).

[62] I. Shoji, T. Kondo, A. Kitamoto, M. Shirane, and R. Ito. *Absolute scale of second-order nonlinear-optical coefficients*. Journal of the Optical Society of America B **14**(9), 2268 (1997).

[63] R. W. Boyd. *Nonlinear Optics* (Elsevier, 2003).

[64] T. A. Ortega, H. M. Pask, D. J. Spence, and A. J. Lee. *Stimulated polariton scattering in an intracavity $RbTiOPO_4$ crystal generating frequency-tunable THz output*. Optics Express **24**(10), 10254 (2016).

[65] T. A. Ortega, H. M. Pask, D. J. Spence, and A. J. Lee. *THz polariton laser using an intracavity Mg:$LiNbO_3$ crystal with protective Teflon coating*. Optics Express **25**(4), 3991 (2017).

[66] A. J. Lee, D. J. Spence, and H. M. Pask. *Tunable THz polariton laser based on 1342 nm wavelength for enhanced terahertz wave extraction*. Optics Letters **42**(14), 2691 (2017).

[67] J.-i. Shikata, K. Kawase, K.-i. Karino, T. Taniuchi, and H. Ito. *Tunable terahertz-wave parametric oscillators using $LiNbO_3$ and MgO:$LiNbO_3$ crystals*. IEEE Transactions on Microwave Theory and Techniques **48**(4), 653 (2000).

[68] K. Kawase, M. Sato, T. Taniuchi, and H. Ito. *Coherent tunable THz-wave generation from $LiNbO_3$ with monolithic grating coupler*. Applied Physics Letters **68**(18), 2483 (1996).

[69] L. Xu, X.-C. Zhang, and D. Auston. *Terahertz beam generation by femtosecond optical pulses in electro-optic materials*. Applied Physics Letters **61**(15), 1784 (1992).

[70] K. Kawase, M. Sato, K. Nakamura, T. Taniuchi, and H. Ito. *Unidirectional radiation of widely tunable THz wave using a prism coupler under noncollinear phase matching condition*. Applied Physics Letters **71**(6), 753 (1997).

[71] K. Kawase, J.-i. Shikata, H. Minamide, K. Imai, and H. Ito. *Arrayed silicon prism coupler for a terahertz-wave parametric oscillator*. Applied optics **40**(9), 1423 (2001).

[72] T. Ikari, X. Zhang, H. Minamide, and H. Ito. *THz-wave parametric oscillator with a surface-emitted configuration*. Optics Express **14**(4), 1604 (2006).

[73] J.-i. Shikata, M. Sato, T. Taniuchi, H. Ito, and K. Kawase. *Enhancement of terahertz-wave output from $LiNbO_3$ optical parametric oscillators by cryogenic cooling*. Optics Letters **24**(4), 202 (1999).

[74] K. Ken-ichi, S. Jun-ichi, K. Kodo, I. Hiromasa, and S. Ietaka. *Terahertz-wave parametric generation characteristics of MgO: $LiNbO_3$*. Electronics and Communications in Japan (Part II: Electronics) **85**(4), 22 (2002).

[75] T. Ikari, R. Guo, H. Minamide, and H. Ito. *Energy scalable terahertz-wave parametric oscillator using surface-emitted configuration*. Journal of the European Optical Society-Rapid Publications **5**(10054), 1 (2010).

[76] Z. Li, P. Bing, J. Yao, D. Xu, and K. Zhong. *High-powered tunable terahertz source based on a surface-emitted terahertz-wave parametric oscillator*. Optical Engineering **51**(9), 091605 (2012).

[77] W. Wang, X. Zhang, Q. Wang, Z. Cong, X. Chen, Z. Liu, Z. Qin, P. Li, G. Tang, N. Li, et al. *Multiple-beam output of a surface-emitted terahertz-wave parametric oscillator by using a slab MgO: $LiNbO_3$ crystal*. Optics Letters **39**(4), 754 (2014).

[78] D. H. Wu and T. Ikari. *Enhancement of the output power of a terahertz parametric oscillator with recycled pump beam*. Applied Physics Letters **95**(14), 141105 (2009).

[79] Y.-C. Chiu, Y.-C. Huang, T.-D. Wang, and G. Zhao. *Generation of 4 THz radiation from lithium-niobate off-axis THz parametric oscillator*. In *2018 43rd International Conference on Infrared, Millimeter, and Terahertz Waves (IRMMW-THz)*, pp. 1–3 (IEEE, 2018).

[80] S. Hayashi, K. Nawata, T. Taira, J.-i. Shikata, K. Kawase, and H. Minamide. *Ultra-bright continuously tunable terahertz-wave generation at room temperature*. Scientific Reports **4**, 5045 (2014).

[81] Y. Takida, S. Maeda, T. Ohira, H. Kumagai, and S. Nashima. *Noncascading THz-wave parametric oscillator synchronously pumped by mode-locked picosecond Ti: sapphire laser in doubly-resonant external cavity*. Optics Communications **284**(19), 4663 (2011).

[82] Y. Takida, T. Ohira, Y. Tadokoro, H. Kumagai, and S. Nashima. *Tunable picosecond terahertz-wave parametric oscillators based on noncollinear pump-enhanced signal-resonant cavity*. IEEE Journal of Selected Topics in Quantum Electronics **19**(1), 8500307 (2013).

[83] A. M. Warrier, R. Li, J. Lin, A. J. Lee, H. M. Pask, and D. J. Spence. *Tunable terahertz generation in the picosecond regime from the stimulated polariton scattering in a* $LiNbO_3$ *crystal*. Optics Letters **41**(18), 4409 (2016).

[84] W. Wang, Z. Cong, Z. Liu, X. Zhang, Z. Qin, G. Tang, N. Li, Y. Zhang, and Q. Lu. *Thz-wave generation via stimulated polariton scattering in* $KTiOAsO_4$ *crystal*. Optics Express **22**(14), 17092 (2014).

[85] T. A. Ortega, H. M. Pask, D. J. Spence, and A. J. Lee. *Tunable 3-6 THz polariton laser exceeding 0.1 mW average output power based on crystalline* $RbTiOPO_4$. IEEE Journal of Selected Topics in Quantum Electronics **24**(5) (2018).

[86] F. Gao, X. Zhang, Z. Cong, Z. Qin, X. Chen, Z. Liu, J. Lu, Y. Li, J. Zang, D. Wu, *et al.* *Terahertz parametric oscillator with the surface-emitted configuration in* $RbTiOPO_4$ *crystal*. Optics & Laser Technology **104**, 37 (2018).

[87] T. Kleine-Ostmann, P. Knobloch, M. Koch, S. Hoffmann, M. Breede, M. Hofmann, G. Hein, K. Pierz, M. Sperling, and K. Donhuijsen. *Continuous-wave THz imaging*. Electronics Letters **37**(24), 1461 (2001).

[88] M. Scheller, J. M. Yarborough, J. V. Moloney, M. Fallahi, M. Koch, and S. W. Koch. *Room temperature continuous wave milliwatt terahertz source*. Optics Express **18**(26), 27112 (2010).

[89] R. Sowade, I. Breunig, I. C. Mayorga, J. Kiessling, C. Tulea, V. Dierolf, and K. Buse. *Continuous-wave optical parametric terahertz source*. Optics Express **17**(25), 22303 (2009).

[90] J. Kiessling, F. Fuchs, K. Buse, and I. Breunig. *Pump-enhanced optical parametric oscillator generating continuous wave tunable terahertz radiation*. Optics Letters **36**(22), 4374 (2011).

[91] B. S. Williams, S. Kumar, Q. Hu, and J. L. Reno. *Operation of terahertz quantum-cascade lasers at 164 K in pulsed mode and at 117 K in continuous-wave mode*. Optics Express **13**(9), 3331 (2005).

[92] Q. Lu, D. Wu, S. Sengupta, S. Slivken, and M. Razeghi. *Room temperature continuous wave, monolithic tunable THz sources based on highly efficient mid-infrared quantum cascade lasers*. Scientific Reports **6**, 23595 (2016).

[93] H. M. Pask. *The design and operation of solid-state Raman lasers*. Progress in Quantum Electronics **27**(1), 3 (2003).

[94] J. A. Piper and H. M. Pask. *Crystalline Raman lasers*. IEEE Journal of Selected Topics in Quantum Electronics **13**(3), 692 (2007).

[95] A. Lee, H. M. Pask, P. Dekker, and J. Piper. *High efficiency, multi-Watt CW yellow emission from an intracavity-doubled self-Raman laser using Nd:GdVO$_4$*. Optics Express **16**(26), 21958 (2008).

[96] J. Lin, H. M. Pask, D. J. Spence, C. J. Hamilton, and G. P. Malcolm. *Continuous-wave VECSEL Raman laser with tunable lime-yellow-orange output*. Optics Express **20**(5), 5219 (2012).

[97] H. Pask, P. Dekker, R. Mildren, D. Spence, and J. Piper. *Wavelength-versatile visible and UV sources based on crystalline Raman lasers*. Progress in Quantum Electronics **32**(3-4), 121 (2008).

[98] S. Brosnan and R. Byer. *Optical parametric oscillator threshold and linewidth studies*. IEEE Journal of Quantum Electronics **15**(6), 415 (1979).

[99] K. Kawase, J.-i. Shikata, K. Imai, and H. Ito. *Transform-limited, narrow-linewidth, terahertz-wave parametric generator*. Applied Physics Letters **78**(19), 2819 (2001).

[100] A. Sato, K. Imai, K. Kawase, H. Minamide, S. Wada, and H. Ito. *Narrow-linewidth operation of a compact THz-wave parametric generator system*. Optics Communications **207**(1-6), 353 (2002).

[101] K. Kawase, H. Minamide, K. Imai, J.-i. Shikata, and H. Ito. *Injection-seeded terahertz-wave parametric generator with wide tunability*. Applied Physics Letters **80**(2), 195 (2002).

[102] K. Imai, K. Kawase, H. Minamide, and H. Ito. *Achromatically injection-seeded terahertz-wave parametric generator*. In *Terahertz Electronics Proceedings, 2002. IEEE Tenth International Conference on*, pp. 56–59 (IEEE, 2002).

[103] R. Guo, K. Akiyama, H. Minamide, and H. Ito. *All-solid-state, narrow linewidth, wavelength-agile terahertz-wave generator*. Applied Physics Letters **88**(9), 091120 (2006).

[104] S. Hayashi, K. Nawata, H. Sakai, T. Taira, H. Minamide, and K. Kawase. *High-power, single-longitudinal-mode terahertz-wave generation pumped by a microchip Nd:YAG laser*. Optics Express **20**(3), 2881 (2012).

[105] G. Tang, Z. Cong, Z. Qin, X. Zhang, W. Wang, D. Wu, N. Li, Q. Fu, Q. Lu, and S. Zhang. *Energy scaling of terahertz-wave parametric sources*. Optics Express **23**(4), 4144 (2015).

[106] K. Imai, K. Kawase, J.-i. Shikata, H. Minamide, and H. Ito. *Injection-seeded terahertz-wave parametric oscillator*. Applied Physics Letters **78**(8), 1026 (2001).

[107] D. Stothard, T. Edwards, D. Walsh, C. Thomson, C. Rae, M. Dunn, and P. G. Browne. *Line-narrowed, compact, and coherent source of widely tunable terahertz radiation*. Applied Physics Letters **92**(14), 141105 (2008).

[108] J. R. Paul, M. Scheller, A. Laurain, A. Young, S. W. Koch, and J. Moloney. *Narrow linewidth single-frequency terahertz source based on difference frequency generation of vertical-external-cavity source-emitting lasers in an external resonance cavity*. Optics Letters **38**(18), 3654 (2013).

[109] Y. Sato and T. Taira. *The studies of thermal conductivity in $GdVO_4$, $YVO_4$, and $Y_3$ $Al_5O_{12}$ measured by quasi-one-dimensional flash method*. Optics Express **14**(22), 10528 (2006).

[110] H.-D. Jiang, H.-J. Zhang, J.-Y. Wang, H.-R. Xia, X.-B. Hu, B. Teng, and C.-Q. Zhang. *Optical and laser properties of Nd:$GdVO_4$ crystal*. Optics Communications **198**(4-6), 447 (2001).

[111] http://www.castech-us.com/ndgdvo4.htm.

[112] Y. Sato and T. Taira. *Comparative study on the spectroscopic properties of Nd:$GdVO_4$ and Nd:$YVO_4$ with hybrid process*. IEEE Journal of Selected Topics in Quantum Electronics **11**(3), 613 (2005).

[113] H. Yu, J. Liu, H. Zhang, A. A. Kaminskii, Z. Wang, and J. Wang. *Advances in vanadate laser crystals at a lasing wavelength of 1 micrometer*. Laser & Photonics Reviews **8**(6), 847 (2014).

[114] T. Jensen, V. Ostroumov, J.-P. Meyn, G. Huber, A. Zagumennyi, and I. Shcherbakov. *Spectroscopic characterization and laser performance of diode-laser-pumped Nd:$GdVO_4$*. Applied Physics B **58**(5), 373 (1994).

[115] W. Koechner. *Solid-state Laser Engineering*, vol. 1 (Springer, 2013).

[116] T. Omatsu, M. Okida, A. Lee, and H. Pask. *Thermal lensing in a diode-end-pumped continuous-wave self-Raman Nd-doped $GdVO_4$ laser*. Applied Physics B **108**(1), 73 (2012).

[117] http://www.las-cad.com/.

[118] H. Kogelnik and T. Li. *Laser beams and resonators*. Applied Optics **5**(10), 1550 (1966).

[119] D. Romanini, A. Kachanov, N. Sadeghi, and F. Stoeckel. *CW cavity ring down spectroscopy*. Chemical Physics Letters **264**(3-4), 316 (1997).

[120] G. Sridhar, S. K. Agarwalla, S. Singh, and L. Gantayet. *Cavity ring-down technique for measurement of reflectivity of high reflectivity mirrors with high accuracy*. Pramana **75**(6), 1233 (2010).

[121] Y. Furukawa, K. Kitamura, S. Takekawa, K. Niwa, and H. Hatano. *Stoichiometric Mg:LiNbO$_3$ as an effective material for nonlinear optics*. Optics Letters **23**(24), 1892 (1998).

[122] D. E. Zelmon, D. L. Small, and D. Jundt. *Infrared corrected sellmeier coefficients for congruently grown lithium niobate and 5 mol.% magnesium oxide–doped lithium niobate*. Journal of the Optical Society of America B **14**(12), 3319 (1997).

[123] X. Wu, C. Zhou, W. R. Huang, F. Ahr, and F. X. Kärtner. *Temperature dependent refractive index and absorption coefficient of congruent lithium niobate crystals in the terahertz range*. Optics Express **23**(23), 29729 (2015).

[124] Y. Furukawa, A. Yokotani, T. Sasaki, H. Yoshida, K. Yoshida, F. Nitanda, and M. Sato. *Investigation of bulk laser damage threshold of lithium niobate single crystals by Q-switched pulse laser*. Journal of Applied Physics **69**(5), 3372 (1991).

[125] S. M. Sze and K. K. Ng. *Physics of semiconductor devices* (John wiley & sons, 2006).

[126] D. G. Peterson and A. Yariv. *Interferometry and laser control with solid Fabry–Perot étalons*. Applied Optics **5**(6), 985 (1966).

[127] https://commons.wikimedia.org/wiki/File:Golay_Cell_Schematic.png.

[128] M. J. Golay. *Theoretical consideration in heat and infra-red detection, with particular reference to the pneumatic detector*. Review of Scientific Instruments **18**(5), 347 (1947).

[129] M. J. Golay. *The theoretical and practical sensitivity of the pneumatic infrared detector*. Review of Scientific Instruments **20**(11), 816 (1949).

[130] http://www.tydexoptics.com/products/thz_devices/golay_cell/.

[131] https://oceanoptics.com/.

[132] https://www.bristol-inst.com/products/spectrum-analyzers/771-series-laser-spectrum-analyzer.

[133] A. A. Michelson and E. W. Morley. *On the relative motion of the earth and of the luminiferous ether*. Sidereal Messenger, vol. 6, pp. 306-310 **6**, 306 (1887).

[134] P. Hariharan. *Basics of Interferometry* (Academic Press, 2010).

[135] https://www.thorlabs.com/.

[136] A. W. Lee and Q. Hu. *Real-time, continuous-wave terahertz imaging by use of a microbolometer focal-plane array*. Optics Letters **30**(19), 2563 (2005).

[137] N. Karpowicz, H. Zhong, J. Xu, K.-I. Lin, J.-S. Hwang, and X. Zhang. *Comparison between pulsed terahertz time-domain imaging and continuous wave terahertz imaging*. Semiconductor Science and Technology **20**(7), S293 (2005).

[138] V. Lupei, N. Pavel, Y. Sato, and T. Taira. *Highly efficient 1063-nm continuous-wave laser emission in Nd:GdVO$_4$*. Optics Letters **28**(23), 2366 (2003).

[139] Y. Ma, X. Yu, and X. Li. *Performance improvement in a directly 879 nm dual-end-$\pi$-polarized-pumped CW and pulsed GdVO$_4$/Nd:GdVO$_4$ laser*. Applied Optics **51**(5), 600 (2012).

[140] Y.-F. Lü, J. Xia, J.-G. Wang, G.-C. Sun, X.-H. Zhang, A.-F. Zhang, X.-D. Yin, L. Bao, and H. Quan. *High-efficiency Nd:GdVO$_4$ laser at 1341 nm under 880 nm diode laser pumping into the emitting level*. Optics Communications **282**(17), 3565 (2009).

[141] Y. Lü, X. Zhang, J. Xia, A. Zhang, X. Yin, and L. Bao. *Highly efficient continuous-wave 912 nm Nd:GdVO$_4$ laser emission under direct 880 nm pumping*. Laser Physics Letters **6**(11), 796 (2009).

[142] N. Pavel and T. Taira. *High-power continuous-wave intracavity frequency-doubled Nd:GdVO$_4$/-LBO laser under diode pumping into the emitting level*. IEEE Journal of Selected Topics in Quantum Electronics **11**(3), 631 (2005).

[143] Y.-F. Lü, J. Xia, J.-G. Wang, X.-H. Zhang, L. Bao, H. Quan, and X.-D. Yin. *Highly efficient Nd:GdVO$_4$/BiBO laser at 456 nm under direct 880 nm diode laser pumping*. Optics Communications **282**(24), 4793 (2009).

[144] Y. Lü, X. Zhang, J. Xia, X. Yin, A. Zhang, L. Bao, D. Wang, and H. Quan. *Highly efficient intracavity frequency-doubled Nd:GdVO$_4$-LBO red laser at 670 nm under direct 880 nm pumping*. Laser Physics **19**(12), 2174 (2009).

[145] P. Dekker, H. M. Pask, and J. A. Piper. *All-solid-state 704 mW continuous-wave yellow source based on an intracavity, frequency-doubled crystalline raman laser*. Optics Letters **32**(9), 1114 (2007).

[146] A. J. Lee, H. M. Pask, J. A. Piper, H. Zhang, and J. Wang. *An intracavity, frequency-doubled $BaWO_4$ Raman laser generating multi-Watt continuous-wave, yellow emission*. Optics Express **18**(6), 5984 (2010).

[147] H. Yu, Z. Li, A. J. Lee, J. Li, H. Zhang, J. Wang, H. M. Pask, J. A. Piper, and M. Jiang. *A continuous wave $SrMoO_4$ raman laser*. Optics Letters **36**(4), 579 (2011).

[148] P. Dekker, H. M. Pask, D. J. Spence, and J. A. Piper. *Continuous-wave, intracavity doubled, self-raman laser operation in Nd:$GdVO_4$ at 586.5 nm*. Optics Express **15**(11), 7038 (2007).

[149] J. Lin and H. Pask. *Nd:$GdVO_4$ self-Raman laser using double-end polarised pumping at 880 nm for high power infrared and visible output*. Applied Physics B **108**(1), 17 (2012).

[150] Y.-F. Chen. *Design criteria for concentration optimisation in scaling diode end-pumped lasers to high powers: influence of thermal fracture*. IEEE Journal of Quantum Electronics **35**(2), 234 (1999).

[151] L. McDonagh, R. Wallenstein, R. Knappe, and A. Nebel. *High-efficiency 60 W $TEM_{00}$ Nd:$YVO_4$ oscillator pumped at 888 nm*. Optics Letters **31**(22), 3297 (2006).

[152] J. R. Schwesyg, M. Falk, C. R. Phillips, D. H. Jundt, K. Buse, and M. M. Fejer. *Pyroelectrically induced photorefractive damage in magnesium-doped lithium niobate crystals*. Journal of the Optical Society of America B **28**(8), 1973 (2011).

[153] O. Althoff and E. E. Kraetzig. *Strong light-induced refractive index changes in $LiNbO_3$*. In *Nonlinear Optical Materials III*, vol. 1273, pp. 12–20 (International Society for Optics and Photonics, 1990).

[154] F. Chen. *Optically induced change of refractive indices in $LiNbO_3$ and $LiTaO_3$*. Journal of Applied Physics **40**(8), 3389 (1969).

[155] D. Bryan, R. Gerson, and H. Tomaschke. *Increased optical damage resistance in lithium niobate*. Applied Physics Letters **44**(9), 847 (1984).

[156] Y. Furukawa, M. Sato, F. Nitanda, and K. Ito. *Growth and characterization of mgo-doped linbo3 for electro-optic devices*. Journal of Crystal Growth **99**(1-4), 832 (1990).

[157] Y. Furukawa, K. Kitamura, S. Takekawa, A. Miyamoto, M. Terao, and N. Suda. *Photorefraction in* $LiNbO_3$ *as a function of Li/Nb and MgO concentrations*. Applied Physics Letters **77**(16), 2494 (2000).

[158] M. Nakamura, S. Higuchi, S. Takekawa, K. Terabe, Y. Furukawa, and K. Kitamura. *Optical damage resistance and refractive indices in near-stoichiometric MgO-doped* $LiNbO_3$. Japanese Journal of Applied Physics **41**(1A), L49 (2002).

[159] E. Yablonovitch, D. Hwang, T. Gmitter, L. Florez, and J. Harbison. *Van der waals bonding of GaAs epitaxial liftoff films onto arbitrary substrates*. Applied Physics Letters **56**(24), 2419 (1990).

[160] Private Communication with Andrew Lee and David Spence.

[161] X. Yu, K. Zhang, J. Gao, F. Chen, X. Li, R. Yan, J. Yu, and Y. Wang. *Quasi-three-level* $Nd{:}GdVO_4$ *laser under diode pumping directly into the emitting level*. Laser Physics Letters **5**(11), 797 (2008).

[162] N. Pavel. *In-band pumping of Nd-based solid-state lasers*. Romanian Reports in Physics **60**(4), 995 (2008).

[163] X. Li, X. Yu, F. Chen, R. Yan, J. Yu, and D. Chen. *Laser properties of continuous-grown* $Nd{:}GdVO_4/YVO_4$ *and* $YVO_4$ *composite crystals under direct pumping*. Optics Express **17**(15), 12869 (2009).

[164] A. Danylov. *Thz laboratory measurements of atmospheric absorption between 6% and 52% relative humidity*. Submillimeter-Wave Technology Laboratory University of Massachusetts Lowell, http://stl. uml. edu (2006).

[165] M. Leidinger, K. Buse, and I. Breunig. *Influence of dry-oxygen-annealing on the residual absorption of lithium niobate crystals in the spectral range from 500 to 2900 nanometers*. Optical Materials Express **6**(1), 264 (2016).

[166] H.-B. Liu, H. Zhong, N. Karpowicz, Y. Chen, and X.-C. Zhang. *Terahertz spectroscopy and imaging for defense and security applications*. Proceedings of the IEEE **95**(8), 1514 (2007).

[167] G. M. Bonner, J. Lin, A. J. Kemp, J. Wang, H. Zhang, D. J. Spence, and H. M. Pask. *Spectral broadening in continuous-wave intracavity Raman lasers*. Optics Express **22**(7), 7492 (2014).

[168] R. Casula, J.-P. Penttinen, A. J. Kemp, M. Guina, and J. E. Hastie. *1.4 μm continuous-wave diamond Raman laser*. Optics Express **25**(25), 31377 (2017).

[169] H. Danielmeyer. *Stabilized efficient single-frequency Nd: YAG laser*. IEEE Journal of Quantum Electronics **6**(2), 101 (1970).

[170] M. Hercher. *Tunable single mode operation of gas lasers using intracavity tilted etalons*. Applied Optics **8**(6), 1103 (1969).

[171] W. R. Leeb. *Losses introduced by tilting intracavity etalons*. Applied Physics **6**(2), 267 (1975).

[172] T. T. Basiev, A. A. Sobol, P. G. Zverev, V. V. Osiko, and R. C. Powell. *Comparative spontaneous Raman spectroscopy of crystals for Raman lasers*. Applied Optics **38**(3), 594 (1999).

[173] C. Pedersen, P. L. Hansen, T. Skettrup, and P. Buchhave. *Diode-pumped single-frequency Nd:YVO$_4$ laser with a set of coupled resonators*. Optics Letters **20**(12), 1389 (1995).

[174] Anthony E. Siegman. *Lasers*, vol. 1 (University Science Book, 1986).

[175] D. J. Spence *et al. Spatial and spectral effects in continuous-wave intracavity Raman lasers*. IEEE J. Sel. Top. Quantum Electron. **21**(1), 1400108 (2015).